

REPORT DOCUMENTATION PAGE				Form Approved OMB No. 0704-0188	
Public reporting burden for this collection of information is estimated to average 1 hour per response, including the time for reviewing instructions, searching existing data sources, gathering and maintaining the data needed, and completing and reviewing this collection of information. Send comments regarding this burden estimate or any other aspect of this collection of information, including suggestions for reducing this burden to Department of Defense, Washington Headquarters Services, Directorate for Information Operations and Reports (0704-0188), 1215 Jefferson Davis Highway, Suite 1204, Arlington, VA 22202-4302. Respondents should be aware that notwithstanding any other provision of law, no person shall be subject to any penalty for failing to comply with a collection of information if it does not display a currently valid OMB control number. PLEASE DO NOT RETURN YOUR FORM TO THE ABOVE ADDRESS.					
1. REPORT DATE (MM/DD/YYYY) January 2014		2. REPORT TYPE Thesis		3. DATES COVERED (From - To) 1/2/2011 – 12/31/2013	
4. TITLE AND SUBTITLE Multi-phase Combustion and Transport Processes Under the Influence of Acoustic Excitation				5a. CONTRACT NUMBER	
				5b. GRANT NUMBER	
				5c. PROGRAM ELEMENT NUMBER	
6. AUTHOR(S) Jeffrey L. Wegener				5d. PROJECT NUMBER	
				5e. TASK NUMBER	
				5f. WORK UNIT NUMBER Q0YA	
7. PERFORMING ORGANIZATION NAME(S) AND ADDRESS(ES) Air Force Research Laboratory (AFMC) AFRL/RQRC 10 E. Saturn Blvd. Edwards AFB, CA 93524				8. PERFORMING ORGANIZATION REPORT NO.	
9. SPONSORING / MONITORING AGENCY NAME(S) AND ADDRESS(ES) Air Force Research Laboratory (AFMC) AFRL/RQR 5 Pollux Drive. Edwards AFB, CA 93524				10. SPONSOR/MONITOR'S ACRONYM(S)	
				11. SPONSOR/MONITOR'S REPORT NUMBER(S) AFRL-RQ-ED-OT-2013-287	
12. DISTRIBUTION / AVAILABILITY STATEMENT Approved for public release; distribution unlimited.					
13. SUPPLEMENTARY NOTES Ph.D. Mechanical Engineering Thesis; UCLA; PA No. 14080.					
14. ABSTRACT This experimental study examined the coupling of acoustics with reactive multiphase transport processes and shear flows. The first portion of this dissertation deals with combustion of various liquid fuels when under the influence of externally applied acoustic excitation. For this study, an apparatus at the Energy and Propulsion Research Laboratory, UCLA, used a horizontal waveguide to create a standing acoustic wave, wherein burning fuel droplets were positioned near pressure nodes within the waveguide. Alcohol fuels (ethanol and methonal) as well as aviation fuel replacements (Fischer-Tropsch (FT) synfuel and an FT blend with JP-8) were studied here. During acoustic excitation, the flame surrounding the droplet was observed to be deflected in a manner consistent with the direction of a theoretical acoustic radiation force, analogous to a buoyancy force, acting on the burning system. The second portion of this dissertation utilized a similar, but more advanced facility which was recently constructed at the Air Force Research Laboratory, Propulsion Directorate (RQR). These experiments explored the interaction between acoustics and nonreactive shear-coaxial jets under high chamber pressure, acoustically resonant conditions, using liquid nitrogen as the inner jet and gaseous helium as the outer jet.					
15. SUBJECT TERMS					
16. SECURITY CLASSIFICATION OF:			17. LIMITATION OF ABSTRACT	18. NUMBER OF PAGES	19a. NAME OF RESPONSIBLE PERSON
a. REPORT	b. ABSTRACT	c. THIS PAGE			Douglas G. Talley
Unclassified	Unclassified	Unclassified	SAR	283	19b. TELEPHONE NO (include area code) 661 275-6174

UNIVERSITY OF CALIFORNIA
Los Angeles

**Multi-phase Combustion and Transport Processes
Under the Influence of Acoustic Excitation**

A dissertation submitted in partial satisfaction
of the requirements for the degree
Doctor of Philosophy in Mechanical Engineering

by

Jeffrey L. Wegener

2014

ABSTRACT OF THE DISSERTATION

Multi-phase Combustion and Transport Processes Under the Influence of Acoustic Excitation

by

Jeffrey L. Wegener

Doctor of Philosophy in Mechanical Engineering

University of California, Los Angeles, 2014

Professor Ann R. Karagozian, Chair

This experimental study examined the coupling of acoustics with reactive multi-phase transport processes and shear flows. The first portion of this dissertation deals with combustion of various liquid fuels when under the influence of externally applied acoustic excitation. For this study, an apparatus at the Energy and Propulsion Research Laboratory, UCLA, used a horizontal waveguide to create a standing acoustic wave, wherein burning fuel droplets were positioned near pressure nodes within the waveguide. Alcohol fuels (ethanol and methonal) as well as aviation fuel replacements (Fischer-Tropsch (FT) synfuel and an FT blend with JP-8) were studied here. During acoustic excitation, the flame surrounding the droplet was observed to be deflected in a manner consistent with the direction of a theoretical acoustic radiation force, analogous to a buoyancy force, acting on the burning system. Based on this degree of deflection, a method was developed for experimentally quantifying the acoustic acceleration and relating it to the theoretical acoustic acceleration. This technique employed phase-locked optical imaging of the flame in the ultraviolet band in order to capture hydroxyl radical (OH^*) chemiluminescence as an indication of the flame structure and shape. The flame was observed to be deflected in a bulk manner, but also with micro-scale oscillations in

time. The bulk or mean flame alteration was used to determine an experimental value of the acoustic acceleration for a range of different fuels and excitation conditions. This investigation showed experimentally determined acoustic accelerations which were quite consistent qualitatively with theory, but which were quantitatively inconsistent with theoretical predictions. Observed flame deformations were greatest for a droplet situated immediately next to a pressure node, in contrast to the theory, while milder flame deflections were observed for droplets positioned closer to a pressure antinode. These observations were consistent among all fuels studied, qualitatively and with the same mean qualitative trends. Phase-locked OH^* chemiluminescence imaging revealed significant differences in the amplitude of flame oscillation based on the applied frequency and droplet location. Low frequency acoustic excitation and proximity to the pressure node produced higher amplitude flame oscillations, suggesting an enhanced degree of acoustically-coupled combustion that could be responsible for qualitative differences between theory and experimental measurements of acoustic acceleration.

The second portion of this dissertation utilized a similar, but more advanced facility which was recently constructed at the Air Force Research Laboratory, Propulsion Directorate (RQR). These experiments explored the interaction between acoustics and nonreactive shear-coaxial jets under high chamber pressure, acoustically resonant conditions, using liquid nitrogen as the inner jet and gaseous helium as the outer jet. The shear-coaxial jet was placed within the chamber, for which piezoelectric sirens could create a standing wave. The coaxial jet could thus be situated at either a pressure node or a pressure antinode location, and backlit high-speed imaging was used to resolve the naturally unstable mixing layer between the inner and outer jets. For jets with and without exposure to acoustic forcing, two different reduced basis methods were applied to the gray-scale pixel intensity data in order to extract instability frequencies and mode shapes from image sets; these included proper orthogonal decomposition (POD) and dynamic mode decomposition (DMD). A new POD-based method was used to quantify the

susceptibility of coaxial jets to external acoustic forcing by comparing the pixel intensity variance induced by the acoustic mode to the total variance of pixel intensity caused by fluctuations in jet mixing. A novel forcing susceptibility diagram was then created for coaxial jet momentum flux ratios of 2 and 6 for both pressure node and pressure antinode locations. Measurements of the critical forcing amplitude were made to quantify the acoustic perturbation amplitudes required in order for the forced mode to overtake the natural mode as the most dominant instability in the jet, which is generally classified as “lock-in” to the applied mode. It was found that, for forcing frequencies greater than the natural frequency of the jet, an increase in the forcing frequency caused the jet to be less susceptible to applied acoustic disturbances, thus requiring higher acoustic forcing to achieve “lock-in”. This relationship held true for both pressure node and pressure antinode conditions. The shear layer instability characteristics of unforced jets were also investigated, and a theoretical convection velocity which depends on inner and outer jet velocities and densities was validated for the range of experimental flow conditions used in this study. An extensive description of the design of the experimental reactive facility is also offered, including preliminary results for oxygen-hydrogen coaxial jet flames acquired using high-speed OH* chemiluminescence imaging.

The dissertation of Jeffrey L. Wegener is approved.

Chris R. Anderson

Jeff D. Eldredge

Ivett A. Leyva

Owen I. Smith

Ann R. Karagozian, Committee Chair

University of California, Los Angeles

2014

to Samantha and Ian

TABLE OF CONTENTS

1	Introduction and Background	1
1.1	Combustion Instabilities	2
1.1.1	Physical Mechanisms	2
1.1.2	Gas Turbine Engines	7
1.1.3	Liquid Rocket Engines	8
1.2	Fuel Droplet Combustion	13
1.2.1	Alternative Fuels	13
1.2.2	Fundamental Droplet Combustion	15
1.2.3	Effects of Acoustics on Fuel Droplet Combustion	16
1.3	Shear-Coaxial Jets	21
1.3.1	Nonreactive Shear-Coaxial Jets	21
1.3.2	Reactive Shear-Coaxial Jets	39
1.4	Present Studies	46
2	Experimental Facility and Methods - Acoustically Coupled Fuel Droplet Combustion	56
2.1	Acoustic Waveguide	56
2.2	Droplet Generation and Ignition	60
2.3	Imaging	60
2.3.1	Optics	61
2.3.2	Image Acquisition	62

2.3.3	Acoustics-Imaging Synchronization	63
2.4	Measurement Methods	64
2.4.1	Burning Rate Constant	64
2.4.2	Acoustic Acceleration	65
2.4.3	Flame Standoff Distance	66
2.5	Experimental Procedure	67
2.6	Measurement Uncertainties	69
2.6.1	Precision Uncertainty	69
2.6.2	Bias Uncertainty	71
3	Results - Acoustically Coupled Fuel Droplet Combustion	86
3.1	Burning Rate Constant	86
3.1.1	Baseline Burning Rate Constant	86
3.1.2	Effect of Acoustics on Burning Rate Constant	87
3.2	Flame Behavior	88
3.2.1	Flame Deflection and Acoustic Acceleration	89
3.2.2	Standoff Distance	92
4	Experimental Facility and Methods - Shear-Coaxial Jets	116
4.1	High Pressure Chamber and Fluid Delivery Systems	117
4.1.1	Chamber	117
4.1.2	Propellant Systems	117
4.2	Inner Chamber	126
4.2.1	Inner Chamber Dimensions and Instrumentation	126

4.2.2	Inner Chamber Nitrogen Flows	127
4.3	Waveguide Design and Characterization	127
4.3.1	Acoustic Drivers	128
4.3.2	Waveguide	129
4.3.3	Resonant Frequencies	132
4.4	Nonreactive Jet Imaging	136
4.5	Reduced Basis Methods	137
4.5.1	Proper Orthogonal Decomposition	137
4.5.2	Application of Proper Orthogonal Decomposition	142
4.5.3	Dynamic Mode Decomposition	146
4.5.4	Application of Dynamic Mode Decomposition	152
4.6	Measurement Uncertainty	155
5	Results - Shear-Coaxial Jets	182
5.1	Qualitative Observations of Liquid Nitrogen-Gaseous Helium Shear-Coaxial Jets	182
5.2	Comparisons of POD and DMD	186
5.3	Susceptibility of Nitrogen-Helium Shear-Coaxial Jets to Acoustic Forcing	191
5.3.1	Unforced Shear-Coaxial Jets	192
5.3.2	Shear-Coaxial Jets Subject to Acoustic Forcing	197
6	Conclusions and Future Work	226
6.1	Studies on Acoustically-coupled Droplet Combustion	226
6.2	Studies on Shear-coaxial Jets	227

A	Shear-Coaxial Jet Experimental Methods Details	230
A.1	Acoustic Forcing System	230
A.2	Positive Semidefinite Proof	232

LIST OF FIGURES

1.1	Bimodal combustion instability feedback loop.	47
1.2	Three-part combustion instability feedback loop.	47
1.3	Photos of the Delta IV and Ariane 5 launch vehicles.	48
1.4	LRE gas generator cycle diagram.	48
1.5	Hydrogen temperature ramping plot for a LRE stability verification test.	49
1.6	Various configurations of the shear-coaxial injector element.	49
1.7	Diagram of the nonreactive shear-coaxial jet.	50
1.8	Liquid core break up images for coaxial jets of the membrane and fibre-type regime.	51
1.9	A convective shear layer diagrammed in the vortex frame of reference.	51
1.10	Five regimes of liquid-gas coaxial jet break up plotted with respect to Re and We	52
1.11	Liquid nitrogen-gaseous helium coaxial jets issuing into subcritical and supercritical environments.	52
1.12	Velocity ratio plotted versus density ratio with absolute-convective instability transition lines.	53
1.13	Flow diagram of a reactive shear-coaxial jet.	54
1.14	Combustion instability feedback with controlled acoustic forcing.	55
2.1	Experimental setup of the acoustic waveguide and feed droplet system.	76
2.2	Frequency sweep for the speaker-speaker configuration with speakers operated 180° out-of-phase and a PN occurring at the center of the waveguide.	77

2.3	Frequency sweep for the speaker-speaker configuration with speakers operated in-phase (0°) and a PAN occurring at the center of the waveguide.	78
2.4	Frequency sweep for the speaker-reflector configuration.	79
2.5	Acoustic pressure amplitude measurements for the speaker-reflector configuration.	80
2.6	Acoustic pressure amplitude measurements for the speaker-speaker configuration ($\phi = 180^\circ$).	81
2.7	Acoustic pressure amplitude measurements for the speaker-speaker configuration ($\phi = 0^\circ$).	82
2.8	OH* chemiluminescence optics	83
2.9	Transmission versus wavelength for the optical system.	84
2.10	OH* chemiluminescence image for ethanol under acoustic forcing.	85
2.11	Abel transformed ethanol flame image.	85
3.1	OH* chemiluminescence images of burning droplets in the absence of acoustic forcing.	98
3.2	Pressure perturbations, estimated theoretical and actual acoustic accelerations g_a , and average burning rate constant K as a function of waveguide location for the ethanol droplet burning in the vicinity of a pressure node at a frequency of 332 Hz and $p'_{max} = 150$ Pa.	99
3.3	Pressure perturbations, estimated theoretical and actual acoustic accelerations g_a , and average burning rate constant K as a function of waveguide location for the ethanol droplet burning in the vicinity of a pressure node at a frequency of 898 Hz and $p'_{max} = 150$ Pa.	100

3.4	Pressure perturbations, estimated theoretical and actual acoustic accelerations g_a , and average burning rate constant K as a function of waveguide location for the ethanol droplet burning in the vicinity of a pressure node at a frequency of 1500 Hz and $p'_{max} = 150$ Pa.	101
3.5	Pressure perturbations, estimated theoretical and actual acoustic accelerations g_a , and average burning rate constant K as a function of waveguide location for the methanol droplet burning in the vicinity of a pressure node at a frequency of 332 Hz and $p'_{max} = 150$ Pa.	102
3.6	Pressure perturbations, estimated theoretical and actual acoustic accelerations g_a , and average burning rate constant K as a function of waveguide location for the methanol droplet burning in the vicinity of a pressure node at a frequency of 898 Hz and $p'_{max} = 150$ Pa.	103
3.7	Pressure perturbations, estimated theoretical and actual acoustic accelerations g_a , and average burning rate constant K as a function of waveguide location for the methanol droplet burning in the vicinity of a pressure node at a frequency of 1500 Hz and $p'_{max} = 150$ Pa.	104
3.8	Pressure perturbations, estimated theoretical and actual acoustic accelerations g_a , and average burning rate constant K as a function of waveguide location for the FT droplet burning in the vicinity of a pressure node at a frequency of 332 Hz and $p'_{max} = 150$ Pa.	105
3.9	Pressure perturbations, estimated theoretical and actual acoustic accelerations g_a , and average burning rate constant K as a function of waveguide location for the FT droplet burning in the vicinity of a pressure node at a frequency of 898 Hz and $p'_{max} = 150$ Pa.	106

3.10	Pressure perturbations, estimated theoretical and actual acoustic accelerations g_a , and average burning rate constant K as a function of waveguide location for the FT droplet burning in the vicinity of a pressure node at a frequency of 1500 Hz and $p'_{max} = 150$ Pa.	107
3.11	Pressure perturbations, estimated theoretical and actual acoustic accelerations g_a , and average burning rate constant K as a function of waveguide location for the JP8FT droplet burning in the vicinity of a pressure node at a frequency of 332 Hz and $p'_{max} = 150$ Pa.	108
3.12	Pressure perturbations, estimated theoretical and actual acoustic accelerations g_a , and average burning rate constant K as a function of waveguide location for the JP8FT droplet burning in the vicinity of a pressure node at a frequency of 898 Hz and $p'_{max} = 150$ Pa.	109
3.13	Pressure perturbations, estimated theoretical and actual acoustic accelerations g_a , and average burning rate constant K as a function of waveguide location for the JP8FT droplet burning in the vicinity of a pressure node at a frequency of 1500 Hz and $p'_{max} = 150$ Pa.	110
3.14	Ethanol flame images under the influence of acoustics. Flames are consistently deflected away from the pressure node (PN).	111
3.15	A pair of ethanol flame images acquired at different points within the acoustic cycle.	111
3.16	Horizontal flame standoff distance plotted versus the acoustic pressure phase. All fuels and acoustic frequencies are shown for three select waveguide locations.	112
3.17	Standoff distance oscillation amplitude plotted versus waveguide location.	113
3.18	Time-averaged standoff distance plotted versus waveguide location. . . .	114

3.19	Time-averaged standoff distance plotted versus theoretical acoustic acceleration.	114
3.20	Time-averaged standoff distance plotted versus nondimensional horizontal velocity	115
4.1	Three-dimensional CAD rendering of the AFRL combustion chamber. . .	161
4.2	Oxygen heat exchanger diagram.	162
4.3	Hydrogen heat exchanger diagram.	163
4.4	Time series plot of a typical firing sequence.	164
4.5	Minimum inner jet temperatures with oxygen flow.	165
4.6	Minimum outer jet temperatures with helium flow.	166
4.7	Minimum inner and outer jet temperatures with nitrogen flow.	167
4.8	Experimental facility parametric mapping of density ratio S vs. chamber pressure p_c	168
4.9	The dimensions of the coaxial injector used for new experiments in this study.	168
4.10	Cross sectional CAD view of the shear-coaxial injector.	169
4.11	Experimental facility parametric mapping of inner jet Reynolds number Re_{ij} vs. outer jet Reynolds number Re_{oj}	170
4.12	Shear-coaxial jet velocity profile diagram.	171
4.13	Experimental facility parametric mapping of momentum flux ratio J vs. mixture ratio MR	172
4.14	Acoustic pressure spectra results for both the left and right piezo sirens when placed outside of the combustion chamber.	173
4.15	Diagram of a rigid-walled duct of variable cross-sectional area $A(y)$. . .	174

4.16	Chamber cross sectional area plotted versus the transverse direction y , including the left waveguide, inner chamber, and right waveguide.	174
4.17	Acoustic frequency sweep results for PAN conditions at various chamber pressures.	175
4.18	A single row of matrix \mathbf{A} constructed from an $m \times n$ image for POD analysis.	176
4.19	Matrix \mathbf{A} constructed from N images and M pixels for POD analysis. . .	176
4.20	Instantaneous, time-averaged, and cropped image samples.	177
4.21	POD singular values computed for $J = 2$ and $f_F = 2050$ Hz at a PN. . .	177
4.22	POD eigenvalues computed for $J = 2$ and $f_F = 2050$ Hz at a PN.	178
4.23	POM images for mode-1 and mode-2 at $J = 2$ and $f_F = 2050$ Hz at a PN.	178
4.24	PSD spectra for POD mode-1 at $J = 2$ and $f_F = 2050$ Hz at a PN. . . .	179
4.25	CPSD spectra for POD modes-1 and mode-2 at $J = 2$ and $f_F = 2050$ Hz at a PN.	180
4.26	Mode frequencies, amplitudes, and growth rates identified by DMD for $J = 2$ and $f_F = 2050$ Hz at a PN.	181
4.27	Reconstructed images of the unstable mode identified by DMD at $J = 2$ and $f_F = 2050$ Hz at a PN.	181
5.1	Enlarge sample of the shear-coaxial jet field of view, accompanied by snapshot samples.	206
5.2	Sample of four consecutive OH* chemiluminescence snapshots.	207
5.3	Cross power spectral density for modes 3 and 4 of an unforced jet at $J = 6$.	208
5.4	POD eigenvalues computed for $J = 2$ without acoustic forcing.	209
5.5	Reconstructed jet images for POMs 1-12 for an unforced jet at $J = 6$. . .	210

5.6	PSD and eigenvector images shown for mode-3 and mode-4, representing the natural mode pair for $J = 6$	211
5.7	Mode frequencies, amplitudes, and growth rates identified by DMD for $J = 6$ without acoustic forcing.	212
5.8	Instability frequency versus shear layer convective velocity.	213
5.9	Jet Strouhal number versus J using a theoretical convection velocity. . .	214
5.10	Time-average coaxial jet image which defines the inner shear layer curve s . .	214
5.11	The pixels located on the inner shear layer curve s plotted versus time. .	215
5.12	Measured shear layer convection velocity $U_{c,meas}$ versus a theoretical convection velocity $U_{c,th}$	216
5.13	Jet Strouhal number versus J using a measured convection velocity. . .	216
5.14	Forcing susceptibility diagram for a shear-coaxial jet at a PN.	217
5.15	LN ₂ -GHe shear-coaxial jets exposed to acoustic forcing at a PN.	218
5.16	PSD and eigenvector images shown for mode-2 and mode-3, representing the forced mode pair for $J = 2$ at a PN.	219
5.17	Forced mode variance contribution versus forcing amplitude (PN).	220
5.18	Forcing susceptibility diagram for a shear-coaxial jet at a PN.	221
5.19	LN ₂ -GHe shear-coaxial jets exposed to acoustic forcing at a PAN.	222
5.20	PSD and eigenvector images shown for mode-1 and mode-2, representing the forced mode pair for $J = 2$ at a PAN.	223
5.21	Forced mode variance contribution versus forcing amplitude (PAN). . . .	224
5.22	Forced mode variance contribution versus a nondimensional forcing amplitude (PAN).	225

A.1	Piezoelectric acoustic siren.	235
A.2	Cross sectional CAD rendering of the left waveguide.	235
A.3	Acoustic forcing flow chart.	236
A.4	Acoustic pressure spectra results for $p_c=400$ psia.	237
A.5	Facility piping and instrumentation diagram (PID) page 1.	238
A.6	Facility piping and instrumentation diagram (PID) page 2.	239

LIST OF TABLES

2.1	Experimental and Theoretical Resonant Frequencies	73
2.2	Fuel Properties	74
2.3	Camera Specifications	75
3.1	Comparison of measured values of burning rate constant K for various fuel droplets in the absence of acoustic excitation.	97
4.1	AFRL injector dimensions.	159
4.2	Pressure transducer uncertainty values.	160
A.1	Data for unforced LN ₂ -GHe nonreactive experiments.	233
A.2	Data for acoustically forced LN ₂ -GHe nonreactive experiments.	234

NOMENCLATURE

Symbols or Abbreviations

\mathbf{A}	matrix form of pixel intensities for an image set
$\tilde{\mathbf{A}}$	matrix form of mean pixel intensities for an image set (POD)
a	set of pixel intensities for an image set
c	speed of sound
\mathbf{D}	eigenvalue matrix (DMD)
f	frequency
f_F	acoustic forcing frequency
f_{nat}	natural jet instability frequency
g_a	acoustic acceleration
g_o	gravitational acceleration
I	acoustic intensity
J	outer-to-inner jet momentum flux ratio
K	burning rate constant
L	distance between acoustic drivers
M	number of pixels in one image
MR	oxygen-to-fuel mixture ratio
N	number of images
Oh	Ohnesorge number
p_c	mean chamber pressure
p'	pressure perturbation

Symbols or Abbreviations (continued)

Q_v	volumetric flow rate
R	outer-to-inner jet velocity ratio
\mathbf{R}	covariance matrix (POD)
Re	Reynolds number
S	outer-to-inner jet density ratio
$\tilde{\mathbf{S}}$	companion matrix (DMD)
St	Strouhal number
T_∞	ambient temperature
\mathbf{U}	orthogonal matrix containing temporal information (POD)
U_∞	bulk flow velocity
U_c	shear layer convection velocity
u_k	vector of temporal amplitude coefficients for mode k (POD)
u'	velocity perturbation
\mathbf{V}	orthogonal matrix containing spatial information (POD)
v_k	vector of proper orthogonal mode k (POD)
We	Weber number
z_a	acoustic impedance

Greek Symbols

α	density difference correction factor
ϕ	phase
ϕ_f	flame deflection angle
$\phi_{f/o}$	fuel-to-oxygen equivalence ratio
Λ	product of the singular value matrix and its transpose (POD)
λ	acoustic wavelength
ω	complex eigenvalues (DMD)
ρ	density
Σ	diagonal matrix singular values (POD)

Subscripts

B	buoyancy
$eqvs$	equivalent volume of a sphere
exp	experimental
f	flame
i	imaginary
ij	inner jet
oj	outer jet
p	hot combustion products
R	acoustic radiation
r	real
s	surface
th	theoretical
II	image intensifier

ACKNOWLEDGMENTS

The shear-coaxial jet experimental work was sponsored by the Air Force Office of Scientific Research (AFOSR), Laboratory Task 11RZ07COR, under Dr. Mitat Birkan, program manager, and facility development support was provided by AFRL Commander's Revitalization Funds. AFOSR must also be thanked for the equipment grant that allowed the Energy and Propulsion Laboratory at UCLA to purchase the NanoStar Camera, without which ultraviolet imaging of burning droplet experiments would not be possible. I am also thankful for the departmental fellowship I received from the UCLA Mechanical and Aerospace Engineering Department, which allowed me to begin full-time graduate study in the 2009-2010 academic year. The department also supported me as a Teaching Assistant for the 2010-2011 academic year.

I owe Drs. Doug Talley and Ivett Leyva for this opportunity. I was entrusted with a tremendous amount of responsibility during the construction of this facility, and as a result, I am better prepared for what lies ahead. Many of my tasks involved on-the-job training, which required patience on their part. Much of this on-the-job training occurred under the watch of Randy Harvey. Randy is a technician with the analytical approach of an engineer. Working with Randy, I was confident someone was always watching over me and ready to catch my engineering mistakes. Together, Randy and I built a spectacular machine which will bear fruit for many years. I am also indebted to Dr. David Forliti for emphasizing scientific education and fundamental research where basic engineering and facility validation often took precedence. Thanks to his emphasis, this dissertation contains merit with regard to both scientific research and facility engineering. Finally, I thank Prof. Ann Karagozian for trusting me and my abilities, even when progress was much slower than expected. Her encouragement was a boost of confidence when I needed it the most.

VITA

2003	High School Diploma, Raytown High School, Raytown, MO
2007	B.S. Mechanical Engineering, Missouri Univ. of Science and Technology (ST)
2007-2009	Departmental Fellowship, Mechanical and Aerospace Engineering Department, Missouri ST
2009	M.S. Mechanical Engineering, Missouri ST
2009	Propulsion Research Scientist, Air Force Research Laboratory (AFRL), Edwards AFB, CA
2009-2010	Departmental Fellowship, Mechanical and Aerospace Engineering Department, UCLA
2010	Teaching Assistant, Mechanical and Aerospace Engineering Department, UCLA. MAE 157 - Basic Mechanical Engineering Laboratory
2011	Teaching Assistant, Mechanical and Aerospace Engineering Department, UCLA. MAE 150C - Combustion
2011	M.S. Aerospace Engineering, UCLA
2011-2013	Graduate Student Researcher, AFRL, Edwards AFB, CA
2013	American Institute of Aeronautics and Astronautics (AIAA) Liquid Propulsion Student of the Year

PUBLICATIONS AND PRESENTATIONS

J.L. Wegener, I.A. Leyva, D.J. Forliti, and D.G. Talley, Development of a Facility for Combustion Stability Experiments at Supercritical Pressure, 52nd AIAA Aerospace Sciences Meeting, National Harbor, MD, January 13-17, 2014.

C.I. Sevilla-Esparza, J.L. Wegener, S. Teshome, J.I. Rodriguez, O.I. Smith, and A.R. Karagozian, Droplet Combustion in the Presence of Acoustic Excitation, to be published in Combustion and Flame.

J.L. Wegener, C. Sevilla, J. Smolke, A. Sung, K. Chen, O.I. Smith, and A.R. Karagozian, Transient OH* Chemiluminescence Imaging of Acoustically Coupled Fuel Droplet Combustion, APS/DFD Meeting, Baltimore, MD, November 20-22, 2011.

H. Lan, J.L. Wegener, B.F. Armaly, and J.A. Drallmeier, Simulations and Measurements of 3-D Gravity Driven Liquid Film Flow, J. Fluids Eng., Vol. 132, 081301, 2010.

J.L. Wegener and J.A. Drallmeier, Measurement of Thin Liquid Film Characteristics using Laser Focus Displacement Instruments for Atomization Applications, 22nd Annual ILASS-Americas Conference, Cincinnati, OH, May 16-19, 2010.

J.L. Wegener, M.A. Friedrich, J.A. Drallmeier, and B.F. Armaly, Experimental Validation of a Film Separation Criterion, 11th Triennial ICLASS Conference, Vail, CO, July 26-30, 2009.

CHAPTER 1

Introduction and Background

Acoustic fluctuations are coupled to condensed phase combustion in an array of important power generation and propulsion applications, including liquid rocket engines (LREs), gas turbine engines, and other air-breathing engines. Although each combustion system exhibits unique problems caused by acoustic fluctuations, a broad view of the field reveals an inability to suppress combustion instabilities due to a lack of fundamental knowledge regarding the coupling of combustion and acoustics. The inability to control these instabilities has led to engine and engine component failures in the case of liquid rocket and gas turbine engines, and a consequential increase in combustion instability research.

This study contributes to this field by isolating the problem in two ways. First, a set of alternative fuel combustion experiments performed at the UCLA Energy and Propulsion Research Laboratory investigate the behavior of burning droplets placed within standing acoustic waveforms. Second, a study at the advanced experimental facility of the Air Force Research Laboratory at Edwards AFB, CA explores coaxial, cryogenic non-reactive and reactive jets in the presence of strong acoustic forcing in a high pressure chamber. Each respective study concentrates effort towards behaviors which have a direct impact on the instabilities observed in the predominant applications (gas turbine engines and LREs). Such behaviors include but are not limited to acoustically altered fuel burning rates, droplet flame deformations, and acoustically enhanced jet mixing and atomization. These phenomena hold paramount importance in that they impact

performance, efficiency, and robustness of the system.

1.1 Combustion Instabilities

Combustion instabilities are characterized by large amplitude oscillations of one or more acoustic modes or injector modes of a combustion chamber. The pressure and velocity perturbations produced by these instabilities are problematic because they result in thrust oscillations, severe vibrations that interfere with control system operation, increased heat transfer and thermal stresses to combustor walls, oscillatory mechanical loads that fatigue hardware components, and flame blowoff or flashback [1]. This study provides an overview of combustion instability by first describing the physical mechanisms which fundamentally create the phenomena. The physical mechanisms section is followed by discussion of instability in two primary power systems. A brief background of combustion instabilities in gas turbine engines is given first, due to its relevance to the fuel droplet combustion results in chapter 3. This is followed by a historical summary of LRE combustion instability, which is directly related to the shear-coaxial jet research of chapter 5. A literature review is then presented for fundamental research of fuel droplet combustion and shear-coaxial jets.

1.1.1 Physical Mechanisms

In the most fundamental sense, a system's stability relies on competing mechanisms of driving and damping. The stability of a combustion system and its associated heat release as shown in Fig. 1.1 is determined by acoustic feedback, which can cause driving or damping. The genesis of acoustics though, often lies in unsteady heat release generated by changes in local propellant reaction rates. These changes in reaction rate can also be governed by fuel-oxidizer mixing fluctuations in the flame region. In this case a third

mechanism, fluid mixing, is the origin of unsteady heat release and thus, the production of acoustic energy [2]. A discussion on the combustion instability feedback loop, then, will begin here with a fluid dynamics mechanism.

This physical sequence of events is depicted in Fig. 1.2, which is a detailed version of the more common bimodal representation in Fig. 1.1 [3–5]. The thermoacoustic feedback loop is reduced to three major phenomena, a graphical representation also utilized by Candel [6] and others [7, 8]. These three are represented by oscillations in fluid velocity u' , heat release q' , and acoustic pressure p' in Fig. 1.2, which are perturbations from the time averaged value, i.e.

$$u = \bar{u} + u' \quad (1.1)$$

$$q = \bar{q} + q' \quad (1.2)$$

$$p = \bar{p} + p' \quad (1.3)$$

Reactive flows can exhibit velocity oscillations due to several perturbation sources, many of which naturally occur in the absence of the acoustic fluctuations. Fluid dynamic instability inherent to a reactive flow instigates the existence of thermoacoustic instability, and only after the onset of acoustic pressure perturbations will acoustic waves act upon the propellant velocity u to complete the instability feedback loop. Natural fluid dynamic instabilities can be provoked by large-scale events such as inlet flow oscillations [9], engendering shear layer instability [10] or vortex development, whereas small scale events like droplet formation and atomization can also have an important role through enhanced mixing and entrainment. High Reynolds number flows supply broadband turbulence to the flame region [11], enhancing molecular mixing processes. Flow instabilities with distinct frequencies often accompany broadband noise, asserting high amplitude velocity fluctuations, and thus mixing oscillations, in the flame region.

Ultimately, these mixing fluctuations will alter flame location and shape via changes in species concentration. This relationship is the link between “Fluid Dynamic Insta-

bility” and “Unsteady Heat Release” in Fig. 1.2. For example, inlet flow oscillations of fuel or oxidizer can globally alter mixture ratio and flame strain rates to the point of extinction [12]; this behavior is shown to be influenced by pressure [13]. Shear flow instabilities produce locally unsteady heat release due to continually changing species mass fractions and densities [14, 15], and heat release fluctuations may adopt the instability frequency naturally occurring in the shear layer. Vortex shedding may result from the puffing behavior of inlet flow oscillations [16] or from shear layer vorticity. In the case of two-phase flow, oscillatory behavior can result from differences in time scales associated with breakup, vaporization, and mixing processes. The extent to which chemical reaction processes and fluid mechanical/mixing processes control combustion is described by the Damkohler number

$$Da = \frac{\tau_m}{\tau_{ch}} \quad (1.4)$$

which is a ratio of the characteristic fluid mixing time τ_m and the characteristic reaction time τ_{ch} . For large-scale fluid structures, τ_m is often large in comparison to reaction time scales, hence combustion is limited by reactant mixing of diffusive processes. For small-scale mixing such as that which occurs during droplet atomization and reaction, τ_m is often small compared with reaction rates, and as such are instead limited by kinetics (τ_{ch}). Overall, both fluid mechanics and chemical kinetics must be considered to ascertain the controlling factor in an unsteady combustion system.

In acoustically-coupled combustion, the flame will significantly impact the fluid dynamics, making this interaction two-way coupled. The natural instability frequencies of different types of two-phase shear flows have been shown to be dependent on density, velocity, and viscosity gradients [10], which are manipulated by a flame’s temperature distribution when in the presence of a reaction. In addition, the flame’s elevated temperatures introduce rapid dilatation and alter the pressure and density distributions which can produce vorticity through baroclinic torque. Subsequently, the interdependence of

fluid dynamics and the flame create a strong coupling which is critical in combustion stability.

As spatio-temporal flame oscillations cause unsteady heat release, thermal expansion and contraction will be concomitant with pressure oscillations which propagate through the surrounding media at the speed of sound. In Fig. 1.2, the enhancement of acoustics by unsteady heat release is represented by the link between “Unsteady Heat Release” and “Acoustic Waves”. Increasing pressure perturbations may result when heat release oscillation frequencies equal resonant modes of the combustion chamber. Resonant chamber modes can be radial, tangential, longitudinal, or a mixture of the three, and are determined by geometric chamber dimensions [8, 17–19]. Acoustic pressure oscillations alone may have little direct effect on combustion processes. For example, this is supported by experiments of droplet combustion [20–22] at velocity nodes, i.e. locations of maximum pressure perturbation and zero velocity perturbation in a standing acoustic wave. In this example, there is little coupling between acoustic waves and unsteady heat release, exemplified by minimal changes in burning rate and flame shape.

However, acoustic perturbations in general have an influence on fluid dynamic processes. Both pressure nodes (PNs) ($p' = 0$, $u' = u'_{max}$) and pressure antinodes (PANs) ($p' = p'_{max}$, $u' = 0$) have a unique effect on fluid dynamic processes. Large tangential acoustic velocity oscillations at a PN act to increase mixing and vorticity by inducing additional velocity perturbations within the shear flow, and the natural mode of a shear layer may be overtaken by that of external acoustic forcing [23, 24], especially if the shear layer is convectively unstable [25]. In the case of coaxial jets, a PN condition may also intensify mixing [16, 19, 26] and create a sinuous yet cohesive jet shape [27–30]. If located at a PAN, an incoming flow may be impeded by a periodic rise in chamber pressure [16]. The resulting flow rate pulsations induce a time dependent mixture ratio MR , and large-scale yet relatively symmetric chugging instability. Flow rate pulsations

may also occur for traveling waves which can result in behaviors representative of both a PAN and a PN.

Hence, acoustic feedback serves to amplify or attenuate unsteady heat release through both pressure and velocity perturbations which affect the flow field. Past studies have described this relationship via the well-known the Rayleigh criterion [31]. The Rayleigh criterion addresses the problem using the phase relationship between pressure and heat release oscillations. This two-part approach reduces the complexities described above by including only the pressure oscillation amplitude p' and the heat release oscillation amplitude q' , and is often explained using the bimodal diagram in Fig. 1.1 [3–5]. Amplification is said to occur if the pressure perturbation p' occurs in-phase with the heat release perturbation q' . Damping occurs when p' and q' are out-of-phase. The associated Rayleigh index G is given by

$$G(x) = \frac{1}{T} \int_T p'(x, t) q'(x, t) dt \quad (1.5)$$

which integrates the pressure and heat release oscillations over the time period T to quantify the extent to which the instability is amplified ($G > 0$), or the system experiences damping ($G < 0$). The Rayleigh index is a valuable tool for measuring the coupling of acoustics and combustion or lack thereof, but it does not describe the underlying physics of combustion instability. Utilization of the Rayleigh criterion for measuring the coupling of acoustics and combustion has been used in an experimental dump combustor study by Smith and Zukoski [32] which later inspired more detailed work by Yu *et al.* [33] and Schadow and Gutmark [34] in similar geometries, where low frequency convective modes in the combustion chamber triggered pulsating inlet flow rates which resulted in uncontrolled p' amplification and positive values of the Rayleigh index G . McManus *et al.* [2] and Candel [6] review the Rayleigh criterion's use within other unsteady combustion systems. The Rayleigh criterion is an appropriate quantitative gauge of acoustic-flame coupling, but is particularly valuable in explaining causality when also

accompanied by a investigation of fluid dynamic instability in a three-part approach including heat release, pressure perturbations, and fluid mixing associated with velocity perturbations.

1.1.2 Gas Turbine Engines

The 1980s marked the start of a momentous increase in the importance of instabilities in gas turbine engines. Added attention arose from the challenges of meeting NOx emission standards, chiefly the Gas Turbine New Source Performance Standards (NSPS) in 1979 and the EPA's Best Available Control Technology (BACT) approach in 1987, which were followed by the more broad Clean Air Act Amendments of the 1990s [35, 36]. Formation of nitrogen oxides (NO_x) most commonly has an exponential dependence on temperature via the 'thermal' NO mechanism, and thus NOx reduction requires a decrease in combustor flame temperatures [37]. This is often achieved with leaner fuel-air mixtures [37], which can create lower flame temperatures. Lower flame temperatures bring the combustor closer to the lean blowout condition, where small temporal variations in fuel-air ratio can significantly affect the heat release rate, burning rate, and flame position and shape. Leaner conditions are often associated with pulsations in the flow field. The ensuing combustor pressure oscillations in gas turbines can reach amplitudes as high as 6 psi (rms). Resulting problems have included cracking of combustion chambers, fretting of the outside of the fuel injector, intolerable noise, and other damage [38, 39].

Premixing or partially-premixing of fuel and air has also been employed in gas turbine engines to reduce NOx by eliminating localized high temperatures characteristic of the presence of local diffusion flames. Yet the premixing technique has also shown to contribute to instabilities. Thus, combustion guidelines are being developed for new diffusion flame combustor concepts to eliminate potential instability problems [39]. Consequently, the renewed value of research in non-premixed flames in the presence of acous-

tics calls for salient relationships describing the behavior of jet and droplet/spray flames within acoustic flow fields. These relationships depend on fuel type, which is gaining recognition due to the increasing popularity of alternative fuels for aircraft engines [40].

1.1.3 Liquid Rocket Engines

Historically, only one propulsion method has been used for a vehicle to escape the earth's gravitational field and travel into outer space. Currently and in the near future, this technique remains chemical propulsion. Solid motors, liquid rocket engines (LREs), and hybrid engines, or a combination thereof, have been incorporated into multiple stages to provide the necessary thrust for successful launch vehicles to date [41]. Liquid rocket engines are part of the foundation of any launch vehicle's propulsion system due to their ability to endure long periods of operation with the required levels of thrust. Pairing LREs with high thrust solid rocket boosters to constitute a vehicle's first stage is a common configuration for providing greater acceleration early in flight, followed by disposal of the spent solid motors. For example, the Atlas V uses this technique, as well as the Ariane 5 and the Delta IV, shown in Fig. 1.3.

Liquid rocket engines typically achieve higher specific impulses than their solid and hybrid counterparts, but at the cost of more complexity. An LRE stores propellants as a liquid and uses a system of pipes, valves, manifolds, and injectors to feed fuel and oxidizer into the combustion chamber. In the most simple design, high pressure propellant tanks supply propellants to the chamber. The pressure-fed cycle though, requires thick-walled propellant tanks, limited chamber pressure, or a combination thereof in order to produce the required propellant flow rates. The pressure-fed cycle can be used for upper stage engines, where heavy tanks are acceptable because the upper stage constitutes a relatively small portion of the launch vehicle's total weight at low altitudes. On the other hand, first stage LREs often adopt turbopumps to drive high propellant supply

pressures and combustion chamber pressures while using low pressure tanks. There are exceptions to this rule though, and one example is the upper stage RL10 engine, driven by turbopumps. One type of pump-fed system is the gas-generator engine cycle, which is discussed here as an exemplary illustration of the intricacies within an LRE.

In a gas-generator cycle, a small amount of fuel and oxidizer flow is diverted to produce energy to drive the propellant pumps. The “gas generator” of this engine cycle burns a propellant mixture with a small flow rate and spins a turbine with the hot exhaust products before diverting the exhaust outside the engine. The pre-burner, an alternative to the gas-generator, serves a similar purpose but routes the turbine exhaust into the main combustion chamber. The fuel pump and oxygen pump can be placed on the same shaft such that both propellant pumps are driven by a single turbine, thus minimizing weight and complexity. This configuration is shown in the flow diagram in Fig. 1.4. Alternatively, the gas-generator exhaust can drive two separate turbines, one for each pump. Fuel is commonly used as a chamber and nozzle coolant by routing cold fuel through channels in the chamber and nozzle walls prior to flowing into the injector plenum. In the J-2 engine used in the Apollo program, for example, hydrogen at less than 25 K traveled through tubes welded to the outside of the nozzle wall and was subsequently heated to 110 K before reaching the hydrogen injector distribution dome [42].

These propellant feed systems, as well as the chamber’s acoustic modes and the engine structure, can interact with chamber pressure oscillations to sustain instability. The existence of pressure amplitudes exceeding the amplitude of the noise floor is considered combustion instability, and in this sense, a liquid rocket engine is never perfectly smooth. Pressure fluctuations having peak-to-peak magnitudes less than 5% of the chamber pressure, $\frac{p'}{p_c} < 0.05$, are considered “smooth” and larger amplitudes generally designate “rough” combustion [41]. However, payload considerations often can only tol-

erate combustion instabilities having amplitudes much less than 5% of p_c . Furthermore, the nondimensional value of $\frac{p'}{p_c}$ has become the most common method for quantitative evaluation of combustion instability in LREs.

Combustion instabilities are also classified with regard to frequency. Frequencies less than 400 Hz are considered low frequency instabilities, also termed “chugging” instabilities. Interaction between injector feed systems and the combustion chamber is often the cause of low frequency instability [3], whereby chamber pressure momentarily rises above the propellant supply pressure(s), impeding inlet flow and initiating pulsations in propellant flow rate. Frequencies between 400 Hz and 1000 Hz are intermediate frequency instabilities and are commonly related to vibrations of the engine structure, but can also be caused by combustion processes. High frequency instability occurs at frequencies greater than 1000 Hz. Instabilities of this type, called “screeching” instabilities, generally involve excitation of acoustically resonant chamber modes and can rapidly amplify to destructive magnitudes; this makes diagnosis and prevention very challenging.

For LREs, early recognition of combustion instabilities has lead to a vast history of research. By the 1950s, German rocket technology from the Peenemuende program had literally been moved to France, the Soviet Union, and also the United States, where slight modifications to existing German V-2 and V-4 rockets exhibited combustion instability. After changing the concave injector face of the V-4 to a flat injector arrangement for the Navaho engine [43], the Navaho was unstable until injector baffles were added in 1960 [44]. During the same period of time, the X-1 engine was developed strictly for scientific exploration by an experimental engines group in the US Department of Defense. This program identified stability problems during staged startup tests and throttling tests [45], an issue which still occurs in modern engine development programs [44].

One of the first major campaigns in the engine stability discipline occurred in the

1960s, largely motivated to suppress vibrations in human-carrying flights to the moon [46]. Of the 3200 full-scale tests of the Saturn V's F-1 engines from 1962-1966, about 2000 of these tests were principally focused on combustion instability as part of a program called Project First [47]. It was learned that injector design, which controlled interactions between jets of fuel and oxidizer, was of utmost importance. The F-1 engine, in particular, used impinging style injectors where two jets of fuel and two jets of oxygen converge on a single impingement point to atomize and burn. Injector configurations which were originally deemed as producing 'absolutely' stable engine conditions were later shown to have less stability for different fuels and flow conditions [46, 48], revealing an incomplete understanding of the problem.

In parallel, the J-2 engine was also developed in the 1960s, but with key design differences from the F-1 and much better stability characteristics. The J-2 was one of the first successful hydrogen fueled rocket engines, whereas the F-1 used kerosene based fuel (RP-1). The J-2 also utilized shear-coaxial injectors [42]. The engine's first tests resulted in high frequency instability, but was reduced to an acceptable level using radial baffles. Particular conditions also resulted in low frequency chugging, which was eliminated using a metering orifice at the inlet of the oxygen tube. This technique effectively made oxygen flow insensitive to chamber pressure perturbations by increasing the pressure drop across the injector, but did not alter the high frequency instability margin [45]. Thus, although high and low frequency modes coexisted, tolerable high frequency instability endured from its own prevailing cause. This inadequate state of the practice resulted in inefficient approaches involving many expensive tests, often in a trial-and-error method. New programs specifically dealing with combustion instabilities in liquid rockets did not appear again in the U.S. until the 1980s, which coincided with a comprehensive research program in France following the failure of an Ariane vehicle due to combustion instability in a Viking engine [49].

LRE instability testing and abatement empirical techniques have improved since the extensive tests of the F-1, but a lack of reliable design criteria has made use of these techniques a requirement for new engine development programs. As mentioned above, acoustic baffles were an early choice for unstable engines, but additional hardware was avoided due to cost and weight. Instead, engineers adopted the injector, injector plenum geometry, and acoustic cavities as primary variables to control mixing while preventing propellant flow oscillations. Margins of stability were found to be sensitive to small changes in the geometry of shear-coaxial injectors. For example, in a subscale engine study a mild recess of the oxygen tube was found to shift the range of operating conditions in which the engine was stable [50]. Fig. 1.6 shows the numerous ways in which the oxygen tube or “LO_x post” has been manipulated in the past, and one or more of these designs is still used today [45]. Stability testing, on the other hand, has been aimed at identifying three areas of operations: stable, dynamically unstable, and spontaneously unstable. When the engine is subject to an initial, controlled perturbation, or “bomb”, measured pressure oscillations will return to original levels if the engine is stable. In such tests, the chamber is required to reach stability within a limited time, which is calculated as a function of frequency. Conversely, a dynamically unstable engine will sustain significant chamber pressure oscillations after the perturbation subsides. An operating point is deemed spontaneously unstable if the engine is self-excited [51]. Finally, hydrogen temperature ramping is a stability testing method that should be mentioned due to its relevance to this study. A range of fuel temperatures is included while testing gas generator cycle and expander cycle LREs, because variables such as run time and throttle set point will determine the amount of heat energy added to the fuel upstream of the injector. Hydrogen temperature ramping has been used extensively in LH₂-LO_x engines, which is reviewed by Hulka and Hutt [45]. Hydrogen temperature variations dynamically alter fuel density, viscosity, and injector feed pressure, which can result in instability for a specific temperature band as shown in Fig. 1.5, for example.

Thus, hardware designs and stability verification tests provide the answers needed, but require a trial-and-error approach. Stability verification tests are intended for engine qualification, not engine development. Results indicate whether an engine is stable or unstable without explaining why, and this information is gathered and applied after engine development is complete. To reduce the number of design iterations and improve computational combustion tools, the community must turn to scientific research of the underlying physics.

1.2 Fuel Droplet Combustion

1.2.1 Alternative Fuels

Rapid rise in the demand for fossil fuels, combined with constricting emission regulations, is resulting in expanded interest in alternative fuel sources. Although long term goals focus on reducing dependence on crude oil, the current infrastructure requires near term solutions which involve hydrocarbons [52]. As a result, the U.S. is witnessing tremendous growth in the use of biofuels in automotive transportation, while the aircraft industry is exploring the use of fuels derived from a range of sources (coal, natural gas, etc.) from the Fischer-Tropsch (FT) process [53].

Ethanol and biodiesel have led the recent expansion of the biofuel industry. Since 2000, global ethanol and biodiesel production has increased by more than 200% and 500%, respectively, with the largest growth occurring in the U.S. [54]. Alcohols, such as ethanol and methanol, serve as gasoline substitutes with less pollutant emissions and higher octane performance [55]. However, the use of pure alcohols is unfeasible without significant changes to current engine designs. Gasoline-biofuel blends, on the other hand, maintain characteristics similar to those of gasoline and can be used in existing internal combustion (IC) engines with zero or few modifications. These blends are effective

in the current transportation infrastructure, which is cultivating a global market for blends of gasoline and 10% ethanol (E10) and 85% ethanol (E85). Thus, there remains an immediate demand for understanding the behavior of these fuels in the presence of acoustic forcing as their usage is increasingly diversified. Although the IC engine, the most popular biofuels application, features acoustic pressure waves in the intake manifold and ports [56], the term “combustion instability” is used in the realm of IC engines to describe unwanted cycle-to-cycle variation in cylinder pressures, temperatures, and species concentrations. Therefore, the effects of sound waves on IC engine combustion are quite different from that of a gas turbine combustor or liquid rocket combustion chamber. Still, suppressing or exploiting acoustics within intake systems is desired for IC engines [57], presenting a need to explore the behavior of biofuels in the presence of acoustic flow fields.

For aircraft propulsion, the use of Fischer-Tropsch (FT) fuels is seeing increased use as an alternative fuel. These synthetic fuels are produced by converting carbon based materials into liquid fuels using the Fischer-Tropsch process [58], and the USAF plans to meet half of domestic fuel needs with FT fuel by 2016. Progress toward this goal is being achieved by using a 50-50% by volume blend of JP-8 and FT fuel, and nearly the entire USAF fleet has been certified for use with this FT blend [53, 59].

Thus, near term progress in the search for alternative fuel sources is being made using multiple fuel types and blends thereof. However, increased use of these fuels must be accompanied by a better fundamental understanding of the fuels’ performance in typical engine operating conditions. As discussed previously, typical conditions often involve resonant acoustic waves, which have repercussions unique to the fuel being used. The diffusive, convective, and reactive time scales affiliated with one fuel will differ from another, altering the effects of flow instabilities on the combustion process. Therefore, the successful proliferation of alternative fuels requires studies which define the relationship

between acoustic fluctuations and combustion processes for each fuel.

1.2.2 Fundamental Droplet Combustion

Droplet combustion plays a role in a significant portion of condensed phase combustion applications. Fuel injectors may create dilute sprays of tiny droplets, or instead liquid jets which form free ligaments and then break up into large droplets [60, 61]. In either scenario, the combustion of the field of droplets is largely governed by the combustion of individual droplets. Therefore, fundamental studies of the combustion of a single droplet offer conclusions which apply to a field of many burning droplets in a fuel spray. Such studies involve spherical or semi-spherical droplets, which are placed in quiescent flow or convective flow with slip. A diffusion flame front forms away from the droplet surface where fuel vapor, evaporated from the droplet surface, diffuses into and reacts with the oxidizer, usually air. Aside from sprays, droplet combustion is often used as a model for heterogeneous combustion in general [62].

Droplet sizes and lifetimes for quasi-steady droplet burning are described by the well-known d^2 law [63, 64]:

$$d^2(t) = d^2(t = 0) - Kt \quad (1.6)$$

where the square of the droplet diameter d varies linearly with time t according to the burning rate constant K . The d^2 law has been shown to accurately describe droplet burning for spherical droplets in micro-gravity environments and semi-spherical droplets in normal gravity, but in the latter case the scaled diameter of an equivalent spherical droplet is required [65], as described below.

Micro-gravity droplet burning experiments provide ideal conditions for application of the d^2 law. Without gravitational forces, the droplet and the surrounding flame both maintain a spherical shape. This setting provides for straightforward determination of the droplet diameter d and thus the burning rate constant K . Experimental validation

of the d^2 law in micro-gravity conditions is shown by Law and Faeth [62] and Marchese *et al.* [66, 67], among many others. Work by Marchese *et al.* also includes imaging of electronically excited hydroxyl (OH^*) radical chemiluminescence for the flame surrounding the droplet in order to validate the accuracy of a droplet combustion model, but more importantly, to confirm OH^* chemiluminescence as an appropriate flame location indicator. For both fuels used, methanol and n-heptane, this is confirmed as an appropriate technique. To the knowledge of the current author, work by Dattarajan *et al.* [22] is the only set of experiments utilizing OH^* chemiluminescence imaging for burning droplets in acoustically forced conditions. This technique is used for micro-gravity and normal gravity conditions, and Dattarajan *et al.* also successfully uses the d^2 law in quantifying burning rate constants for both sets of experiments.

Both micro-gravity and normal gravity environments require additional steps in the application of the d^2 law due to alterations in the shape of the droplet and flame. A more ellipsoidal droplet shape is formed by the balance of weight (for normal gravity) and surface tension, and is addressed by using an equivalent diameter d_{eqvs} , which is determined as the diameter of a sphere with a volume equal to that of the non-spherical droplet [65]. In normal gravity, the natural convection caused by thermal buoyancy creates an elongated flame shape with variations in flame standoff distance. Thus, the droplet combustion phenomena in normal gravity require understanding of steady flow effects even in the absence of forced convection. Still, the d^2 law has shown accuracy for droplets in non-quiescent flows [68, 69] when d_{eqvs} is used.

1.2.3 Effects of Acoustics on Fuel Droplet Combustion

Burning droplets exhibit salient changes in behavior when exposed to acoustic forcing. First and foremost, this has been documented by several experimental works which show burning rate constants increased by surrounding acoustic flow fields. Early observation

of the influence of acoustic forcing on burning rate is documented by Kumagai and Isoda [68], where an increase in the burning rate is thought to occur due to greater mass and heat transfer rates at the droplet surface due to steeper temperature gradients and species concentration gradients. This relationship has since been further explored by several others, including various studies by Saito *et al.* [70, 71]. Saito *et al.* [70, 71] record the effects of burning kerosene droplets in a normal gravity environment when the droplet is positioned near a pressure node (PN) or pressure antinode (PAN) of a standing acoustic wave. Locations of maximum and minimum velocity perturbations coincide with the location of a PN and PAN, respectively. Results show evaporation and burning rate constants of the burning droplet near a PN which are more than twice that of the unforced case, while positions near a PAN yield no significant alteration of these behaviors when compared to the unforced case.

Experiments performed in micro-gravity environments, on the other hand, lack the natural convective flow caused by thermal buoyancy, and thus isolate the effects of acoustic forcing. Burning droplets in zero gravity conditions are examined by several experimentalists [20–22, 72, 73]. Okai *et al.* [72] explore the influence of frequency and oscillation amplitude for n-octane single droplets and droplet pairs. Results show burning rates having a dependence on amplitude, with burning rates increasing with amplitude until flame extinction occurs, which is an event requiring more detailed inspection conducted by others [74, 75]. Experiments by Tanabe *et al.* [20, 21] confirm the burning rate conclusions noted above for both micro-gravity and normal gravity with n-decane droplets. Their studies situate the droplet at a pressure node, or between a pressure node and antinode of a standing acoustic wave. Moreover, their work reveals flame deformations in the presence of acoustic forcing, captured by flame imaging in the visible spectrum, and thus visualization of soot in the flame. Qualitative observations show flame deflections toward a PAN, or away from a PN.

To explain and predict this behavior, Tanabe *et al.* [20] propose an acoustic radiation force theory. Acoustic radiation forces are studied in a multitude of theoretical and experimental works extending back several decades. These forces are theorized and physically manifested by the existence of acoustic streaming, steady flow induced by an oscillating flow. Early experimental and theoretical study of acoustic streaming dates back more than one century [76, 77], which later allowed for theoretical formulations of the acoustic radiation force [78–80]. Expanding acoustic radiation force theory into the realm of combustion, Tanabe *et al.* [20] treat the region of hot products surrounding the droplet as a sphere of density ρ_p , which is less than the density of the gas surrounding the flame ρ_o . This discrimination between lighter and heavier gases permits a formulation from the work of Nyborg [79], where an equation is derived for the acoustic radiation force on a sphere of different density than that of the surrounding gas. Adding the assumption that $\rho_p \ll \rho_o$, Tanabe *et al.* reach an expression for the acoustic radiation force, F_R , acting on a sphere of hot products

$$F_R = \alpha(\rho_p - \rho_o)V \frac{\partial \overline{u'^2}}{\partial x} \quad (1.7)$$

where V is the volume of the sphere containing the hot products, x is the displacement of the droplet from the pressure node or pressure antinode location, and $\overline{u'^2}$ is the mean of the square of the local perturbation velocity u' . The coefficient α is defined as

$$\alpha = \frac{3\rho_o}{2(2\rho_p + \rho_o)} \quad (1.8)$$

The formulation in equation (1.7) is remarkably similar to that of a buoyancy force, which led Tanabe *et al.* to treat the acoustic radiation force acting on a burning droplet as analogous to a buoyancy force. In testing this theory, the flame behaviors observed in their imaging experiments affirm the prediction of the direction of flame deflection, where the acoustic radiation force calls for the hot products to shift towards a PAN. These experiments utilize a horizontal waveguide configuration, and thus involve only

horizontal acoustic radiation forces (i.e. parallel with sound wave propagation). The same group also tested this theory in a vertical waveguide configuration, generating forces which act upward, against thermal buoyancy forces [73]. Droplet combustion imaging in this experiment showcases a flame adopting a more spherical shell surrounding the droplet and claims gravitational forces are effectively “cancelled”, but further evidence of this behavior is unavailable.

Droplet burning rate and flame orientation are also subject to extensive study in works performed at UCLA with regard to normal gravity [75, 81, 82], and experiments led by the same group in the micro-gravity facility at the NASA Glenn Research Center [22]. These phenomena were experimentally investigated using a horizontally oriented, long cylindrical waveguide, or Kundt’s tube, either with a loudspeaker positioned at both ends or with one loudspeaker replaced by a sound reflector. Work by Dattarajan *et al.* [22] used the speaker and reflector configuration to create standing acoustic waves for methanol droplet experiments in micro-gravity. Similar to results discussed above, burning rates measured by Dattarajan *et al.* exhibit an increase over the unforced case when the droplet is located near a PN. In fact, for sound pressure levels of 135 dB, burning rate constants are as much as 200% greater than the unforced value for droplets situated near a PN. A smaller increase of 75% is shown for droplets near a PAN. For the same apparatus in normal gravity at 138 dB a smaller relative increase of 11-15% is measured for droplet near a PN, and the burning rate shows no alteration for droplets positioned near a PAN. With regard to flame deformation, the same study notes a trend in the direction of flame direction, where flames consistently deflect away from the approximate location of the PN, consistent with the theory of Tanabe *et al.* [20]. This flame deflection behavior is seen for both micro-gravity and normal gravity experiments, but with the micro-gravity conditions revealing a more obvious flame deflection direction due to the absence of thermal buoyancy.

Studies conducted solely in normal gravity by Rodriguez *et al.* [75] and Teshome *et al.* [82] offer results which agree with experiments above over a wider range of acoustic frequencies and for an array of fuels (ethanol, methanol, pure FT, and a JP-8/FT blend), but with more detail concerning the location of the burning droplet relative to the PN. Whether using a speaker-reflector configuration or a speaker-speaker configuration, the speaker assembly was moved as a unit within the waveguide while holding the droplet location constant. In this fashion, the location of the droplet could be varied with respect to the acoustic waveform. Further details on this technique are included in Section 2.1.

This technique exposes a trend of increasing burning rate as the droplet is moved from a PAN to a PN, with increases in the burning rate constant of up to 20%. These studies also give attention to the amount of flame deflection captured by imaging. Flame orientation generally agrees qualitatively with the theory of Tanabe *et al.* and with other pertinent experiments, but quantifying flame deflection brings light to certain unexplainable behavior. Imaging shows the largest deflections immediately next to a PN, with a dramatic switch in flame orientation when comparing results to the left and right of a PN. Teshome *et al.* [82] quantifies these deflections by measuring the flame deflection angle relative to the unforced, vertically oriented flame. To relate deflection angle measurements to the acoustic radiation force of Tanabe *et al.*, Teshome *et al.* balances the acoustic radiation force with the buoyancy force for the flame surrounding the droplet using a technique to be described further in 2.4.2. The resulting comparisons show that although equation (1.7) predicts flame orientation accurately, experimental results show significant quantitative differences. The trends and actual quantities evidenced by experiment are not captured by the same theory, and this is explored further in the present studies.

1.3 Shear-Coaxial Jets

A variety of coaxial jets have been used for injection of reactants in LREs. These include swirl coaxial jets, gas-centered coaxial jets, and impinging coaxial jets (shown in Fig. 1.6), to name a few. Unless otherwise noted, this study focuses hereafter on *parallel* shear-coaxial jets with an outer, annular jet of fuel and an inner jet of oxidizer, or an inert simulant in the inner jet and/or outer jet for a nonreactive configuration. Other coaxial jet types have been successful in LREs to date, but the parallel shear-coaxial jet still offers the most ideal condition for fundamental research due to its simplicity in injector design and exit flow conditions.

1.3.1 Nonreactive Shear-Coaxial Jets

1.3.1.1 General Characterization

The shear-coaxial jet involves three separate bodies of fluid in a concentric arrangement, creating two different shear layers. First, the inner jet and outer jet form the inner shear layer, where the traditionally denser fluid of the inner jet is disturbed by the surrounding outer jet, often at a higher velocity than the inner flow. A mixing layer is formed near the injector exit and increases in thickness in the streamwise direction, entraining more of the two fluids into the inner shear layer. Meanwhile, the outer shear layer forms between the outer jet and the ambient gas having zero bulk velocity. Each shear layer can exhibit large differences in velocity, density, and temperature, and as a result, become separate independent sources of instability which may interact. The two phenomena mentioned here, mixing and instability, are the primary foci of this discussion.

The streamwise development of these two shear layers was characterized in early research by Kwan and Ko [83] as shown in Fig. 1.7. Three zones are used to appropriately differentiate between regions containing an intact outer jet core, inner jet core, or the

existence of a single, fully merged jet. The region near the injector exit consists of both an intact inner jet core and outer jet core, and the downstream end of the outer jet core defines the end of the *initial merging zone*. The *intermediate zone* then, is defined as the region downstream of the outer potential core tip, but where distinguishable outer and inner mixing layers still exist. Primary vortices of the inner shear layer with convective velocity U_{c1} and secondary vortices of the outer shear layer with convective velocity U_{c2} reside in the initial merging zone, and then begin to interact in the intermediate zone. Last, the *fully merged zone* covers the region where the mixed jet behaves and appears as an equivalent single jet of equal thrust.

Important nondimensional numbers and their definitions include the outer-to-inner density ratio $S \equiv \frac{\rho_{oj}}{\rho_{ij}}$, velocity ratio $R \equiv \frac{U_{oj}}{U_{ij}}$, and the momentum flux ratio $J \equiv \frac{\rho_{oj} U_{oj}^2}{\rho_{ij} U_{ij}^2}$. These three values are the most common measures for mixing and stability relationships and traditionally, $S \ll 1$ due to the jet's denser inner core. Additionally, with comparable mass flow rates ($\dot{m}_{oj} \sim \dot{m}_{ij}$), the outer jet velocity is much greater than that of the inner jet. This is certainly true for LO_x/GH_2 applications, as well as many of the nonreactive experiments of interest in this section. Consequently, at sub-critical pressure the shear forces at the inner shear layer cause a liquid inner jet to break up in a classical cascade of ligament and droplet formation, and finally atomization. For nonreactive jets, the break up process is characterized by J , the inner jet Reynolds number $\text{Re}_{ij} \equiv \frac{U_{ij} D_1 \rho_{ij}}{\mu_{ij}}$, and the gaseous Weber number $We \equiv \frac{\rho_{oj} U_{oj}^2 D_1}{\sigma}$, where D_1 is the inner jet exit diameter and σ is the surface tension. These parameters can be used to identify multiple regimes of recognizably different break up processes [16]. Instantaneous images of inner jet break up for high We flows are shown in Fig. 1.8 due to their direct relevance to this study. More detailed characterization of mixing and stability is still subject to research.

1.3.1.2 Near-field Mixing

The earliest purported experimental study of coaxial jets was done by Forstall and Shapiro [84] for single-phase flow, where firm qualitative trends were established for the mixing of the gas inner and outer jets at atmospheric pressure. As the velocity of the air outer jet was increased, it was shown that the helium-air inner jet was less distinct. The boundary between the two jets eventually became ambiguous with downstream distance, and the streamwise position at which this occurred advanced upstream as the jet's velocity ratio increased.

Chigier and Beer [85] confirmed the general conclusions of Fortall and Shapiro [84] by quantitatively investigating the velocity distributions of air inner and outer jets issuing into quiescent air. Velocities were calculated using differential pressure measurements to give radial velocity distributions at several axial positions from the injector exit to $8D_1$ downstream. The injector used by Chigier and Beer [85] contracted the inner diameter and outer annulus near the exit rather than using a parallel shear-coaxial element. Velocity ratios ranging from 0.024 to ∞ were used to span from conditions nearly equal to a single jet and an annular jet, respectively. For a low velocity ratio, $R = 0.085$, the outer jet completely merged with the inner jet within a distance $D_2 - D_1$ from the exit and the central potential core extended far downstream similar to a single air jet. For a larger velocity ratio, $R = 2.35$, the potential core to end at a distance was just $3D_1$ from the exit.

In the 1970s, several bodies of work investigated near-field mixing of coaxial jets with attention to area ratio $AR \equiv \frac{A_{oj}}{A_{ij}}$ as well as R (Champagne and Wygnanski [86], Ko and Kwan [87], and Ko and Kwan [88]). Again, these experiments used air jets injected from contracting coaxial nozzles into air, with Reynolds numbers as high as 10^5 for each nozzle. Champagne and Wygnanski [86] noted that when increasing the outer diameter of the annulus to increase AR from 1.28 to 2.94 while holding R constant, an

increase in the outer jet potential core length was observed. However, this length was not affected by changes in R for the flow conditions used in their work ($0 < R \leq 10$). The inner jet behavior though, depended on both AR and R . In this respect, Champagne and Wygnanski [86] deduced that the outer jet core length acts similar to a single jet in the ambient gas, having little sensitivity to changes in the inner jet. Ko and Kwan [88] also compared the coaxial jet to a single jet, but clearly defined regions for each class of flow. The outer shear layer was called the *secondary mixing region*, which was deemed equivalent to a single jet in potential core length and spreading behavior. The inner shear layer was called the *primary mixing region*, which was said to function like the layer between a single jet in a co-flowing ambient gas as opposed to a co-flowing stream of finite thickness. But, experimental conditions in Ko and Kwan [88] were limited to $R < 1$ ($R=0.3, 0.5, 0.7$). The results of both groups reaffirmed the finding of previous researchers that the velocity difference ($|U_{oj} - U_{ij}|$) is positively correlated with mixing due to enhanced shear between the inner and outer jets.

An extensive array of analytical derivations and experiments on coaxial jet and two-dimensional shear layer mixing were pursued by Dimotakis [89], and later by Dahm and Dimotakis [90], Dimotakis [91], and Dahm *et al.* [92]. These works aim to describe mixing layers by quantifying mass entrainment, shear layer convection velocity, circulation, and vortex size, to name a few. Dimotakis [89] used empirical relations to derive an expression for the volume flux entrainment ratio E_v and the mean vortex spacing to position ratio $\frac{l}{x}$. More importantly, a relation for shear layer convection velocity was derived by applying the Bernoulli equation to a two-dimensional shear layer. Dimotakis [89] asserted that a stagnation point must exist between vortices when in the Galilean rest frame of the vortices, and thus, Bernoulli's equation would apply along a line through this point. Following this frame of reference in Fig. 1.9, neglecting gravity, and assuming that differences in static pressure can be ignored, then the dynamic

pressures in each free stream were matched, i.e.

$$\rho_1 (U_1 - U_c)^2 \approx \rho_2 (U_c - U_2)^2 \quad (1.9)$$

Solving for the convection velocity, as in Dahm *et al.* [92], yields

$$U_c \approx \frac{U_{ij} \rho_{ij}^{\frac{1}{2}} + U_{oj} \rho_{oj}^{\frac{1}{2}}}{\rho_{ij}^{\frac{1}{2}} + \rho_{oj}^{\frac{1}{2}}} \quad (1.10)$$

for a shear-coaxial jet. In contrast to prior studies of isodensity jets, this relation accounts for different densities as well as velocities, and is far more pertinent to bi-propellant applications and research thereof. Other studies have since validated and applied eqn. 1.10 for this reason [92, 93].

Modern coaxial jet research has sought to account for an even larger body of variables to describe mixing and break up, in addition to velocity and density. These include chamber pressure, outer and inner jet temperature, viscosity, and surface tension forces present in two-phase flows. Reactive experiments are often the most holistic approach for research of combustion systems, but construction and maintenance of combustion facilities remains costly, especially for cryogenic applications such as LREs. In terms of scientific value, nonreactive experiments can also simplify the physics of otherwise complex flows, clarifying the results. Therefore, nonreactive experiments have remained an excellent research strategy throughout the 1990s, 2000s, and today.

During this period, a significant effort was made to categorize two-phase coaxial jets according to the break up process of the inner liquid core. Chigier and Farago [94] used Re_{ij} and We to characterize several regimes of inner jet break up, and Lasheras and Hopfinger [95] extended their work to include the effects of J and the Ohnesorge number $Oh \equiv \mu_{ij} / (\rho_{ij} \sigma D_1)^{\frac{1}{2}}$. The culmination of this work is shown in Fig. 1.10, where five regimes of break up for air-water jets at atmospheric pressure are shown to occur according to the values of Re_{ij} , We , J , and Oh . These five regimes are axisymmetric

and nonaxisymmetric Rayleigh break up, shear break up, membrane break up, and fibre-type break up. The latter two regimes are of particular interest here, because LRE flow conditions often exhibit high We values produced by high velocity gas in the outer jet which strips the outer perimeter of the denser inner jet. Membrane and fibre-type break up were characterized in Lasheras and Hopfinger [95] as having an inner core length L_b less than $8D_1$. Under the action of the gaseous jet turbulence, the liquid core breaks into clusters and ligaments near the injector exit and atomization can occur less than $2D_1$ from the exit for $We \sim 1000$. Their experiments support the correlation

$$\frac{L_b}{D_1} = \frac{6}{\sqrt{J}} \left(\left| 1 - \frac{1}{R} \right| \right)^{-1} \quad (1.11)$$

for use in LREs, but devise a separate relation for low We flows not in the fibre-type regime. Extensive experiments by Baillot *et al.* [16] not only support the numerous regime boundaries in Fig. 1.10, but also support the $L_b \sim J^{-\frac{1}{2}}$ relationship, despite using an impinging inner jet shear-coaxial injector (see Fig. 1.6c). However, their experiments also included tests at very slightly elevated chamber pressure. At just 2.16 and 3.6 kPa above atmospheric pressure, the Re_{ij} and We values for break up regime boundaries were clearly altered, revealing the importance of pressure in shear-coaxial jet break up and atomization.

The effects of pressure are particularly important to the LRE community, where high chamber pressures are desired in order increase specific impulse. Although, supercritical pressure introduces less understood physics into the mixing process. The well-known features of liquid jet break up (e.g., ligaments, droplets, and atomization) are replaced with indiscernible fluid interfaces and obscure lumps rather than droplets. The first apparent set of experiments on jets in supercritical environments was done by Newman and Brzustowski [96] in 1971. Their experiments involved backlit shadowgraphy of single jets of liquid CO_2 in a gaseous nitrogen environment. With the chamber pressure above the critical pressure of CO_2 and the temperature below the critical temperature of CO_2 ,

i.e. $p_c > p_{crit,CO_2}$ and $T_c < T_{crit,CO_2}$, CO_2 droplet sizes were observed. As T_c approached T_{crit,CO_2} , droplets became smaller until the liquid-gas interfaces became unobservable for $T_c \geq T_{crit,CO_2}$. At this point, the flow could no longer be described as heterogeneous two-phase flow.

Since the work of Newman and Brzustowski [96], a large body of work has supported and expanded upon their findings. A number of studies have been done at both the U.S. Air Force Research Laboratory (AFRL) and the German Aerospace Center (DLR), and a thorough review of their advancements prior to 2006 is found in Oschwald *et al.* [97]. Nonreactive, near-critical and supercritical experiments at AFRL began with single liquid nitrogen (LN_2) jets in a quiescent nitrogen environment and later experiments added a nitrogen outer jet in a shear-coaxial configuration. For the single jet, drops at the liquid-gas interface were no longer detected when the chamber pressure reached $\frac{p_c}{p_{crit,N_2}} = 1.03$. Instead, finger-like entities were seen at the interface. Chamber pressures greater than $2.5p_{crit,N_2}$ were eventually tested, and the continuous shrinking of the dense liquid core was observed as pressure increased to and beyond this point, as well as the suppression of droplet production for single jets and coaxial jets [97–99]. Chehroudi *et al.* [98] also showed quantitative evidence of gas jet behavior to support the gas-like appearance of the jet in supercritical environments for a specific range of jet densities.

Meanwhile, nonreactive experiments at DLR by Telaar *et al.* [100] and Mayer and Smith [14] used LN_2 and gaseous helium (GHe) coaxial jets to better replicate the density ratios of LO_x - GH_2 rocket engines. A sample of their shadowgraphy results is shown in Fig. 1.11. These results reinforced the LN_2 - GN_2 results noted above, even for species with very different critical pressures and temperatures. The development of the inner jet was said to be dependent on its own fluid properties. Complementary experiments were performed with LN_2 - GH_2 flows by Oschwald *et al.* [101] using Raman scattering for quantitative density measurements. This diagnostic technique provided Raman signals of

nitrogen and hydrogen at two different wavelengths and appropriately filtered the signals to effectively measure the species fraction of each. The results were analyzed to measure a streamwise location at which the jet was completely mixed with the background gas, culminating in salient evidence of mixing or lack thereof. This was the first study measuring species fractions in sub and supercritical pressure environments.

Since the composite review by AFRL and DLR in Oschwald *et al.* [97], further backlit image analysis of coaxial jets at AFRL has accumulated strong indications of a correlation to predict inner core length L_b for a wide range of flow conditions. First, Davis and Chehroudi [102] and Davis [103] used low speed imaging (< 1 kHz) to optically measure L_b , and organized a large amount of data from the literature to create a comprehensive review of the dark core length's dependence on chamber pressure. Leyva *et al.* [29] advanced this study to include variations in J and the influence of acoustic forcing, both of which were found to have a significant impact on L_b and jet spread angle. With the use of high speed imaging (> 10 kHz), coherent jet oscillations were also recognized when acoustic forcing was applied. For example, L_b measured for jets at a PN location in the chamber were found to be less than those measured for jets at a PAN location [75, 81]. Rodriguez [75] also included variations in injector area ratio AR in a study which was expanded to include a recessed inner post by Graham *et al.* [104]. In conclusion, an array of variables encompassing injector geometry, density ratio S , velocity ratio R ($J = SR^2$), chamber pressure, and acoustic forcing conditions have been shown by works at AFRL to alter shear-coaxial jet mixing as evidenced by variations in dark core length.

Experimental data from testing of two shear-coaxial injectors, sub and super-critical pressures, and J values ranging from 1 to 23 was used by Teshome [23] to find an empirical correlation for L_b . This new data was supplemented with experimental data from studies mentioned above ([23, 75, 104, 105]) to create an empirical solution to

predict L_b . Injector geometry and momentum flux ratio were combined to create the nondimensional parameter G , which takes the form

$$G = c_1 J^{c_2} \left(\frac{t}{D_1} \right)^{c_3} (AR)^{c_4} \quad (1.12)$$

where t is the wall thickness of the coaxial injector's inner tube. The constants c_1 , c_2 , c_3 , and c_4 were chosen to fit the data of four injectors, all having different combinations of large or small values for $\frac{t}{D_1}$ and AR . Again, this study demonstrated the importance of chamber pressure through the difficulty in producing a correlation applicable both above and below the critical pressure. Teshome [23] was instead forced to choose two unique sets of constants; the first set was chosen to fit L_b vs. G data for sub-critical pressure and a second set was required for super-critical pressure. Although a physics-based approach may identify the missing factors necessary to predict dark core length across a range of pressures in the future, this correlation remains the most comprehensive empirical formula to quantify mixing for LRE-like coaxial injectors by including the majority of the variables identified in the studies cited above. Future work at AFRL will explore the effects of these variables for reactive propellants.

1.3.1.3 Stability Consideration

Early jet turbulence researchers recognized that many combustion systems are diffusion-controlled, having chemical kinetics which are so rapid that the reaction rate is entirely dictated by turbulent mixing [86]. When isolating these mixing processes in nonreactive experiments, these researchers also recognized the existence of high amplitude modes of fluid instability which would completely dominate the mixing processes of a combustion system. Several key studies will be discussed here which give attention to the frequencies and amplitudes of these coherent instabilities rather than chaotic turbulence.

Crow and Champagne [106] characterized the natural instability of single jets according to the Strouhal number St and explored the relationship between instability

amplitude and St . The Strouhal number is a nondimensional measure of frequency f generally defined as

$$St = \frac{fx}{u} \quad (1.13)$$

where x is a characteristic length scale and u is a characteristic velocity scale. Crow and Champagne [106] explored single jets of water, and later air, and defined x as the jet exit diameter D which was held constant while the mean jet exit velocity U_e was controlled. The jet spectra was probed at various positions downstream of the exit, and a natural oscillation was found to occur at $St = 0.30$. This mode was amplified downstream of the exit until reaching a peak amplitude at $x/D=9.5$. Crow and Champagne then used a loudspeaker upstream of the jet exit to force the jet at a controlled frequency, unequal to the jet's natural frequency. In this way, St was controlled using f and U_e to employ a range of $0.15 < St < 0.60$. They found that the forcing frequency could be measured and controlled in the near-exit region $x/D < 8$, but the natural mode, or “preferred” mode, dominated and saturated in the region $x/D > 8$ regardless of the forcing frequency. This conflicted with existing linear stability theory which failed to predict $St = 0.30$, but rather asserted an increasing instability amplitude for increasing St . A significant conclusion of Crow and Champagne's study was that linear stability theory could not be used to predict the jet's dominant mode because nonlinearity established the preferred mode of $St = 0.30$. This is a classical work in single jet instability due to its clear demonstration that jet instability has a preferred mode which can be scaled using St .

Since the work of Crow and Champagne, single jet preferred modes have been shown to adopt different values of St and definitions thereof. As an example, the systematic experimental study by Birbaud *et al.* [107] defined a preferred mode Strouhal number for both the jet and the shear layer existing between the jet column and the surrounding quiescent gas, St_D and St_θ , respectively. St_D was defined using the jet exit diameter D and St_θ was defined using the initial momentum thickness θ_0 , a measured quantity. For low Reynolds number air jets at atmospheric pressure, the jet mode frequency f_D and

the shear layer mode frequency f_θ were measured for natural jets and for jets subject to upstream acoustic forcing at f_0 . This study not only asserted that two natural modes can exist in single jets, but also that the values of the preferred Strouhal numbers, St_D^p and St_θ^p , can be used to predict the response of jets to acoustic forcing. Particularly, when f_0 was chosen to be near the preferred mode f_p , the jet adopted and amplified the forced mode as the convective instability moved downstream. When f_0 was much greater than f_p , the jet was insensitive to upstream modulations and did not display evidence of the forced mode. This study represents the field's advancement since the work of Crow and Champagne, demonstrating that even without the added complexities of a coaxial jet, single jet natural modes feature several key behaviors. Mainly, St can be intuitively defined by parameters characteristic of the source of the instability, such as θ_0 , and a jet is more likely to amplify a forced mode if the forcing frequency is near that of the natural jet instability.

Coaxial jets may also manifest the same principles as single jets, albeit with more complexity. In early work by Kwan and Ko [83] and Ko and Kwan [88], similar concepts were explored for shear-coaxial jets. Velocity fluctuation measurements revealed two modes in the initial merging zone; a low frequency mode was measured from primary vortices in the inner shear layer and a high frequency mode was measured from secondary vortices in the outer shear layer. In the intermediate zone the low and high frequency vortices merged and one overtook the other to dominate the fully merged zone. Like Crow and Champagne [106], Ko and Kwan [88] described modes according to St and attempted to find one St value to predict the jet's preferred mode over a range of flow conditions. However, Ko and Kwan acknowledged that the complexity of a coaxial jet not only required different length and velocity scales than the single jet, but also called for separate length and velocity scales for the inner shear layer and the outer shear layer.

These two definitions followed as

$$St = \frac{f D_1}{[0.6 (U_{ij} - U_{oj}) + U_{oj}] / 0.6} \quad (1.14)$$

$$St = \frac{f D_3}{U_{oj}} \quad (1.15)$$

where eqns. 1.14 and 1.15 applied to the inner shear layer mode and outer shear layer mode, respectively. Experimental validation in Kwan and Ko [83] and Ko and Kwan [88] supported these definitions. Although the experiments were limited to $R < 1$, this work clearly described two sources of shear layer instability in coaxial jets and stark differences between them. The definition of eqns. 1.14 and 1.15 is the earliest attempt to differentiate multiple sources of coaxial jet instability with individual scaling laws. Other researchers have since defined St to include variables such as jet exit boundary layer thickness and a combined jet mean velocity to reach a St scaling which holds for greater values of R [108, 109].

Advances in stability theory have since isolated additional sources of instability in two-dimensional shear layer mixing, which can provide insight to possible sources of instability in three-dimensional coaxial jets. The field of linear stability theory has seen vast development and application since its ineffectiveness in explaining the results of Crow and Champagne, and could be reviewed to designate flows which are accurately and inaccurately predicted by stability theory. A lengthy review of this kind will not be offered here. However, a few select studies of this kind will be discussed, because despite the shortcomings of linear stability theory when treating LRE-like flows with complex geometry and nonlinear effects, *linear stability results offer intuition for scaling laws such as St .*

A straightforward classification of modes was included in a theoretical stability study by Yecko *et al.* [10], where a two-dimensional, liquid-gas shear layer of unequal density, velocity, and viscosity was subject to temporal stability calculations. The common

Kelvin-Helmholtz instability was identified resulting from a velocity deficit at the interface, as expected. Inviscid theory will capture this mode, which is said to be the cause of instability in the experiments of Crow and Champagne (Talamelli and Gavarini [108]), but will not capture Tollmien-Schlichting (T-S) type modes. A liquid T-S mode and a gas T-S mode were identified by Yecko *et al.* [10] as the result of Reynolds stress at a liquid-gas or liquid-liquid interface, which cannot be neglected in the cryogenic flows of rocket engines. Later experimental work by Matas *et al.* [93] showed that viscous models often predict higher frequencies in spatial stability calculations though, and a correct estimation of the shear layer convection velocity U_c is more critical for obtaining accurate frequencies. Their own calculations assumed the formula of eqn. 1.10 for U_c from Dimotakis [89]. Lastly, Matas *et al.* [93] noted that instability frequencies between streams with finite thicknesses would be even more difficult to estimate, because the modes of multiple shear layers will communicate.

The presence of global instability in a number of different types of shear flows is well known [25]. As noted by [110], evidence in the spatial evolution of the disturbance amplitude for a nonlinear global mode in an infinite domain consists of a sharp front located at the upstream boundary of the absolute instability region, where the disturbance amplitude abruptly increases and stays high as one moves downstream. Under such conditions the flow behaves as an oscillator rather than a noise amplifier. Flows that can become globally unstable include low density axisymmetric jets in quiescent surroundings below a critical jet-to-surroundings density ratio [111, 112], countercurrent mixing layers above a critical velocity difference [113, 114], and wake flows above a critical Reynolds number [115, 116]. The evidence for such transitions includes phenomena that have already been documented for the transverse jet [117], e.g., (1) clear changes in the spectral character of the shear-layer, with strong oscillations at narrow spectral peaks for global instability, representing pure tones with higher harmonics, (2) a rather dramatic alteration in the value of the Strouhal number associated with the initial insta-

bility as the influencing flow parameter is brought into the range for globally unstable flow, and (3) little spectral alteration of the globally unstable flow in response to low to moderate flow excitation, in contrast to significant spectral alteration of the convectively unstable flow during such excitation. Additional phenomena associated with a transition to globally unstable conditions include: (4) a rather abrupt increase in the amplitude of the disturbance within and near the shear-layer as one approaches the critical flow parameter, consistent with the characteristics of the Landau equation [25, 113], and (5) a reduction in the energy transfer from fundamental to subharmonic frequencies along the shear-layer, and hence a reduction in the strength of subharmonics and corresponding inhibition of the vortex pairing process after the transition. In addition, for the low density free jet it has been shown that very strong external sinusoidal excitation can be used to overcome the fundamental instability mode for globally unstable conditions [118, 119]. These findings are consistent with theoretical work [120] which suggests that for spatially developing flows, external forcing upstream of the transition from convective to absolute instability can overwhelm the naturally occurring absolute instability. The low density jet experiments show that at forcing frequencies f_F that are relatively close to the global instability frequency f_{nat} and/or at very high amplitude forcing, the global frequency is not observed at all, and the forcing frequency dominates the flow's spectral character, with the capacity to either reduce or enhance jet mixing. The excitation amplitude at which the flow “locks” on to the forcing frequency f_F increases in proportion to $|f_{nat} - f_F|$, consistent with the flow transition to a global mode via a Hopf bifurcation [25, 110]. The capacity for strong sinusoidal forcing to alter the global instability is viewed as a means of controlling the low density jet.

Jendoubi and Strykowski [121] used inviscid, spatio-temporal stability theory to describe the modes created by axisymmetric jets with ambient co-flow and counter-flow. This study focused on the behavior of two particular modes with regard to large changes in the density ratio and velocity ratio. “Mode I” was described as a shear layer insta-

bility, having peak velocity perturbations at the interface which were not felt in the center of the jet nor at a position far from the jet. “Mode II” was deemed a jet column mode, because peak perturbations were located at the shear layer as well as the jet centerline. These two modes were found to not only produce convectively unstable modes, but for a specific range of velocity and density ratios each mode predicted absolute instability. The transition from convective to absolute instability was the focus of Jendoubi and Strykowski [121]. This transition is important because should a mode become absolutely unstable, it becomes time-amplifying in a localized area and basically self-excited, whereas convective modes develop as the waves are conveyed downstream. If an LRE, for example, sustained absolutely unstable propellant flows, then the self-excited mixing of reactants may become insensitive to acoustic feedback. To explore this possibility, a plot from Jendoubi and Strykowski [121] is presented in Fig. 1.12, showing convective-absolute transition lines calculated as a function of the velocity and density ratio. The operating conditions of a typical $\text{LO}_x\text{-GH}_2$ LRE are added, showing that absolute instability brought on by these particular modes is unlikely.

Absolute instability is especially relevant to combustion instability when considering its resistance to external forcing. This feature has been investigated experimentally for single jets by Getsinger *et al.* [122], among others [115, 118, 123]. For low density jets in crossflow, Getsinger *et al.* [122] found an absolutely unstable jet to be resistant to upstream forcing in a way which was dependent on the jet-to-crossflow momentum flux ratio and the forcing frequency. It was observed that as the forcing amplitude increased, a “lock-in” amplitude was eventually reached such that the formerly absolutely unstable jet adopted a convective instability with a frequency equal to the forcing frequency. The lock-in amplitude was found to be dependent on momentum flux ratio and linearly dependent on the nondimensional forcing frequency F , defined as a ratio of the forcing frequency f_F to the jet’s natural frequency f_0 . Other lock-in experiments of single jets have also observed this relationship, namely nonreactive work by Sreenivasan *et al.* [123]

and nonreactive and reactive experiments recently presented in Juniper *et al.* [118]. To the author's knowledge, the first experimental evidence of the lock-in phenomenon was shown in Provansal *et al.* [115] for the wake behind a cylinder. If applied to coaxial jets, this concept could aid investigators when diagnosing an acoustically forced flow condition as absolutely or convectively unstable or when classifying flows according to their resistance to said forcing, which is the foremost objective of the present study.

From a theoretical standpoint, to predict absolute or convective instability for coaxial jet flow conditions requires that the results of Jendoubi and Strykowski [121] be supplemented with an analysis specific to coaxial jets. The analysis must account for sources of instability in the outer shear layer and the inner post wake, both of which were not present in Jendoubi and Strykowski's study. Their results indicate that LRE coaxial jets are far from the convective-to-absolute transition due to high speed co-flow and dense inner jets, preventing both the jet column and shear layer modes from reaching absolute instability. This is supported by Fig. 1.12. But, a finite thickness inner post creates a potential source of absolute instability in the wake region.

In a more recent theoretical study by Talamelli and Gavarini [108], the outer shear layer as well as a finite inner post thickness were included in an effort to explore these two regions as possible sources of absolute instability. Three unstable modes were identified: one in the outer shear layer and two associated with the inner post wake. For a small but nonzero wake velocity, one of the wake modes was shown to become locally absolutely unstable. It is also notable that the absolutely unstable mode could be described by $St \approx 0.24$ when St was calculated using the wake thickness and mean free stream velocity, i.e. $(U_{ij} + U_{oj})/2$. Further inspection of this mode showed that the absolute instability exists for a limited range of R , and the extent of this range depended on the assumed momentum thickness θ and the wake velocity. Specifically, a significant amount of reverse flow in the wake increased the likelihood of absolute instability. As

will be shown later, wake induced modes are particularly important in the present study due to the injector's finite inner post thickness t , which creates a visually identifiable recirculation zone in the near-field.

Although inviscid and incompressible assumptions were made in Talamelli and Gavarini's analysis, LRE coaxial jets may manifest the absolutely unstable wake mode described above. Teshome [30] extended the previously discussed work at AFRL [75, 81, 104, 105] by measuring natural and acoustically forced coaxial jet instability frequencies for sub- and near-critical chamber pressures, simulating the cryogenic propellants of LREs in a nonreactive $\text{LN}_2\text{-GN}_2$ configuration. Images from high-speed shadowgraphy were used to determine the frequencies most representative of a range of flow conditions, both acoustically forced and unforced. This was achieved by extracting spectral information from image sets using a partial orthogonal decomposition (POD) algorithm to reconstruct modes with a high energy content garnered from fluctuating image intensities. Separate spectra plots were obtained for each flow condition. It was observed that for high J and $AR(\equiv \frac{A_{oj}}{A_{ij}})$ the jet appeared to sustain its natural instability frequency even when acoustically forced, displaying absolutely unstable behavior. Conversely, low J and AR conditions were sensitive to forcing, adopting a instability frequency equal to f_F . In this study, high amplitudes of acoustic forcing were used to replicate the severity of an actual engine instability rather than the low level forcing technique of Getsinger *et al.* [122], for example. Thus, an absolutely unstable wake mode may be present in the experiments of Teshome [30], and a more detailed alteration of forcing amplitudes to confirm frequency lock-in could be performed as reinforcement.

Due to the limited amount of experiments regarding forcing of absolutely unstable coaxial jets, it is difficult to anticipate the appearance of this phenomenon. The behavior of convectively unstable jets though, is well documented for experiments where these flows are subject to transverse acoustic forcing, and a short list of studies will be discussed

here to classify the expected results. The earliest experiments of this kind were reported by Miesse [124] and Buffum and Williams [27], both of which involved two-phase flow. Miesse [124] recorded a definite jet response to external acoustic forcing, regardless of whether wave propagation was parallel (longitudinal) or perpendicular (transverse) to the jet axis. Buffum and Williams [27] focused on single water jets exposed to transverse, standing acoustic waves. When placed at a pressure node (PN) for frequencies less than 500 Hz, a whipping motion was observed which is analogous to a jet injected into an oscillating crossflow. For $\text{SPL} > 161$ dB, increased atomization was also recorded. Subsequent studies focused on the increased break up and atomization caused by acoustic forcing. For example, Carpentier *et al.* [26] also studied single liquid jets in transverse acoustic fields, but noted steady jet flattening for acoustic frequencies ranging from 500 to 1864 Hz. The jet was constricted in the wave propagation direction and stretched in the direction perpendicular to wave propagation, a phenomenon also reported for high pressure in Chehroudi *et al.* [98]. However, Carpentier *et al.* [26] did not observe the sinuous jet motions as in Buffum and Williams [27], and used a simple analytical model to explain the existence of both regimes of jet response, primarily categorized by frequency. In conclusion, their model mathematically explained that if the values of the acoustic velocity u' and $1/(f_F D_1)$ are large, then sinuous jet forms can result. Otherwise, an acoustic radiation force F_R similar to that discussed in section 1.2.3 induces steady flattening and fanning in the plane of the PN.

When tested for coaxial jets, these conditions produce quite different results. Baillet *et al.* [16] tested liquid-gas coaxial jets with regard to the relationships stated by Carpentier *et al.* and discerned different behaviors at PNs and PANs. At a PN, Baillet *et al.* [16] also observed jet flattening, but noted that for a sufficient amount of outer jet flow no flattening occurred. Again, this phenomenon was also observed by Leyva *et al.* [29] and Chehroudi *et al.* [98] for elevated pressures. At a PAN, jet break up was only influenced by acoustics if in the presence of outer jet flow, which is a feature that

emerged as a result of outer jet flow pulsations. By periodically impeding outer jet flow with chamber pressure fluctuations at a PAN, acoustics increased mixing and breakup via the formation of axisymmetric vortices. Although the nonreactive experiments cited above exclude the effects of speed of sound gradients inherent in high temperature combustion systems, many of these rules hold true for acoustic forcing of reactive flows, as discussed below.

1.3.2 Reactive Shear-Coaxial Jets

1.3.2.1 General Characterization

The flame of a reactive coaxial jet adds complexity to fluid instability and mixing, but many key features are retained from nonreactive jets. As shown in Fig. 1.13, the vortex structures at the inner shear layer manipulate the reaction zone, creating a wrinkled flame. A ring shaped flame forms a distance x_f downstream from the inner post, and its flame thickness δ_f grows in the streamwise direction x until the flame merges to become a single, broad flame downstream of the liquid core tip. An attached flame corresponds to $x_f = 0$. Near the reaction zone, steep temperature gradients promote a rapid density reduction of both the liquid oxygen core and the outer gaseous fuel, a process controlled by convective transport of hot gases. Thus, the state of the dense inner jet is significantly altered by the wrinkled flame, and if reaction rates are controlled by mixing or liquid vaporization then this can generate combustion instability. Analysis by Snyder *et al.* [125] confirmed that combustion of $\text{LO}_x\text{-GH}_2$ coaxial jets in LREs is indeed a oxygen vaporization limited process, because the characteristic vaporization time scale t_v is longer than both the characteristic chemical and mixing time scales, t_c and t_m , i.e. $t_c < t_m < t_v$ (see also Candel *et al.* [126]). Therefore, the interfacial instabilities of the liquid oxygen core and measure of its length, L_b , are paramount for understanding combustion instability.

As a direct result of the added heat release of a combustion system, fluid mixing and instability cannot be easily isolated as in the nonreactive flows discussed heretofore. Measures of mixing such as L_b are consequently studied concurrent with instability, because fluid mechanics are difficult to decouple from unsteady heat release and the ensuing chamber acoustics of a combustion instability feedback loop, shown in Fig. 1.2. Suitably, the following section reviewing reactive coaxial jet research is ameliorated by discussing mixing and stability phenomena together in light of their close coupling in reactive flows.

1.3.2.2 Propellant Mixing and Stability Consideration

Although $\text{LO}_x\text{-GH}_2$ engines were thoroughly tested by engineers as early as the 1950s and '60s, little fundamental research was done during this period. At the Lewis Laboratory (now the NASA Glenn Research Center) in 1958, Baker and Steffen [127] used a bench scale thrust chamber with multiple propellant combinations to measure high frequency pressure chamber pressure fluctuations for various chamber lengths. Little high frequency instability was observed for hydrogen-oxygen propellants in particular, and in experiments with coaxial injectors no instability was present. Other propellant combinations brought about significant longitudinal modes.

Early experiments of this kind were limited to direct probe measurements as opposed to optical techniques. A later set of experiments from Heidmann [128] at the same laboratory in 1965 included some of the first images with evidence of mixing alterations caused by combustion instability. For a small shear-coaxial injector ($D_1 = 0.7$ mm) $\text{LO}_x\text{-GH}_2$ combustion images resolved the outline of the liquid core, and the core length L_b was shown to respond to transverse waves. Their imaging technique could not resolve break up and vaporization, but clearly displayed a reduced L_b in the presence of transverse acoustic modes, a behavior likened to a liquid jet in gaseous cross-flow.

Numerous other experiments of small-scale thrust chambers by NASA in the 1960s confirmed Baker and Steffen’s conclusion that $\text{LO}_x\text{-GH}_2$ coaxial jets produce stable conditions relative to their marginally stable $\text{LO}_x\text{-Hydrocarbon}$ counterpart. In fact, it was the Apollo program’s difficulty with combustion instability in the kerosene based F-1 engine that largely motivated the surge in research during this period. Meanwhile, the J-2 engine, a hydrogen fueled upper stage engine flown during Apollo missions, exhibited minor instabilities which were quickly abated (see section 1.1.3). Oxygen-hydrogen coaxial jets were being adopted as a stable configuration by both the engineering and the scientific communities. At the conclusion of NASA’s subscale campaign of experiments at the Lewis Laboratory, it was even stated that “. . . all liquid oxygen-hydrogen staged combustion tests in the U.S. have been stable at high frequency.” [45] The knowledge acquired up to this time was consolidated in NASA SP-194, *Liquid Rocket Engine Combustion Instability*.

Motivation for fundamental research in this area then subsided until two in-flight incidents of combustion instability occurred for engines of the European Ariane rocket [3]. These unexpected events renewed research activity in the field, and several key research groups have developed new test facilities to experimentally replicate the complex flows of LREs while using modern imaging techniques. These facilities attempt to reproduce the hazardous, high-pressure conditions of LREs at subscale while also applying novel concepts for high-fidelity acoustic control. Below, this review highlights the diverse experiences of five modern combustors which are particularly relevant to this study. These are the Multi-injector Combustor (MIC) and the Very High Amplitude Modulator (VHAM), both operated jointly by the French Aerospace Research Agency (ONERA) and the French National Center for Scientific Research (CNRS), the Common Research Combustor (CRC) operated jointly by CNRS and DLR, the BKH combustor operated by DLR, and the Continuously Variable Resonance Combustor (CVRC) operated by Purdue University.

The CRC originated in 2002 from the efforts of a German-French working group which now operates identical experimental combustors at the Research Institute for Equilibrium Systems (IRPHE) in Marseilles, France and DLR in Lampoldshausen, Germany. The CRC injects propellants from one side of a flat, cylindrically shaped chamber through a single injector which is 1/10th scale of a typical LRE injector. With high-speed shadowgraphy and OH* chemiluminescence imaging, the dynamics of a single LO_x/GH₂ flame can be isolated to fundamentally relate spatial and temporal heat release oscillations to pressure oscillations controlled by external acoustic forcing from a secondary nozzle. A single injector element though, provides only partial representation of thermoacoustic cycles occurring in LREs with multiple injectors and interactions between adjacent flames.

The BKH combustor is part of a recently constructed facility at DLR Lampoldshausen, Germany which focuses on high frequency combustion instability for LO_x/GH₂ and LO_x/LH₂ combustion. Simultaneous high speed backlit shadowgraphy and OH* chemiluminescence imaging was used to measure liquid core length L_b in addition to flame shape, both of which had a strong response to external acoustic forcing. Dark core length L_b values were reduced by up to 70% when forced at resonant chamber frequencies, and a curve-fit between L_b/D_1 and a nondimensional acoustic pressure amplitude predicted core length with reasonable accuracy for the conditions used in Hardi [24]. The pressure amplitude p' was nondimensionalized by the chamber pressure, i.e. p'/p_c , in one attempt to collapse L_b data into a single relationship. A second nondimensionalization method used the dynamic pressure of the outer jet, which followed as

$$\frac{\rho_c u'^2}{\rho_{oj} u_{oj}^2} \quad (1.16)$$

where ρ_c is the chamber gas density and the acoustic velocity amplitude u' is calculated from p' measurements. Both attempts to scale acoustic perturbation amplitudes with dark core length showed promise.

Hardi [24] also describes linear and nonlinear instability events which occurred during high frequency acoustic excitation. First, pressure measurements of unforced coaxial jet combustion confirmed the system’s natural excitation of the first longitudinal (1L) and first transverse (1T) modes via small increases in p' values at those frequencies. Second, transverse forcing at the 1T frequency (≈ 4 kHz) strongly excited this mode while also creating low frequency chugging far from the excitation frequency. A similar event occurred when forcing at the 1L1T frequency. The chugging mode only occurred during high frequency excitation of transverse modes, and was said to occur due to nonlinear effects.

The BKH combustor also includes five shear-coaxial injectors in a cross formation to investigate interactions between neighboring flames. Although Hardi [24] was unable to give flame interaction detailed attention, this feature is expected to be investigated in future work. The MIC, located in Paris, shares many design features with the BKH combustor. The MIC also uses multiple injectors, but always in a linear arrangement to isolate interactions between pairs of flames when using two-dimensional imaging. Unless utilizing laser sheet flame illumination as in OH-PLIF, a cross injector formation prevents one from distinguishing between foreground and background flames when viewing OH* emission images. But, even OH-Planar Laser Induced Fluorescence (PLIF) imaging in these configurations has been challenging because it is difficult to penetrate the dense oxygen jet with a laser sheet [129, 130].

The VHAM is a modified version of the MIC which creates much greater acoustic pressure amplitudes in an effort to replicate the high amplitude oscillations documented in actual LRE combustion instabilities. The VHAM uses a toothed wheel to periodically block gas flow through exhaust nozzles, creating high pressure amplitudes inside the combustion chamber. The tooth wheel exhaust nozzle technique is also employed in the MIC, BKH, and CRC designs for the same purpose [18, 131]. With this method, the

periodic nozzle imposes an acoustic boundary condition on the chamber wall, where the acoustic frequency is controlled by the wheel speed. The resulting pressure perturbation amplitude though, is not controlled, and is instead determined by hardware geometry such as nozzle diameter and tooth shape. In the MIC, BKH, and CRC configurations, the toothed wheel is placed over a secondary exhaust nozzle which is located on the side of the chamber, perpendicular to the primary exhaust nozzle. In the VHAM though, zero secondary nozzles exist and two primary exhaust nozzles located at the end of the chamber are excited by a single toothed wheel. The VHAM design was recently used to create pressure amplitudes as high as 20% of p_c in Mery *et al.* [19]. Consequently, the VHAM induced a strong flame response whereas previous tests with smaller amplitudes in the MIC design yielded very little flame response.

The MIC used $\text{LO}_x\text{-GH}_2$ propellants in early experiments but quickly moved to $\text{LO}_x\text{-CH}_4$ propellants in an effort to achieve a more dramatic flame response to acoustic forcing. Again, this was linked to low amplitude acoustic pressure created by the single toothed wheel. Eventually, $\text{LO}_x\text{-CH}_4$ tests of subcritical and supercritical chamber pressure revealed a notable flame response to external forcing. A Ph.D. thesis by Richecoeur [8] presents results with similarity to Heidmann [128], mainly an increased spread angle caused by a shortened mixing region. Also, the combustor's five element injector arrangement showed evidence of interaction of adjacent flames. The VHAM is expected to produce a substantial flame response, even with $\text{LO}_x\text{-GH}_2$ propellants, and these results may be publicized in the future.

Controlled acoustic excitation in the manner described above allows experimentalists to partially decouple a portion of the combustion instability feedback loop. Without an external acoustic source, chamber pressure perturbations exist due to combustion instabilities alone. But, when user-controlled acoustic excitation contributes to chamber acoustics, dual feedback dependencies exist as shown in Fig. 1.14. This configuration

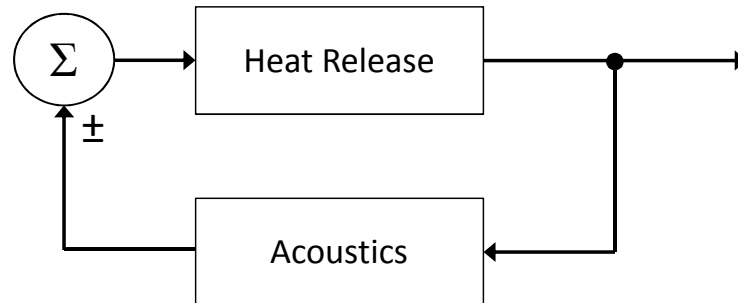
allows one to isolate the effects of acoustic waves on fluid dynamic instability and heat release by controlling acoustic pressure amplitude and frequency. With this strategy, the degree to which perturbation amplitudes and their inherent frequencies can be varied is highly dependent on the specific hardware design used for external acoustic forcing. However, if the flame is self-excited then added acoustic forcing will compete with naturally occurring modes, and the experimentalist forfeits *complete* control over chamber acoustics. An analytical comparison of the excited acoustic energy and combustion energy was made by Rey *et al.* [132] and this relationship will be considered for the chamber used in the present study.

In contrast to the nozzle modulation method used by all four aforementioned combustors, the CVRC of Purdue uses an acoustic control system relying on variable injector geometry [17]. By altering the size of the oxidizer plenum, the resonant frequency of the injector flow is controlled such that chamber pressure amplitudes range from less than 10% to 60% of the chamber pressure. The highest pressure amplitudes are achieved when the oscillation frequency of the injector matches a chamber resonant frequency, whereas a mismatch dampens the chamber mode. Thus, the CVRC design forgoes the electro-mechanical system of a typical acoustic source [8, 23, 24], and instead relies on injector flow oscillations to create unsteady heat release. This method reliably induces high amplitude instability, but requires mindful choice of fuel species and propellant flow conditions to manipulate the preferred frequency and amplitude of the instability.

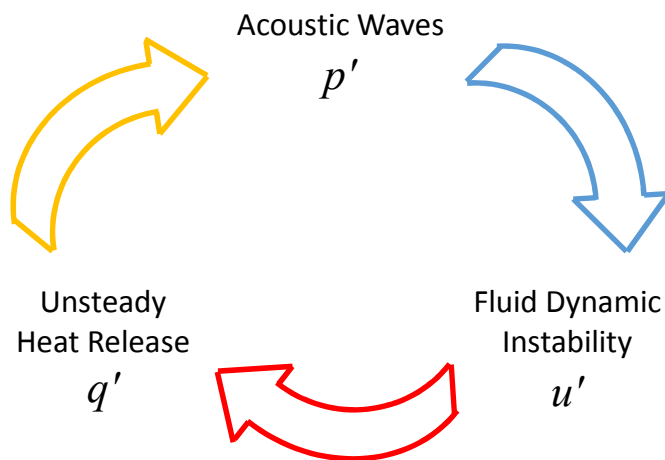
The lessons learned from the experimental facilities described above were instrumental in the design and construction of the shear-coaxial jet combustion facility used in this study. Many concepts introduced here are revisited in section 4.3, with new observations regarding the stability of $\text{O}_2\text{-H}_2$ flames.

1.4 Present Studies

The goal of the present studies is to explore acoustically-coupled combustion and transport processes in two fundamental configurations. One involves a continuously burning liquid fuel droplet exposed to acoustic excitation in a cylindrical waveguide at background atmospheric pressure. These experiments have been conducted at UCLA in the Energy and Propulsion Research Laboratory. The other configuration involves a coaxial jet of transcritical fluid injection into a high pressure (2.75 MPa) chamber at AFRL, also with exposure to acoustic excitation, and with the ultimate goal of exploring reactive flow. A detailed exploration of each system helps to shed light on important phenomena associated with acoustically-coupled combustion instabilities.



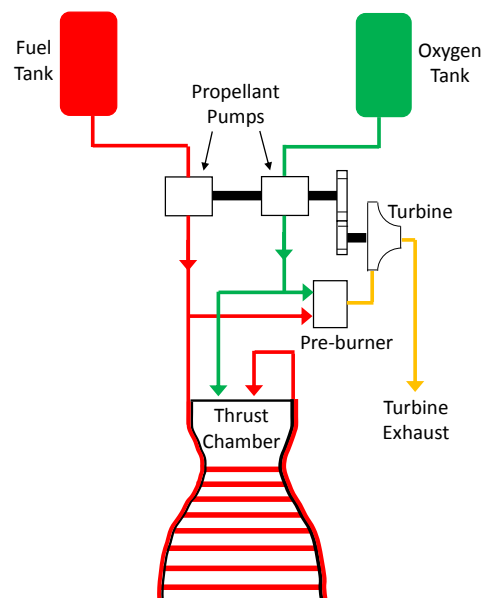
1.1: The bimodal combustion instability feedback loop [4, 5].



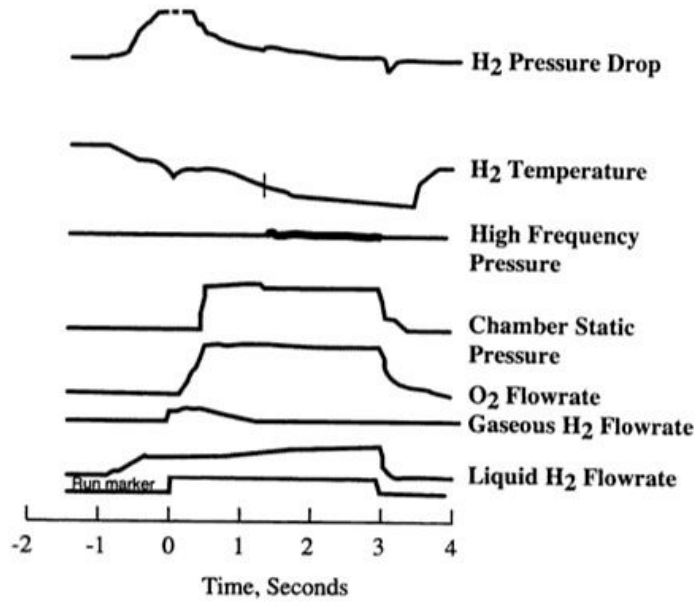
1.2: Three-part combustion instability feedback loop.



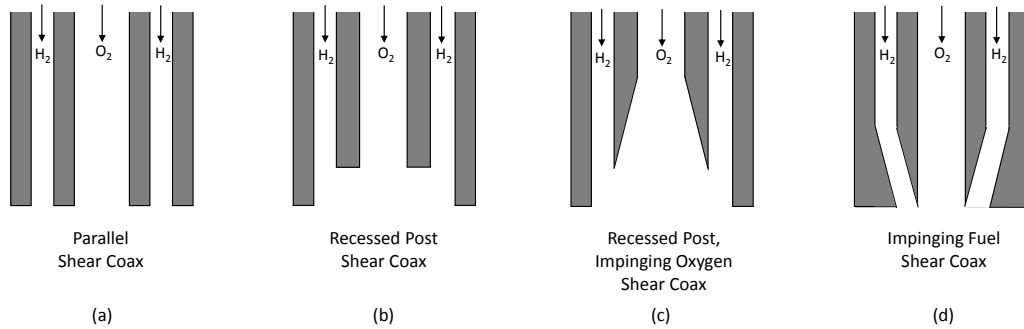
1.3: Modern launch vehicles using $\text{O}_2\text{-H}_2$ LREs. Delta IV (left, ULA 2011) Ariane 5 (right, ESA 2013)



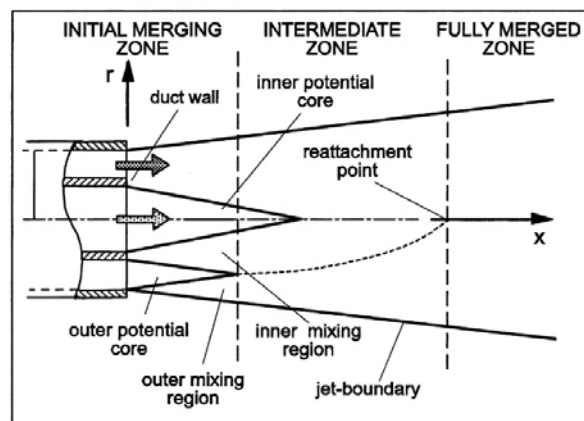
1.4: Diagram of the gas generator cycle in a liquid rocket engine.



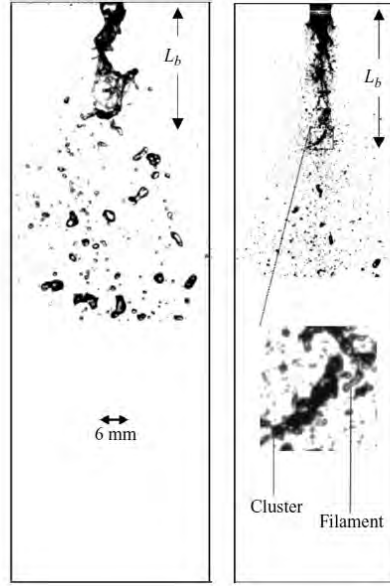
1.5: Fuel temperature ramping has been a common technique for verifying LRE stability for a wide range of fuel properties in hydrogen-oxygen engines. This plot, taken from Hulka and Hutt [45], reveals an instability occurring after a temperature drop engendered a lower hydrogen supply pressure.



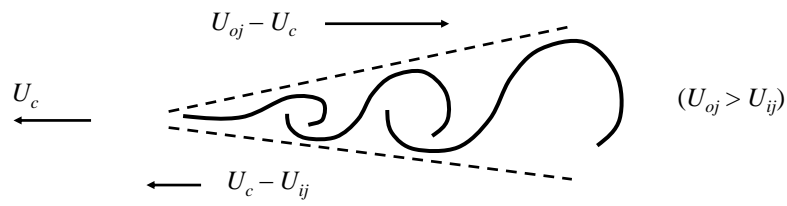
1.6: As early as the 1960s, multiple configurations of the shear-coaxial injector had been used to enhance mixing and prevent instability in hydrogen-oxygen LREs.



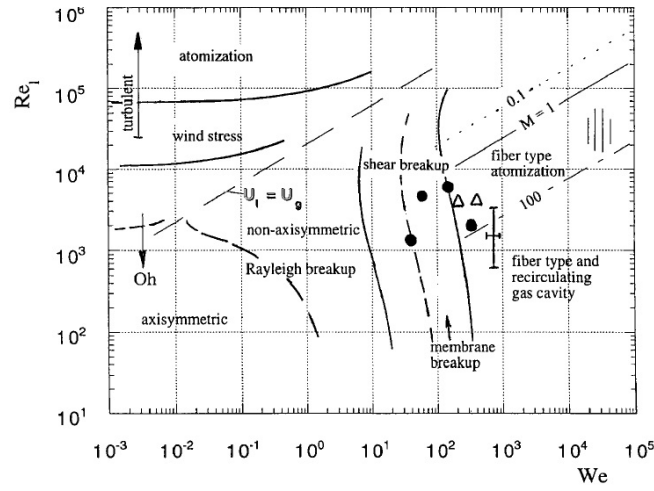
1.7: The mixing of the nonreactive shear-coaxial jet is characterized by three merging zones and two mixing regions. (diagram by Talamelli and Gavalini [108], adopted from Ko and Kwan [88])



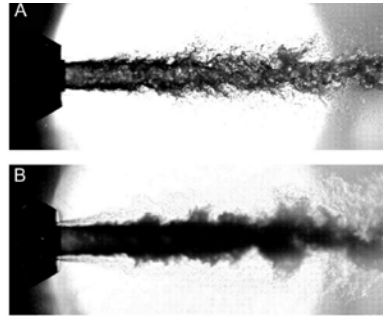
1.8: Coaxial jet images from Baillot *et al.* [16] show the membrane break up regime (left) and the fibre-type break up regime (right).



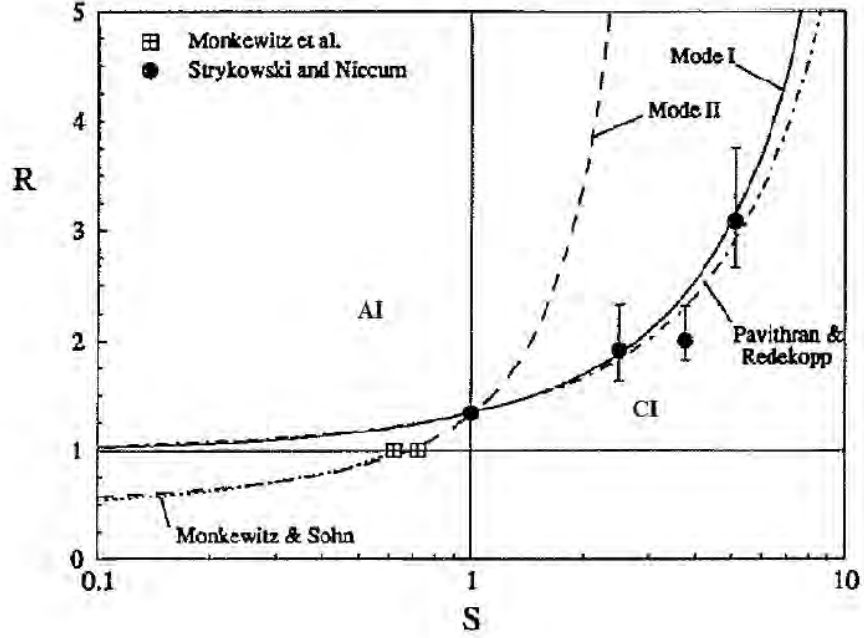
1.9: A convective shear layer diagram drawn in the vortex frame of reference.



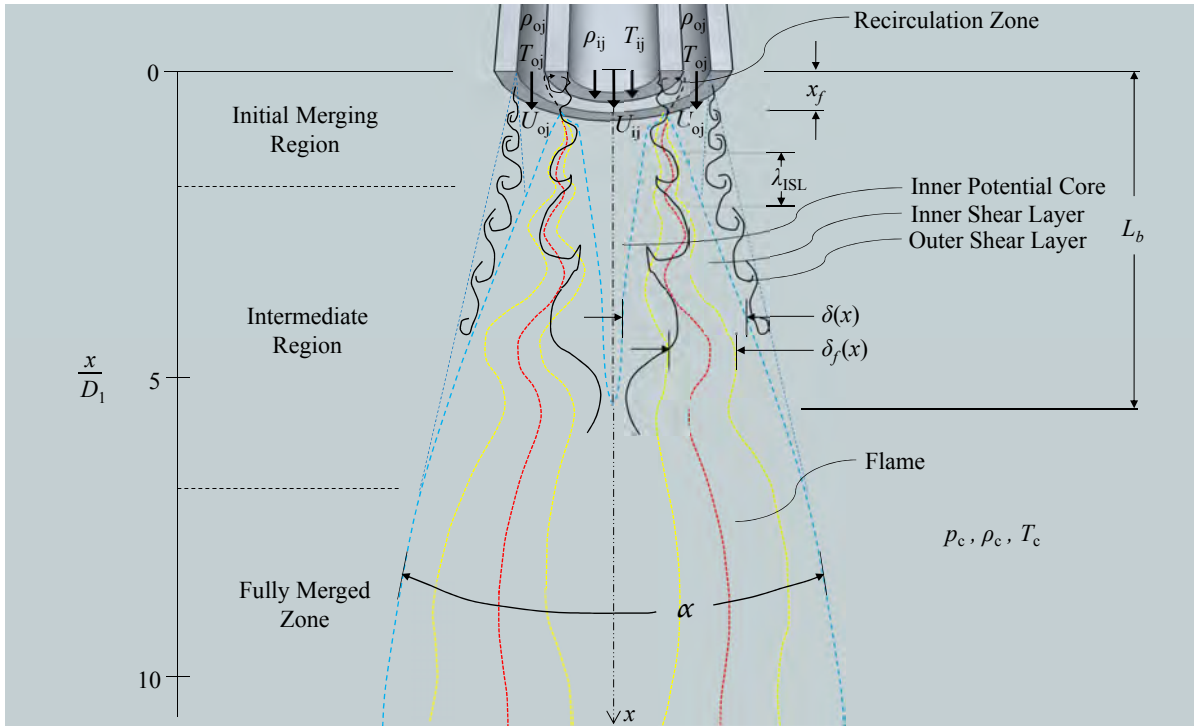
1.10: Break up characteristics of liquid-gas coaxial jets separated into five regimes (axisymmetric Rayleigh, antisymmetric Rayleigh, shear, membrane, and fibre-type break up) according to liquid Reynolds number and Weber number. M is the momentum flux ratio. (plot from Lasheras and Hopfinger [95])



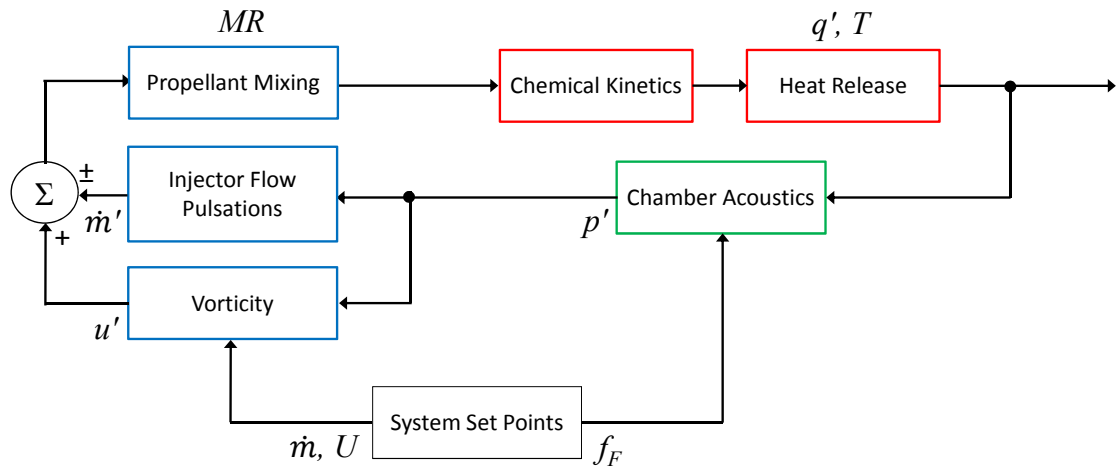
1.11: Shear-Coaxial jets of liquid nitrogen and gaseous helium issuing into high pressure chambers. $D_1 = 1.9$ mm, $U_{ij} = 5$ m/s, $U_{oj} = 100$ m/s, $T_{ij} = 97$ K, $T_{oj} = 280$ K (A) 1.0 MPa (B) 6.0 MPa (Mayer and Smith [14])



1.12: Absolute-convective instability transition lines from Jendoubi and Strykowski [121] with results from several others [113, 114, 133, 134]. The upper left region represents absolutely unstable operating space, and the lower right region represents convectively unstable operating space. Following the definitions of [121] for the x and y axes, $R > 1$ represents ambient counter-flow and $R < 1$ represents co-flow ($R \equiv (U_1 - U_2)/(U_1 + U_2)$). $S > 1$ represents jets *heavier* than the surrounding fluid, and $S < 1$ represents jets *lighter* than the surrounding fluid ($S \equiv \rho_1/\rho_2$). The typical conditions of a $\text{LO}_x\text{-GH}_2$ shear-coaxial jet lie in the convective instability operating space for $R < 0$, not shown here.



1.13: Flow diagram of a reactive shear-coaxial jet.



1.14: An expanded portrayal of the three part combustion instability feedback loop showing fluid mechanical features in blue, reactive features in red, and acoustic pressure oscillations in green. User-controlled acoustic forcing acts as an additional input to chamber pressure oscillations. Injector exit flow conditions act as a potential control of shear layer vortex structures.

CHAPTER 2

Experimental Facility and Methods - Acoustically Coupled Fuel Droplet Combustion

The experimental apparatus in these studies is the same as that used by Dattarajan *et al.* [22] and Rodriguez *et al.* [75], with several modifications. Modifications include, but are not limited to, the pressure perturbation measurement system and the flame imaging system, both of which will be described in this chapter.

2.1 Acoustic Waveguide

A long, cylindrical waveguide, similar to a Kundt's tube, was used to create standing acoustic waves by placing a loudspeaker at each end. The system was operated at atmospheric background pressure and room temperature. A continuously fed, burning fuel droplet was situated at the center of the waveguide. The waveguide was made of aluminum tubing with an inner diameter of 11.4 cm and a full length of 90 cm, and quartz windows placed in the side of the waveguide nearest the droplet allowed for optical access. The 8 Ω woofer loudspeakers were connected using three long rods, allowing the pair to be moved as an assembly while remaining a constant distance apart. The same apparatus was also used in a speaker-reflector configuration by replacing one speaker with an aluminum reflector plate. The complete apparatus is shown in Figure 2.1.

Using a function generator, a sinusoidal signal was sent to each loudspeaker with

the two signals in-phase ($\Delta\phi = 0^\circ$) or out-of-phase ($\Delta\phi = 180^\circ$). Due to a constant waveguide length L the loudspeaker frequency, or acoustic frequency f_a , is the controlling parameter in creating a resonant standing waveform within the waveguide. Theoretically, f_a can be chosen such that the waveguide length L is an integral multiple of half the acoustic wavelength, $\lambda/2$, that is,

$$L = \frac{n}{2}\lambda = \frac{n}{2}\left(\frac{c}{f_a}\right), \quad (2.1)$$

where c is the speed of sound. Regardless of the value of the f_a and n , speakers operated out-of-phase ($\Delta\phi = 180^\circ$) will create a PN at the center of the waveguide and speakers operated in-phase ($\Delta\phi = 0^\circ$) will create a PAN at the center [135]. But, to create an acoustically resonant condition with maximum pressure perturbations, then f_a must take on a value such that n is an integer. More specifically, for speakers operated out-of-phase, if f_a is chosen to give an odd value of n then the pressure amplitude is maximized in the waveguide. For speakers operated in-phase, if f_a is chosen to give an even value of n then the pressure amplitude is maximized in the waveguide. Thus, resonant conditions hold for a select few frequencies, but for any frequency the center of the waveguide will take on a PN or PAN condition for $\Delta\phi = 180^\circ$ and $\Delta\phi = 0^\circ$, respectively. These conclusions assume the perturbation amplitudes created by the speakers to be identical. In the special case where one speaker is instead replaced with a rigid wall, eqn. (2.1) still holds true. Theoretically, in this speaker-reflector configuration odd values of n produce a PN at the waveguide center, and even values of n produce a PAN at the waveguide center.

Experimental acoustic characterization relied on point-like pressure measurements made using a Kulite XCE-093-50D miniature pressure transducer with an output resolution 0.29 mV/kPa and diameter of 2.4 mm. The sinusoidal pressure transducer output signal was amplified and then used to find the pressure perturbation amplitude p' . With the sensor placed at the center of the waveguide, the most ideal f_a was determined by

sweeping through a wide range of frequencies in search of p' minima (PN) for $\Delta\phi = 180^\circ$ or p' maxima (PAN) for $\Delta\phi = 0^\circ$. The result of this frequency sweep technique is shown in Figures 2.2 and 2.3 for $\Delta\phi = 180^\circ$ and $\Delta\phi = 0^\circ$, respectively. Pressure measurements at the speaker are also shown, which will exhibit maxima for all resonant frequencies. Along these lines, a speaker-reflector frequency sweep was performed with a pressure sensor located at the reflector, and results are shown in Figure 2.4. All three frequency sweeps presented here can be used to extract experimental resonant wave frequencies, which can then be compared to theoretical resonant frequencies calculated using eqn. (2.1). This comparison is shown in Table 2.1.

Experiments by Dattarajan *et al.* [22] and Rodriguez *et al.* [75] employed a speaker-reflector configuration, but Teshome *et al.* [82] improved upon this by instead using the speaker-speaker configuration, citing a more symmetric pressure distribution about the center. This claim is explored more thoroughly here by measuring p' throughout the axial length of the waveguide for each frequency of interest. The resulting collection of pressure versus waveguide location plots is divided into speaker-reflector conditions in Figure 2.5, speaker-speaker out-of-phase conditions in Figure 2.6, and speaker-speaker in-phase conditions in Figure 2.7. Comparison with theoretical pressure distributions are also shown, with the pressure maximum based on matching of theory and experiment at the closest peak to the waveguide center.

First considering the speaker-reflector pressure distributions, the amplitudes are shown to be generally symmetric for frequencies near the theoretical values of Table 2.1. Figure 2.7 includes two frequencies which produce a PN at the waveguide center, 308 Hz and 784 Hz, and one other frequency which produces a PAN at the center, 562 Hz. Upon closer inspection though, the pressure distribution is mildly asymmetric for the lowest frequency, 308 Hz. The correspondingly longer wavelength associated with 308 Hz appears to exacerbate any asymmetric speaker boundary conditions, having a

greater impact on the distribution at the center. Moreover, previous work has shown conditions producing a distinct PN at the waveguide center to also produce a quite asymmetric velocity distribution according to hot wire measurements [75].

For the speaker-speaker results shown in Figure 2.6, operating the speakers 180° out-of-phase creates standing waves at the waveguide center regardless of acoustic frequency. For five different frequencies ranging from 332 Hz to 1500 Hz the primary difference is instead the maximum measured pressure amplitude. Similar plots are found in Figure 2.7 for speakers in-phase, which produces a PAN near the center for all five frequencies explored here. Also, when comparing two conditions with an equal speaker input voltage but different frequencies, choosing a frequency close to the resonant frequency will provide a larger pressure amplitude. For example, contrasting Figures 2.7(c) for 898 Hz and 2.7(d) for 1088 Hz shows a much larger amplitude for 1088 Hz. This principle holds true for all frequencies explored here, such that the difference in sound pressure level between a resonant and non-resonant flow condition could be easily detected by the human ear. The same body of work revealing asymmetric velocity distributions for the speaker-reflector configuration measured a very symmetric velocity distribution for the speaker-speaker configuration, largely motivating previous [82] and current experiments to employ a two speaker configuration. With this established, one must also note that additional hot wire measurements are needed to complete the current acoustic characterization and confirm the assumption that VAN locations indeed coincide with PN locations and vice versa. Hotwire measurements in Teshome *et al.* [82] were uncalibrated and preliminary, but did show a symmetric velocity profile with a VAN at the waveguide center.

2.2 Droplet Generation and Ignition

The fuel delivery system consisted of a hollow borosilicate glass capillary and a KDS Model 100 syringe pump. The fuel droplet was suspended within the waveguide at the tip of the glass capillary of approximately 0.37 mm outer diameter. Liquid fuel was delivered to the capillary during droplet combustion at a constant volumetric flow rate Q_v , set by the syringe pump. The volumetric flow rate and the droplet size were used to determine the burning rate constant K , as will be described below. A protective copper shroud was placed above the end of the glass capillary in order to prevent vaporization of the fuel within the glass capillary just above the droplet. The distance between the end of the shroud and the end of the tip of the capillary was fixed at 3.2 mm, a regime for which the droplet burning rate constant did not depend on this length [22]. The droplet was ignited by means of a resistive heating Ni-Cr wire mounted on a push-type solenoid. A TattleTale Model 8 data logger/controller board was used to synchronize the extension of the solenoid arm and the passage of current in the ignitor wires. This mechanism created an efficient means for igniting the droplet remotely without having to open, manually ignite, and close the waveguide. After ignition, the flame remained intact unless extinguished by strong convective flow or by a fuel vapor jet formed at the capillary exit due to overheated incoming fuel. This ignition technique was identically performed for all fuels, which are listed in Table 2.2 with their respective properties.

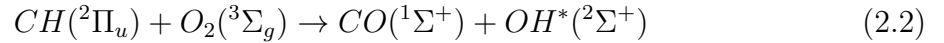
2.3 Imaging

Flame imaging was performed using an intensified camera and image acquisition system designed to capture OH^* chemiluminescence at various instants within an acoustic cycle. This imaging system is discussed in several parts. First, the optical train assembled to capture OH^* chemiluminescence is described, including a quantitative estimation of

transmission versus wavelength. Second, a description of the components, communications, and controls required to coordinate image acquisition will include equipment specifications and variables set by the user, with justification. Last, a timing system based upon the acoustic pressure cycle is explained.

2.3.1 Optics

There are several well-documented reactions occurring within hydrocarbon flames which produce chain carriers in route to the final combustion products. If sufficiently energetic, such reactions will produce radicals in electronically excited states which then undergo deexcitation through one of two mechanisms. More specifically, hydrocarbon flames commonly exhibit the reaction



where electronically excited hydroxyl radicals (OH^*) then experience spontaneous radiative deexcitation (chemiluminescence) or collisional deexcitation (quenching). The exact proportions of quenched OH^* and OH^* which produces chemiluminescence are governed, for example, by fuel type (e.g. carbon to hydrogen ratio) and flow conditions (e.g. pressure). Regardless of these precise quantities though, regions of OH^* chemiluminescence are shown to coincide with primary reaction zones and lie close to, if not coincide with, maximum temperature [66, 136]. This correlation between OH^* chemiluminescence and flame topology has limitations with turbulent premixed flames or flames near extinction [137], but is quite sufficient for laminar diffusion flames in steady state conditions. Thus, for droplet combustion this study tracks light emission created via the deexcitation reaction



which is observed in the ultraviolet (UV) band at approximately 308 nm.

The optical arrangement passes a span of UV wavelengths to isolate this particular source of chemiluminescence. Figure 2.8 shows the receiving optics from the flame to the camera. The quartz waveguide window and the UV lens (UV-Nikkor 105 mm f/4.5) pass with over 70% transmission for low UV to high infrared (IR) wavelengths, while the camera photocathode is designed for best capture with low wavelengths. The UV bandpass filter provides 88% maximum transmission centered around 320 nm, and also transmits 20-50% of IR light. The camera photocathode (NanoStar S20 type) achieves greatest quantum efficiencies for 200-450 nm. The combined transmission of the receiving optics is quantified in Figure 2.9. To confirm capture of OH* chemiluminescence and blocking of other sources of chemiluminescence, results from the work of Kojima *et al.* [138] are shown for comparison. The transmission range is consistent with this prior work for methane.

2.3.2 Image Acquisition

Acquiring and storing flame images for specific parts of an acoustic cycle is made possible by the interconnection of image acquisition equipment shown in Figure 2.1. The function generator which controls loudspeakers sends a second signal, equal to the first in phase and frequency, to a Programmable Timing Unit (PTU) for camera control. This parallel control of the acoustic and imaging systems by a single function generator permits image capture which is phase-locked to a short span of time within the acoustic cycle.

The PTU sends a signal to the camera which can be custom manipulated within LaVision's software interface, but always maintains a frequency equal to the acoustic frequency. Custom manipulations include specifying the image intensifier gate width, image intensifier gain, number of intensifier pulses within one image frame (burst count), and the phase angle marking the start of the intensifier gate. For all imaging in this study, the gate width time is set equal to $1/64$ of the acoustic period, $T_a/64$, while the

intensifier gain and burst count must be varied to ration the total intensity captured by the CCD sensor. For example, high luminosity flames such as JP-8 require a lower intensifier gain and burst count than low luminosity flames such as methanol. Otherwise, the CCD sensor will be damaged by over-exposure. Depending on fuel type, the intensifier gain and burst count range from 30/100 to 80/100 and 20 to 200, respectively. Other specifications are listed in Table 2.3. Last, the phase angle marking the start of the intensifier gate is specified by a repeating loop of 18 different phase angles, $\phi_{II} = 20: 20: 360$. However, this phase angle sequence is in reference to the PTU output signal, which is not in phase with the acoustic pressure cycle due to time delays caused by components within both the acoustic system and the imaging system. Thus, these time delays, or phase delays, must be measured in order to convert ϕ_{II} to its equivalent value referenced by the acoustic pressure cycle ϕ_p .

2.3.3 Acoustics-Imaging Synchronization

Reformatting ϕ_{II} in terms of ϕ_p is possible by comparing two signals and their associated phase delays. First, the pressure perturbation signal is measured by a pressure transducer and observed via oscilloscope, creating phase delays due to the transducer unit and pressure transducer amplifier. Second, the camera produces a TTL output pulsed with the image intensifier gate, thus providing a pulsed signal corresponding to the actual time period captured by the camera. Relating these two signals allows one to identify the exact slice of time within the acoustic pressure cycle which is captured by the camera. Moreover, this technique strategically avoids individual measurement of the phase delays associated with each individual component within the acoustic and imaging systems (e.g. speaker amplifier, loudspeakers, sound travel, PTU, etc.).

Specifically, the problem is represented as $\phi_p = \phi_{II} + \Delta\phi$. Setting $\phi_{II} = 0$ and measuring $\Delta\phi$ gives a solution for ϕ_p . $\Delta\phi$ is uniquely determined for each forcing

frequency as the difference between the two signals listed above plus pressure transducer and pressure transducer amplifier phase delays, as listed above. The pressure transducer phase delay is $< 1^\circ$, and negligible. The pressure transducer amplifier phase delay is measured as part of a complete frequency response measurement, thus recording both the amplifier gain and phase delay as a function of frequency. The camera’s TTL output representing the image intensifier gate is delayed by 20 ns and the delays associated with all wiring are ~ 1 ns, both negligible.

2.4 Measurement Methods

2.4.1 Burning Rate Constant

From continuity for a spherical droplet of diameter d , the instantaneous burning rate constant K may be evaluated as

$$K = \frac{4Q_v}{\pi d(t)} - 2d\dot{d} \quad (2.4)$$

A constant volumetric flow rate Q_v provided by the syringe pump was chosen in order to maintain a roughly constant droplet size. This technique makes the first term in eqn. (2.4) the dominant term, while the second term is close to zero. This is the opposite of the typical “non-fed” burning droplet governed by the d^2 law when $Q_v = 0$ [63, 64]. Due to the normal gravity environment of the present experiments, eqn. (2.4) required a droplet diameter equivalent to that of a sphere with volume equal to the oblong droplet volume, as done by Struk *et al.* [65] and described in section 1.2.2. A custom image processing MATLABTM algorithm was used to fit an ellipse to the droplet in each image, thus providing the data needed to calculate d_{eqvs} for each image and \dot{d}_{eqvs} for a set of images. Additional LED back-lighting provided ample contrast between the liquid fuel and the back-light in order for the image processing algorithm to detect the silhouette of the droplet. Time-averaged K values were then computed according to eqn. (2.4)

for a complete flow condition. The same calculation could be performed for a given acoustic phase angle within a flow condition, but this task reveals fuel droplet sizes to be independent of phase and thus K values also independent of phase. Investigation of burning rate versus acoustic phase could instead require utilizing chemiluminescence intensity variations with respect to acoustic phase, which has not been explored in previous works.

2.4.2 Acoustic Acceleration

In the absence of acoustic forcing the only net force is the buoyancy force, acting on the volume V of hot products with density ρ_p . When surrounded by a cooler gas of density ρ_o the buoyancy force follows as $F_B = (\rho_p - \rho_o)Vg_o$, which results in a vertically oriented, symmetric flame. With acoustic excitation, the flame orientation became aligned with the resultant force due to buoyancy and an analogous acoustic radiation force, $F_R = (\rho_p - \rho_o)Vg_a$, where g_a is the acoustic acceleration. This type of behavior is shown in Figure 2.10. According to the theory suggested by Tanabe *et al.* [21], based on the work of Nyborg [79], the acoustic acceleration g_a depends on the position of the droplet with respect to the PN or PAN. In light of the preceding relationship, this study experimentally determines acoustic acceleration as done by Teshome *et al.* [82]. The actual acoustic acceleration at the location of the droplet is estimated using the measured deflection angle ϕ_f and gravitational acceleration

$$g_{a,exp} = g_o \tan \phi_f \quad (2.5)$$

The degree of flame deflection ϕ_f was estimated by measuring the average change in angle between the tangent lines of an unforced and forced flame edge, as shown in Figure 2.10. For extreme cases of flame deflection where the flame is nearly horizontal, more uncertainty can be attributed to ϕ_f because the plume region turns upward in the far wake of the flame.

2.4.3 Flame Standoff Distance

A burning droplet in normal gravity is encompassed by a quasi-ellipsoidal flame front as shown by Figure 2.10, an image for the special case of an acoustically excited burning droplet. For both unforced and forced burning droplets, the flame standoff distance δ_f is clearly a function of the angle θ measured from the positive x -axis in the x - y plane. One should also deduce that unlike the unforced case, the acoustically forced flame is not axisymmetric because δ_f is also a function of the out-of-plane angle ϕ . But, for the two-dimensional standoff distance measurements discussed here, this discrimination will not bear importance.

Flame standoff distance is defined as the difference between the flame and droplet radii, $\delta_f = r_f - r_s$, each of which is measured by image analysis algorithms. First, r_s is defined as a function of θ using the droplet ellipse fit technique identical to that employed in d_{eqvs} measurements. Second, r_f is defined as the distance from the center of the droplet to the location of maximum OH^* chemiluminescence intensity for a given value of θ . This particular definition of the “flame” is common to many experimental works in the fields of both diffusion and premixed flames [66, 67, 137, 138]. Several other definitions have been used as a reliable measure of flame topology, including the point of maximum temperature, maximum C_2^* or CH^* chemiluminescence, or maximum HCO mole fraction. Moreover, different flame measurement methods can provide conflicting results in the realm of turbulent premixed flames or flames near the extinction strain limit. Extinction studies have actually revealed shortcomings in the traditional OH^* chemiluminescence technique when carbon-based chain carriers sustain reaction where a lack of OH^* chemiluminescence would otherwise predict extinction [137]. The questions arising from these inconsistencies are highly motivated by combustion instability research and imply a loss of robustness for this study’s r_f definition. But, the set of results analyzed here avoid extinction for even the strongest convective and oscillating

flows. In conclusion, the maximum OH^* chemiluminescence flame definition is imperfect, but quite effective for a diffusion flame in the current flow conditions, where a lack of extinction and turbulent flame structure provide for an unbroken flame front in all flame images.

Finally, δ_f data analysis will focus attention on the upstream side of the flame, the location of which is determined by acoustic flow conditions. For example, Figure 2.10 shows a stagnation point on the flame's right side. A different droplet position though, can switch flame orientation and move the stagnation point, thus moving the area of interest. Therefore, it is important to clarify that δ_f is measured on the upstream side only. These measurements include $\delta_f(\theta = 0^\circ)$ and $\delta_f(\theta = 180^\circ)$, depending on flame orientation. Other valuable analysis includes minimum standoff distance created by natural convection $\delta_f(\theta = 270^\circ)$ and standoff distance at the stagnation point $\delta_f(\theta = \alpha_f)$, but little study of these points is included in this body of work.

2.5 Experimental Procedure

Upon beginning a set of experiments, a clean syringe was loaded with the desired fuel and connected to the glass capillary by a rubber tube. The flow rate maintained by the syringe pump was chosen to achieve quasi-steady droplet burning for a given fuel and flow condition. For all experiments in this study, fuel flow rate fell within the range $53.3 \text{ mL/hr} < Q_v < 63.3 \text{ mm}^3/\text{s}$. The acoustic amplitude for a given condition was identified using p' measured at the PAN with the smallest positive x location, which required knowledge gained from pressure distributions shown in Section 2.1. This amplitude is represented as p'_{max} , i.e. $p'_{max}(f_a = 332 \text{ Hz}) = p'(x = 28 \text{ cm})$, $p'_{max}(f_a = 898 \text{ Hz}) = p'(x = 10 \text{ cm})$, $p'_{max}(f_a = 1500 \text{ Hz}) = p'(x = 5 \text{ cm})$. Finally, before each ignition, the waveguide was purged with air to remove combustion products from prior experiments.

Droplet ignition was performed using the heater wire and push-type solenoid assembly, and ignition was immediately followed by initiating the acoustics. Under the steady conditions used here, burning droplets could be sustained for as long as 10 minutes without flame extinction. Within this burning period an image recording loop cycled through 18 different phase-locked acoustic phase angles, $\phi_{II} = 20 : 20 : 360$, acquiring 5 images at each phase before proceeding to the next. This method of capturing 90 images was performed 4 times to complete 1 recording session, which required 2 to 5 minutes of recording. Each image was immediately digitized in .im7 file format with an associated clock time. The imaging procedure was completed by acquiring a set of 50 background images with the capillary and shroud removed from the field of view, and thus the LED creating the only source of light and variations thereof.

The experiment was followed by two steps of image processing. First, a flame image was processed using LaVision's DaVis software, where the average of 50 background images was subtracted from the flame image. Second, the resulting pair of flame images (original and background subtracted) were reoriented and analyzed using a MATLABTM algorithm. The original image was utilized only to detect the droplet edge, and then calculate the position and dimensions of an ellipse coinciding with the droplet silhouette. Using the pixel coordinates of the ellipse center, the background subtracted image was converted from cartesian coordinates to cylindrical coordinates with an origin at the ellipse center, and this final image was used for all remaining flame analysis. It should be noted that imperfections in the background subtraction technique arise because although the shroud, capillary, and droplet shield backlighting, the backlight is still subtracted from these areas, creating biased regions in the final flame image. The pixel intensities of these regions are lower than actual intensities, but this bias error does not interfere with the conclusions of this study.

2.6 Measurement Uncertainties

2.6.1 Precision Uncertainty

The sources of precision uncertainty in the measured values of the burning rate constant K in eqn. (2.4) stem from uncertainties in the fuel volumetric flow rate Q_v and determining the equivalent sphere diameter d_{eqvs} for the droplet. The technique for calculating the uncertainty in d_{eqvs} is similar to the method used by Dattarajan *et al.* [22] which utilizes the principles of uncertainty propagation in Mills and Chang [139], but with improved resolution due to a reduced pixel view. First, the equivalent sphere diameter is found in terms of the major and minor axes of the droplet ellipse, resulting in $d_{eqvs} = 2a^{\frac{2}{3}}b^{\frac{1}{3}}$. Then, if the uncertainty in the axes lengths, a and b , are equal, then the method cited above follows as

$$\begin{aligned}
 \Delta d_{eqs} &= \sqrt{\left(\frac{\partial d_{eqs}}{\partial a} \Delta a\right)^2 + \left(\frac{\partial d_{eqs}}{\partial b} \Delta b\right)^2} \\
 &= \sqrt{\left(\frac{2}{3} \frac{2b^{\frac{1}{3}}}{a^{\frac{1}{3}}} \Delta a\right)^2 + \left(\frac{1}{3} \frac{2a^{\frac{2}{3}}}{b^{\frac{2}{3}}} \Delta b\right)^2} \\
 &= \sqrt{\left(\frac{4}{3} \Delta a \left[\frac{b}{a}\right]^{\frac{1}{3}}\right)^2 + \left(\frac{2}{3} \Delta b \left[\frac{a}{b}\right]^{\frac{2}{3}}\right)^2} \\
 &= \Delta ab \sqrt{\frac{16}{9} \left[\frac{b}{a}\right]^{\frac{2}{3}} + \frac{4}{9} \left[\frac{b}{a}\right]^{-\frac{4}{3}}}
 \end{aligned} \tag{2.6}$$

where it is assumed $\Delta a = \Delta b = \Delta ab$. Uncertainty in d_{eqvs} is then calculated using $d_{eqvs} \approx 1.5$ mm, $\Delta ab \approx 0.05$ mm, and $\frac{b}{a} \approx 1.5$, giving an uncertainty of $\frac{\Delta d_{eqvs}}{d_{eqvs}} \approx 5.4\%$. Uncertainty in Q_v though, is based solely in the precision uncertainty of the syringe pump. Thus, the manufacturer's rating of 0.1% is used for $\frac{\Delta Q_v}{Q_v}$.

The resulting uncertainties in K follow as

$$\begin{aligned}
\Delta K &= \sqrt{\left(\frac{\partial K}{\partial Q_v} \Delta Q_v\right)^2 + \left(\frac{\partial K}{\partial d_{eqs}} \Delta d_{eqs}\right)^2} \\
&= \sqrt{\left(\frac{4\Delta Q_v}{\pi d_{eqs}}\right)^2 + \left(-\frac{4Q_v}{\pi d_{eqs}^2} \Delta d_{eqs}\right)^2} \\
&= \sqrt{\left(K \frac{\Delta Q_v}{Q_v}\right)^2 + \left(-K \frac{\Delta d_{eqs}}{d_{eqs}}\right)^2} \\
&= K \sqrt{\left(\frac{\Delta Q_v}{Q_v}\right)^2 + \left(\frac{\Delta d_{eqs}}{d_{eqs}}\right)^2}
\end{aligned} \tag{2.7}$$

Therefore, $\frac{\Delta K}{K} = 5.4\%$ when $\frac{\Delta d_{eqs}}{d_{eqs}} \approx 5.4\%$ and $\frac{\Delta Q_v}{Q_v} = 0.1\%$, and the influence of fuel flow uncertainty has a negligible affect on total uncertainty in K . The transient term in eqn. (2.4) also has a negligible affect in this analysis and is not included here. Last, the precision uncertainty of time-averaged K values, which is of primary importance in this study, can be found by accounting for the minimum number of experimental points used to encompass the burning rate constant for one flow condition, 30. The resulting precision uncertainty in average K values is estimated to be $5.4\%/\sqrt{30} \approx 0.99\%$.

The source of precision uncertainty for pressure perturbation measurements, on the other hand, lies only in the accuracy rating of the pressure transducer. The XCE-093-50D has an output signal reproducibility of 0.5% of the full scale output, $\Delta V = (0.005)(FSO) = (0.005)(100 \text{ mV}) = 0.5 \text{ mV}$. With a signal resolution of 0.292 mV/kPa and a signal amplifier gain of 495, the calculation follows as

$$\begin{aligned}
\Delta p' &= \sqrt{\left(\frac{\partial p'}{\partial V} \Delta V\right)^2} \\
&= \frac{\partial p'}{\partial V} \Delta V \\
&= \frac{\partial}{\partial V} \left(\frac{V}{\delta G}\right) \Delta V \\
&= \frac{0.5 \text{ mV}}{(0.292 \frac{\text{mV}}{\text{kPa}}) (495)} = 3.5 \text{ Pa}
\end{aligned} \tag{2.8}$$

For the pressure amplitude used most in this study, $p' = 150$ Pa, the precision uncertainty is $\frac{\Delta p'}{p'} \approx 2.31\%$.

2.6.2 Bias Uncertainty

Concerning K , sources of bias uncertainty include a 1% accuracy rating for Q_v , quoted from the syringe pump manufacturer, and bias due to pixel representation of the droplet edge. The latter form of uncertainty is present in all experiments where image analysis algorithms are used for edge detection. For this particular study, the camera's high spatial resolution results in a pixel view of $7.3 \mu\text{m}$ and therefore, droplet edge detection bias is negligibly small when compared to precision uncertainties and error from the droplet ellipse fit process. This ellipse fit technique, the third source of bias uncertainty discussed here, is largely connected to errors from equating the diameter of the droplet ellipse with the diameter of a sphere of equivalent diameter. Extensive analysis is included in Dattarajan *et al.* [22], where other techniques for choosing an appropriate droplet diameter d are quantitatively compared. Additional attention though, could be given to the accuracy of the ellipse fit itself. Surface tension and gravitational forces cause the droplet to form a teardrop-like shape, where an ellipse fit consistently matches the lower edge of the droplet, but over estimates the volume in the upper portion of the droplet. Ultimately, the burning rate constant K is under estimated by an enlarged droplet volume. Flame standoff distance measurements are uninfluenced by this effect because this study is interested in standoff distance for the lower hemisphere of the droplet, where the majority of burning occurs.

Although, the standoff distance measurement technique contains a second source of bias uncertainty. Droplet flame images represent a 3-D reaction zone in a 2-D manner, which misrepresents flame curvature. Well documented deconvolution methods, such as the Abel transform [140], can transform an axisymmetric image of a 3-D field into an

image representing a 2-D plane view. For example, an Abel transformed image of an unforced droplet flame is shown in Figure 2.11. Adversely, acoustically forced flames are non-axisymmetric, leaving the vast majority of images analyzed in this study subject to line-of-sight error. When defining the flame as the point of peak OH* chemiluminescence, as described in section 2.4.3, the measured flame standoff distance is less than the actual distance. Correction requires a value for flame curvature perpendicular to the image plane, which is unknown and unequal to the known flame curvature within the image plane for acoustically forced flames.

2.1: Experimental and Theoretical Resonant Frequencies

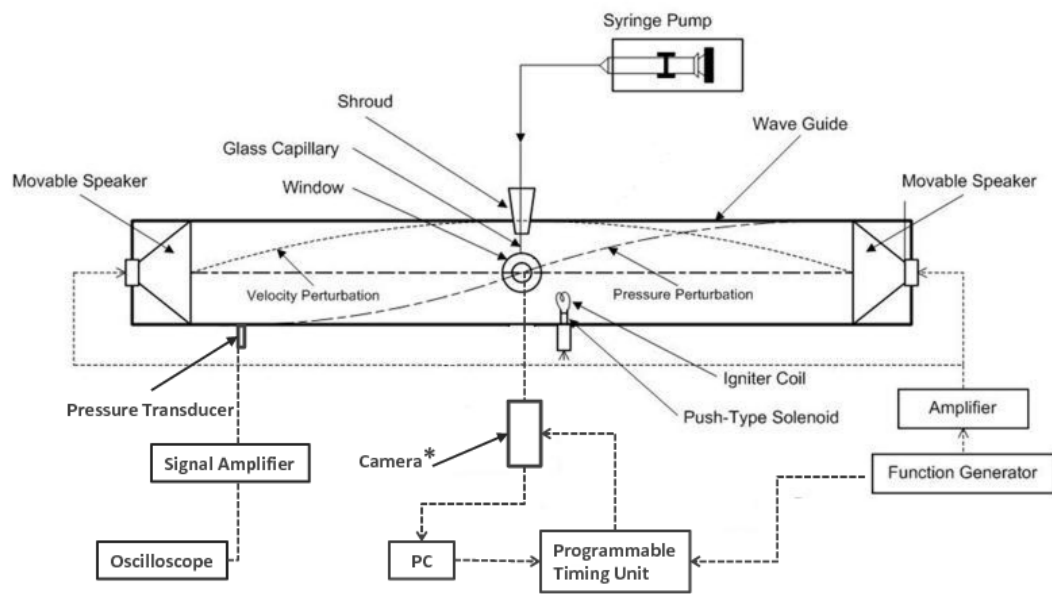
Speaker-Speaker				Speaker-Reflector			
$\Delta\phi = 0^\circ$ (PAN)		$\Delta\phi = 180^\circ$ (PN)		PN		PAN	
f_{exp} [Hz]	f_{th} [Hz]	f_{exp} [Hz]	f_{th} [Hz]	f_{exp} [Hz]	f_{th} [Hz]	f_{exp} [Hz]	f_{th} [Hz]
154		332	281.2	562	527.9	308	263.9
558	562.5	898	843.7	1108	1055.7	796	791.8
1132	1125.0	1500	1406.2		1583.6	1370	1319.7

2.2: Fuel Properties (alcohol fuels [64]; hydrocarbon fuels [141])

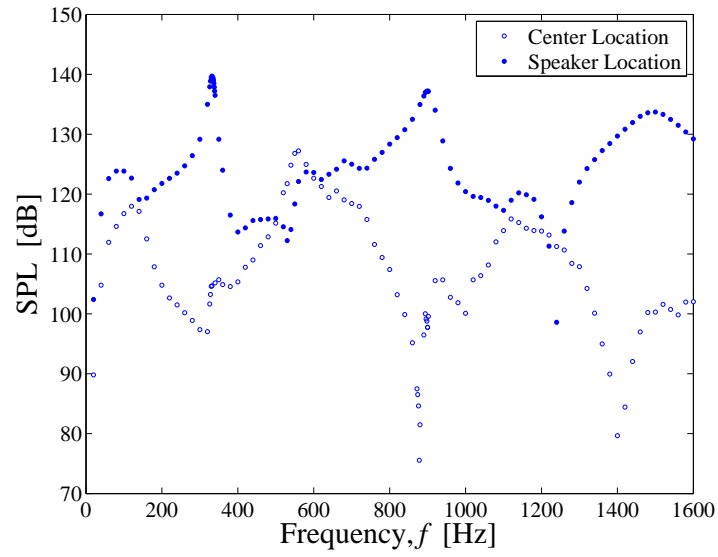
Fuel	Chemical Formula	Specific Heat Capacity c_p [kJ/kg·K]	Thermal Conductivity k [W/m·K]	Heat of Vaporization h_{fg} [kJ/kg]	Lower Heating Value LHV [kJ/kg]
Ethanol	C_2H_5OH	2.815	0.0533	841	26952
Methanol	CH_3OH	2.531	0.0616	1104	19930
Pure FT	$C_{12}H_{25}$	2.793	0.00935	339	44136
JP-8/FT	$C_{11}H_{22}$	2.01	0.0134	297	43745

2.3: Camera Specifications

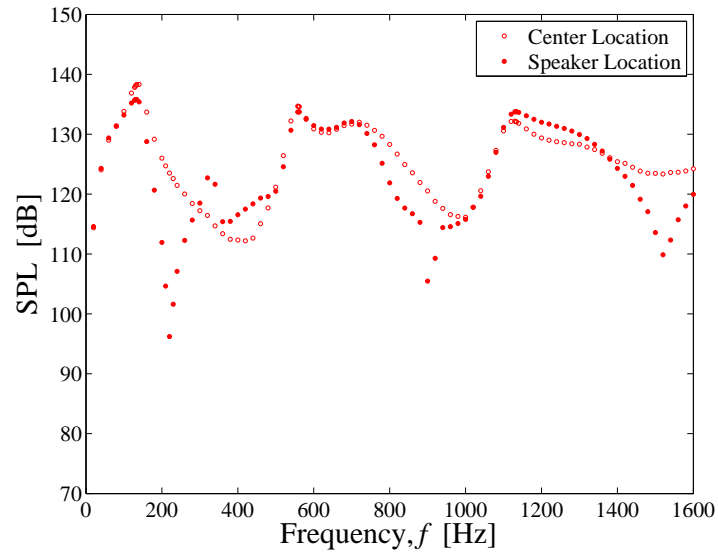
Maximum Frame Rate	8 Hz
Dynamic Range	4096
Active Image Area	1280 x 1024 pixels
Pixel Size	6.7 μm x 6.7 μm
Field of View	9.3 mm x 7.4 mm
Pixel View	7.3 μm x 7.3 μm
Depth of Field	2 mm
CCD Readout Noise	< 2 counts (RMS)



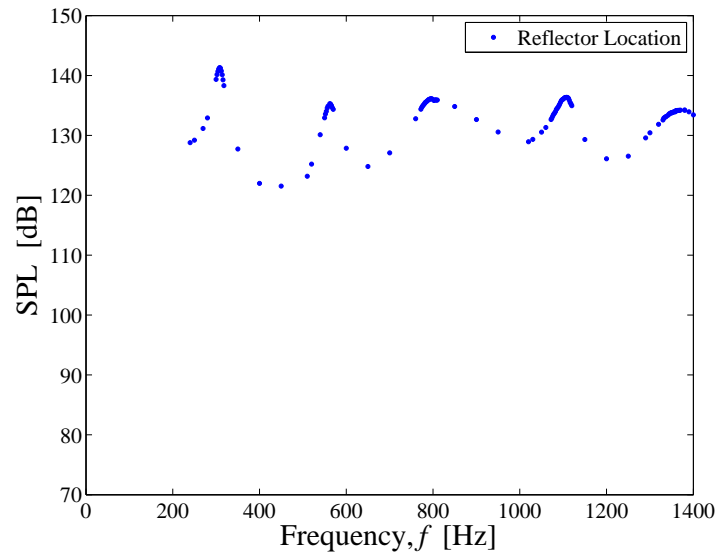
2.1: Experimental setup of the acoustic waveguide and feed droplet system.



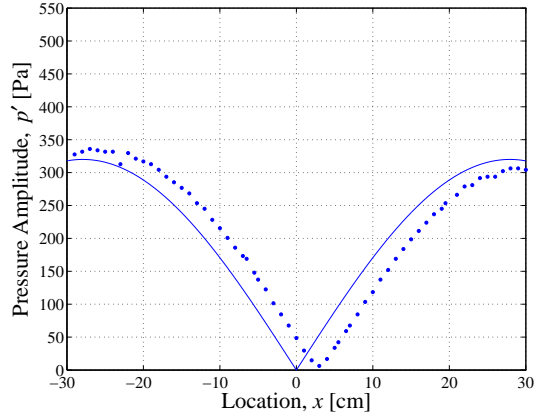
2.2: Frequency sweep for the speaker-speaker configuration with speakers operated 180° out-of-phase and a PN occurring at the center of the waveguide. The distance between speakers is approximately 61 cm. Resonant frequencies are shown to occur near 332 Hz, 898 Hz, and 1500 Hz.



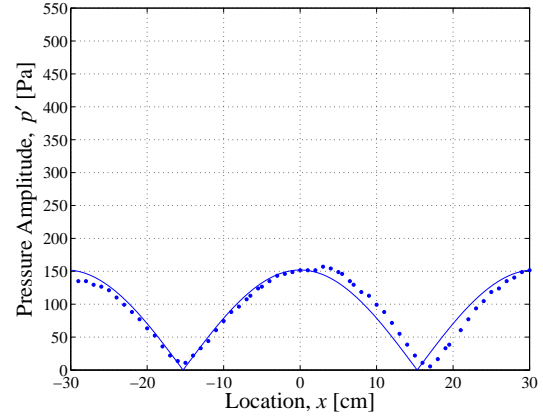
2.3: Frequency sweep for the speaker-speaker configuration with speakers operated in-phase (0°) and a PAN occurring at the center of the waveguide. The distance between speakers is approximately 61 cm. Resonant frequencies are shown to occur near 134 Hz, 558 Hz, and 1132 Hz.



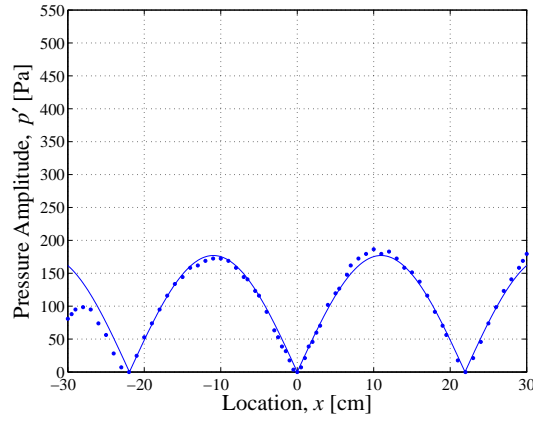
2.4: Frequency sweep for the speaker-reflector configuration. The distance between speaker and reflector is approximately 65 cm. Resonant frequencies are shown to occur near 562 Hz and 1108 Hz for a PAN occurring the waveguide center and 308 Hz, 796 Hz, and 1370 Hz for a PN occurring at the waveguide center.



(a) 308 Hz PN (200 mV input)

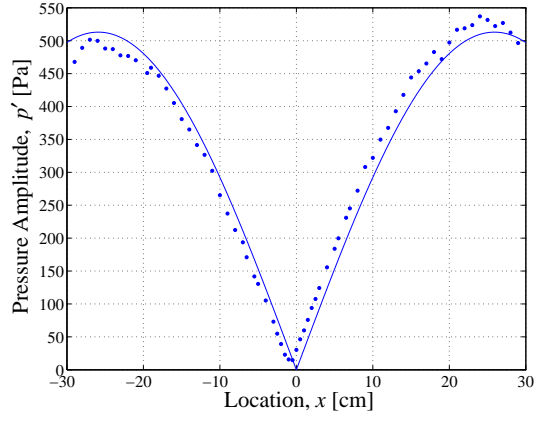


(b) 562 Hz PAN (200 mV input)

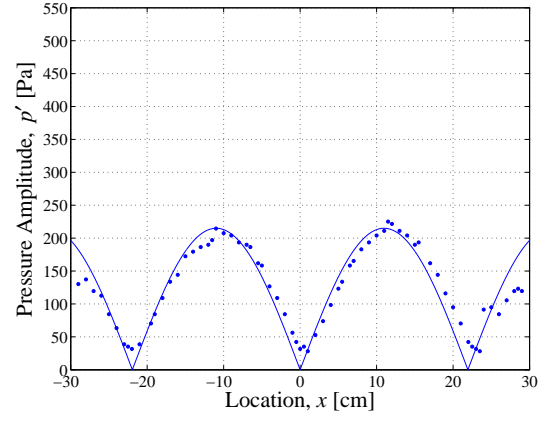


(c) 784 Hz approximate PAN (400 mV input)

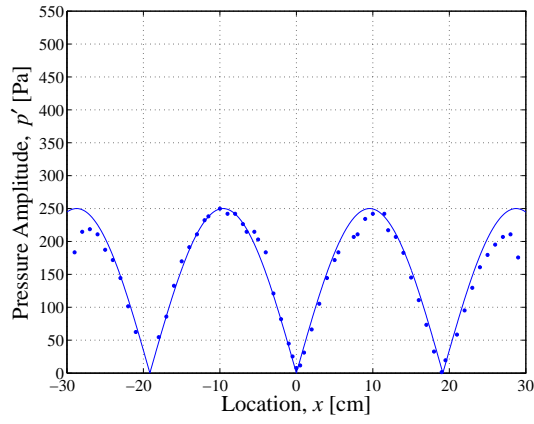
2.5: Acoustic pressure amplitude measurements for the speaker-reflector configuration. The distance between speaker and reflector is approximately 65 cm, and the reflector is located at the positive end of the waveguide.



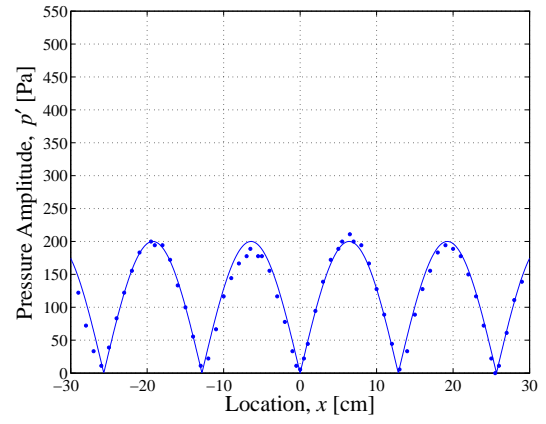
(a) 332 Hz PN



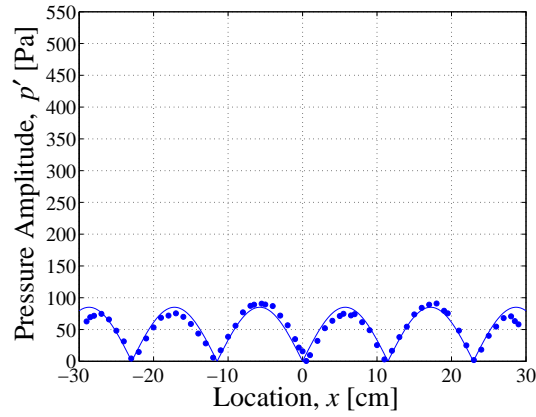
(b) 784 Hz



(c) 898 Hz PN

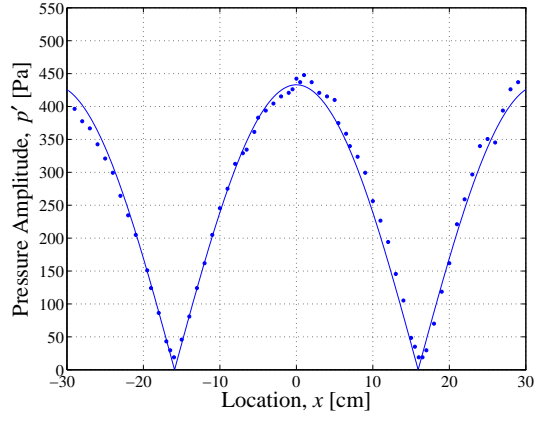


(d) 1340 Hz

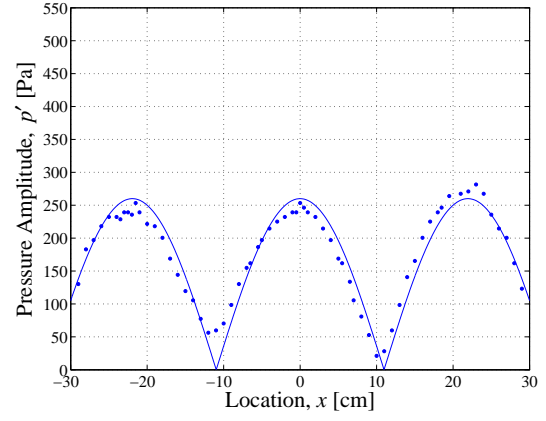


(e) 1500 Hz PN

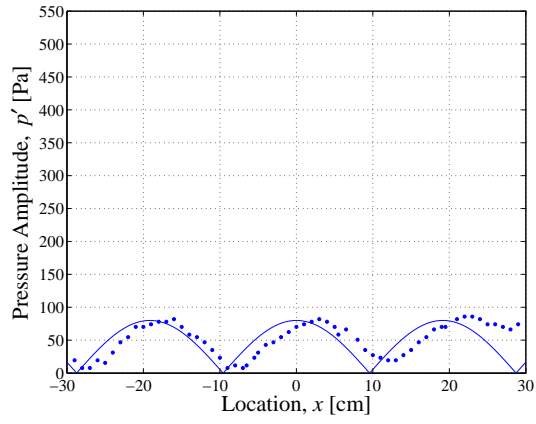
2.6: Acoustic pressure amplitude measurements for the speaker-speaker configuration ($\phi = 180^\circ$). The distance between the speakers is approximately 61 cm. (200 mV speaker input)



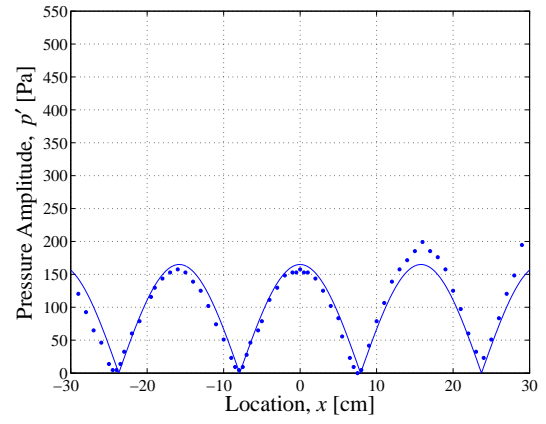
(a) 540 Hz PN



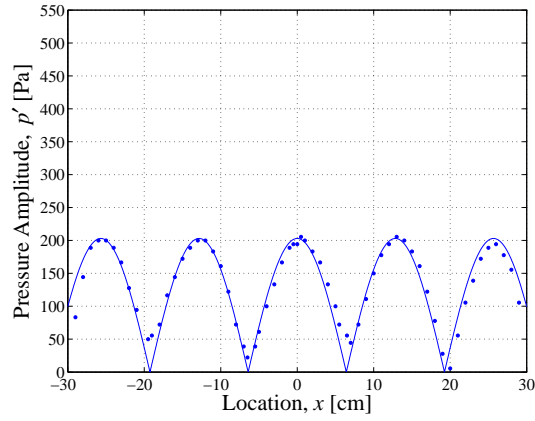
(b) 784 Hz



(c) 898 Hz PN

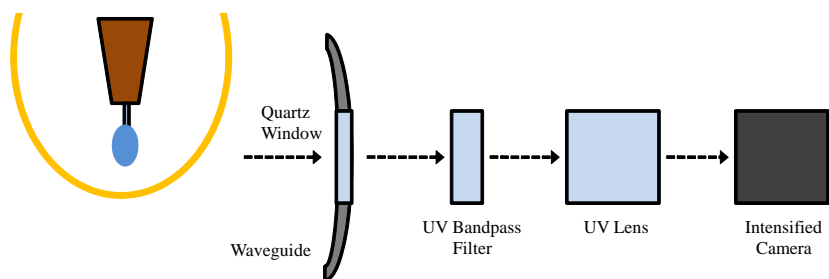


(d) 1088 Hz

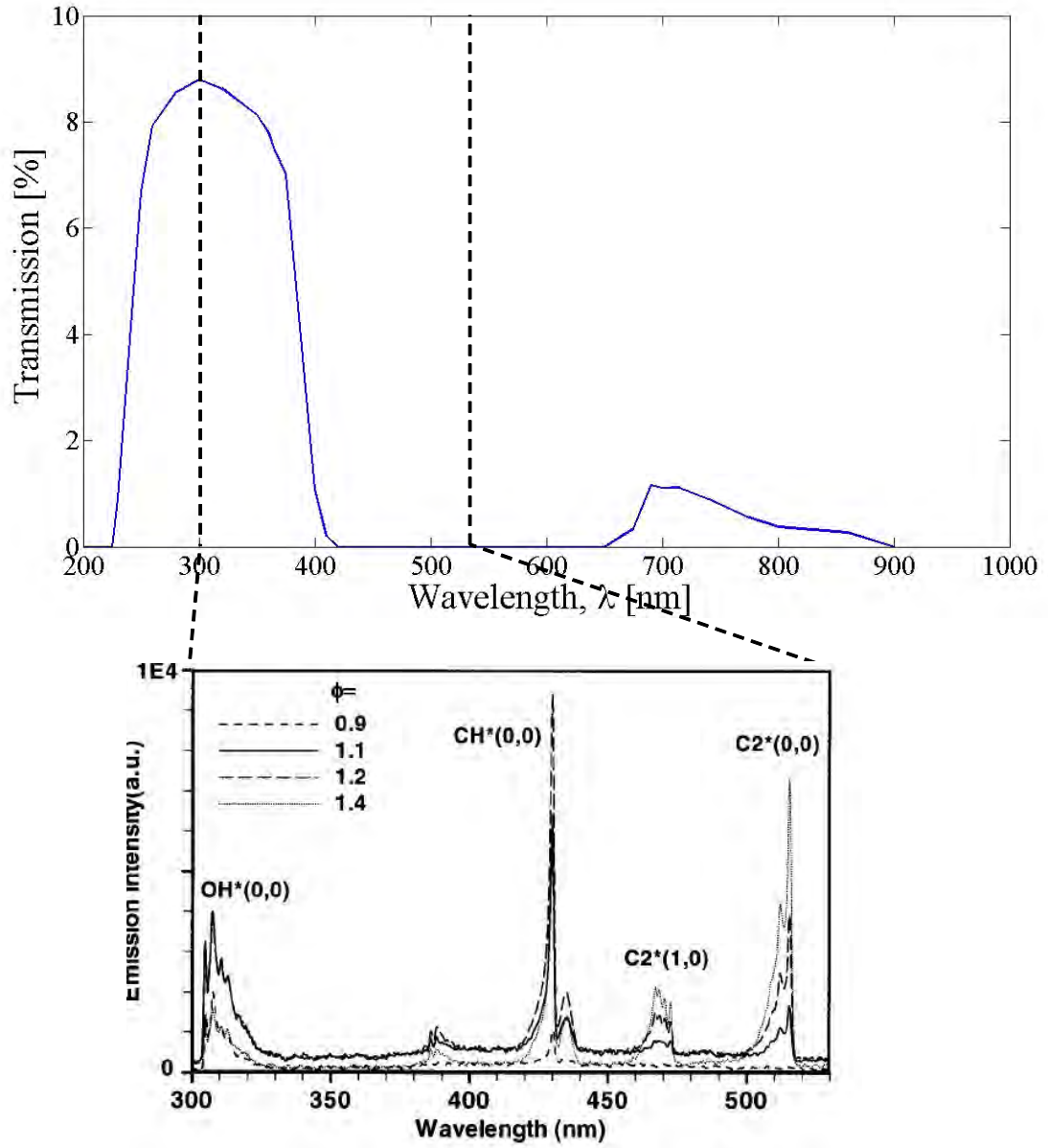


(e) 1340 Hz PN

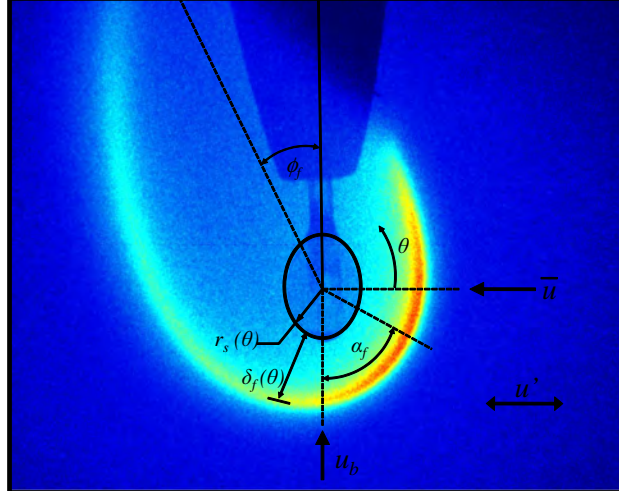
2.7: Acoustic pressure amplitude measurements for the speaker-speaker configuration ($\phi = 0^\circ$). The distance between the speakers is approximately 61 cm. (200 mV speaker input)



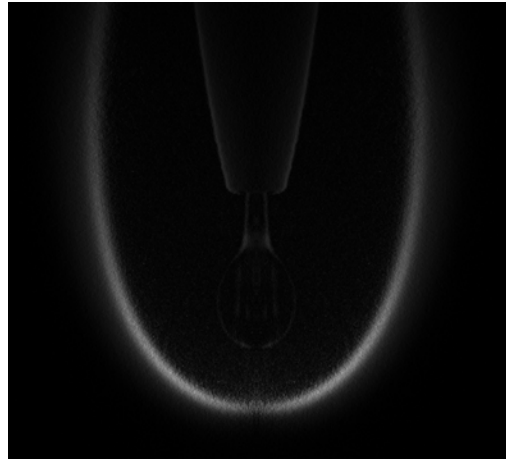
2.8: OH* chemiluminescence optics showing the path of light transmission from the flame source to the photocathode of the intensified camera.



2.9: To confirm the isolation of OH* chemiluminescence, total light transmission was calculated for the complete optical arrangement. A comparison with experimentally measured excitation wavelengths of methane combustion from Kojima *et al.* [138] affirms the current bandpass range.



2.10: OH^* chemiluminescence image for ethanol under acoustic forcing. The droplet radius r_s and flame radius r_f are dependent on the angle θ defined in a cylindrical coordinate system with an origin at the center of the droplet. Maximum chemiluminescence intensity occurs near the stagnation point, which is located at an angle α_f from the negative y -axis.



2.11: An ethanol flame in the absence of acoustic forcing is imaged by capturing light emitted from three-dimensional space, which can then be deconvoluted using the Abel transform [140] to create the image above, representing a two-dimensional slice of the axisymmetric flame.

CHAPTER 3

Results - Acoustically Coupled Fuel Droplet Combustion

3.1 Burning Rate Constant

Concerning the burning rate constant K , the primary interests are in the difference in K between unforced and acoustically forced conditions and the effect of various acoustic flow conditions on K . This portion of the study first presents baseline (unforced) burning rate constant measurements and comparisons with established values, then presents measurements for acoustically forced cases.

3.1.1 Baseline Burning Rate Constant

A sample image of chemiluminescence for the unforced burning droplet is shown in Figure 3.1 for each of the four fuels of interest. Gravitational forces give the fuel droplet an oblong shape and produce an elongated flame shape due to natural convection. Although not shown by UV chemiluminescence images, the alcohol and hydrocarbon fuels vary greatly in visible color. The alcohols, due to oxygenated chemical compounds, emit radiative energy mostly in lower wavelengths and appear blue. The hydrocarbons, on the other hand, appear bright yellow due to chemiluminescence in longer wavelengths dominated by electronically excited CH and C₂ radicals.

Baseline burning rate constants for all four fuels used in this study were measured

and compared with other available data, as shown in Table 3.1. Although not quantitatively discussed here, K decreased over long periods of time due to increasing product concentrations surrounding the reaction zone. A reduction in reaction rate can be expected for regions with concentrations saturated by hot products and thus a reduction in oxidizer mass fraction, and this process is especially significant for unforced conditions. For the acoustically excited case, forced convection prevents a large build up of products surrounding the flame and burning rate constants have negligible long term reductions within the time spans used here. To prevent adverse influence by this phenomenon, burning rate constants for unforced conditions were determined using only the first 30 seconds after ignition.

3.1.2 Effect of Acoustics on Burning Rate Constant

Burning droplets were placed at various locations relative to a PN within a standing wave, which allows one to investigate the difference between the forced and unforced K values as well as the changes which occur for different forced conditions. As discussed earlier, applying acoustic perturbations to the field surrounding the droplet will increase the burning rate constant [20–22, 72, 75, 82], but the following results aim to further quantify the increase occurring for various locations relative to the PN as done only by recent studies at UCLA [75, 82].

For acoustic frequencies of 332 Hz, 898 Hz, and 1500 Hz, PNs were located at the center of the waveguide by speakers 180° out-of-phase. All results presented within this chapter were produced from these three frequencies, but nearly two hundred different acoustic flow conditions were tested by positioning the droplet in different locations within these three waveforms (see Figure 2.6a,c,e). Figures 3.2-3.13 present K values measured at these different locations, along with acoustic acceleration values, as discussed below.

The complete set of acoustically excited K measurements show values greater than or equal to baseline measurements. More specifically, positioning a droplet near the PN consistently produces burning rate constants higher than baseline values, while moving towards the PAN ($x \approx \pm\lambda/4$) produces burning rate constants closer to baseline values. These trends are manifested by three different frequencies and four different fuels, with a select few conditions producing burning rate constants as high as 20% greater than the baseline value near the PN. The higher frequency results show K values extending to PANs in both the positive and negative directions, which are precisely the locations where burning droplets consistently behave similar the unforced burning droplet. Much like previous works have shown, there is no appreciable difference in K at these locations [70, 71, 75, 82]. The increase in K towards the PN though, is believed to occur due to decreased flame standoff distance, causing steeper temperature gradients near the droplet surface and thus greater fuel evaporation rates. These topics are discussed in more detail with flame behavior results.

3.2 Flame Behavior

The imaging system provides the ability to measure flame behavior in multiple ways, ranging from deflection of the flame’s plume to chemiluminescence intensity in the reaction zone. Using phase-locked imaging techniques described earlier, acoustic forcing is shown to alter the flame both in a constant manner and a time-dependent manner. In fact, examining flame front location with respect to acoustic phase reveals flame oscillation frequencies equal to the acoustic frequency f_a . These observations and others are illustrated in the following sections, including an interpretation of flame behaviors in terms of the acoustic radiation force.

3.2.1 Flame Deflection and Acoustic Acceleration

The most prevalent flame alteration induced by acoustic forcing is the deflection of the flame to one side. Deflection occurs primarily in the plume of the flame, and examples of this behavior are shown for ethanol in Figure 3.14. The observed deflections are independent of the micro-scale changes in time within each acoustic cycle. Instead, any infrequent changes in flame deflection occur throughout long periods, ~ 1 s. Recent experimental work at UCLA quantifies flame deflection to evaluate an acoustic radiation force theory [20] which has previously been validated qualitatively [21, 75, 82]. Further quantitative comparisons are presented here using the flame deflection measurement techniques of Teshome *et al.* [142].

For a standing wave, the acoustic radiation force equation can be expressed per the analysis of Tanabe *et al.* [20]:

$$F_R = (\rho_p - \rho_o)V[\pm 4\alpha(\frac{I}{z_a})(\frac{2\pi f_a}{c})\sin(\frac{2\pi x}{\lambda})\cos(\frac{2\pi x}{\lambda})] \quad (3.1)$$

Here I represents the acoustic intensity, which depends on the maximum sound pressure level (SPL) inside the waveguide, $z_a = \rho c$ is the acoustic impedance, and c represents the speed of sound. The term in square brackets represents an equivalent acoustic acceleration term, $g_a = \alpha \frac{\partial u^2}{\partial x}$, for a condition where a standing wave is present in the waveguide. The coefficient α defined in eqn. 1.8 is approximated as one in subsequent analyses. Concerning the plus-minus sign in eqn. 3.1, the minus sign corresponds to the case where a PN or VAN was positioned at the center of the waveguide, $x = 0$, whereas the plus sign corresponds to a PAN or VN at that location. Thus, the minus sign is used to calculate theoretical acoustic acceleration $g_{a,th}$ for the waveguide and flow conditions in this study. Inspecting eqn. 3.1, one observes that a burning droplet located to the left ($x < 0$) or right ($x > 0$) of the PN will experience a finite acoustic radiation force F_R due to a nonzero acoustic acceleration g_a . Then, Tanabe *et al.* concludes that the physical consequence of this force on a burning droplet would be flame deflection/deformation in

the opposite direction of F_R , assuming that the hot products with density ρ_p occupy a volume V and are separated from the surrounding gas with density ρ_o .

Noting the analogy between thermal buoyancy and the acoustic radiation force formulated above, Teshome *et al.* [142] utilize well known flame behaviors when buoyant from gravitational acceleration g_o in order to experimentally determine acoustic acceleration g_a . The two accelerations are interpreted as similar in effect, whereas gravitational acceleration is vertically orientated and acoustic acceleration is horizontal (i.e. in the direction of sound propagation). Using the definition of flame deflection angle shown in Figure 2.10, an experimental acoustic acceleration can be calculated as $g_{a,exp} = g_o \tan(\phi_f)$. The flame deflection angle ϕ_f is measured between the vertical axis and the semi-major axis of an ellipse which is fit to the elongated flame shape. In this way, $\phi_f = 45^\circ$ corresponds to an experimental acoustic acceleration equal to gravitational acceleration, while ϕ_f tending towards 90° corresponds to an infinitely large experimental acoustic acceleration.

Figures 3.2-3.13 compare theoretical and experimental g_a values, including the absolute value of each ($|g_{a,exp}|$ and $|g_{a,th}|$) juxtaposed with burning rate constants for illustration. Both experimental and theoretical values exhibit a switch in sign near the PN, where experimental images reveal a distinct switch in deflection from leftward orientation for $x < 0$ and rightward orientation for $x > 0$ as shown in Figure 3.14. In this regard, the acoustic radiation force theory consistently agrees with experiments across a wide range of flow conditions and fuel types. These results confirm that acoustically forced flames will deflect away from the nearest PN, or towards a PAN. But, although theoretical values predict a maximum absolute acceleration at $x = \pm\lambda/8$, centered between a PN and PAN, $|g_{a,exp}|$ values reveal maximums closer to the PN. In fact, maximum flame deflections often occur immediately adjacent to the PN, engendering acoustic acceleration values which exceed 9.8 m/s^2 and are much larger than maxima estimated by

Tanabe’s theory. If acoustic and gravitational acceleration constants are indeed similar mechanisms for deforming a volume of low density products, then $g_a > 9.8 \text{ m/s}^2$ would presumably produce acoustic radiation forces which are greater than buoyancy forces. Tanabe *et al.* [21, 73] cite this relationship when producing droplet flames in a vertically oriented waveguide such that the acoustic radiation force and buoyancy force oppose one another, causing the flame to form a sphere-like shape similar to burning droplets in micro-gravity. This effective “cancellation” of gravity has not been reproduced by other experimentalists though, including several attempts by droplet combustion experiments at UCLA.

There are particular flow conditions though, where the location of flame switch does not coincide with a PN. Specifically for the lowest acoustic frequency, $f_a = 332 \text{ Hz}$, flame switch occurs somewhat far from the PN. For all fuels tested in this study, this lower forcing frequency provides a less distinct flame switch and concurrently, the observed deflections are generally larger when oriented in the negative direction (i.e. leftward). Pressure distributions in Figure 3.2 show a waveform which is slightly asymmetric with a PN favoring the left side of the waveguide, which may contribute to the asymmetries evidenced by burning droplets. The same pressure distribution also shows maximum pressure perturbations which are nearly 10% larger on the waveguide’s positive side. Therefore, acoustic pressure asymmetries combined with a lack of acoustic velocity measurements warrant further investigation to verify the absence of traveling waves, and in addition, determine the true waveform characteristic which causes flame switch. One should also note that all acoustic pressure fluctuations were measured at room temperature without combustion, but the temperature and species distribution alterations caused by a burning droplet may not be negligible.

3.2.2 Standoff Distance

3.2.2.1 Standoff Distance Oscillation

Using the phase-locked imaging techniques discussed in Section 2.3, the flame front position can be investigated as a function of acoustic phase. The resulting behavior is best understood by first viewing Figure 3.15, which shows a pair of flame images acquired at two different points within an acoustic cycle. Acoustic excitation manifests a difference in flame position between such a pair of images, and moreover, the flame position is found to oscillate at a frequency equal to the acoustic frequency f_a . In fact, the entire flame appears to maintain a constant global shape while moving horizontally in a sine-like manner, changing position relative to the droplet. Again, the acoustic waveforms used here are assumed to be one-dimensional, which is supported by a lack of vertical flame movement within microscale changes in time.

The flame standoff distance δ_f , defined in Figure 2.10, is dependent on the coordinate angle θ . As a result of the one-dimensional oscillation of the flame, the maximum standoff distance oscillation amplitude δ'_f occurs near $\theta = 0^\circ$ or $\theta = 180^\circ$. For example, Figure 3.15 shows a case where $\delta'_{f,max} = \delta'_f(\theta = 0^\circ)$. Note that the flame's wake region is not examined when investigating standoff distance. Rather, the hemisphere centered around the flame's stagnation point is of paramount interest because it is believed that maximum temperatures and mass burning rates occur in this hemisphere [61]. Then, focusing on the upstream side of the droplet, Figure 3.16 shows $\delta_f(\theta = 0^\circ)$ versus ϕ_p for each fuel and acoustic frequency at a select few locations within the waveguide. Four acoustic periods worth of phase-locked images show four distinct oscillation cycles for δ_f . The oscillation amplitude δ'_f varies with respect to position within the waveguide though, with effectively zero oscillation for droplets near a PAN (VN). Near a PN (VAN) on the other hand, high amplitudes are observed due to greater velocity perturbations. A greater velocity amplitude u' causes large changes in the total velocity $u = \bar{u} + u'$,

and thus greater changes in mass diffusion rates of air. Physically, these perturbations of oxidizer mass fraction within the reaction zone cause the fuel-air equivalence ratio to change, and the heart of the reaction zone, or flame, must move in order to maintain the prescribed mixture composition for peak reaction rates.

However, the chemical kinetics processes exhibit their own frequency response. Lower acoustic frequencies permit longer periods before flow is reversed at the minimum or maximum of u' , and as a result, these lower frequencies (e.g. Figure 3.16a for $f_a = 332$ Hz) allow for greater values of δ'_f . Meanwhile, higher frequencies (e.g. Figure 3.16c for $f_a = 1500$ Hz) with a similar value of u' will prohibit large values of δ'_f due to shorter diffusion time scales relative to the kinetics time scale. Figure 3.17 demonstrates this relationship in a comprehensive manner in a plot of δ'_f versus waveguide location x . This broader perspective reveals a direct relationship between the acoustic period $T_a (= \frac{1}{f_a})$ and δ'_f for the acoustic intensities and frequencies used here, where a three-fold increase in T_a results in approximately the same relative increase in δ'_f . But, this relationship cannot hold for all frequencies. Also, amplitudes as high as $275 \mu\text{m}$ are observed for $f_a = 332$ Hz at a PN ($x = 0$), while amplitudes are approximately zero for droplets placed at a PAN ($x = \pm\lambda/4$). Thus, trends observed in δ'_f roughly coincide with the trends observed in the burning rate constant K , experimental acoustic acceleration $g_{a,exp}$, and the assumed trend in u' , all of which exhibit maximum values at or near a PN. In contrast, there is not a correlation between flame oscillation amplitude and the theoretical acoustic acceleration $g_{a,th}$ of Tanabe *et al.* [20, 21, 73], which predicts a maximum effect mid-way between a PN and PAN, $x = \pm\lambda/8$.

3.2.2.2 Mean Standoff Distance

Acoustic radiation force theory [78, 79] describes the time-averaged forces caused by acoustic fluctuations. Therefore, a more direct validation of the theory of Tanabe *et al.*

should inspect time-averaged flame behaviors rather than flame alterations occurring throughout microscale changes in time. The mean standoff distance $\overline{\delta_f}$ could offer a better correlation than the analysis above. If indeed the acoustic radiation force should act to displace or deform the droplet's surrounding flame as though it were a sphere of hot products, then the flame front will presumably shift towards the droplet surface on one side of the droplet and away from the droplet on the other side. This concept is partially captured in Section 3.2.1 by using flame deflection angle as a representation of the constant displacement generated by the combined forces of thermal buoyancy and the acoustic radiation force. Instead, a different flame angle can be produced by mean standoff distance measurements which focus on the time-averaged deformations occurring in the stagnation point region of the flame as opposed to the deflection angle of the flame's plume. The aforementioned technique, as well as other comparisons, will be discussed below in an effort to more confidently evaluate the theory of Tanabe *et al.*

First, consider Figure 2.10, where acoustic forcing has altered the location of the flame's stagnation point. The stagnation point is defined here as the location of minimum flame standoff distance and occurs at an angle α_f from the negative y -axis. Thus, $\alpha_f = 0^\circ$ for the unforced flame, which is governed only by natural convection represented by u_b in Figure 2.10. A second velocity component \bar{u} is also shown, representing horizontal steady flow induced by the fluctuating component u' . In this discussion, the horizontal steady component \bar{u} will be interpreted in two ways. First, this bulk flow can represent flow caused by an acoustic radiation force similar to buoyancy. In other words, high flame temperatures cause the surrounding gases to expand due to increasing temperature, then these low density gases are swept into the reaction zone at a velocity \bar{u} by a buoyancy-like acoustic radiation force. The second interpretation considers \bar{u} as an acoustic streaming velocity [80, 143, 144]. Acoustic streaming is not a result of temperature or density differences, but instead occurs throughout the entire waveguide as a result of wave attenuation near boundaries and dissipation in open space. Both interpretations call for

an increase in \bar{u} as acoustic intensity increases, and therefore a decrease in $\bar{\delta}_f$ as more air diffuses into the reaction zone.

If the acoustic radiation force in eqn. (3.1) is indeed valid, then the minimum flame standoff distance $\bar{\delta}_{f,min}$ will occur at $x = \pm\lambda/8$. Whether the flame front is displaced by a shift of the entire sphere of hot gases contained within the flame or by a rise in oxidizer diffusion rates via \bar{u} , $\bar{\delta}_{f,min}$ will coincide with maximum $|g_{a,th}|$ if Tanabe *et al.*'s application of acoustic radiation force theory to flames is valid. The exact quantities one expects are obfuscated by gradual variations in temperature and density, but the qualitative expectations are clear. Figure 3.18 shows the relationship between $\bar{\delta}_f$ and waveguide location x when $\bar{\delta}_f$ is measured at either $\theta = 0^\circ$ or $\theta = 180^\circ$, depending on flame orientation. $\bar{\delta}_{f,min}$ is shown to occur near the PN ($x = 0$), as opposed to the predicted value of $x = \pm\lambda/8$ from eqn. (3.1). As the droplet is positioned closer to the PAN, $\bar{\delta}_{f,min}$ adopts the unforced value shown by dashed lines. This relationship disagrees with that of the prescribed theory, and this point is ameliorated by Figure 3.19. Figure 3.19 confirms a contradicting correlation between flame displacement and theoretical acoustic acceleration, where standoff distance increases with an increase in acoustic acceleration as calculated per the bracketed term in eqn. (3.1). It is thus clear that flame oscillations, which are not represented in the Tanabe theory, may in part be responsible for the discrepancy between theoretical and experimental values of acoustic acceleration.

For future work, a separate technique for comparing the effects of acoustic excitation to those of thermal buoyancy is proposed here. Utilizing the measured angle of minimum standoff distance α_f , a simple nondimensional velocity estimation is proposed

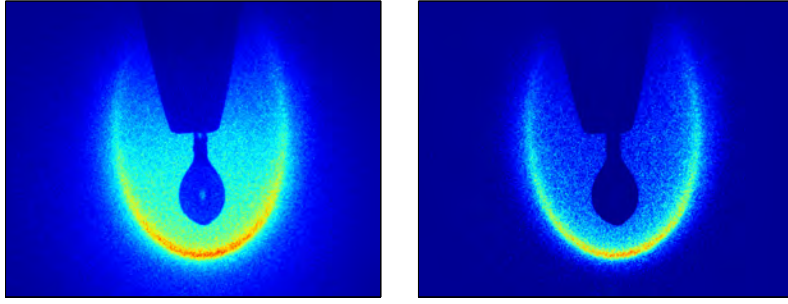
$$\frac{\bar{u}}{u_b} = \tan \alpha_f \quad (3.2)$$

where it is assumed that the steady flow velocity into the flame is equal to the combined magnitude of a vertical vector u_b and a horizontal vector \bar{u} . A preliminary plot of $\bar{\delta}_f$ ver-

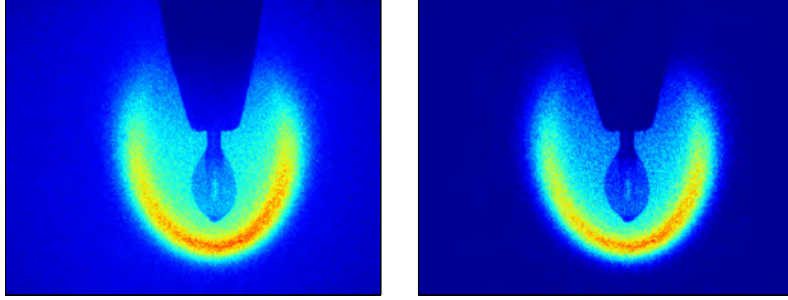
sus the nondimensional velocity $\frac{\bar{u}}{u_b}$ can be found in Figure 3.20. Briefly, this comparison shows a relationship between standoff distance and convective velocity very similar to that predicted by the classical droplet combustion model with forced convection [61, 64]. In light of the shortcomings of the acoustic radiation force theory discussed above, this calculation is suggested for future analysis of this and similar burning droplet data with more focus allocated to predicting steady flow velocities such as \bar{u} , which could better explain the flow fields manipulating flame behavior.

3.1: Comparison of measured values of burning rate constant K for various fuel droplets in the absence of acoustic excitation.

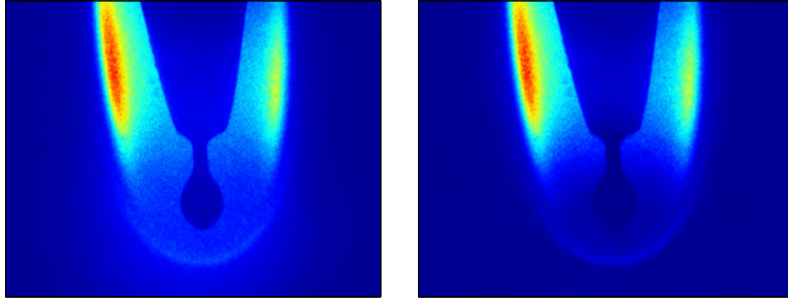
Fuel	K , present (mm^2/s)	K , established (mm^2/s)
Ethanol	0.87-0.96	0.81-0.86 [60]
Methanol	0.94-1.04	0.85-1.2 [145, 146]
Pure FT	0.96-1.05	-
JP-8/FT	0.98-1.05	-



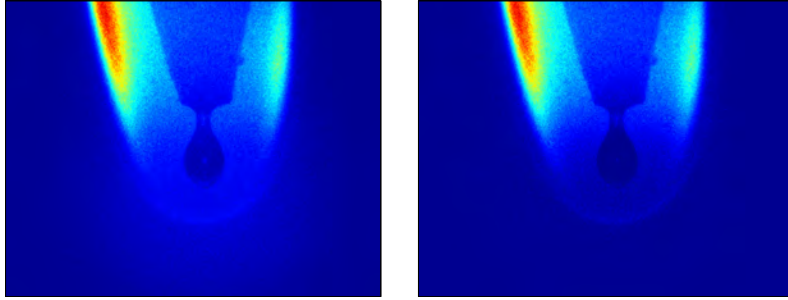
(a) Ethanol



(b) Methanol

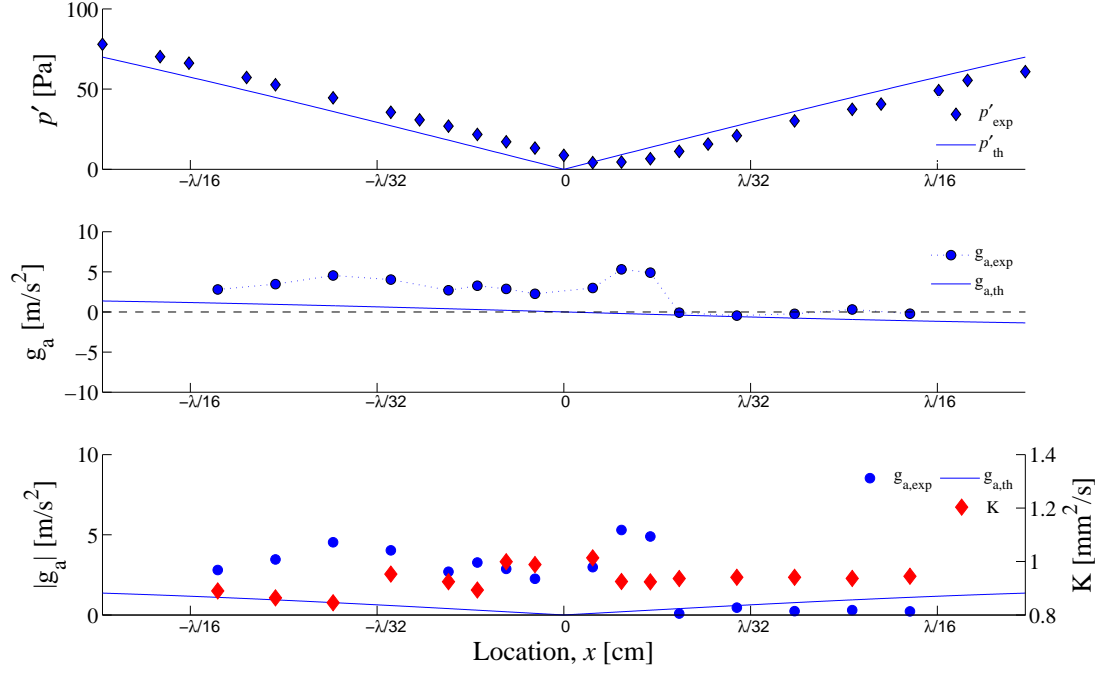


(c) Pure FT

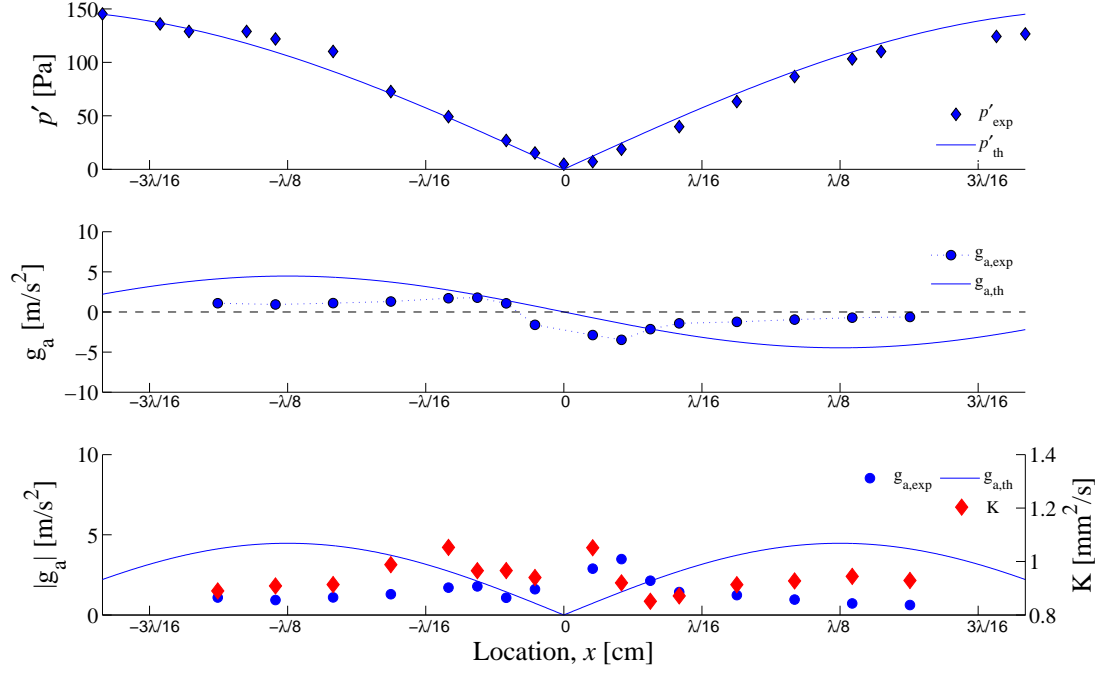


(d) JP-8/FT Blend

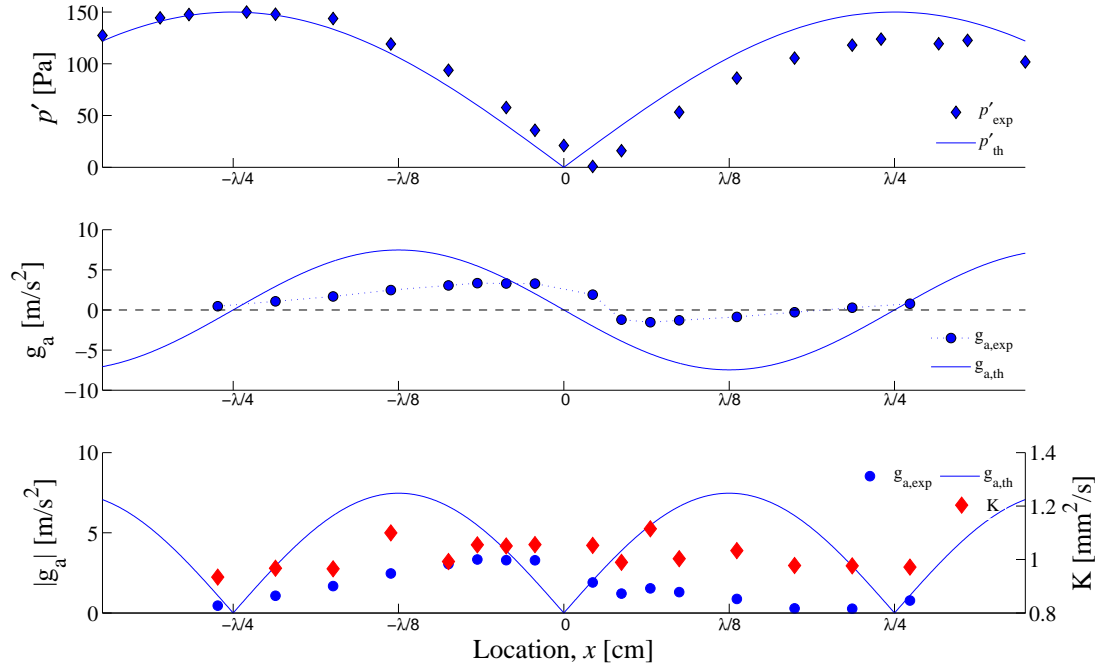
3.1: OH^* chemiluminescence images of burning droplets in the absence of acoustic forcing. The left column shows an image as captured. The right column shows the same image after background light subtraction.



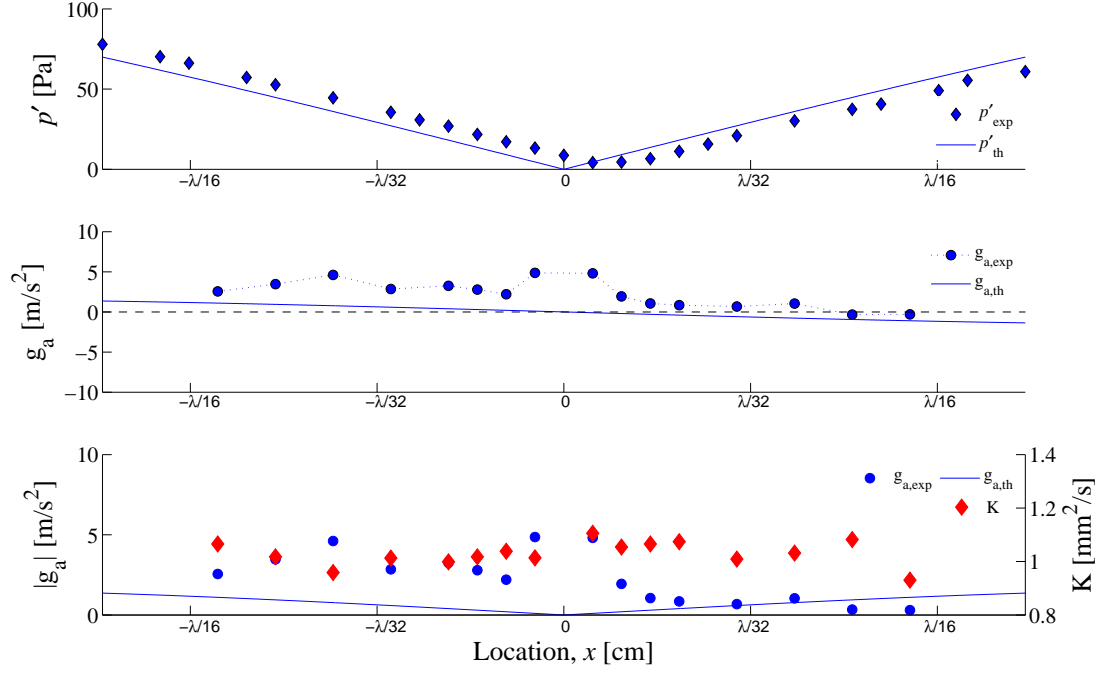
3.2: Pressure perturbations, estimated theoretical and actual acoustic accelerations g_a , and average burning rate constant K as a function of waveguide location for the ethanol droplet burning in the vicinity of a pressure node at a frequency of 332 Hz and $p'_{max} = 150$ Pa.



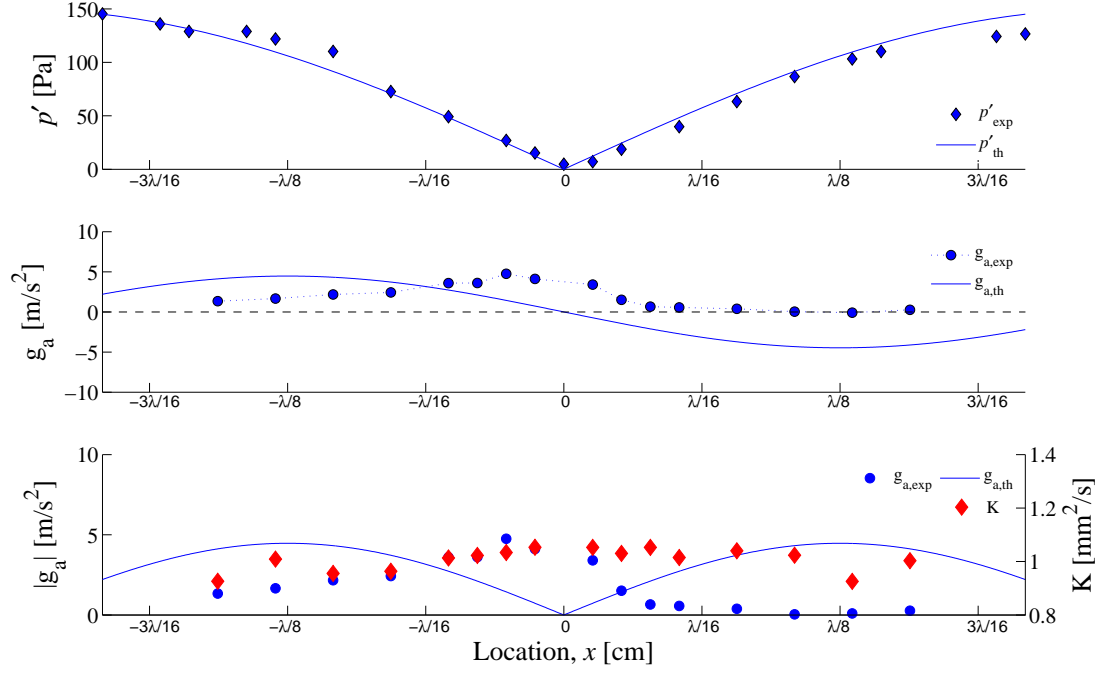
3.3: Pressure perturbations, estimated theoretical and actual acoustic accelerations g_a , and average burning rate constant K as a function of waveguide location for the ethanol droplet burning in the vicinity of a pressure node at a frequency of 898 Hz and $p'_{\text{max}} = 150$ Pa.



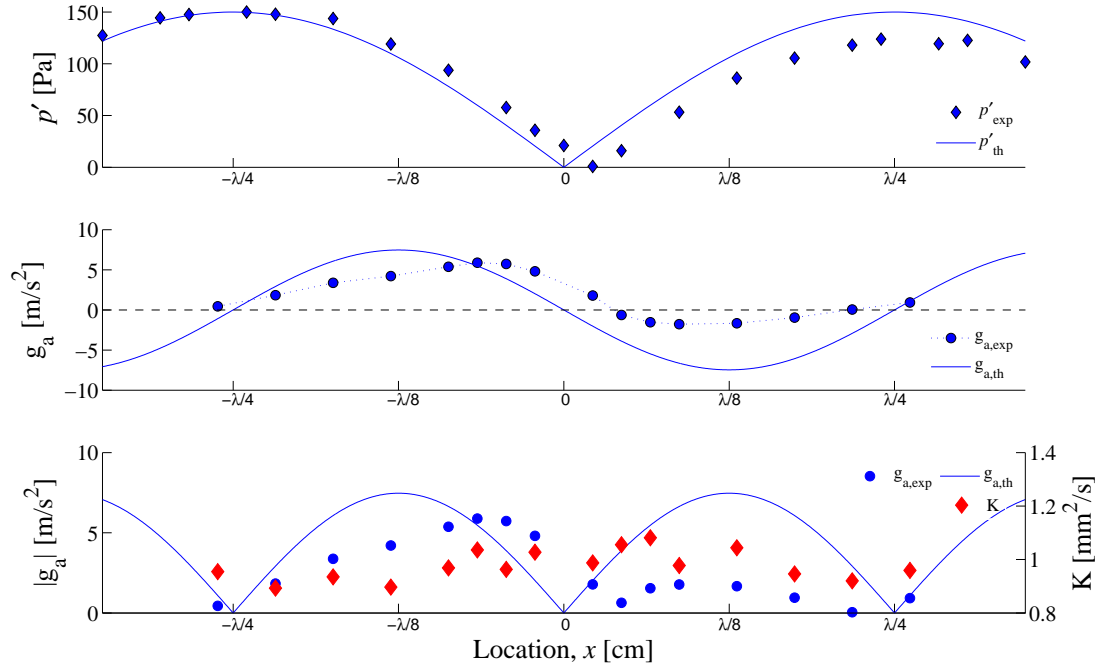
3.4: Pressure perturbations, estimated theoretical and actual acoustic accelerations g_a , and average burning rate constant K as a function of waveguide location for the ethanol droplet burning in the vicinity of a pressure node at a frequency of 1500 Hz and $p'_{\text{max}} = 150$ Pa.



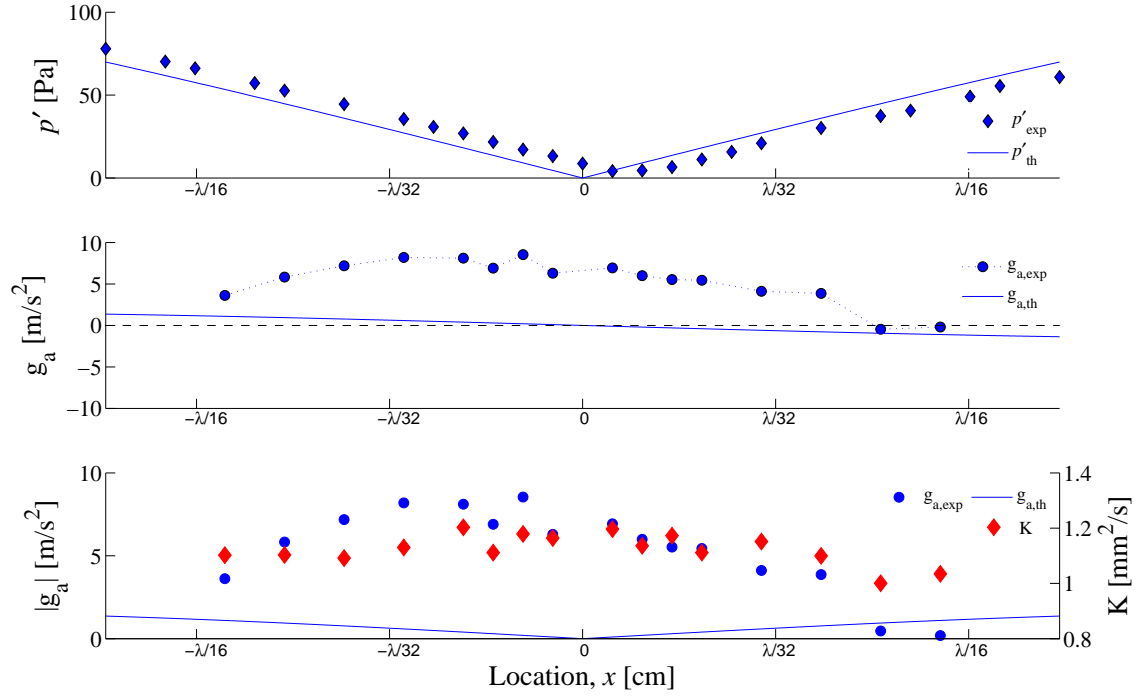
3.5: Pressure perturbations, estimated theoretical and actual acoustic accelerations g_a , and average burning rate constant K as a function of waveguide location for the methanol droplet burning in the vicinity of a pressure node at a frequency of 332 Hz and $p'_{\text{max}} = 150$ Pa.



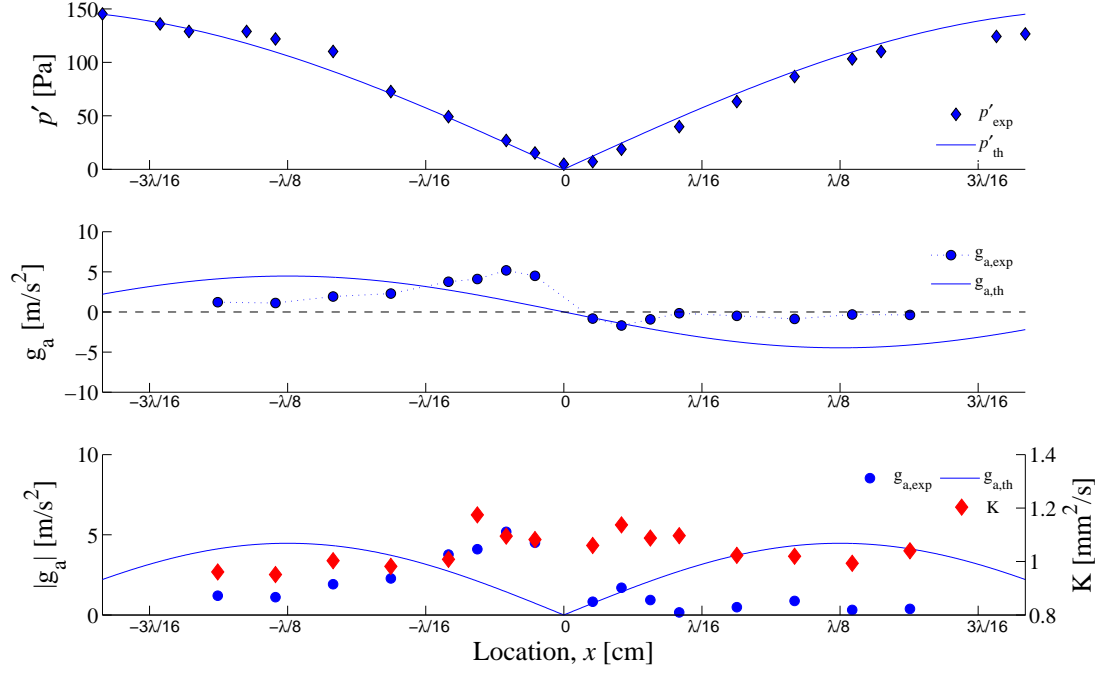
3.6: Pressure perturbations, estimated theoretical and actual acoustic accelerations g_a , and average burning rate constant K as a function of waveguide location for the methanol droplet burning in the vicinity of a pressure node at a frequency of 898 Hz and $p'_{\text{max}} = 150$ Pa.



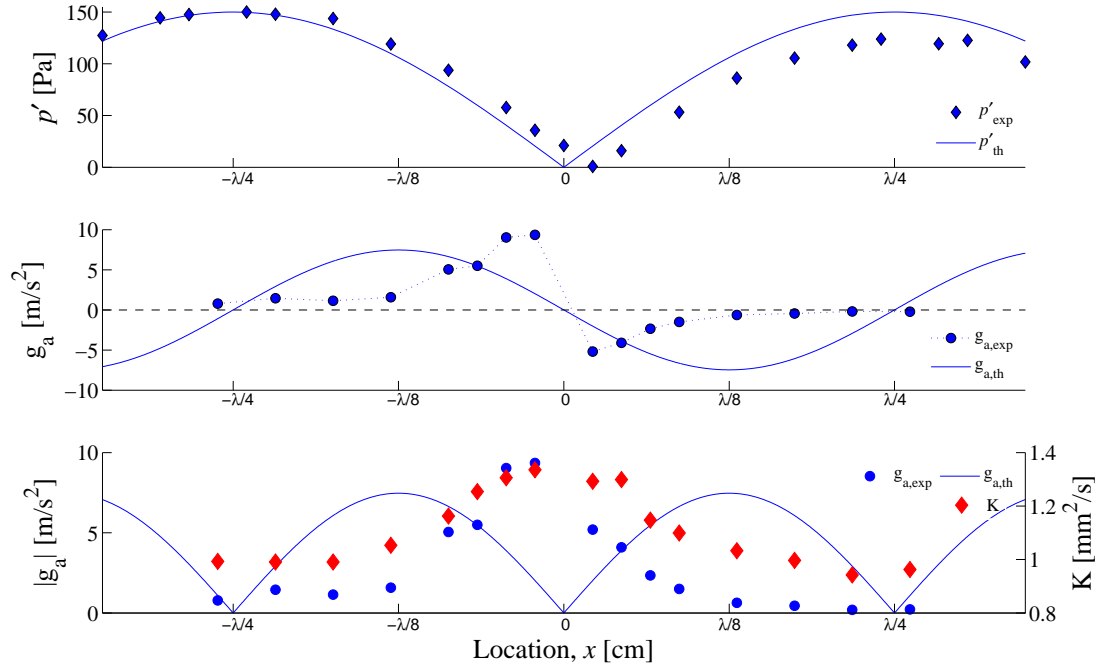
3.7: Pressure perturbations, estimated theoretical and actual acoustic accelerations g_a , and average burning rate constant K as a function of waveguide location for the methanol droplet burning in the vicinity of a pressure node at a frequency of 1500 Hz and $p'_{\text{max}} = 150$ Pa.



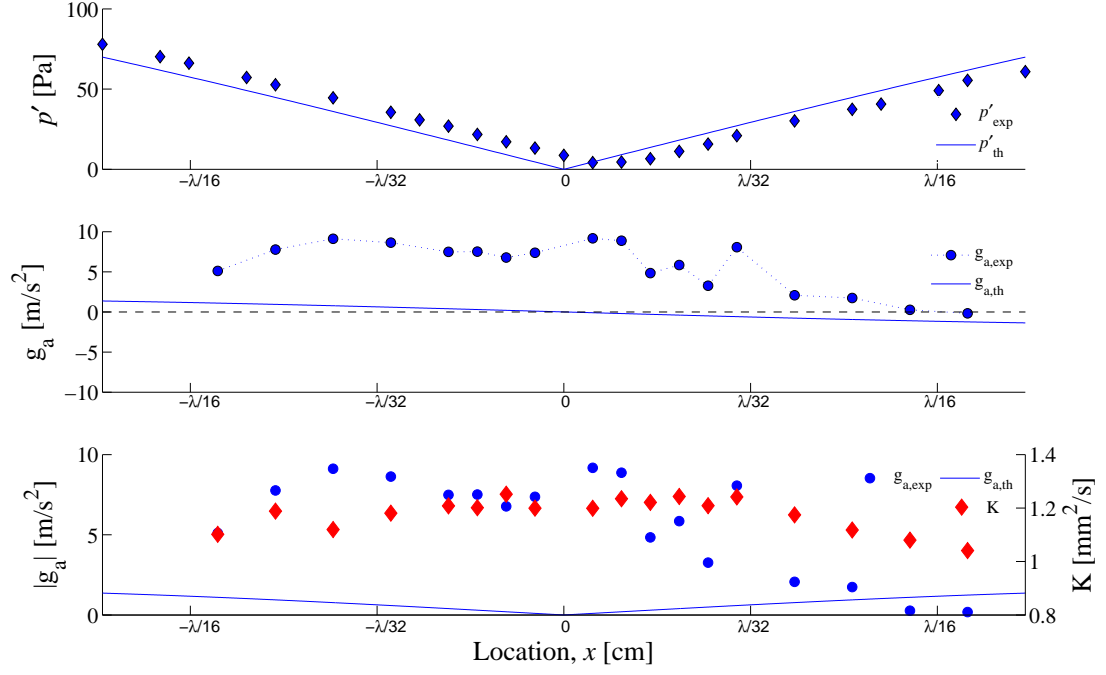
3.8: Pressure perturbations, estimated theoretical and actual acoustic accelerations g_a , and average burning rate constant K as a function of waveguide location for the FT droplet burning in the vicinity of a pressure node at a frequency of 332 Hz and $p'_{\text{max}} = 150$ Pa.



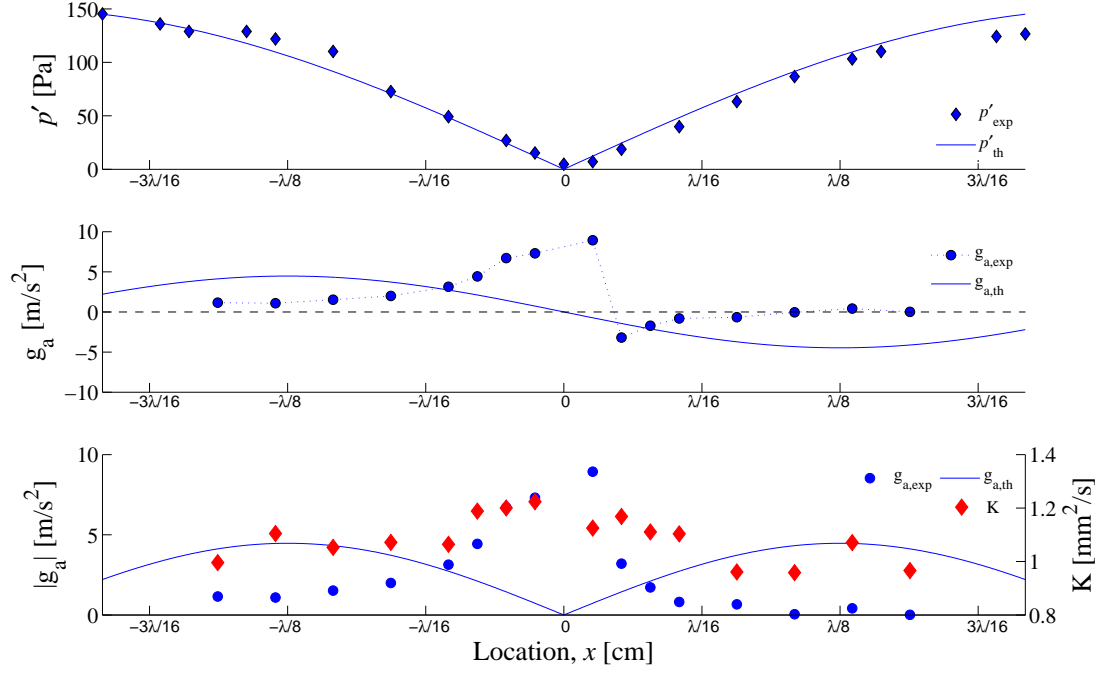
3.9: Pressure perturbations, estimated theoretical and actual acoustic accelerations g_a , and average burning rate constant K as a function of waveguide location for the FT droplet burning in the vicinity of a pressure node at a frequency of 898 Hz and $p'_{\text{max}} = 150$ Pa.



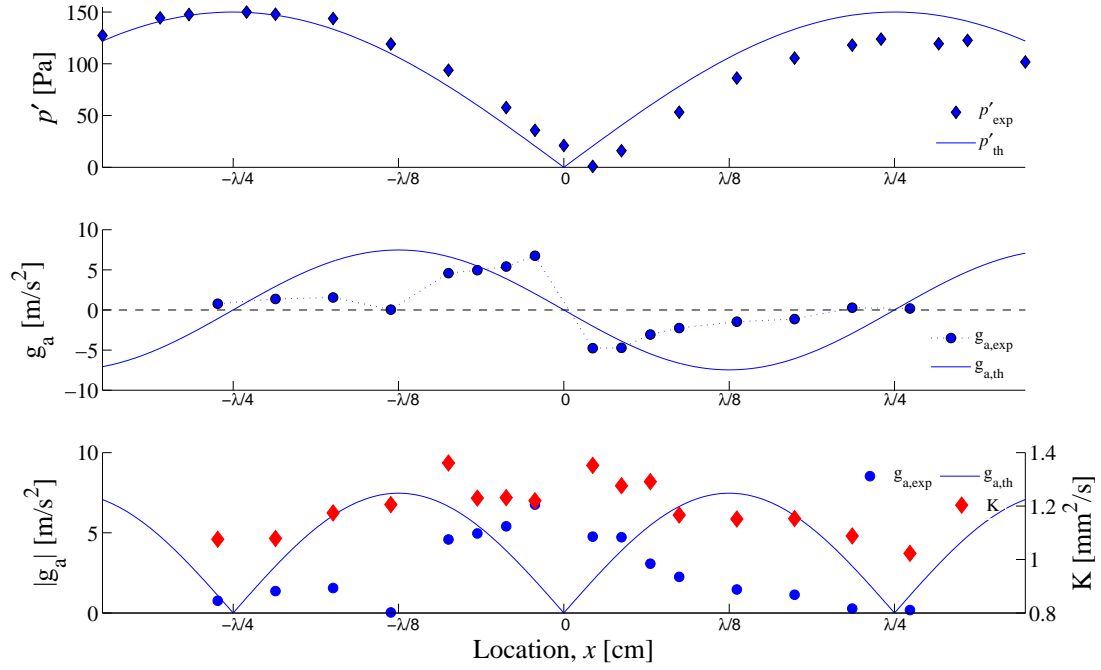
3.10: Pressure perturbations, estimated theoretical and actual acoustic accelerations g_a , and average burning rate constant K as a function of waveguide location for the FT droplet burning in the vicinity of a pressure node at a frequency of 1500 Hz and $p'_{\text{max}} = 150$ Pa.



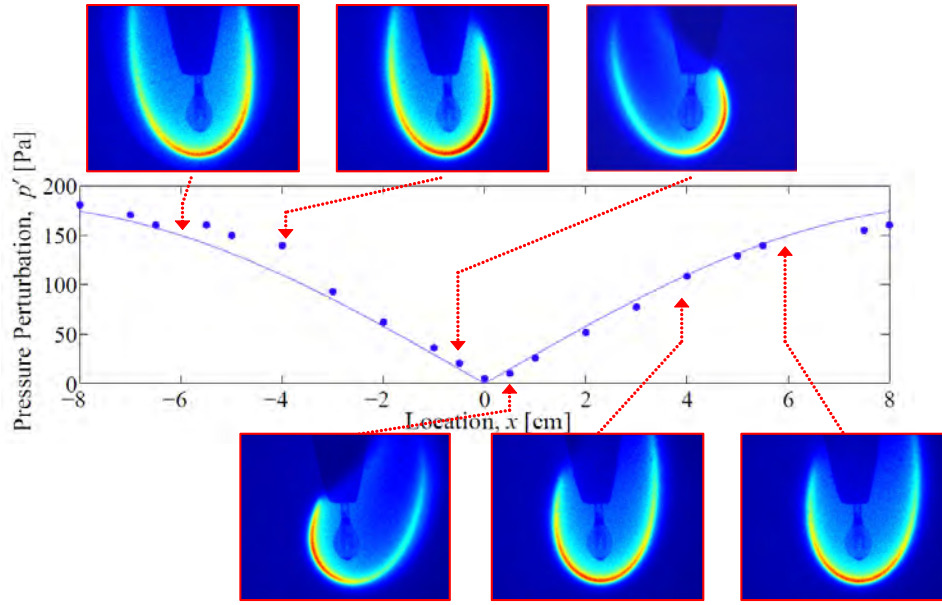
3.11: Pressure perturbations, estimated theoretical and actual acoustic accelerations g_a , and average burning rate constant K as a function of waveguide location for the JP8FT droplet burning in the vicinity of a pressure node at a frequency of 332 Hz and $p'_{\text{max}} = 150$ Pa.



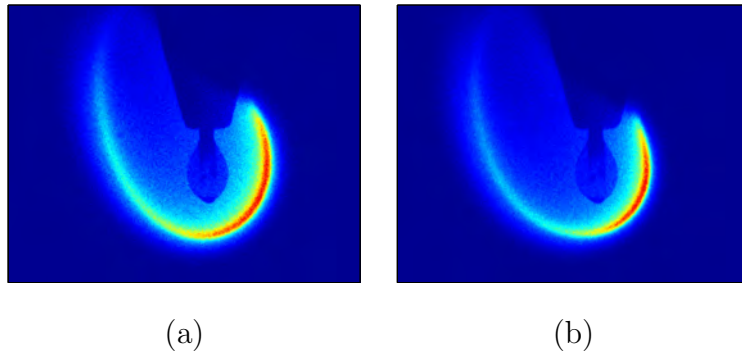
3.12: Pressure perturbations, estimated theoretical and actual acoustic accelerations g_a , and average burning rate constant K as a function of waveguide location for the JP8FT droplet burning in the vicinity of a pressure node at a frequency of 898 Hz and $p'_{\text{max}} = 150$ Pa.



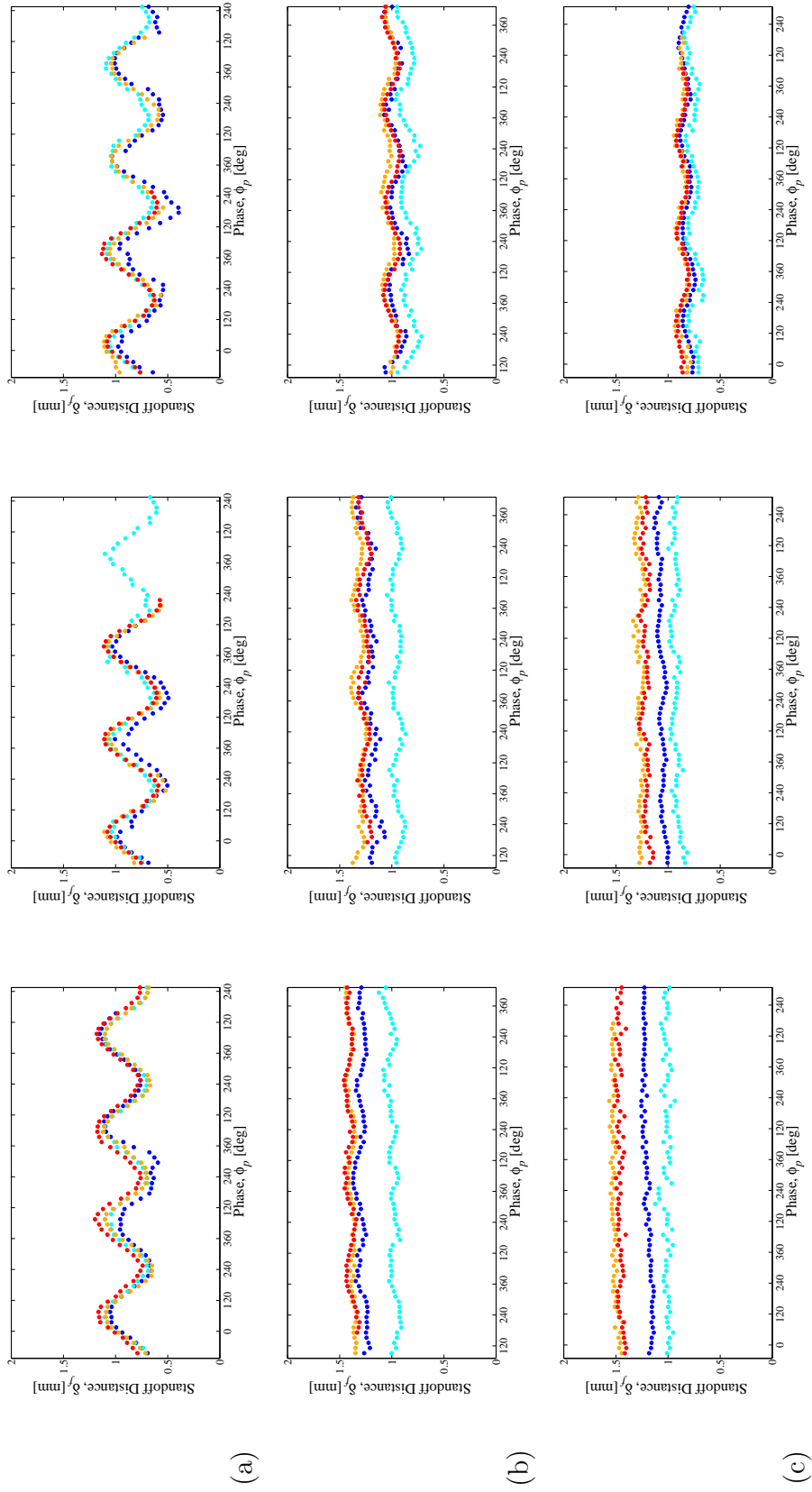
3.13: Pressure perturbations, estimated theoretical and actual acoustic accelerations g_a , and average burning rate constant K as a function of waveguide location for the JP8FT droplet burning in the vicinity of a pressure node at a frequency of 1500 Hz and $p'_{\text{max}} = 150$ Pa.



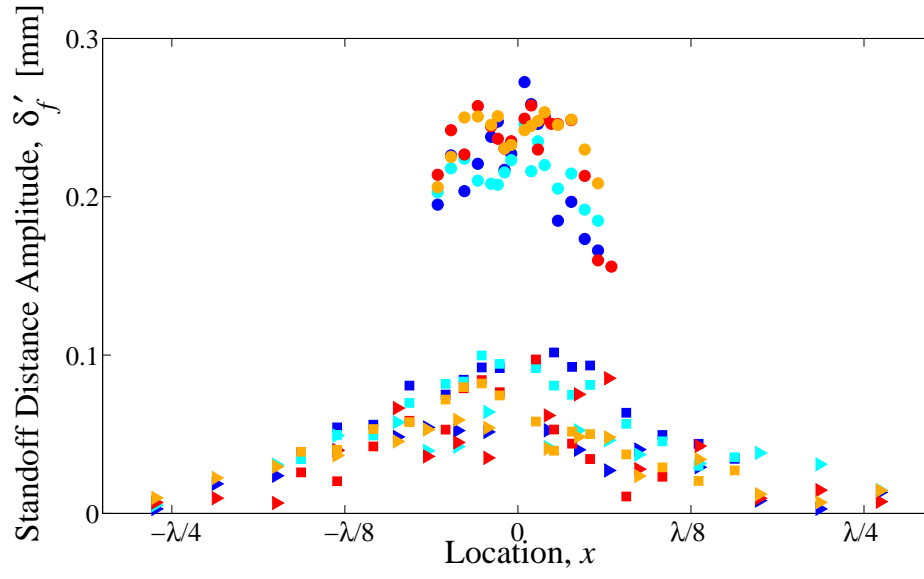
3.14: Ethanol flame images under the influence of acoustics. Flames are consistently deflected away from the pressure node (PN) with a flame “switch” occurring near the PN.



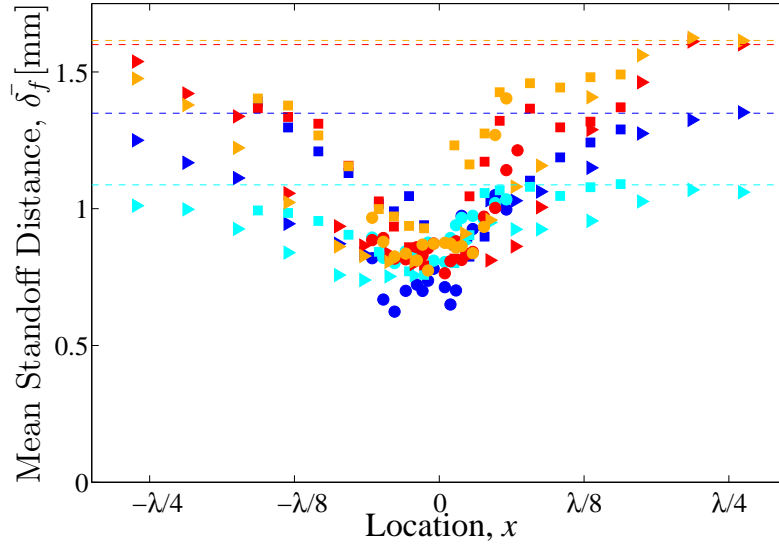
3.15: A pair of ethanol flame images acquired at different points within the acoustic cycle. ((a) $\phi_p = 80^\circ$ (b) $\phi_p = 260^\circ$) Horizontal flame standoff distance δ_f oscillations cause the flame to exhibit a maximum δ_f in (a) and a minimum δ_f in (b) when viewing the right side of the flame.



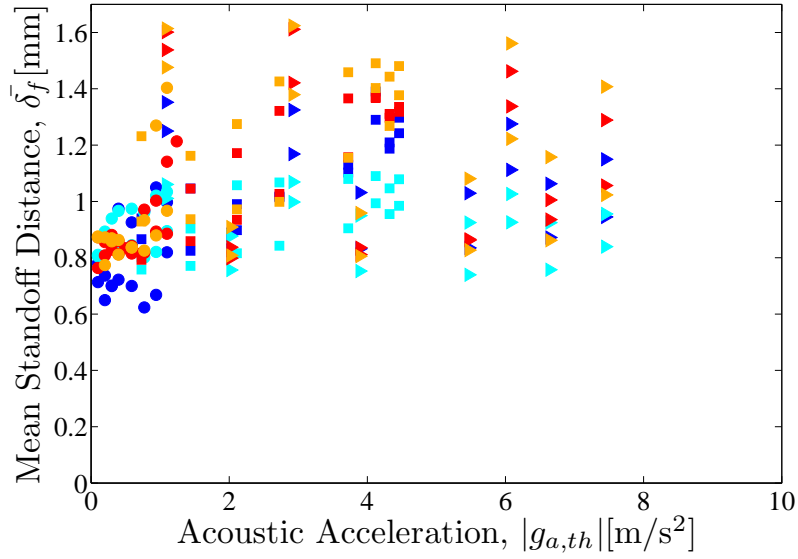
3.16: Horizontal flame standoff distance plotted versus the acoustic pressure phase. All fuels and acoustic frequencies are shown for three select waveguide locations. (rows: (a) $f_a = 332$ Hz (b) $f_a = 898$ Hz (c) $f_a = 1500$ Hz; columns: (left) $x = -6$ cm (middle) $x = -4$ cm (right) $x = -2$ cm; fuels: (●) ethanol (●) methanol (●) FT (●) JP-8/FT blend).



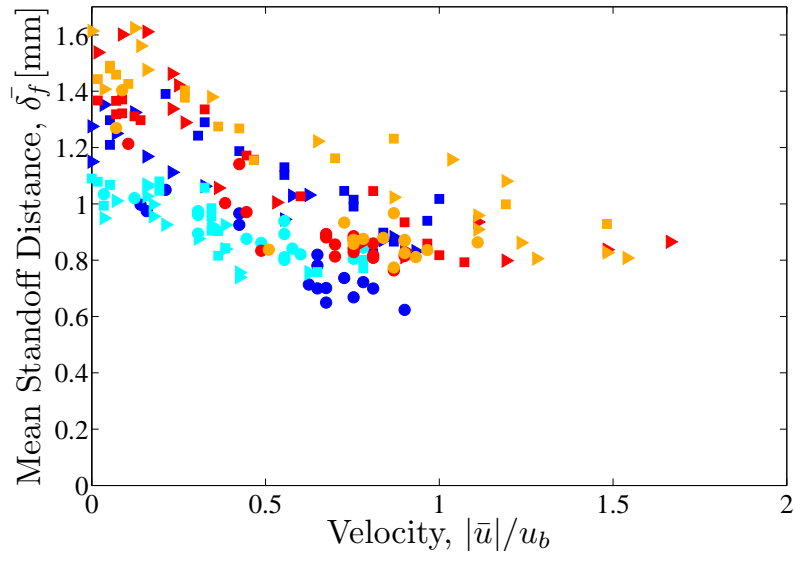
3.17: Standoff distance oscillation amplitude plotted versus waveguide location. (fuels: (●) ethanol (●) methanol (●) FT (●) JP-8/FT blend; frequencies: (●) $f_a = 332$ Hz (■) $f_a = 898$ Hz (►) $f_a = 1500$ Hz).



3.18: Time-averaged standoff distance plotted versus waveguide location. (fuels: (●) ethanol (●) methanol (●) FT (●) JP-8/FT blend; frequencies: (●) $f_a = 332$ Hz (■) $f_a = 898$ Hz (►) $f_a = 1500$ Hz).



3.19: Time-averaged standoff distance plotted versus theoretical acoustic acceleration. (fuels: (●) ethanol (●) methanol (●) FT (●) JP-8/FT blend; frequencies: (●) $f_a = 332$ Hz (■) $f_a = 898$ Hz (►) $f_a = 1500$ Hz).



3.20: Time-averaged standoff distance plotted versus nondimensional horizontal velocity calculated using eqn. (3.2). (fuels: (●) ethanol (●) methanol (●) FT (●) JP-8/FT blend; frequencies: (●) $f_a = 332$ Hz (■) $f_a = 898$ Hz (►) $f_a = 1500$ Hz).

CHAPTER 4

Experimental Facility and Methods - Shear-Coaxial Jets

To best describe the newly-constructed experimental facility used for the study on shear-coaxial jets at high pressures, the nonreactive apparatus used for previous super-critical jet experiments at AFRL must be mentioned. The two chambers lie on opposite sides of a single test cell, and in fact, the reactive chamber adopted many features from the existing nonreactive chamber in order to utilize experience gained from extensive nonreactive testing over many years. These features include the separation of inner and outer chamber volumes, heat exchangers to control propellant temperature, and generating sound using acoustic horns as waveguides. Unlike the nonreactive facility, the reactive facility must address the hazards associated with high pressure combustion of cryogenic oxygen and hydrogen, which requires remote control and sensing of the apparatus. The data acquisition system monitors over 200 sensors and the control system operates over 60 control devices. Thus, the complete system rivals the complexity of a rocket engine test stand, and navigating the intricacies of the entire facility is outside the scope of this chapter. To describe the complete capabilities of the facility though, parametric maps are provided which reach well beyond the experimental conditions explored in chapter 5.

4.1 High Pressure Chamber and Fluid Delivery Systems

4.1.1 Chamber

Similar to the previously existing apparatus used in nonreactive AFRL work [23, 75, 104], the chamber is designed as a chamber within a chamber. The inner chamber creates a near ideal environment for one-dimensional acoustic wave resonance, but is not sealed from the surrounding volume. This surrounding volume is the outer chamber, which has the structural integrity to withstand operating pressures of 1500 psi (10.34 MPa). Thick walls and windows are not necessary for the inner chamber, allowing more freedom when placing instrumentation and integrating new injector designs. A CAD rendering of the chamber assembly is shown in Fig. 4.1.

The outer chamber is fabricated from a forged naval brass alloy and has an octagon shape to offer optical access from multiple views. The current configuration contains six windows in the outer chamber wall, which includes large sapphire windows in the front and rear walls and four smaller quartz windows located at each corner. Large openings in the two remaining chamber side walls (left and right) are used for acoustic excitation sources. The injector assembly and exhaust port are located at the top and bottom of the outer chamber, respectively, creating downward propellant flows which exit the outer chamber through a cylindrical exhaust manifold. The exhaust manifold serves as a dilution and cooling point for the combustion products, and the resulting mixture exits the pressurized volume through a variable diameter exhaust orifice which is set to 4.8 mm, and is the chamber's only exhaust path.

4.1.2 Propellant Systems

To properly compose propellant density and velocity ratios, the oxygen and hydrogen feed systems must control the pressure, temperature, and flow rate of each. In this con-

text, the differential pressure between the injector exit and the chamber is assumed to be small, and the propellant pressure is simply taken as the chamber pressure. Temperature and flow rate though, are actively controlled upstream of the injector.

4.1.2.1 Propellant Flow Rate

Propellants are pressure fed by high pressure tanks located outside of the experimental cell, and flow rate is controlled by a remote needle valve for each propellant at ambient temperature. The needle valve often acts as a sonic nozzle, whereby flow rate remains constant although small changes in the downstream pressure occur, e.g. a rise in chamber pressure following ignition. To gather reliable propellant flow rates a Porter 123 series thermal mass flow meter is used in both the inner and outer jet systems, allowing maximum flow rates of 0.71 g/s, 2.02 g/s, 9.90 g/s, and 10.79 g/s for hydrogen, helium, nitrogen, and oxygen, respectively. Unique calibration data for each gas species is used when converting voltage output to mass flow rate for hydrogen, nitrogen, and oxygen, while helium mass flow rates are calculated using conversion factors published by Porter. These propellant flow rates, albeit low, create a flame similar to that of an $\text{O}_2\text{-H}_2$ LRE environment when used in conjunction with a sub-scale injector (see section 4.1.2.3) and considerable gaseous nitrogen flow to produce high chamber pressures (see section 4.1.2.4).

4.1.2.2 Heat Exchangers

Concerning temperature, LRE propellant tanks often hold fuel and oxidizer as a liquid, storing large masses of propellants within small cryogenic tanks. This is the case for many sub-scale test facilities as well [8, 24], and appropriate plumbing insulation allows propellants to be injected at temperatures only slightly above storage temperatures. For example, the BKH combustor maintains low hydrogen temperatures by submerging the

hydrogen supply lines in a liquid nitrogen bath between the liquid hydrogen tank and the test article [24]. Instead, this facility relies on ambient temperature propellant tanks storing gaseous oxygen and hydrogen at pressures exceeding 2000 psi (13.8 MPa). Thus, downstream of the flow meters, hydrogen and oxygen pass through separate cryogenic heat exchangers which cool propellants to the desired temperature.

Both heat exchangers operate under similar principles where propellant passes through a coiled tube which is cooled by liquid nitrogen. Liquid nitrogen is supplied from a 1500 gallon (5680 L) vacuum jacketed vessel pressurized to 90 psig (0.6 MPa). Approximately 9 m of vacuum jacketed tubing transfers liquid nitrogen from the vessel to the experimental cell, where the supply is split to deliver coolant to each individual heat exchanger. With this arrangement, the temperature of the process fluid is controlled by individually regulating liquid nitrogen flow rates through each system with separate control valves. A detailed drawing of the components and instrumentation of the heat exchangers can be found in the complete piping and instrumentation diagram in appendix A.

For the oxygen heat exchanger, which was designed and constructed by Sierra Lobo Inc., 2.82 m of inconel tubing is coiled on a vertical axis near the perimeter of an aluminum casting to carry process fluid. The casting also contains approximately 2 m of coiled tubing in the center of the casting for liquid nitrogen flow. In this way, heat energy from room temperature process gas enters the outer perimeter of the casting and transmits heat inward via conduction, where liquid nitrogen flow continually removes energy via convection. A vacuum jacket surrounds the assembly and is maintained at 10-100 mTorr. In its simplest form, this design can result in inaccurate control of fluid temperature, because liquid nitrogen flow rate control may be too coarse to obtain the desired process fluid temperature. For a test matrix in which propellant density ratio control is imperative, oxygen temperatures near the saturation point require accurate control to avoid large changes in density, caused by a large $\frac{\partial \rho}{\partial T}$. Inaccurate oxygen

temperatures also influence heat transfer phenomena in the flame region where propellant temperatures, as well as other thermodynamic variables such as chamber pressure, will engender a specific flame location and temperature.

As a direct result of these factors, the oxygen heat exchanger contains additional features to improve temperature control. First, a second coolant control valve is installed in parallel with the larger main control valve such that initial liquid nitrogen flow rates are set using the main control valve. Then, fine adjustments in liquid nitrogen flow rate are made with the small control valve as the process fluid outlet temperature approaches the target temperature. The flow capacity rating C_v is 2.0 for the main control valve and 0.075 for the small control valve. Second, electric heaters are mounted to the aluminum casting to offer additional energy in the event that the casting is chilled below the target temperature. The heating system consists of six heater elements individually controlled by a closed-loop control system written in LabVIEW. In this way, coolant control valves are set to slightly sub-cool the casting, reducing the process gas to a temperature 2 to 5 K below the target temperature. The heater power is then manually applied and automatically adjusted to hold the process fluid outlet temperature equal to the target temperature with an accuracy of ± 1 K. To achieve optimal accuracy, the heaters are used unless the target temperature is equal to the system's minimum possible temperature. Only four of the six heaters were used for the results shown in this study. A three-dimensional rendering of the oxygen heat exchanger is shown in Fig. 4.2.

The hydrogen heat exchanger, on the other hand, lacks many of these additional features. As shown in Fig. 4.3, the hydrogen heat exchanger consists of 2.5 m of process fluid tubing directly submerged in a liquid nitrogen bath. In this configuration, the flow direction of coolant is opposite that of the process fluid. This arrangement ensures a minimum process fluid temperature at the outlet region by encompassing said region with unheated coolant. Liquid nitrogen flow is regulated using a single control valve

downstream of the heat exchanger, and the position of this valve is the only variable directly controlled by the user for achieving the desired process fluid temperature. Process fluid outlet temperature then, is actively controlled by the user rather than employing an automatic control loop. Similar to the oxygen heat exchanger, the nitrogen bath is insulated by a vacuum jacket.

Although the propellant heat exchangers offer variable control of temperature, a cooling process is required to condition plumbing hardware prior to achieving a desired, stable temperature. The temperature conditioning process requires approximately 30 minutes and is performed using nitrogen not only as the coolant, but also as the process fluid in order to preserve propellant. When a stable temperature and flow rate are reached, remote valves are used to switch from the nitrogen simulant supply to the propellant supply. Due to differences in viscosity, density, and heat conduction constants, alternating between nitrogen simulant flow and propellant flow causes significant changes in mass flow rate and temperature. A time series plot of the transition from nitrogen simulant to propellant is shown for oxygen and hydrogen in Fig. 4.4. The difference between the process fluid temperature at the injector before and after the species transition was found to be highly dependent on both chamber pressure and mass flow rate.

To characterize the capability of each heat exchanger, the minimum achievable temperature was measured for a range of chamber pressures. This was done by utilizing high liquid nitrogen flow rates over a long period of time to cool the hardware of each system. Thus, the injector flow temperature for each process fluid was minimized, representing a limiting temperature condition for the facility. The results from this effort are shown in Fig. 4.5 for oxygen, where minimum temperature is shown to have a small dependence on chamber pressure. An oxygen density contour is the background of Fig. 4.5, showing that a liquid phase is achievable for $T_{ij} < T_{sat,ox}$ and $p_c < p_{crit,ox}$ and supercritical fluid

for $p_c > p_{crit,Ox}$. Temperature is shown to have a negative correlation with mass flow rate. Similar measurements were made with the hydrogen propellant system, but to perform these tests safely, helium was used as a surrogate. Minimum helium temperatures are shown in Fig. 4.6, superimposed on a hydrogen density contour map.

To quantify the heat exchangers capability for nonreactive experiments, minimum temperatures for nitrogen are plotted for both the inner and outer jets in Fig. 4.7. A nitrogen density contour is also shown. Reviewing temperature limitations for the outer and inner jets, one observes that two-phase flows can be realized for both reactive (LO_x - GH_2) and nonreactive (LN_2 - GN_2) tests. Single-phase conditions can also be achieved with subcritical gas-gas jets where $T_{ij} > T_{sat,ox}$ for reactive tests and $T_{ij} > T_{sat,N_2}$ for nonreactive tests. If desired, liquid-liquid conditions can also be achieved for nonreactive tests where $T_{ij} < T_{sat,N_2}$ and $T_{oj} < T_{sat,N_2}$. Although heat exchanger performance is also dependent on process fluid mass flow rate, which is not characterized in Figs. 4.7, these results are a valuable tool for the design of experiments with known facility limitations.

The significance of propellant temperature limits is best understood by mapping the possible values for density ratio S . For oxygen-hydrogen flows, Fig. 4.8 shows the range of achievable values for S as a function of chamber pressure. For $p_c < p_{crit,ox}$, single-phase flows allow for density ratios as high as 0.1. Two-phase LO_x - GH_2 flows though, restrict density ratios to a small range of values less than 0.01, which is comparable to a oxygen-hydrogen engine with regenerative nozzle cooling. Supercritical oxygen flows are characterized by a region with pressures greater than 5.04 MPa (731 psia), where oxygen is a supercritical fluid and a distinct phase change does not exist for oxygen.

4.1.2.3 Injector

The injector consists of a single shear-coaxial element designed for hydrogen flow in the annulus and oxygen flow in the center. In terms of total cross-sectional area, the injector

is $1/10^{th}$ scale of the J-2 engine, for example. An injector of this size is challenging to manufacture, but is used here to maintain jet velocities and Reynolds numbers with orders of magnitude similar to an actual LRE while maintaining much smaller propellant mass flow rates. This technique was also employed in the design of shear-coaxial injectors for the Common Research Combustor of CNRS and DLR. The cross-sectional dimensions of the injector are shown in Fig. 4.9, and dimensions for all recent AFRL injectors are shown in Table 4.1 for comparison. In comparison with previous AFRL shear-coaxial injectors, the current injector has a small area ratio, $\frac{A_{oj}}{A_{ij}} = 1.68$. The inner post thickness to inner diameter ratio $\frac{t}{D_1}$ has a value of 0.27, which prevents the inner shear layer from behaving purely as that of co-flowing fluids. Instead, a recirculation zone is expected to form at the exit of the injector between the outer and inner jets. A CAD image of the injector and top flange assembly is shown in Fig. 4.10.

A comparison of Re_{ij} and Re_{oj} for similar research combustors is shown in Fig. 4.11, with operating points of actual oxygen-hydrogen LREs. Operating spaces of four other combustion instability research facilities are shown, including the BKH combustor of DLR, Germany, the Common Research Combustor (CRC) of CNRS, France and DLR, Germany, the Multi-Injector Combustor (MIC) of ONERA and CNRS, France, and the Cryogenic Combustion Laboratory (CCL) of Pennsylvania State University, USA. These facilities were specifically chosen for comparison because detailed flow conditions for oxygen-hydrogen stability experiments for shear-coaxial jets are available, but one must be cognizant that apparatuses such as these often see multiple modifications in only a few years time. As a result, Fig. 4.11 should be considered only a general guide for comparison, because Re values for the facility concerned here, as well as the others in Fig. 4.11, can be revised with simple hardware modifications.

For all conditions shown in Fig. 4.11, two-phase flows lie in the membrane type breakup regime or the fibre-type breakup regime, characteristic of high Re and high

We flows as discussed in section 1.3.1.2. Reynolds numbers of this magnitude are often considered to create fully-developed turbulent conditions at the injector exit. Fully-developed flow at the injector exit is particularly advantageous for establishing a known and canonical velocity profile, imparting momentum boundary conditions for shear layer studies and providing a boundary layer thickness approximately equal to half of the diameter for a range of mean velocities. Rather than matching the design of a particular LRE injector where the fully-developed turbulence assumption may or may not be valid, the current injector design places priority on ensuring fully-developed turbulent flow for the entire effective range of Re values to provide confidence in experimental boundary conditions. A minimum injector length is required to make this assumption valid. According to the development length criterion of Munson *et al.* [147] the minimum nondimensional development length required for fully-developed turbulent flow is

$$\frac{L}{D} \geq 4.4 Re^{\frac{1}{6}} \quad (4.1)$$

where D is taken as D_1 for the inner jet and $D_3 - D_2$ for the outer jet. Using the complete range of values for Re_{ij} and Re_{oj} from Fig. 4.11, $\frac{L}{D} > 4.4 Re^{\frac{1}{6}}$ for all conditions and the fully-developed turbulence assumption is valid. One particular flow condition is represented by the diagram in Fig. 4.12, where the $1/7^{th}$ power law [148] is used to plot fully-developed velocity profiles for the inner and outer jets.

The injector design chosen here also deviates from popular LRE injector designs, because the inner jet lacks a recessed exit plane. A recessed inner post, as shown in Fig. 1.6b and 1.6c, is commonly used in LREs in order to enhance mixing in the initial merging zone via an increased transverse velocity of either the inner jet, outer jet, or both. The J-2 and SSME engines both used recessed inner posts for LO_x - GH_2 combustion, for example [45]. Thus, both the injector length and the exit geometry deviate from practical designs in order to create more well-known boundary conditions at the injector exit. This design also serves as a baseline geometry that could be used

for comparison with recessed injectors in the future.

A parametric map of the facility can be obtained by combining the density ranges discussed above with injector dimensions and propellant mass flow rates, but first a range of propellant mixture ratios must be defined to constrain the operating space. For oxygen-hydrogen mixtures, the stoichiometric mixture ratio is 8 and actual LREs operate fuel-rich in the range $4.5 < MR < 7.2$. In terms of the fuel-oxidizer equivalence ratio $\phi_{f/o} = \frac{\dot{m}_f/\dot{m}_o}{(\dot{m}_f/\dot{m}_o)_{st}}$, this range corresponds to $1.11 < \phi_{f/o} < 1.78$. A minimum MR of 2 is used here to capture the lower limit of mixture ratios for a practical specific impulse [149]. A maximum of 8 is taken to include stoichiometric conditions. Using a wide range of mixture ratios offers an expanded range of momentum flux ratios without changing the injector element, as shown in a parametric map of J versus MR in Fig. 4.13.

4.1.2.4 Exhaust

Rather than passing through a single exhaust nozzle, the chambers' exhaust path is staged. Upon exiting the inner chamber through a rectangular hole, the combustion products, which are mixed with nitrogen from the inner chamber, will enter a small manifold. This exhaust manifold serves as a dilution and cooling volume. The exhaust manifold is separated from the outer chamber by a cylindrical wall. Throughout the wall, 3.18 mm diameter holes allow gaseous nitrogen from the outer chamber to flow into the exhaust manifold. Thus, the combustion products are initially cooled and diluted by nitrogen present in the inner chamber and then experience further cooling and dilution due to additional nitrogen in the exhaust manifold.

Consequently, a supplementary flow system introduces gaseous nitrogen into the outer chamber to provide a positive pressure differential between the outer chamber and the exhaust manifold. In turn, this produces a continuous flow of exhaust dilutant into the product mixture. The ensuing nitrogen-rich mixture then exits the exhaust manifold

through a tube with a 22.1 mm inner diameter prior to being choked through a 4.8 mm diameter restricting orifice. Without altering the orifice size, the chamber pressure can be controlled independent of propellant flow rate by adjusting one of several nitrogen flow rates, and the orifice size was chosen to create the desired p_c for a given nitrogen mass flow rate. Assuming that inner chamber nitrogen flows, to be described below, are set according to the experimental needs of the scientifically sensitive region near the flame, the supplementary outer chamber nitrogen flow rate is appropriately used for adjusting the mean chamber pressure. Therefore, this supplementary nitrogen system is termed the chamber pressurization flow system although it also serves as an exhaust dilutant and coolant.

4.2 Inner Chamber

4.2.1 Inner Chamber Dimensions and Instrumentation

The inner chamber is a rectangular volume open to transverse acoustic excitation from circular acoustic drivers on the left and right. The inner chamber depth is 20.32 mm and the height is 36.07 mm, making room for sub-scale injectors only. The width is much larger, reaching 0.82 m from the left acoustic source to the right acoustic source, making the inner chamber volume large in comparison to the injector. One should also note that although the inner chamber cross-sectional area is 20.32 mm \times 36.07 mm near the injector, the far left and far right areas of the inner chamber expand to a large circular area in order to house each acoustic driver. The waveguide design which is used to smoothly transition from a rectangular shape to a circular shape will be described in section 4.3.2. Two quartz inner chamber windows separate the inner chamber from the outer chamber, and because these windows need not withstand a large pressure differential, nine small holes are located throughout the rear inner window at an axial distance

of $12D_1$ from the injector exit, but at various spanwise locations. Three of these nine holes are occupied by dynamic pressure transducers; one of which is spanwise centered in the rear window ($p_{dyn,2}$), while two others are located 25.4 mm to the left and right of the center pressure transducer ($p_{dyn,1}$ and $p_{dyn,3}$). Thermocouples are located 6.35 mm to the left and right of each pressure transducer, totaling six thermocouples measuring temperature at the inside surface of the rear window. Hence, these instruments diagnose the region near the flame at $x = 12D_1$, and one final thermocouple is suspended in the center of the inner chamber exit to measure the flame temperature at $x = 30D_1$. By placing a thermocouple at $x = 30D_1$, the temperature near the end of the flame is measured without disturbing the region captured by high-speed imaging.

4.2.2 Inner Chamber Nitrogen Flows

At the top of the inner chamber, a nitrogen plenum provides two flows parallel to propellant flows. First, window cooling flows enter the inner chamber through slotted holes located immediately inside the top edge of the inner windows. Second, a propellant co-flow system provides gaseous nitrogen to the region surrounding the flame by entering the chamber through dozens of 0.48 mm diameter holes in a circular pattern around the coaxial injector. This co-flow system decreases coaxial jet recirculation in the inner chamber, and will be referred to as the flow straightener flow. The nitrogen used for both the window cooling and flow straightener systems is supplied at ambient temperature.

4.3 Waveguide Design and Characterization

The acoustic system design meets several key requirements. Most importantly, acoustic fluctuations in the transverse direction are maximized and fluctuations in the longitudinal and depth-wise directions are minimized to create approximately one-dimensional

waves. Second, it is possible to create acoustic pressure amplitudes with the same order of magnitude as an actual LRE combustion instability while still maintaining the ability to control and sustain low amplitudes, e.g. $p' < 0.01p_c$. Last, the acoustic system allows for reliable establishment of standing waveforms with pressure nodes or velocity nodes located at the coaxial jet.

4.3.1 Acoustic Drivers

Similar to both the droplet combustion apparatus and the aforementioned nonreactive facility at AFRL, twin acoustic drivers are used in concordance with the general principles of a Kundt's tube. However, in the case of the system described here and the nonreactive facility at AFRL, drivers with a total area more than twice that of the inner chamber's cross sectional area are used. This feature establishes pressure amplitudes much higher than a traditional Kundt's tube when the waveguide shape is designed as a sound amplifying horn, which will be described in the following section. High acoustic pressure amplitudes are also enabled by using circular piezoelectric sirens as acoustic sources. The sirens are made entirely of aluminum, and the construction of which is described further in appendix A.1. The sirens enable much higher amplitudes than classical loudspeakers, but piezoelectric sirens have one drawback to mention here.

As a result of their geometric form, the piezoelectric sirens exhibit a few resonant frequencies. Within the narrow bands located at each resonant frequency, high oscillation amplitudes occur in the siren's cone, and high-amplitude coherent sound is produced. Operating the sirens outside of these narrow bands of efficiency results in much lower amplitudes.

To quantify this limitation, sound pressure measurements were made with the sirens mounted outside of the chamber. In this manner, chamber resonance is avoided by allowing waves to propagate into an open room. Each siren was mounted firmly using

the same technique which is used when mounting the siren inside the chamber, and a dynamic pressure transducer (Kulite model XCE-093-50D) was placed 5 cm from the siren's diaphragm. A frequency sweep over a duration of 15 s was used to ramp the oscillation frequency of the siren from 100 Hz to 6000 Hz while acquiring data at a rate of 80 kHz. Results are shown in Fig. 4.14, revealing three frequency bands of peak performance for both the left and right sirens. A wideband at relatively low frequency occurs at 1638-1915 Hz for the left siren and 1620-1860 Hz for the right siren. Then, two distinct peaks occur at 3076 and 5200 Hz for the left siren, and 3083 Hz and 5100 Hz for the right siren. These resonant frequencies will indeed limit the usable range of chamber acoustic frequencies, but this factor must be considered hand in hand with chamber resonance to fully characterize the acoustic system.

4.3.2 Waveguide

As described above, the sirens have a circular shape while the inner chamber is rectangular. Thus, the waveguide's shape must provide a smooth transition from a 11.24 cm diameter circle to a 2.03 cm \times 3.61 cm rectangular cross-section. To minimize two-dimensional and three-dimensional waves, the circle-to-rectangle transition must be void of abrupt area changes and sharp corners. This requirement, combined with material stress from high chamber pressures, make design and fabrication challenging.

The area reduction from circle to rectangle follows a quasi-one-dimensional model for sound propagation in a rigid-walled duct, which is derived beginning with the acoustic wave equation,

$$\nabla^2 p - \frac{1}{c^2} \frac{\partial^2 p}{\partial t^2} = 0, \quad (4.2)$$

which is then integrated for acoustic pressure p for a three-dimensional segment of the duct shown in Fig. 4.15. In agreement with the coaxial jet diagram in Fig. 1.13, x is the jet streamwise direction, y is the transverse direction, and z is the depthwise direction.

Thus, a perfectly shaped waveguide will prevent acoustic wave propagation in the x and z directions and concentrate 100% of the energy from each siren to produce waves in the y direction ($\frac{\partial^2 u}{\partial x^2} = \frac{\partial^2 u}{\partial z^2} = 0$). Gauss's theorem is then used to convert the volume integral of $\nabla^2 p$ to a surface integral, i.e.

$$\iiint_V (\nabla^2 p) dV = \oiint_S (\nabla p \cdot \hat{n}) dS. \quad (4.3)$$

Then, apply the boundary condition that $\nabla p \cdot \hat{n} = 0$ at the inner wall of the waveguide, divide by Δy , and take the limit as $\Delta y \rightarrow 0$ ($\Delta y = \partial y$). One obtains

$$\frac{\partial}{\partial y} \iint_A \frac{\partial p}{\partial y} dA - \frac{1}{c^2} \frac{\partial^2}{\partial t^2} \iint_A p dA = 0. \quad (4.4)$$

With the exception of a thin acoustic boundary layer near the inner wall of the waveguide, p is uniform over any given cross section, i.e. $\frac{\partial p}{\partial x} = \frac{\partial p}{\partial z} = 0$. The equation above then reduces to

$$\frac{1}{A} \frac{\partial}{\partial y} \left(A \frac{\partial p}{\partial y} \right) - \frac{1}{c^2} \frac{\partial^2 p}{\partial t^2} = 0, \quad (4.5)$$

which is known as Webster's horn equation, after Arthur G. Webster [150]. Following Pierce [151], Webster's horn equation can be simplified as

$$\left\{ \frac{\partial^2}{\partial y^2} + \frac{1}{4A^2} \left[(A')^2 - 2AA'' \right] - \frac{1}{c^2} \frac{\partial^2}{\partial t^2} \right\} A^{\frac{1}{2}} p = 0. \quad (4.6)$$

This is a nonlinear ordinary differential equation with respect to A which can be used to describe the optimal shape of an expanding or constricting waveguide as shown in Fig. 4.15. The general solution is

$$A^{\frac{1}{2}} = A_{th}^{\frac{1}{2}} (\cosh my + T \sinh my), \quad (4.7)$$

where $A_{th} = A(y = 0)$ and $A_{th}^{\frac{1}{2}} T m = \frac{\partial(A^{\frac{1}{2}})}{\partial y}(y = 0)$. The specific solution is found for the catenoidal horn shape for $T = 0$ [151]:

$$A = A_{th} (\cosh my)^2. \quad (4.8)$$

The throat area A_{th} and flare constant m are unique constants which are found according to the boundary conditions of the waveguide. First, the throat area is set equal to the cross-sectional area of the inner chamber,

$$A_{th} = (\Delta x) (\Delta z) = (36.1 \text{ cm}) (2.03 \text{ cm}) = 7.33 \text{ cm}^2, \quad (4.9)$$

and finally, constraining the solution for a specific waveguide length L and siren area gives a value of 0.0910 cm^{-1} for m . Thus, the completed solution for a catenoidal horn area distribution is

$$A(y) = 7.33 \cosh^2 (.091y). \quad (4.10)$$

This formula for $A = f(y)$ was used to calculate an appropriate transverse area distribution in square centimeters for the acoustic waveguides to the left and right of the chamber. The area distribution according to equation 4.10 is plotted in Fig. 4.16 with the inner chamber included in between the left and right waveguides. Thus, Fig. 4.16 represents the area distribution of the completed chamber.

However, Webster's horn equation is limited when applied to waveguides in this way. Effective use of waveguides as sound amplifiers requires an acoustic frequency above a minimum operating frequency, or cutoff frequency f_c , which is a function of the speed of sound c and the flare constant m . According to Pierce [151],

$$f_c = \frac{mc}{2\pi}, \quad (4.11)$$

which can be used to estimate an appropriate minimum acoustic frequency. This cutoff frequency is less important for horns with $mL \leq 1$ [151], but $mL=3.3$ for the waveguides used here. As an example, nitrogen at $T=300 \text{ K}$ gives $f_c=511.5 \text{ Hz}$ and $f_c=552.0 \text{ Hz}$ for $p_c=0 \text{ psig}$ and $p_c=1500 \text{ psig}$ (10.34 MPa), respectively. Although temperature variations may also alter the speed of sound, and large temperature variations exist near the jet, the temperature of gas in the waveguides was found to have a negligible effect on f_c . Therefore, the cutoff frequency criterion will be adhered to for the experiments in this study.

4.3.3 Resonant Frequencies

4.3.3.1 Acoustic Forcing Strategy and Analytical Consideration

Paired with the resonant modes of the acoustic drivers, the resonant modes of the chamber cavity are imperative in determining a useable set of frequencies for experiments involving high amplitude acoustics. A straightforward calculation predicting several transverse chamber modes is described below. Following theoretical discussion, experimental resonant frequencies are presented for a range of chamber pressures.

Akin to the cavity resonance analysis for the cylindrical waveguide discussed in section 2.1, the resonant frequencies of the more complex chamber geometry addressed here can be predicted by eqn. 2.1, which is listed here for convenience.

$$L = \frac{n}{2}\lambda = \frac{n}{2}\left(\frac{c}{f_F}\right) \quad (4.12)$$

Again, regardless of the value of f_F and n , speakers operated out-of-phase ($\Delta\phi = 180^\circ$) will create a PN at the center of the chamber and speakers operated in-phase ($\Delta\phi = 0^\circ$) will create a PAN at the center. To achieve maximum acoustic pressure and velocity amplitudes, f_F must take on a value in accordance with 2.1 where n is a positive integer. But, additional phenomena cause increased error when applying the following assumptions. First, the area changes within each waveguide are neglected when applying one-dimensional theory. Second, the speed of sound c is not constant, but rather is altered by chamber pressure and temperature. Thus, as a result of repeated cooling and firing cycles near the injector, the speed of sound for each experimental test should be considered unique. Temperature, for example, is a minimum at the center of the chamber where cryogenic flows cool the region after long periods of temperature conditioning prior to ignition. During this period, the chamber's maximum temperature is located at ends of each respective waveguide. After ignition though, a sharp temperature rise occurs in the flame region and a small pressure rise occurs due to combustion. Speed of

sound is a function of both time and space as a result of these variations in temperature and pressure.

A second phenomenon which increases error when applying the assumptions of eqn. 2.1 is a result of three-dimensional geometry variations in the waveguides. Although the shape of the internal waveguide walls was carefully designed according to the derivations in Section 4.3.2, resonant modes may occur in three different dimensions. These three are the transverse direction y spanning from the left waveguide to the right waveguide, the secondary transverse direction z spanning from the front window of the inner chamber to the rear window of the inner chamber, and the longitudinal direction x spanning from the upper wall of the inner chamber to the exhaust orifice. Each of these three mode types will be addressed differently.

The transverse modes occurring in the y direction navigate only smooth area changes within the waveguides. Thus, the transverse mode, or “T” mode, will be described using the approximate calculations of eqn. 2.1 using a value of c for pure nitrogen at the mean chamber pressure p_c and the mean chamber temperature T_c . By design, a transverse span of $L = 0.82$ m offers multiple frequencies less than 6000 Hz at which transverse resonance may occur. This mode type will be the focus of all acoustic forcing results presented in this study.

The secondary transverse modes occurring in the z direction will resonate within a very small span created by the depth of the inner chamber. This geometric boundary, created by the front and rear inner windows, is only 20.32 mm in length. Consequently, only very high frequencies are capable of producing resonant conditions in the z direction. A speed of sound of $c=344$ m/s and $n=1$, for example, will result in an acoustic resonant frequency of 8465 Hz. This frequency is far greater than the useable range of the piezoelectric sirens. Thus, secondary acoustic modes in the z direction are assumed to be negligible.

The longitudinal modes occurring in the x direction maneuver a series of abrupt area changes between the inner chamber and the exhaust tube. The inner chamber's exit is a rectangular exhaust gap which connects the rectangular inner chamber with the exhaust manifold. The exhaust manifold introduces additional gaseous nitrogen into the exhaust mixture, cooling the mixture before it exits the outer chamber through a 22.1 mm diameter hole, and then the 4.8 mm exhaust orifice. Thus, three interconnected volumes create a longitudinal space in which “L” modes may exist, but cannot be accurately predicted with brief analytical techniques due to two substantial area changes joining the inner chamber, exhaust manifold, and exhaust tube. For a three-dimensional computational analysis of chamber acoustics, ANSYS and COMSOL have been used to successfully resolve the influence of complex geometry and speed of sound variations [18, 24, 131]. Such an analysis is outside the scope of this work and will be considered in future analysis.

4.3.3.2 Experimental Characterization

Using a single dynamic pressure transducer within the inner chamber, acoustically resonant conditions can be identified for both PAN and PN conditions at the center of the chamber. This type of experimental characterization conveys the final result of merging acoustic resonance attributed to each siren with acoustic resonance attributed to chamber geometry. Due to the sirens' ability to produce high pressure amplitudes for only three limited frequency bands, it is expected that p' measurements will be high for a limited number of transverse chamber modes. Other transverse modes may be resonant, but acoustic chamber modes far from the effective frequency bands of the sirens will create low, unusable amplitudes. To demonstrate this balance, a frequency sweep was performed for PAN conditions.

To experimentally determine resonant PAN conditions, p' was measured at the center

of the chamber using a pressure transducer located in the center of the rear inner window, a distance $12D_1$ below the injector. The pressure measured at this point is $p_{dyn,2}$. A PAN condition was produced at this location by operating the sirens in-phase, i.e. $\Delta\phi = 0^\circ$. Over a time span of 20 s, the sirens were linearly swept from an acoustic frequency of 100 to 6000 Hz while sampling pressure at a rate of 40 kHz. This procedure was repeated for ten different mean chamber pressures from 100 to 1000 psia (6.9 MPa) while at room temperature.

To provide a comparative representation of PAN frequency sweep results, time series data are transformed into a periodogram power spectral density estimate using a Hamming window function. Fig. 4.17 includes the results from each chamber pressure set point, and also includes theoretical lines calculated using eqn. 2.1 for comparison. For $f < 1400$ Hz, amplitudes remain negligible regardless of chamber pressure due to the sirens' ineffective sound production in this range. The 1T and 2T modes cannot be identified. For $1400 \text{ Hz} < f < 4000 \text{ Hz}$, several modes can be identified throughout the sirens' effective frequency range. When comparing the performance of the left and right sirens in Fig. 4.14 with the theoretical transverse resonance values, it is clear that an additional factor must be engendering other peak frequencies shown in Fig. 4.17 for $1400 \text{ Hz} < f < 4000 \text{ Hz}$. The additional factor may be a result of chamber resonance unaccounted for by transverse resonance calculations, such as longitudinal resonance. Unexpected spectral results may also be manifested by imperfect siren operation. For example, although the phase relationship of each siren control channel is set to zero ($\Delta\phi = 0^\circ$), deviations in $\Delta\phi$ can occur over wide variations in frequency. For $\Delta\phi \neq 0^\circ$, perfect resonance cannot be achieved and the PAN deviates from the center of the chamber [135]. These deviations result from the uniqueness of each siren signal amplifier, amounting to a phase difference of several degrees between each amplifier. Variations in $\Delta\phi$ were not corrected during the frequency sweep represented in Fig. 4.17. In conclusion, although significant amplitudes can be achieved near the 3T, 4T,

5T, 6T, and 7T modes, the exact frequency of each mode cannot be determined as a result of unidentifiable frequency peaks, and thus, Fig. 4.17 alone is an imperfect indication of transverse standing waves. Using the acoustic forcing system requires standing wave verification for each individual experimental condition, and this procedure will be described in appendix A.1.

4.4 Nonreactive Jet Imaging

Jet flow visualization was the primary diagnostic tool for studying LN₂-GHe flow dynamics, provided by back-lit high-speed images. A variable power Newport model 66986 power supply controlled a 300 W Xe lamp, which emitted light in the near ultraviolet spectrum. This beam was projected through the rear window as a back-light source. Although the beam was not collimated, this back-lighting technique produced sufficient contrast at fluid interfaces. Differences in the refractive index of the jets and the surrounding medium provided the necessary distinction between the fluids of interest. The low temperature, liquid nitrogen inner jet appeared as a dark column of fluid as viewed by the high-speed camera placed on the opposite side of the light source. The less dense gaseous helium outer jet was also distinguishable from the heavier gaseous nitrogen surrounding the coaxial jet.

A Phantom v7.10 high-speed camera was used to visualize the fast dynamical processes inherent to an unforced coaxial jet flow as well as those present during high frequency acoustic forcing. A 200 mm Nikon MicroNikkor lens was used with a no. 1 close-up lens attachment, giving a spatial resolution of 30 μm per pixel. Image framing rates of 10 kHz were used in order to avoid aliasing up to 5 kHz, which is much greater than the highest forcing frequency used in this study, 2600 Hz. An external trigger from the facility control system was used to start recording the image frames, which were synchronized with all other data using the coordinated universal time (UTC) stamp

from an IRIG-B timecode generator.

4.5 Reduced Basis Methods

Reduced basis methods are growing in popularity as a computational procedure to reduce the complexity of flow systems exhibiting periodic, coherent structures. For computational fluid dynamicists, reduced basis methods have been used to provide inlet flow boundary conditions which capture important flow instabilities without representing all, and thus insignificant, modes in order to increase computational efficiency [152]. For experimentalists, reduced basis methods have been particularly useful image analysis tools. In a study by Arienti *et al.* [153] the shape and instability frequencies of a jet in crossflow were captured using just a few modes which contain the highest energy contribution. Where experimental systems pose installation challenges for direct probing and sensing instruments, which may cause unwanted flow disturbances, reduced basis methods extract spatial and temporal information from images alone. This study uses proper orthogonal decomposition (POD) to determine the spectral content of the most significant modes in a shear-coaxial jet, and uses the same set of results to describe the qualitative shape of these modes. Also, a brief comparison is made between POD and a second reduced basis method, dynamic mode decomposition (DMD).

4.5.1 Proper Orthogonal Decomposition

When used as an image analysis algorithm for flow instability, POD uses high-speed imaging results to reconstruct an approximate representation of a flow using proper orthogonal modes (POMs) which are ranked according to their pixel intensity variations relative to the time-average. This method has been used by Arienti *et al.* [153] and Arienti and Soteriou [154] to determine the dominant vortex shedding frequencies in

jets in crossflow, and Teshome *et al.* [30] have been the first researchers to apply POD to shear-coaxial jet instabilities. In Teshome *et al.* [30], the natural jet instability and the acoustically forced jet instability was identified by truncating the resulting set of POMs to the highest ranked POM conjugate pair with the goal of representing the jet with a single mode. The present study holds a similar approach, and this section serves to describe POD accordingly.

First, the pixel intensity values for a set of images can be represented in continuous form as

$$a(x, t) = \sum_{k=1}^N u_k(t) v_k(x), \quad (4.13)$$

where u_k are vectors of temporal amplitude coefficients, v_k are vectors of proper orthogonal modes, k is the mode number, and N is the number of modes. In order to implement this method, the pixel intensities are arranged into a single aggregate data array for all image frames, giving a a single spatial dimension having a length M equal to the total number of pixels in a single $m \times n$ image. Thus, $M = mn$. First, this is achieved by forming a row vector consisting of all pixel intensity values of each image frame. The row vector is formed in order of increasing pixel columns followed by increasing pixel rows, as shown in Fig. 4.18. Row vectors are then combined for a sequence of N image frames, resulting in the complete matrix \mathbf{A} consisting of N rows by M columns of intensity values. Thus, \mathbf{A} is an array of N sets of M pixel intensities in a single matrix, as shown in Fig. 4.19.

In order to isolate the periodic fluctuations of coherent structures, the intensity fluctuations should be considered rather than the mean. Thus, the time-average of each pixel intensity is subtracted from the mean to produce a matrix of intensity fluctuations $\tilde{\mathbf{A}}$. That is,

$$\tilde{\mathbf{A}}_{ij} = \mathbf{A}_{ij} - \frac{1}{N} \sum_i \mathbf{A}_{ij} \quad (4.14)$$

where $i = 1 \dots N$, $j = 1 \dots M$. Figure 4.20a shows a single image frame, and Fig. 4.20b

shows the corresponding time-averaged image for $N = 100$ frames. Since a single image contains more than 100,000 pixels and the number of images is ~ 1000 , then $\tilde{\mathbf{A}}$ is a rectangular matrix where $N < M$. A singular value decomposition (SVD) can be readily computed for this non-square matrix as opposed to eigenvalue decomposition, which is an alternative to SVD for computing a POD solution, but requires $\tilde{\mathbf{A}}$ to be a square matrix. According to SVD, $\tilde{\mathbf{A}}$ can be represented with the form

$$\tilde{\mathbf{A}} = \mathbf{U}\mathbf{\Sigma}\mathbf{V}^T \quad (4.15)$$

This decomposition is used within POD to divide the complete matrix into a matrix containing temporal information \mathbf{U} , a matrix containing spatial information \mathbf{V} , and a scaling matrix $\mathbf{\Sigma}$. The product of \mathbf{U} and $\mathbf{\Sigma}$ is representative of u_k in eqn. 4.13, and \mathbf{V} is the matrix form of v_k . After removing unused rows in \mathbf{U} in an economic SVD scheme, \mathbf{U} is an $N \times N$ orthogonal matrix taking the form

$$\mathbf{U} = \begin{bmatrix} u_{11} & u_{12} & & & \\ u_{21} & u_{22} & & & \\ & & \ddots & & \\ & & & \ddots & \\ & & & & u_{NN} \end{bmatrix}, \quad (4.16)$$

\mathbf{V}^T is an $M \times M$ orthogonal matrix taking the form

$$\mathbf{V}^T = \begin{bmatrix} v_{11} & v_{21} & & & \\ v_{12} & v_{22} & & & \\ & & \ddots & & \\ & & & \ddots & \\ & & & & \ddots \\ & & & & & v_{MM} \end{bmatrix}, \quad (4.17)$$

and $\mathbf{\Sigma}$ is an $N \times M$ diagonal matrix taking the form

$$\mathbf{\Sigma} = \begin{bmatrix} \sigma_1 & 0 & & & & \\ 0 & \sigma_2 & & & & \\ & & \ddots & & & \\ & & & \sigma_N & 0 & \cdots & 0 \end{bmatrix} \quad (4.18)$$

which contains non-negative, real diagonal elements. With row operations, the structure of $\mathbf{\Sigma}$ was enforced to have the ranking $\sigma_1 \geq \sigma_2 \geq \dots \geq \sigma_N \geq 0$. Thus, POD enforces not only that the singular values of $\mathbf{\Sigma}$ are arranged in descending order, but also enforces orthogonality in \mathbf{U} and \mathbf{V} .

To explain why SVD is an appropriate method for completing POD, the following derivation will show that by enforcing orthogonality in \mathbf{U} and \mathbf{V} we have solved a simplified form of a covariance eigenvalue problem. Thus, this method allows one to approximate the eigenvalues and eigenvectors of the covariance which exists in the acquired data. Each eigenvalue and eigenvector will together represent a single mode of fluctuation which exists in \mathbf{A} . As will be discussed below, the constraints of SVD allow for an optimal reconstruction of \mathbf{A} according to the covariance of each mode, which is a representation of the energy contribution of the spatio-temporal fluctuations of each mode present in the image. This estimate of energy contribution is with regard to pixel intensity variations only, and is not quantitatively correlated with energy. Therefore, this study will use singular values and eigenvalues as a measure of pixel intensity variance for a single mode rather than a measure of energy. First, consider the $M \times M$ covariance matrix $\mathbf{R} = \tilde{\mathbf{A}}^T \tilde{\mathbf{A}}$, or in continuous form

$$\mathbf{R}_{ij} = \sum_{k=1}^N a_{ki} a_{kj}. \quad (4.19)$$

\mathbf{R}_{ij} is the product of the intensity fluctuations of the i^{th} pixel and the j^{th} pixel, hence \mathbf{R} is the covariance of intensity throughout the image. When used within a POD algorithm,

the orthogonality constraint of SVD allows one to solve an eigenvalue problem for \mathbf{R} with real, non-negative eigenvalues.

With $\tilde{\mathbf{A}} = \mathbf{U}\mathbf{\Sigma}\mathbf{V}^T$, the covariance matrix can be rewritten as

$$\mathbf{R} = \mathbf{V}\mathbf{\Sigma}^T\mathbf{U}^T\mathbf{U}\mathbf{\Sigma}\mathbf{V}^T. \quad (4.20)$$

If we assume that \mathbf{U} is orthogonal then $\mathbf{U}^T\mathbf{U}$ is equal to the identity matrix and

$$\mathbf{R} = \mathbf{V}\mathbf{\Sigma}^T\mathbf{\Sigma}\mathbf{V}^T. \quad (4.21)$$

Now, define $\mathbf{\Lambda}$ as the product of the singular value matrix and its transpose ($\mathbf{\Lambda} = \mathbf{\Sigma}^T\mathbf{\Sigma}$), which by definition is the diagonal matrix

$$\mathbf{\Lambda} = \begin{bmatrix} \sigma_1^2 & & & & & \\ & \sigma_2^2 & & & & \\ & & \ddots & & & \\ & & & \sigma_N^2 & & \\ & & & & 0 & \\ & & & & & \ddots \\ & & & & & & 0 \end{bmatrix}, \quad (4.22)$$

where $\mathbf{\Lambda}_{ij} = 0$ for $i > N$ or $j > N$ and the same form is reached by dropping zero columns from $\mathbf{\Sigma}$ to increase computational efficiency. Multiplying both sides of eqn. 4.21 by \mathbf{V} and enforcing orthogonality in \mathbf{V} leads to the desired eigenvalue problem

$$\mathbf{R}\mathbf{V} = \mathbf{V}\mathbf{\Lambda}, \quad (4.23)$$

which is the general form of an eigenvalue problem. An eigenvalue problem defines a non-zero vector that, when multiplied by a square matrix, yields a constant multiple of the non-zero vector. Here, the constant multiplier is $\mathbf{\Lambda}$, and the vector is \mathbf{V} . In other words, \mathbf{V} contains the eigenvectors of \mathbf{R} and $\mathbf{\Lambda}$ contains the eigenvalues. By the

definition of the covariance matrix ($\mathbf{R} = \tilde{\mathbf{A}}^T \tilde{\mathbf{A}}$), \mathbf{R} is both real and symmetric, because $\tilde{\mathbf{A}}$ contains real data. Also, following the proof in appendix A.2, \mathbf{R} is positive semidefinite. For any eigenvalue problem where the square matrix \mathbf{R} is real, symmetric, and positive semidefinite, the eigenvector solutions will be orthogonal, i.e. \mathbf{V} is orthogonal. In addition, this state requires that the eigenvalues σ_i^2 are real and non-negative. Finally, this gives real, non-negative values for σ_i and allows rows of $\mathbf{\Sigma}$ to be ranked such that $\sigma_1 \geq \sigma_2 \geq \dots \geq \sigma_N \geq 0$. The above derivation of the covariance eigenvalue problem is not part of the POD algorithm employed in this study, but can be used in other POD schemes which do not utilize SVD. The derivation is given here to explain why SVD provides a valid reconstruction of the data matrix $\tilde{\mathbf{A}}$. By enforcing \mathbf{U} and \mathbf{V} to be orthogonal, SVD reaches a solution equivalent to the solution of the covariance eigenvalue problem, thus computing eigenvalues and eigenvectors of the covariance matrix.

4.5.2 Application of Proper Orthogonal Decomposition

Proper orthogonal decomposition was applied to shear-coaxial jet high speed image sets with three objectives:

- qualify the appearance of the most dominant mode
- quantify the frequency of the most dominant mode
- quantify the relative significance of the natural mode and the forced mode occurring within a single acoustically forced flow condition

To reach these objectives, a POD algorithm written in MATLAB was used to reach a solution for the orthogonal matrices \mathbf{U} and \mathbf{V} and the diagonal matrix of singular values $\mathbf{\Sigma}$ for a pixel data matrix \mathbf{A} . For a given flow condition, a set of back-lit images was reduced to capture only the pertinent portion of the field of view. The 320×640 field of view was reduced in width and height to only include the jet, thus decreasing

the number of columns M in the aggregate matrix \mathbf{A} and reducing computational time. Figure 4.20 shows a snapshot example, as well as the cropped field of view. The image acquisition rate and duration were chosen to create instability frequency spectra for an appropriate frequency range and resolution. First, the image sampling rate was 10 kHz, which provides a Nyquist frequency of 5 kHz. Second, the number of rows N in matrix \mathbf{A} , i.e. the number of images, was 2000. This was chosen to maintain acceptable computational efficiency while providing sufficient frequency resolution, which was 2.5 Hz ($=5000\text{Hz}/2000$). After subtracting the average image from each instantaneous image frame as in eqn. 4.14, SVD was applied to $\tilde{\mathbf{A}}$ to determine \mathbf{U} , $\mathbf{\Sigma}$, and \mathbf{V} , which must be analyzed further to obtain mode shapes and frequencies.

Following SVD of $\tilde{\mathbf{A}}$, additional data reductions were applied to further reduce computational time. Since $N \ll M$, only the first N diagonal elements of $\mathbf{\Sigma}$ and the first N columns of \mathbf{V} are non-zero. Consequently, $\mathbf{\Sigma}$ and \mathbf{V} were reduced to $N \times N$ and $M \times N$ matrices, respectively. By convention, since the singular values are arranged in descending order of magnitude, the columns of \mathbf{U} and \mathbf{V} , which represent an orthonormal bases set of the column and row space of $\tilde{\mathbf{A}}$, respectively, were arranged to match the order of $\mathbf{\Sigma}$.

Moreover, each column of $\mathbf{Q} = \mathbf{U}\mathbf{\Sigma}$, equivalent to $u_k(t)$ in eqn. 4.13, is a vector of time-dependent amplitude coefficients, while the columns of \mathbf{V} are the proper orthogonal modes. The columns of \mathbf{V} are eigenvectors, or can also be called eigenfunctions. Therefore, the first column of \mathbf{Q} contains the temporal characteristics of the coherent flow structure of the first mode, which contained the highest variance contribution to the flow. Meanwhile, the first column of \mathbf{V} contains the spatial distribution of the first mode, and so on, for subsequent columns of \mathbf{Q} and \mathbf{V} . As an example, Fig. 4.21 shows a plot of the singular values for all modes in the image set of an acoustically forced flow. The set of eigenvalues for this flow condition is calculated as $\Lambda_i = \sigma_i^2$, and is plotted

in Figure 4.22, which can also be regarded as the energy spectrum for the image set, because each eigenvalue is a representation of variance magnitude for a single mode. For this case, the spatial distribution of the flow was reconstructed using only the first mode, corresponding to the mode with the maximum eigenvalue in Fig. 4.22. The reconstruction of mode-1 is shown in Fig. 4.23b using the first column of \mathbf{V} ; this is called the proper orthogonal mode (POM) image, or eigenvector. The spatial distributions of subsequent modes could be constructed similarly from the remaining columns of \mathbf{V} . For example, the second column of \mathbf{V} is used to reconstruct mode-2, and the POM image is shown in Fig. 4.23c. By subtracting out the average pixel intensities prior to SVD processing, POM images will reveal lobes of dark and light regions to indicate locations where fluid was present and absent as it emanated from the dense inner jet flow. The uniform regions colored gray indicate a mean level in a gray-scaled image. Intuitively, the POM images will provide qualitative results regarding symmetry or asymmetry for a given mode. A jet located at a PN, for example, adopts an antisymmetric instability as shown in Fig. 4.23.

Analysis of the time-dependent amplitude coefficients found in \mathbf{Q} can be used to produce power spectral density (PSD) plots corresponding to each POM. Fig. 4.24 shows a PSD plot for mode-1 obtained from the first column of \mathbf{Q} . This is the same mode as shown in Fig. 4.23a. Similar to the measurement of experimental velocity oscillation frequencies using a hot-wire anemometer, Fig. 4.24 provides an indication of flow fluctuations, but only for a single mode. Rather than using an intrusive probe, POD allows one to study oscillations in flow as manifested by density gradients visualized in shadowgraph images. A peak in PSD denotes a recurring flow structure that originates from the inner shear layer with the associated peak frequency.

After forming POM images and PSD plots for a set of high-speed images, one must use both of these outcomes to find the most dominant, *convective* mode in the flow. To

be labeled as the most dominant mode, a solution must meet two requirements. First, its eigenvalue must be greater than those of other modes. In the most simple case, the first eigenvalue is the largest, and therefore the corresponding mode would be the most dominant. Although, a second requirement adds complexity and even subjectivity to the process of determining the most dominant mode. A convective shear-layer instability, or traveling vortex, will be represented by a conjugate POM pair rather than a single POM. Arienti and Soteriou [154] define conjugate mode pairs as any two modes whose cross power spectra magnitude peaks near a phase of 90° and are represented by similar lobe patterns. Following Arienti and Soteriou [154], the cross power spectral density (CPSD) of a conjugate mode pair with temporal amplitude coefficients, a_k and b_k was computed as

$$\text{CPSD} = \sum_{s=0}^{N-1} \text{corr}(a_k, b_k) e^{-i\omega s} \quad (4.24)$$

where $\text{corr}(a_k, b_k)$ represents the cross-correlation of a_k and b_k . For the same acoustically forced condition shown in Fig. 4.24, the CPSD magnitude of mode-1 and mode-2 is shown in Fig. 4.25 along with the phase difference. The magnitude spectra reveals a peak instability at the forcing frequency, $f_F = 2050$ Hz, and a phase difference of 90° also occurs at 2050 Hz. When choosing to pair mode-1 and mode-2 as a single flow instability, Fig. 4.23 can also be used to add confidence. In Fig. 4.23, the reconstructed POM images of mode-1 and mode-2 show the same visual features simply shifted 90° in direction of convection, supporting the pairing of these modes as a single flow phenomenon. In conclusion, because this study seeks to describe convective waves within the jet, an instability having a large energy contribution to the flow must consist of a conjugate mode pair in addition to highly ranked eigenvalues.

Using the post-processing methods described above, the mode identified as most dominant will be described qualitatively by using the POM images from \mathbf{V} and quantitatively by using the PSD of the conjugate mode pair. To meet the final objective

of comparing the significance of natural jet modes and acoustically forced jet modes, a measure of variance contribution will be calculated using the entire collection of N singular values. The pixel intensity variance contribution of a POM pair is calculated as

$$\Psi = \frac{\sigma_{k_1}^2 + \sigma_{k_2}^2}{\sum_{k=1}^N \sigma_k^2} \quad (4.25)$$

where $\sigma_{k_1}^2$ and $\sigma_{k_2}^2$ are the eigenvalues of mode- k_1 and mode- k_2 and the denominator is the sum of all eigenvalues. As noted earlier, the eigenvalue of a mode is equal to the square of the singular value for that mode ($\Lambda = \sigma^2$). Mode- k_1 and mode- k_2 are not necessarily mode-1 and mode-2. In conclusion, this method is used for comparing co-existing modes. In an acoustically forced flow system, a natural instability can maintain an energy contribution greater than or less than the mode asserted by forcing, and Ψ quantifies their relative importance.

4.5.3 Dynamic Mode Decomposition

Like POD, DMD allows one to reconstruct a data matrix in an approximate form, projecting large-scale motions onto a solution which neglects noise and maintains significantly fewer degrees of freedom. In eqn. 4.13, the pixel intensity values contained in a are organized to create an ordinary differential equation with temporal and spatial information separated in the variables u and v , respectively. To best describe DMD, a is written in a similar fashion, but with an amplitude coefficient included, i.e.

$$a(x, t) = \sum_{k=1}^N a'_k d_k(t) \phi_k(x). \quad (4.26)$$

In this form, d_k contains the temporal information, ϕ_k contains the spatial information or dynamic modes, and a'_k is the amplitude of each mode k . Note that the amplitude coefficient is only dependent on the mode number. The time-dependent function d_k takes a sinusoidal form as $d_k = \exp(\omega_k t)$, where ω_k represents the complex frequency of

mode k . ($\exp(ix) = \cos x + i \sin x$) Since sines and cosines are orthogonal, this form of d_k makes a DMD reconstruction orthogonal in *time*, whereas a POD reconstruction is orthogonal in *space* [152].

Dynamic mode decomposition proceeds by assuming that if \mathbf{A} represents a series of snapshots \mathbf{a} where $\mathbf{a}_1 = \mathbf{a}(x_1, t_1)$ from image 1 to image N . We can write \mathbf{A} as

$$\mathbf{A} = \mathbf{A}_1^N = \{\mathbf{a}_1, \mathbf{a}_2, \mathbf{a}_3, \dots, \mathbf{a}_N\}, \quad (4.27)$$

then a linear mapping \mathbf{S} connects any flow field \mathbf{a}_i to a subsequent flow field \mathbf{a}_{i+1} , that is,

$$\mathbf{S}\mathbf{a}_i = \mathbf{a}_{i+1}. \quad (4.28)$$

In complete form, eqn. 4.28 follows as

$$\begin{bmatrix} s_{11} & s_{12} & \cdots & s_{1M} \\ s_{21} & s_{22} & \cdots & s_{2M} \\ \vdots & & \ddots & \vdots \\ s_{M1} & s_{M2} & \cdots & s_{MM} \end{bmatrix} \begin{bmatrix} a_{1i} \\ a_{2i} \\ \vdots \\ a_{Mi} \end{bmatrix} = \begin{bmatrix} a_{1(i+1)} \\ a_{2(i+1)} \\ \vdots \\ a_{M(i+1)} \end{bmatrix}. \quad (4.29)$$

This linear mapping is assumed to be the same over the entire sampling interval $0 < t \leq (N-1)\Delta t$, which is a linear tangent approximation. If we apply the linear tangent approximation to the next flow field, then $\mathbf{a}_{i+2} = \mathbf{S}\mathbf{S}\mathbf{a}_i = \mathbf{S}^2\mathbf{a}_i$, or for all $i \geq 2$ we have $\mathbf{a}_i = \mathbf{S}^{i-1}\mathbf{a}_1$. Using this method for the entire sequence of N flow fields gives a Krylov sequence for \mathbf{A}_1^N ,

$$\mathbf{A}_1^N = \{\mathbf{a}_1, \mathbf{S}\mathbf{a}_1, \mathbf{S}^2\mathbf{a}_1, \dots, \mathbf{S}^{N-1}\mathbf{a}_1\}. \quad (4.30)$$

This formula allows one to predict an entire sequence of flow fields using only a single snapshot \mathbf{a}_1 , but requires a known \mathbf{S} ($M \times M$), which is a complete and exact mapping of the flow field. Although, when applying reduced basis methods to experimental imaging results, \mathbf{S} is unknown. On the other hand, the entire flow field sequence \mathbf{A}_1^N is known. Thus, rather than determining \mathbf{A}_1^N using a complete \mathbf{S} and a limited amount of data as

in eqn. 4.30, DMD determines a limited form of \mathbf{S} using the known data matrix \mathbf{A}_1^N . To this end, eqn. 4.30 is rewritten to better utilize the data matrix and factor out the unknown \mathbf{S} . Namely,

$$\begin{aligned}\mathbf{A}_2^N &= \{\mathbf{a}_2, \mathbf{a}_3, \dots, \mathbf{a}_N\} &= \{\mathbf{S}\mathbf{a}_1, \mathbf{S}^2\mathbf{a}_1, \dots, \mathbf{S}^{N-1}\mathbf{a}_1\} \\ &= \mathbf{S} \{\mathbf{a}_1, \mathbf{S}\mathbf{a}_1, \dots, \mathbf{S}^{N-2}\mathbf{a}_1\} \\ &= \mathbf{S}\mathbf{A}_1^{N-1},\end{aligned}\tag{4.31}$$

which is the reduced form of the linear tangent approximation for the entire sequence of images. A DMD algorithm aims to extract the eigenvalues (time-dependent magnitudes), eigenvectors (spatial distributions), and amplitudes from the dynamical process described by \mathbf{S} based on the pixel data contained in \mathbf{A}_1^N .

In addition to the linear tangent assumption, a second assumption is made. If the physical process represented by an experimental image set, or represented by a numerical flow field in the case of computational fluid dynamics, is periodic and steady in the mean, then after a critical number of flow field snapshots have been acquired there will not be new information presented in any of the following snapshots. Additional images will only contain phenomena already captured in the previous set of images. Mathematically, a critical number of snapshots $N - 1$ is reached such that \mathbf{a}_N is linearly dependent on the previous $N - 1$ snapshots. Thus, each of the vectors $\mathbf{a}_1, \mathbf{a}_2, \dots, \mathbf{a}_{N-1}$ are linearly independent, but \mathbf{a}_N can be written as a linear combination of those vectors when the correct mapping is applied, i.e.

$$\mathbf{a}_N = g_1\mathbf{a}_1 + g_2\mathbf{a}_2 + \dots + g_{N-1}\mathbf{a}_{N-1}.\tag{4.32}$$

Since the mapping coefficients g_1, g_2, \dots, g_{N-1} are scalars, eqn. 4.32 can be written in

matrix form as

$$\begin{bmatrix} a_{1N} \\ a_{2N} \\ \vdots \\ \vdots \\ a_{MN} \end{bmatrix} = \begin{bmatrix} a_{11} & a_{12} & \cdots & a_{1(N-1)} \\ a_{21} & a_{22} & \cdots & a_{2(N-1)} \\ \vdots & & & \vdots \\ \vdots & & & \vdots \\ a_{M1} & a_{M2} & \cdots & a_{M(N-1)} \end{bmatrix} \begin{bmatrix} g_1 \\ g_2 \\ \vdots \\ g_{N-1} \end{bmatrix}, \quad (4.33)$$

or simply

$$\mathbf{a}_N = \mathbf{A}_1^{N-1} \mathbf{g}. \quad (4.34)$$

Note that the vector \mathbf{g} is on the right of \mathbf{A}_1^{N-1} . Further, if we create a matrix $\tilde{\mathbf{S}}$ then \mathbf{A}_2^N can be written as

$$\begin{aligned} \mathbf{A}_2^N &= \{\mathbf{a}_2, \mathbf{a}_3, \mathbf{a}_4, \dots, \mathbf{a}_N\} \\ &= \{\mathbf{a}_2, \mathbf{a}_3, \mathbf{a}_4, \dots, \mathbf{A}_1^{N-1} \mathbf{g}\} \\ &= \mathbf{A}_1^{N-1} \tilde{\mathbf{S}}, \end{aligned} \quad (4.35)$$

which is the reduced form of the linear combination assumption. This form may only be used when $\tilde{\mathbf{S}}$ is taken as a companion matrix, meaning that all columns of $\tilde{\mathbf{S}}$ serve as placeholders except for the last column containing the linear combination coefficients of \mathbf{g} . The complete companion matrix is

$$\tilde{\mathbf{S}} = \begin{bmatrix} 0 & & & g_1 \\ 1 & 0 & & g_2 \\ & \ddots & \ddots & \vdots \\ & & 1 & 0 & g_{N-2} \\ & & & 1 & g_{N-1} \end{bmatrix}. \quad (4.36)$$

where the coefficients $\{g_1, g_2, \dots, g_{N-1}\}$ are unknown. The matrix form of 4.35 is

$$\begin{bmatrix} a_{12} & a_{13} & \cdots & a_{1N} \\ a_{22} & a_{23} & \cdots & a_{2N} \\ \vdots & & & \vdots \\ \vdots & & & \vdots \\ a_{M2} & a_{M3} & \cdots & a_{MN} \end{bmatrix} = \begin{bmatrix} a_{11} & a_{12} & \cdots & a_{1(N-1)} \\ a_{21} & a_{22} & \cdots & a_{2(N-1)} \\ \vdots & & & \vdots \\ \vdots & & & \vdots \\ a_{M1} & a_{M2} & \cdots & a_{M(N-1)} \end{bmatrix} \begin{bmatrix} 0 & & & g_1 \\ 1 & 0 & & g_2 \\ & \ddots & \ddots & \vdots \\ & & 1 & 0 & g_{N-2} \\ & & & 1 & g_{N-1} \end{bmatrix}. \quad (4.37)$$

Finally, joining the linear combination assumption with the linear tangent approximation, $\tilde{\mathbf{S}}$ is clearly an approximated version of the complete mapping \mathbf{S} , because

$$\mathbf{S}\mathbf{A}_1^{N-1} = \mathbf{A}_2^N = \mathbf{A}_1^{N-1}\tilde{\mathbf{S}}. \quad (4.38)$$

With \mathbf{A}_2^N as the single-stepped advancement of \mathbf{A}_1^{N-1} , the i^{th} column of \mathbf{A}_2^N is equal to the $(i+1)^{th}$ column of \mathbf{A}_1^{N-1} for $i = 1, 2, \dots, N-2$. These two data matrices are used to find the last column of $\tilde{\mathbf{S}}$, whose eigenvalues approximate some of the eigenvalues of \mathbf{S} . Hence, it is our objective to determine an approximate mapping $\tilde{\mathbf{S}}$ which serves as a reduced version of \mathbf{S} .

At this point in the derivation, the remaining steps vary depending on the specific DMD algorithm employed. Regardless, the objective is to formulate and solve an eigenvalue problem for the approximate mapping matrix. The general version described here utilizes a proper orthogonal decomposition basis, whereas other DMD methods use entirely different steps in order to define an eigenvalue problem for the companion matrix $\tilde{\mathbf{S}}$. Proceeding with the general method described by Jovanovic *et al.* [155], the displaced data matrix \mathbf{A}_2^N and a singular value decomposition of the initial matrix \mathbf{A}_1^{N-1} are used to evaluate a transformed arrangement of $\tilde{\mathbf{S}}$. By definition, the SVD of \mathbf{A}_1^{N-1} is

$$\mathbf{A}_1^{N-1} = \mathbf{U}\mathbf{\Sigma}\mathbf{V}^H, \quad (4.39)$$

where \mathbf{U} and \mathbf{V} are orthogonal and $\mathbf{\Sigma}$ represents the energy content for each mode, i.e.

singular values. Then, the right-hand portion of eqn. 4.38 can be written as

$$\mathbf{A}_2^N = \mathbf{U}\mathbf{\Sigma}\mathbf{V}^H\tilde{\mathbf{S}}. \quad (4.40)$$

Multiplying eqn. 4.40 by \mathbf{U}^H on the left and $\mathbf{V}\mathbf{\Sigma}^{-1}$ on the right gives

$$\mathbf{U}^H\mathbf{A}_2^N\mathbf{V}\mathbf{\Sigma}^{-1} = \mathbf{\Sigma}\mathbf{V}^H\tilde{\mathbf{S}}\mathbf{V}\mathbf{\Sigma}^{-1}, \quad (4.41)$$

This equation is a new form of $\mathbf{A}_2^N = \mathbf{A}_1^{N-1}\tilde{\mathbf{S}}$ which includes the singular value decomposition of \mathbf{A}_1^{N-1} . For this reason, the general version of DMD can be described as application of the POD modes of \mathbf{A}_1^{N-1} onto the dynamic mode decomposition of \mathbf{A}_1^N .

Along these lines, the general version continues by redefining the approximate map, which was defined as $\tilde{\mathbf{S}}$, as a transformation of $\tilde{\mathbf{S}}$ using the POD modes of \mathbf{A}_1^{N-1} . Remember, $\tilde{\mathbf{S}}$ is known from eqn. 4.37. As done in Jovanovic *et al.* [155], the transformed companion matrix is equivalent to the right hand side of 4.41, and will be called $\tilde{\mathbf{S}}'$. In other words,

$$\tilde{\mathbf{S}}' = \mathbf{\Sigma}\mathbf{V}^H\tilde{\mathbf{S}}\mathbf{V}\mathbf{\Sigma}^{-1}. \quad (4.42)$$

Eqn. 4.42 provides a known $\tilde{\mathbf{S}}'$ which allows one to readily formulate a general eigenvalue problem for $\tilde{\mathbf{S}}'$ which is similar to the eigenvalue problem for \mathbf{R} formulated for POD. The eigenvalue problem for $\tilde{\mathbf{S}}'$ follows as

$$\tilde{\mathbf{S}}'\mathbf{X} = \mathbf{X}\mathbf{D}, \quad (4.43)$$

where \mathbf{D} is a matrix of the eigenvalues $d_k(t)$ as in eqn. 4.26. The matrix \mathbf{X} contains eigenvectors which are used to form the dynamic modes $\phi_k(x)$. One can readily solve the eigenvalue problem to determine the time-dependent function $d_k(t)$ and the spatially dependent function $\phi_k(x)$, which are the outputs desired to complete a limited reconstruction of the flow field. To reach this point, constraints have not been placed on the eigenvectors and eigenvalues; both can be negative, imaginary, and need not be orthogonal. Instead, several other assumptions were made to obtain the correct form in eqn.

4.43. First, the linear tangent assumption was made to relate \mathbf{A}_1^{N-1} with \mathbf{A}_2^N using the linear mapping \mathbf{S} . Second, the mapping \mathbf{S} was approximated as the companion matrix $\tilde{\mathbf{S}}$ by way of the linear combination of a critical number of images N . Last, the initial data matrix \mathbf{A}_1^{N-1} was decomposed using SVD as in the POD algorithm of the previous section. Since $\mathbf{S}\mathbf{A}_1^{N-1} = \mathbf{A}_2^N$, this step is referred to as a projection of the linear operator \mathbf{S} onto a POD basis, which is advantageous for reasons discussed in section 4.5.4.

The preceding derivation of DMD is only one possible procedure for completing the decomposition. A second method of DMD, the full-rank method, utilizes a QR decomposition, $\mathbf{A}_1^{N-1} = \mathbf{Q}\mathbf{R}$, rather than SVD. Here, \mathbf{Q} and \mathbf{R} should not be confused with the nomenclature of section 4.5.1. The full-rank method though, does not provide an order to the identified modes. A magnitude of energy content is not distinguished in QR decomposition as in SVD. As will be shown in the following section, the computation of singular values in the general method enables the ranking of flow instability amplitude: a paramount objective of this study.

4.5.4 Application of Dynamic Mode Decomposition

Dynamic mode decomposition was employed with the same three objectives as the application of POD. Rather than use this algorithm to analyze all experimental flow conditions, a limited number of cases were analyzed using DMD with the primary purpose of comparing the effectiveness of DMD with that of POD. The conclusions gained from this comparison are offered in Section 5.2.

Similar to POD, an algorithm was written in MATLAB to process high speed image sets captured at a frame rate of 10 kHz and store the pixel intensity data in \mathbf{A} . In contrast to POD, DMD uses the raw gray-scale intensities to form \mathbf{A}_1^{N-1} and \mathbf{A}_2^N directly rather than subtracting the mean [152]. Then, the matrix $\tilde{\mathbf{S}}'$ was found using eqns. 4.39 and 4.42, in that order. With a known $\tilde{\mathbf{S}}'$, the eigenvalue problem in eqn. 4.43 was solved

using a MATLAB built-in function, giving the complex eigenvector matrix

$$\mathbf{X} = \begin{bmatrix} x_{r11} + ix_{i11} & x_{r12} + ix_{i12} & & \\ x_{r21} + ix_{i21} & x_{r22} + ix_{i22} & & \\ & & \ddots & \\ & & & x_{rnn} + ix_{inn} \end{bmatrix} \quad (4.44)$$

and complex eigenvalue matrix

$$\mathbf{D} = \begin{bmatrix} d_{r1} + id_{i1} & 0 & & \\ 0 & d_{r2} + id_{i2} & & \\ & & \ddots & \\ & & & d_{rnn} + id_{inn} \end{bmatrix}, \quad (4.45)$$

where $\{d_{r1} = d_{r2}, d_{r3} = d_{r4}, \dots, d_{r(n-1)} = d_{rnn}\}$ and $\{d_{i1} = -d_{i2}, d_{i3} = -d_{i4}, \dots, d_{i(n-1)} = -d_{inn}\}$. These two matrices are processed to form the complex frequencies and images which represent each mode.

As stated earlier, the matrix \mathbf{D} , made up of the individual eigenvalues d_k for each mode, is a periodic form of the frequency of mode k such that

$$d_k = \exp(\omega_k \Delta t). \quad (4.46)$$

Consequently, the complex frequency ω_k was calculated as

$$\omega_k = \omega_r + i\omega_i = \frac{\ln(d_k)}{2\pi\Delta t}, \quad (4.47)$$

and $\Delta t = 1/(10 \text{ kHz}) = 0.1 \text{ ms}$. The real component ω_r is the mode growth rate and the imaginary component ω_i is the mode frequency in Hertz. As depicted by the preceding calculation of ω_i , each mode is marked with a single frequency (a scalar) rather than a frequency spectrum (a vector). Meanwhile, the dynamic mode matrix Φ , made up of the dynamic modes ϕ_k for each mode, is determined using the eigenvector matrix \mathbf{X} and \mathbf{U} . Simply stated,

$$\Phi = \mathbf{UX}. \quad (4.48)$$

Each column of Φ is a spatial distribution of the flow field for a single mode, and a linear combination of several columns of Φ manifests a simplified reconstruction of the flow field neglecting all other modes and insignificant noise.

As a demonstration of this DMD algorithm, the same set of images used to create the POD results in Section 4.5.2 was analyzed with DMD. Because the flow field subject to analysis was acoustically forced, DMD is expected to reveal a coherent mode with $\omega_i = f_F$. In the top plot of Fig. 4.26 the wave growth rate ω_r is plotted versus ω_i for an LN₂-GHe flow condition coupled with acoustic forcing at a PN for $f_F = 2050$ Hz. The mode resulting from acoustic forcing is easily identified at 2050 Hz, with a slightly positive growth rate, identifying an unstable mode. With the exception of the mean flow represented by a point at the origin, all other modes are stable and are analogous to modes with low-ranked singular values as computed using POD. The spectrum of Fig. 4.26 is symmetric about the $\omega_i = 0$ axis, because all pixel intensity data contained real values. Complex data will generally result in an asymmetric appearance about the $\omega_i = 0$ axis.

For this study though, a measure of amplitude of pixel intensity fluctuations, or energy contribution, is more useful for identifying the significance of a given mode. Accordingly, amplitude was calculated using the method by Schmid [156], which follows as

$$\mathbf{a} = \frac{1}{\|\mathbf{V}\Sigma^{-1}\mathbf{X}\|}, \quad (4.49)$$

which can be interpreted as a matrix containing magnitudes of each vector in the two-dimensional space created by the product $\mathbf{V}\Sigma^{-1}\mathbf{X}$. The value of \mathbf{a} is proportional to a'_k in eqn. 4.26. Most importantly, amplitude relies on the singular values created by SVD, a step not included in the full-rank version of DMD. Further, the foundation of DMD does not include a ranking of modes in the linear tangent approximation, nor in the linear combination assumption of eqn. 4.32. Thus, multiple mode ranking techniques

for DMD algorithms have been explored in an effort to simplify flows using only the most important modes. Singular values alone though, impart the energy contribution of an entire spectra as in Fig. 4.24, not the magnitude at a distinct frequency. Thus, eqn. 4.49 relates the energy contributions held in $\mathbf{\Sigma}$ to a single eigenvector in \mathbf{X} . As shown in the lower plot of Fig. 4.26, DMD results convey the highest amplitude for the mean flow, a result which is in agreement with other DMD studies [152, 156, 157]. High amplitudes are also observed at $|\omega_i| = f_F = 2050$ Hz. This is expected for an acoustically forced jet in which the shear layer adopts the acoustic instability as the dominant mode.

A final form of verification lies in the realm of visualization. Like the POM images created using POD, the dynamic mode images of DMD are used for qualitative conclusions, such as jet symmetry or lack thereof. As an example, Fig. 4.27 displays the reconstructed images of one unstable mode shown by the cyan point in Fig. 4.26 where $[\omega_i, \omega_r] = [2050, 6.022]$. Characteristic of PN forcing, Fig. 4.27 shows an antisymmetric jet [29, 30]. The real and imaginary eigenvector images corresponding to ϕ_r and ϕ_i , respectively, are shown to be inherently conjugate by the location of lobes in each image in Fig. 4.27, which are 90° out-of-phase. This pairing occurs for the real and imaginary values found in each column of $\mathbf{\Phi}$, and thus results from the algorithm rather than a choice made by the user. This is one of many differences between DMD and POD, as will be discussed in chapter 5.

4.6 Measurement Uncertainty

The experimental results presented in this study derive from three measured quantities: pressure, temperature, and mass flow rate. These three measurements determine density ρ , velocity U , momentum flux M , and the ratios thereof (S , R , J). Although injector geometry is also used to determine velocity and momentum flux, the uncertainty of injector dimensions was made negligible by using the “as machined” dimensions with

an uncertainty of 0.013 mm (0.0005 in). Also, the precision error of pressure, temperature, and mass flow rate will be ignored due to their small relevance in comparison to bias error. This simplification is valid for two reasons. First, high signal-to-noise ratios were maintained by constructing well-shielded data transfer cables. Second, this study's reported measurements are time-averaged for steady flow conditions. Unsteady measurements, mainly dynamic pressure, were phase-averaged to obtain a mean p' value over more than 10,000 acoustic cycles.

For the inner and outer jets, exit velocities were determined using the relation

$$U_k = \frac{\dot{m}_k}{\rho_k A_k}, \quad (4.50)$$

where k is ij for the inner jet and oj for the outer jet. Following propagation of uncertainty principles of Mills and Chang [139], the uncertainty of U_k can be calculated as

$$\delta U_k = U_k \sqrt{\left(\frac{\delta \dot{m}_k}{\dot{m}_k}\right)^2 + \left(\frac{\delta \rho_k}{\rho_k}\right)^2 + \left(\frac{\delta A_k}{A_k}\right)^2} = U_k \sqrt{\left(\frac{\delta \dot{m}_k}{\dot{m}_k}\right)^2 + \left(\frac{\delta \rho_k}{\rho_k}\right)^2} \quad (4.51)$$

and the uncertainty of the momentum flux, $M_k = \frac{\dot{m}_k^2}{\rho_k A_k}$, is

$$\delta M_k = M_k \sqrt{4 \left(\frac{\delta \dot{m}_k}{\dot{m}_k}\right)^2 + \left(\frac{\delta \rho_k}{\rho_k}\right)^2 + \left(\frac{\delta A_k}{A_k}\right)^2} = M_k \sqrt{4 \left(\frac{\delta \dot{m}_k}{\dot{m}_k}\right)^2 + \left(\frac{\delta \rho_k}{\rho_k}\right)^2}. \quad (4.52)$$

A combination of vendor calibrations and on-site calibrations provide the measurement uncertainties for each instrument. Temperatures measured with both type E and type R thermocouples will be reported with uncertainties according to data published by the manufacturer, Omega. For the range of temperatures measured here, type E thermocouples have a bias uncertainty of ± 1 K while the bias uncertainty of type R thermocouples is ± 1.5 K. The Porter mass flow meters had a nonlinearity error of 1% full scale output (FSO) and a repeatability error of .2% FSO, as reported by Porter calibrations. This creates a combined nonlinearity and repeatability (CNLR) rating of

1.02%, which is the square root of the sum of squares of each source of error. With only negligible error present due to thermal effects, the CNLR is the total error of the mass flow meters. The CNLR and CNLRH ratings are standard methods for determining the static accuracy of an instrument for data without and with hysteresis, respectively. Thus, a mass flow rate uncertainty was chosen as the total error for the gas species of interest, because the FSO of each mass flow meter, and thus the total error, is altered by a change in species. The uncertainties for oxygen, nitrogen, helium, and hydrogen are 0.130 g/s, 0.119 g/s, 0.024 g/s, and 0.009 g/s, respectively. CNLRH ratings for all GP:50 static pressure transducers and Kulite dynamic pressure transducers were determined in calibrations performed on-site with a high pressure Ruska calibrator. Three different pressure transducer models were used for the pressure data reported in this study, each being used for separate purposes. Acoustic pressure fluctuations were measured with the Kulite Model XCE-093-50D, static pressures at room temperature were measured with the GP:50 Model 7200-8475, and static pressures at cryogenic temperatures were measured with the GP:50 Model 7720-JA-8474. For each of these three classifications of pressure measurement and corresponding sensor model, the total error applied to each category was drawn from calibration results of the *least accurate* single pressure transducer within that group. Values are listed in Table 4.2.

The inner and outer jet densities were evaluated based on chamber pressure and temperatures measured immediately upstream of the injector, using NIST REFPROP tables [158]. As shown in Fig. 4.5, density is primarily dependent on temperature when operating away from the saturation temperature. In this region, since density has a much weaker dependence on pressure than on temperature, the uncertainty in density due to pressure variation was deemed negligible. Thus, for measurement error analysis in this study, $\rho(p,T) \approx \rho(T)$.

Lastly, the uncertainties in momentum flux ratio and velocity ratio were calculated

as

$$\delta J = J \sqrt{\left(\frac{\delta M_{ij}}{M_{ij}}\right)^2 + \left(\frac{\delta M_{oj}}{M_{oj}}\right)^2} \quad (4.53)$$

and

$$\delta R = R \sqrt{\left(\frac{\delta U_{ij}}{U_{ij}}\right)^2 + \left(\frac{\delta U_{oj}}{U_{oj}}\right)^2}, \quad (4.54)$$

respectively. In chapter 5, error bars are included in several key plots to ameliorate clarity as one measures the accuracy of conclusions in this study. Conclusions are reached with an awareness of imperfect measurement techniques, and these error bars serve to quantify imperfections for the reader.

4.1: Dimensions of shear-coaxial injectors* used in AFRL experiments [23, 75].

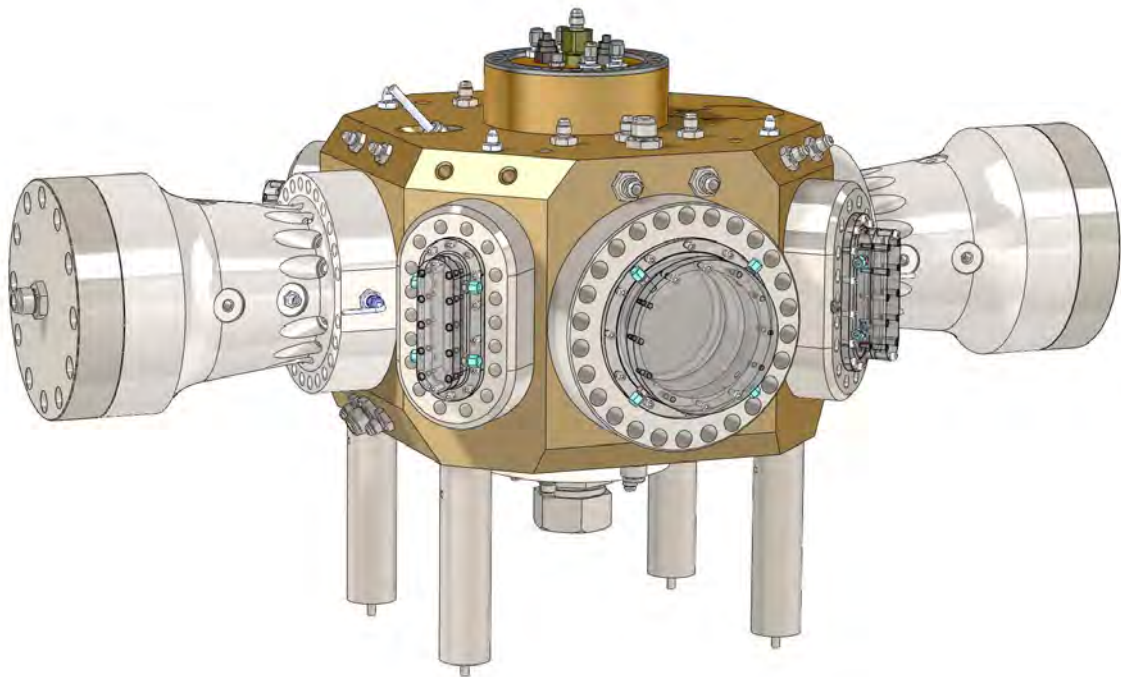
Inj.	t	D_1	$\frac{t}{D_1}$	D_2	D_3	D_4	D_{eff}	$\frac{A_{oj}}{A_{ij}}$
	[mm]	[mm]		[mm]	[mm]	[mm]	[mm]	
I	0.53	0.51	1.05	1.59	2.42	3.18	1.05	12.9
II	0.13	1.40	0.09	1.65	2.44	3.94	1.53	1.65
III	1.24	1.47	0.84	3.96	4.70	6.35	2.72	2.90
IV	0.09	0.70	0.13	0.89	2.44	3.94	0.80	10.6
V	0.38	1.40	0.27	2.16	2.82	3.56	1.78	1.68

* Injector V is used for new experimental results presented in this study, while injectors I-IV were used in previous nonreactive experiments at AFRL.

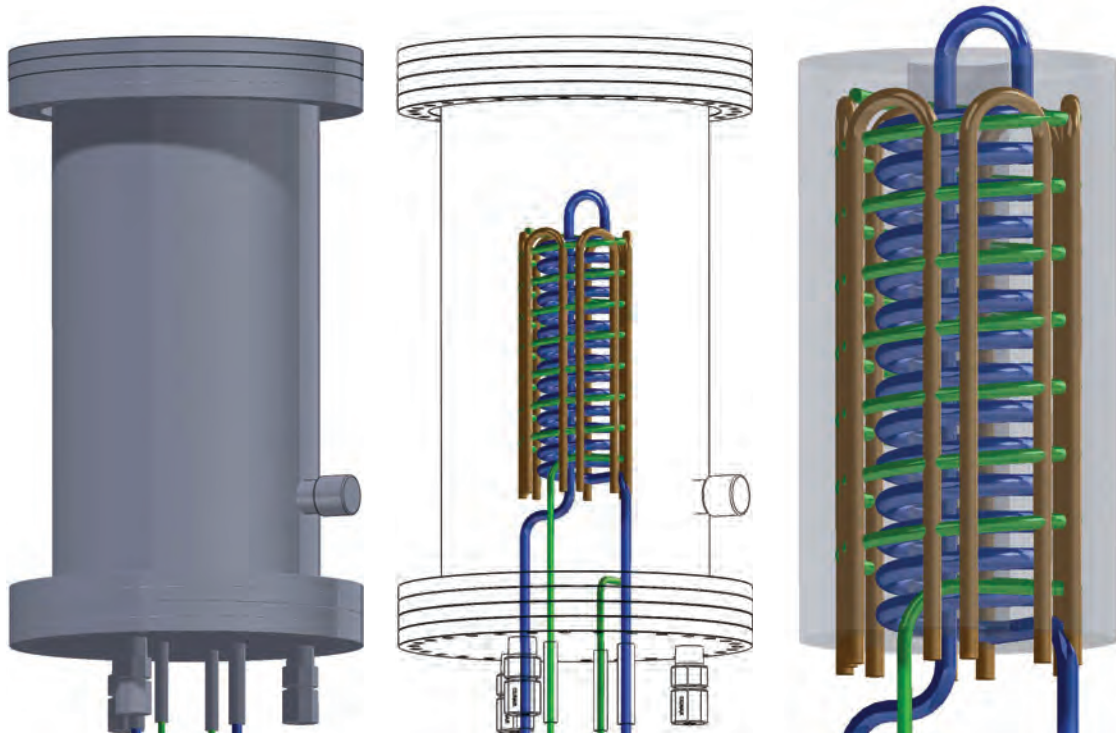
4.2: Pressure transducer uncertainty values*.

Mfr.	Model	Nonlinearity	Repeatability	Hysteresis	Static Accuracy	Thermal Error	Total Error
Kulite	XCE-093-50D	.09%	.16%	.12%	.22%	-	.22%
GP:50	7720-JA-8474	.05%	.12%	.10%	.16%	.37%	.53%
GP:50	7200-8475	.06%	.12%	.12%	.18%	-	.18%

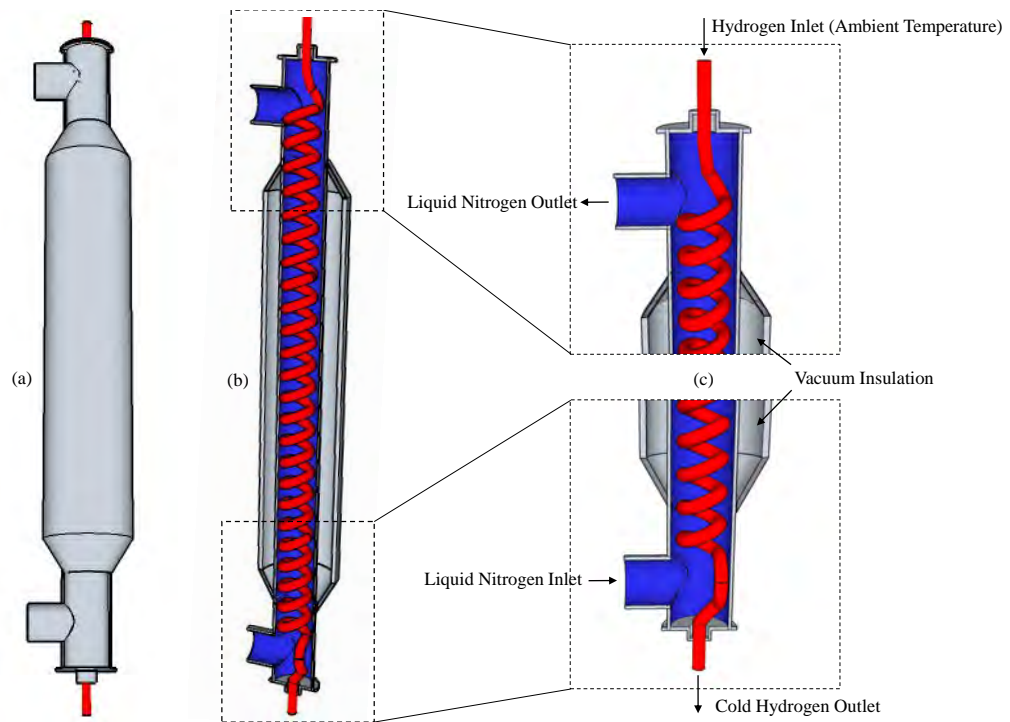
* Uncertainty values are taken as the total error of the instrument, listed here for each of the three transducer models used in this study. Static accuracy is the CNLRH rating calculated using the square root of the sum of squares method, and is the total error in the absence of significant error due to changes in temperature. For example, $CNLRH = \sqrt{(.06\%)^2 + (.12\%)^2 + (.12\%)^2} = .18\%$, which is the total error of pressures measured with the GP:50 7200-8475 at room temperature.



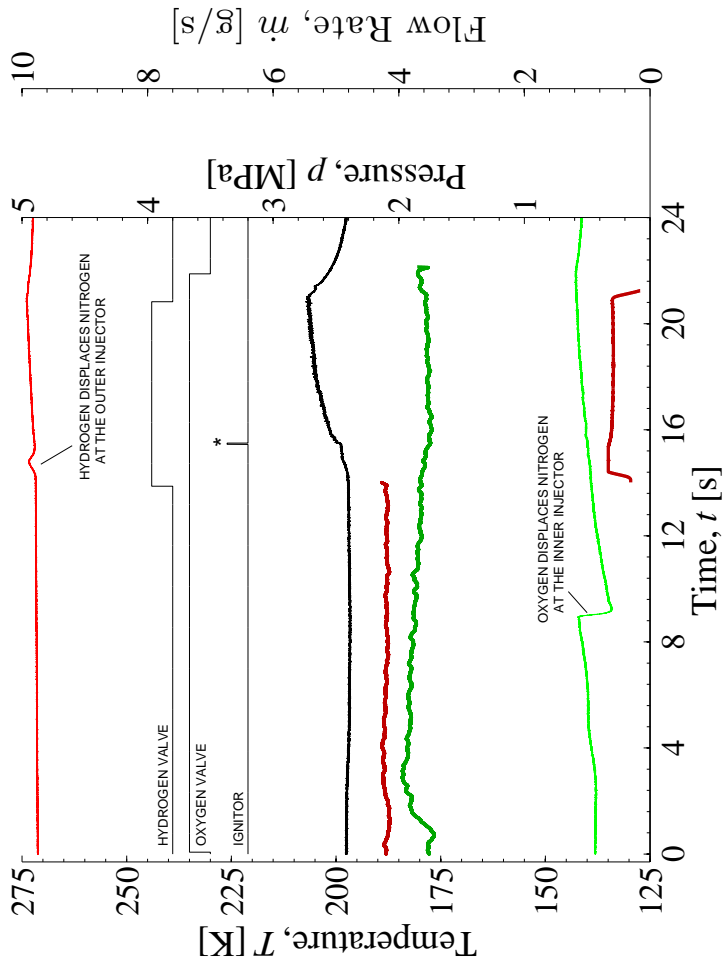
4.1: A three-dimensional CAD rendering of the high pressure combustion chamber at Air Force Research Laboratory at Edwards AFB, CA.



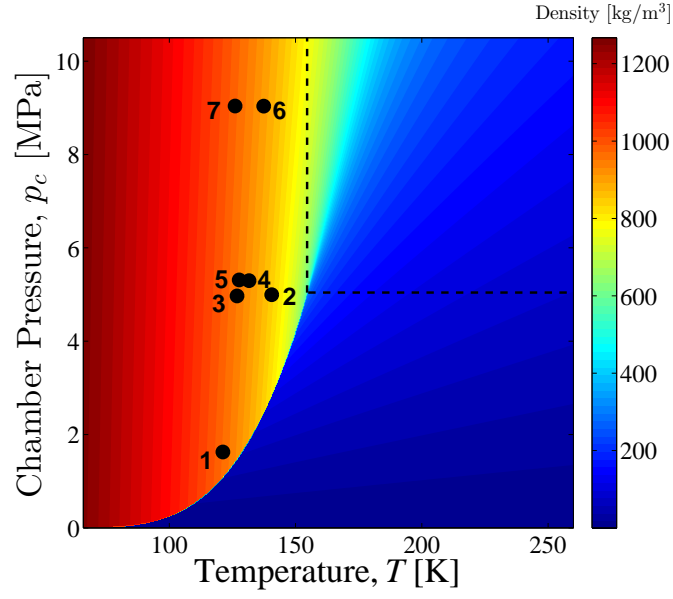
4.2: The oxygen heat exchanger cools oxygen gas (green) using liquid nitrogen (blue). Oxygen is cooled below the target temperature and electric heaters (brown) increase oxygen to the target temperature with a control resolution of ± 1 K. Insulation is provided by a vacuum jacket (shown in left view, outlined in center view). An aluminum casting surrounds the plumbing assembly (shown in right view, gray). Courtesy of Sierra Lobo Inc.



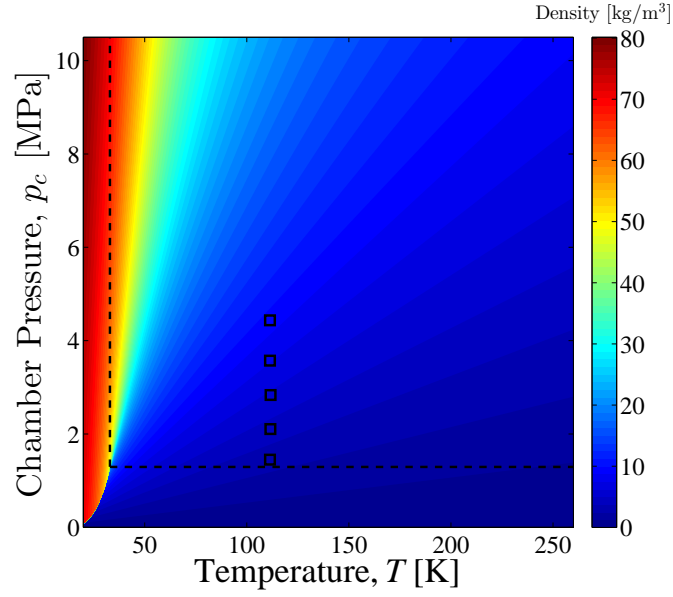
4.3: The hydrogen heat exchanger cools hydrogen gas (red) using liquid nitrogen (blue). Insulation is provided by a vacuum jacket.



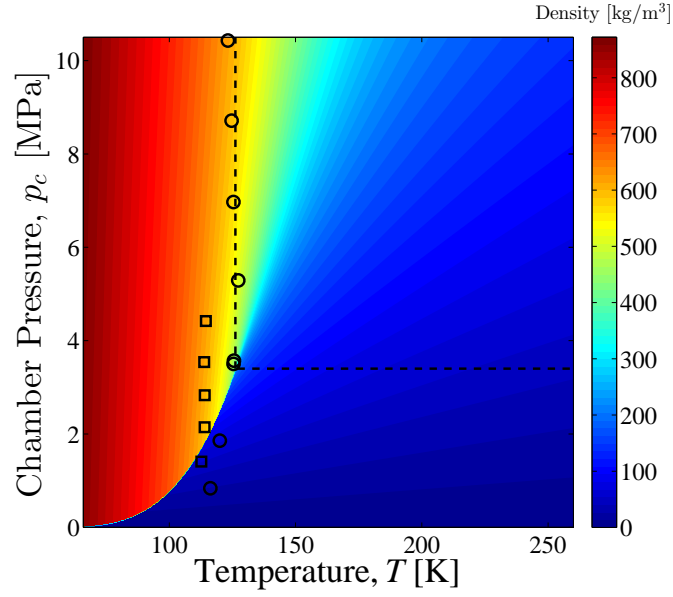
4.4: Time series plot of a reactive test using an oxygen and hydrogen. The transition from nitrogen simulant to propellant occurs after the propellant valve is opened. A step change in outer jet mass flow rate occurs near $t = 14$ s, where a nitrogen flow rate of ≈ 4.2 g/s changes to a hydrogen mass flow rate of 0.65 g/s (dark red). The inner jet mass flow rate shows a species change near $t = 1$ s, where a nitrogen flow rate of 3.6 g/s is overtaken by an oxygen mass flow rate of ≈ 3.9 g/s. Inner jet temperature (light green), outer jet temperature (light red), and chamber pressure (black) are also shown. $MR = 5.9$ ($\phi_{o/f} = 1.36$), $J = 2$



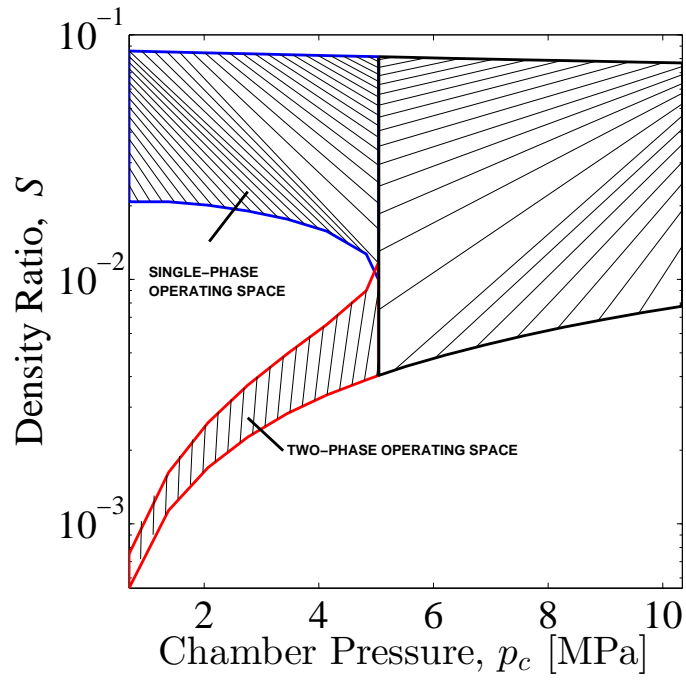
4.5: The facility's minimum achievable oxygen temperatures are plotted with an oxygen density contour overlay. A vertical line and a horizontal line represent the critical temperature and pressure, respectively. Both chamber pressure and mass flow rate are controlled while temperature is measured. (1) 3.7 g/s (2) 2.6 g/s (3) 9.3 g/s (4) 3.0 g/s (5) 11.1 g/s (6) 2.7 g/s (7) 10.4 g/s



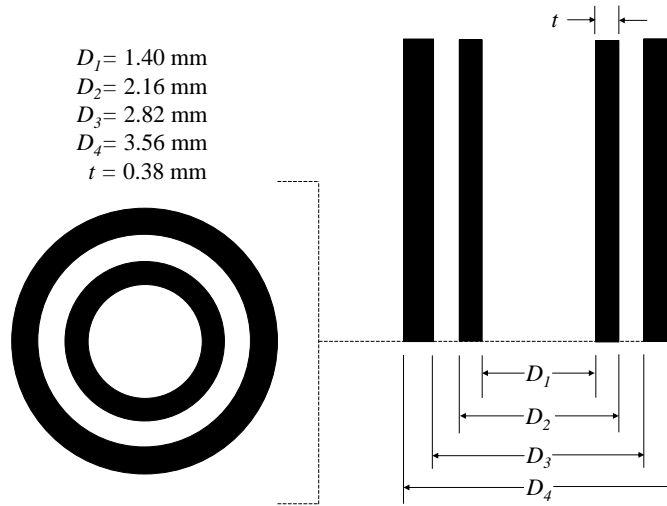
4.6: The facility's minimum achievable helium temperatures are plotted with a hydrogen density contour overlay. A vertical line and a horizontal line represent the critical temperature and pressure, respectively. Helium is used as a surrogate gas, and is representative of minimum hydrogen achievable hydrogen temperatures in the outer jet. The nominal outer jet flow rate is approximately 1.3 g/s.



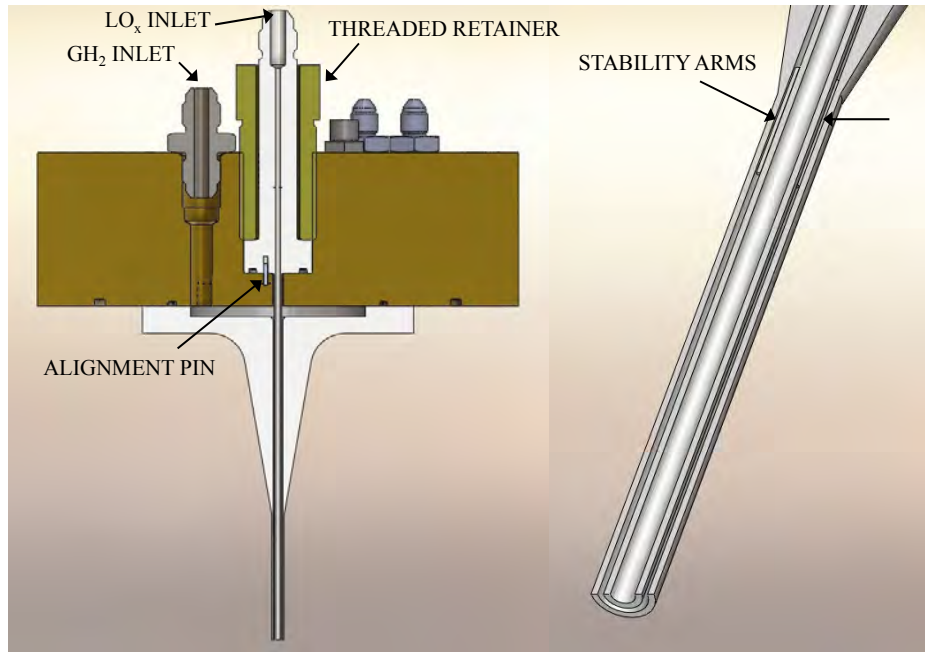
4.7: The facility's minimum achievable nitrogen temperatures for the inner and outer jets are plotted with an nitrogen density contour overlay. A vertical line and a horizontal line represent the critical temperature and pressure, respectively. Both chamber pressure and mass flow rate are controlled while temperature is measured. Flow rates of the inner and outer jets are approximately 9 g/s and 3 g/s, respectively. (\circ) Inner jet (\square) Outer jet



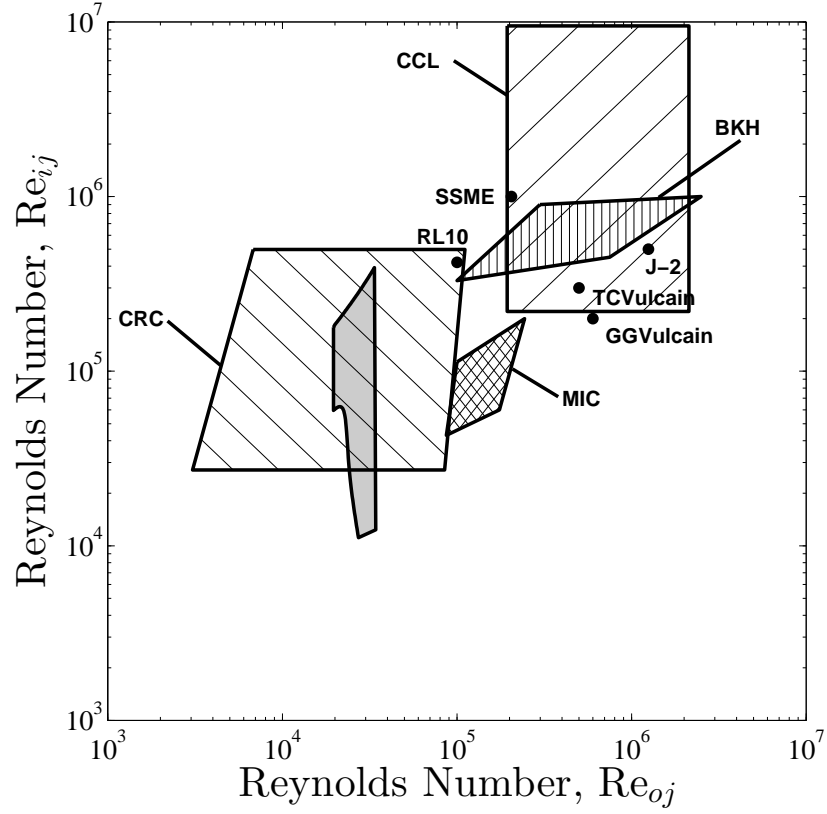
4.8: The facility's range of possible density ratios plotted versus chamber pressure for oxygen and hydrogen propellants.



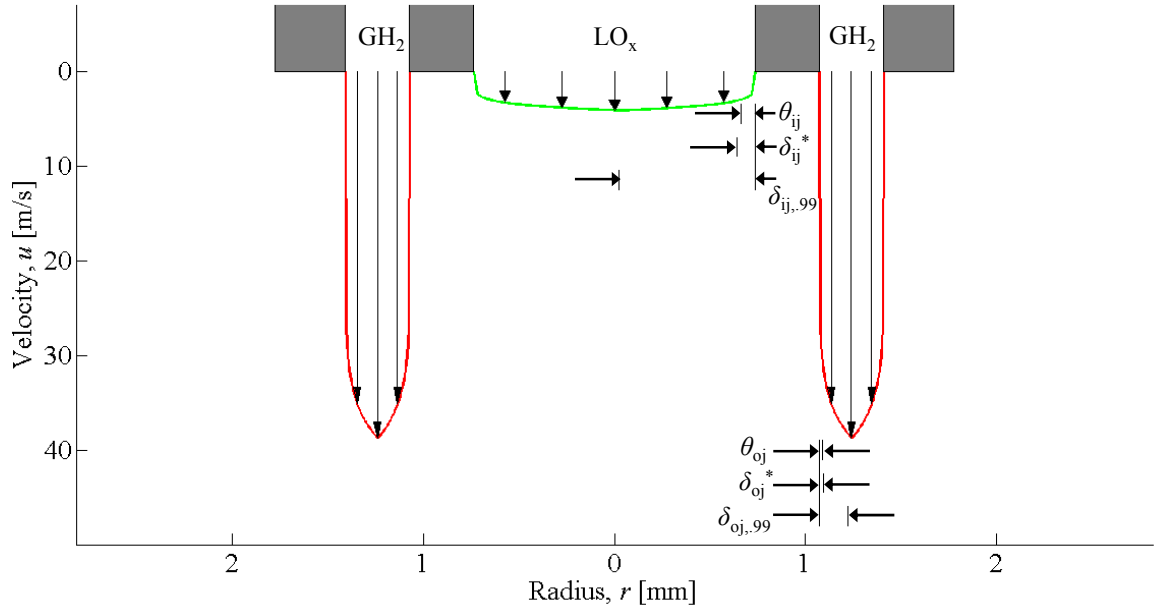
4.9: The dimensions of the coaxial injector used for new experiments in this study.



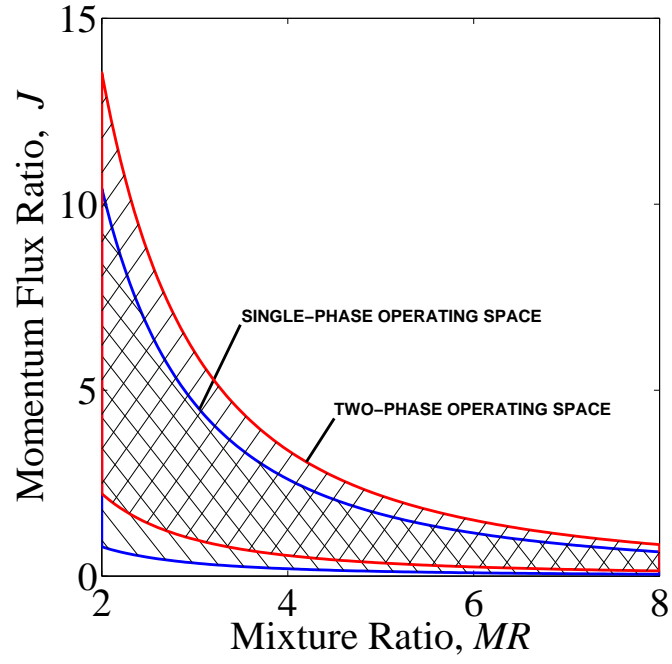
4.10: The inner injector body passes through the center of the brass top flange and is held in place using a retainer. For angular consistency between removal and re-installment, the inner injector is aligned with a dowel pin which is pressed into the top flange. To achieve concentricity between the inner and outer injectors, three stability arms are located on the outside surface of the inner tube (right). The outer injector fastens to the lower surface of the top flange, and an outer jet plenum is located between these two parts. Both the inner and outer injectors are machined from Monel 400 alloy.



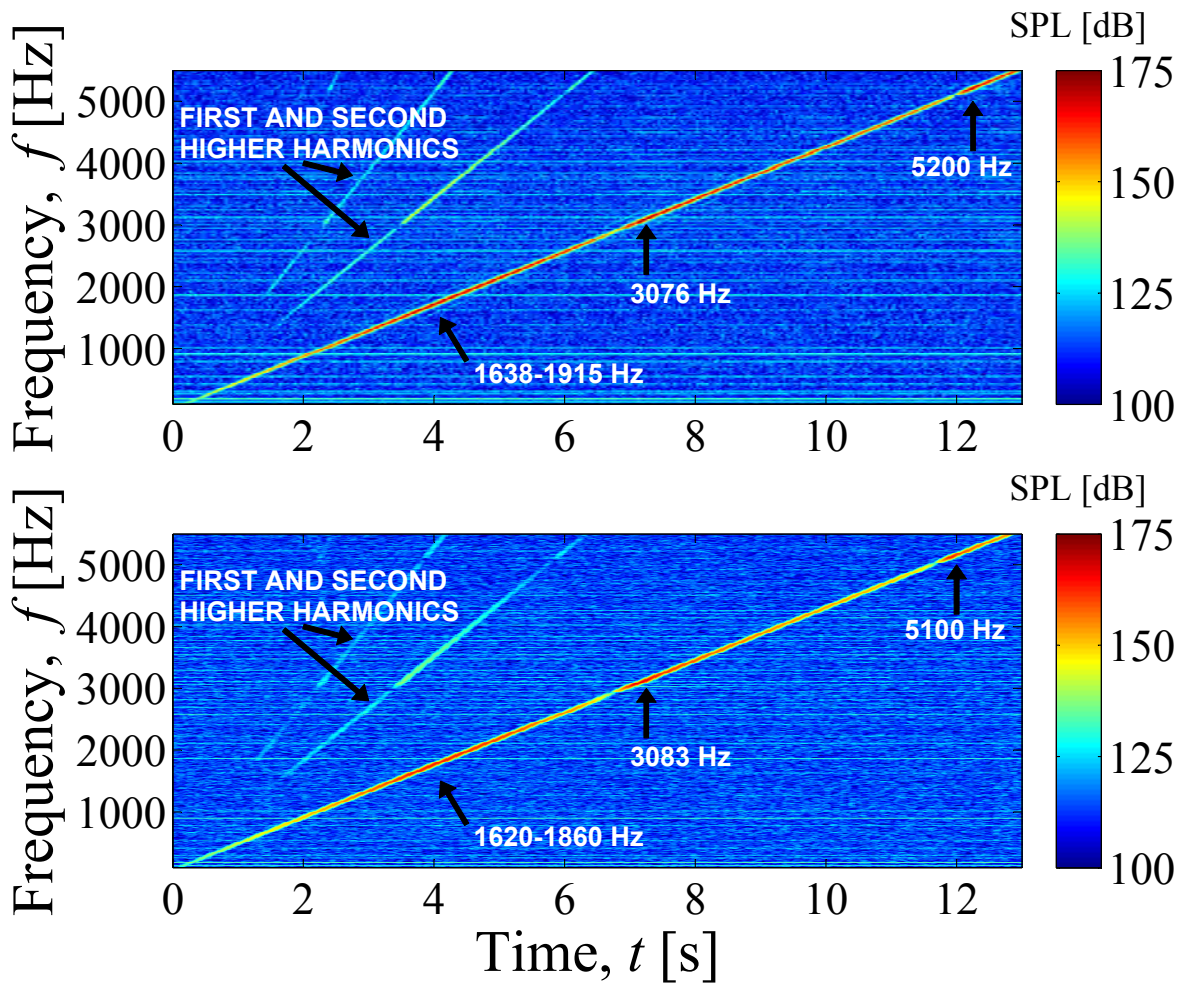
4.11: Shear-coaxial injector Reynolds numbers for the AFRL Combustion Stability Laboratory (gray) with a comparison to other experimental facilities and liquid rocket engines with H_2 - O_2 flows. Data is included for the Vulcain Gas Generator (GGVulcain), Vulcain Main Thrust Chamber (TCVulcain), RL10 engine, Space Shuttle Main Engine (SSME), J-2 engine, BKH combustor and Common Research Combustor (CRC) of DLR in Germany, Cryogenic Combustion Laboratory (CCL) of Pennsylvania State Univ., and the Multi-Injector Combustor (MIC) of ONERA and CNRS in France [8, 24, 45, 131, 159].



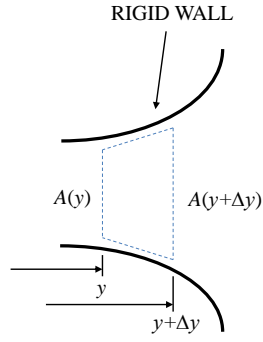
4.12: In a fully-developed turbulent flow, the exit velocity boundary layers of both the outer and inner jets are approximately equal to half the channel width. This particular diagram is an example of the fully-developed turbulent flow of gaseous hydrogen (outer jet) and liquid oxygen (inner jet) where $MR = 7$ ($\phi_{f/o} = 1.14$), $T_{oj} = T_{ij} = 145$ K, $p_c = 700$ psia (4.8 MPa), $\dot{m}_{oj} = 0.65$ g/s, and $\dot{m}_{ij} = 4.55$ g/s.



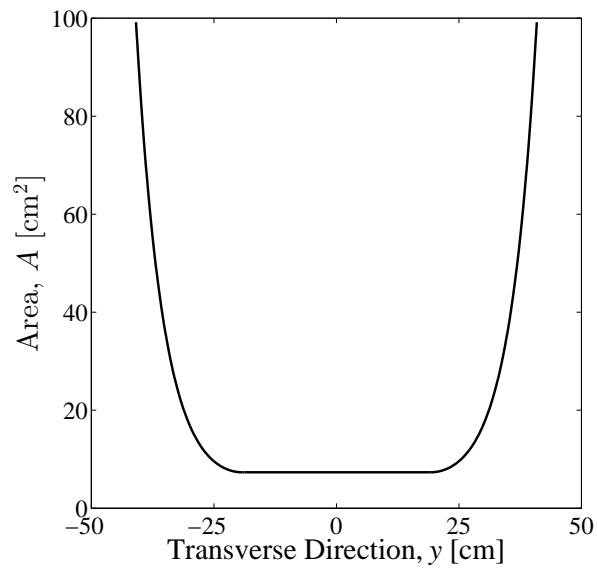
4.13: The facility's range of possible J values is best represented by a parametric map with MR . Single-phase flows ($\text{GO}_x\text{-GH}_2$) are bounded by blue lines and two-phase flows ($\text{LO}_x\text{-GH}_2$) are bounded by red lines. For reference, the stoichiometric condition for oxygen-hydrogen combustion occurs at $MR = 8$ and the fuel-oxidizer equivalence ratio $\phi_{f/o}$ for $MR = [2, 4, 6, 8]$ is $\phi_{f/o} = [4, 2, 1.33, 1]$.



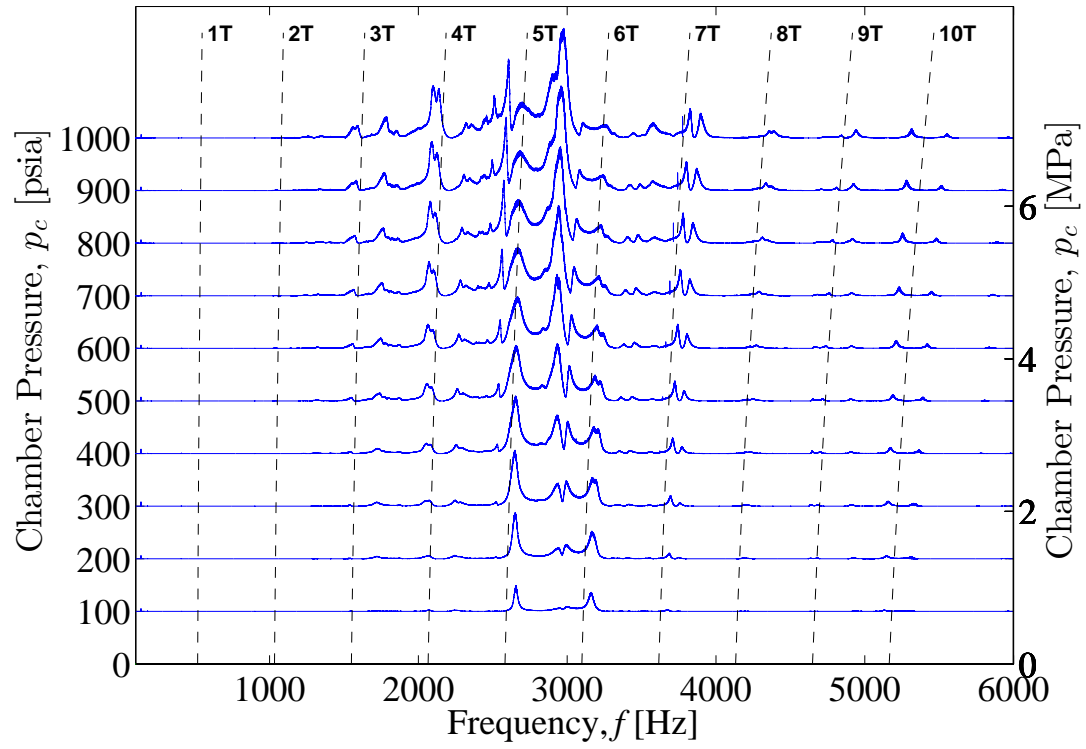
4.14: Acoustic pressure spectra results for the left piezo siren (top) and the right piezo siren (bottom). Magnitude is scaled with a sound pressure level (SPL) colormap, and key regions of piezo siren efficiency are annotated.



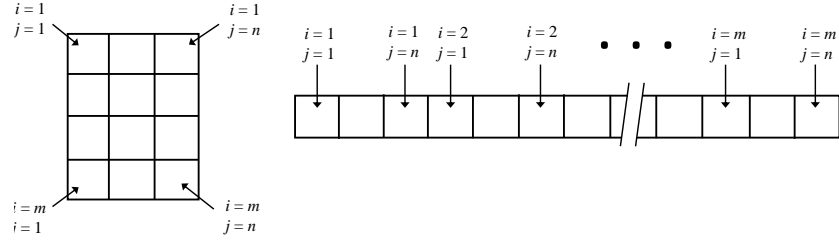
4.15: Area is a function of the transverse coordinate y , and this function is optimized for the design of acoustic waveguides such that wave amplitudes in the x and z directions are minimized while maximizing amplitudes in the y direction.



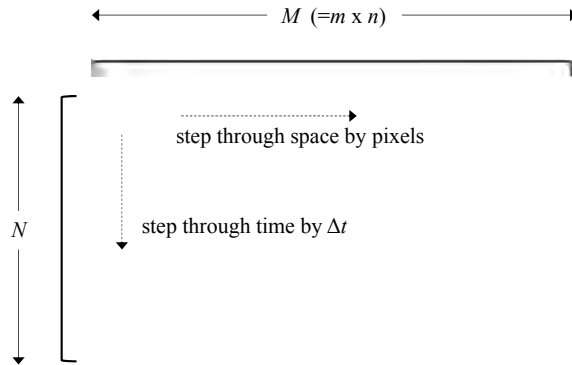
4.16: The left and right waveguides were fabricated according to the area distribution of a catenoidal horn [151]. The waveguides reduce a circular area of 99.18 cm^2 to a rectangular area of 7.33 cm^2 to match the inner chamber. The piezoelectric sirens are located at ± 40 cm.



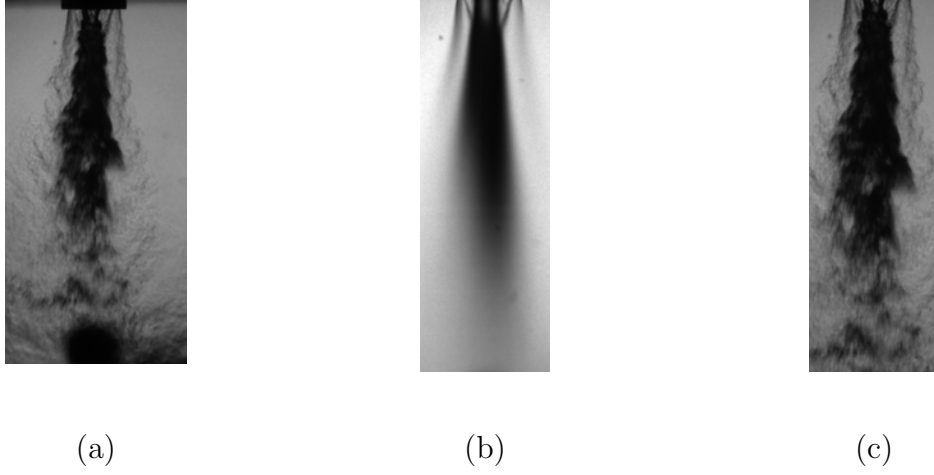
4.17: Acoustic frequency sweep results are plotted as power spectral density for PAN conditions at chamber pressures ranging from 100 to 1000 psia (6.9 MPa). Transverse modes 1T through 10T are identified with theoretical lines which transcend to higher frequency as the chamber pressure increases.



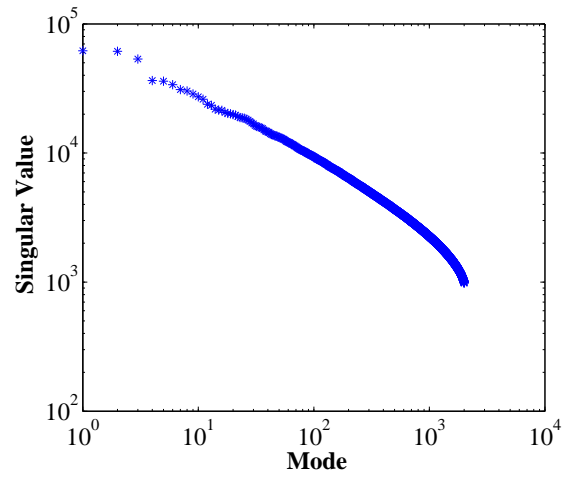
4.18: A single row of matrix \mathbf{A} constructed from an $m \times n$ image for POD analysis.



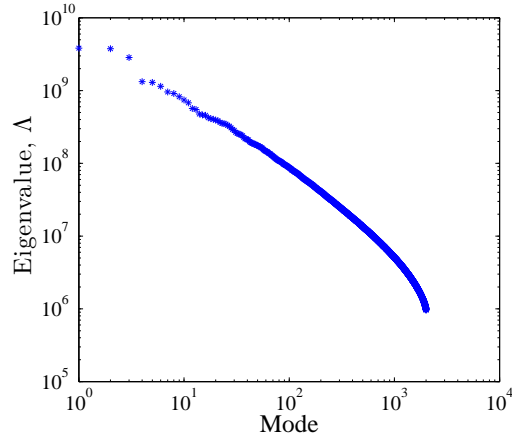
4.19: Prior to applying the POD algorithm, a complete set of images was conditioned to form a single data matrix \mathbf{A} using N images and M pixels. Each row of \mathbf{A} was formed by appending consecutive rows from the top row of pixels to the bottom row of pixels.



4.20: Sample images of a LN₂-GHe shear-coaxial jet for $J = 6$ without acoustic forcing. (a) instantaneous image (b) time-averaged image (c) cropped image used for data processing



4.21: Singular values for an acoustically forced LN₂-GHe jet with $J = 2$ and $f_F = 2050$ Hz at a PN.



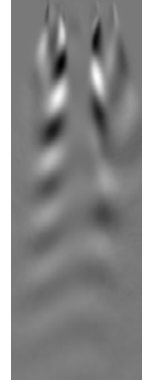
4.22: Eigenvalues for an acoustically forced LN₂-GHe jet with $J = 2$ and $f_F = 2050$ Hz at a PN. $\Lambda = \sigma^2$



(a)

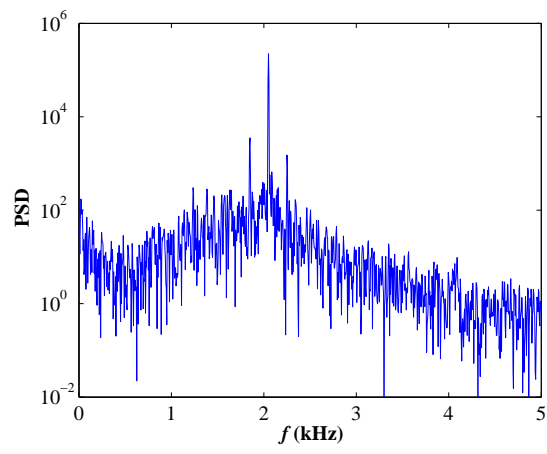


(b)

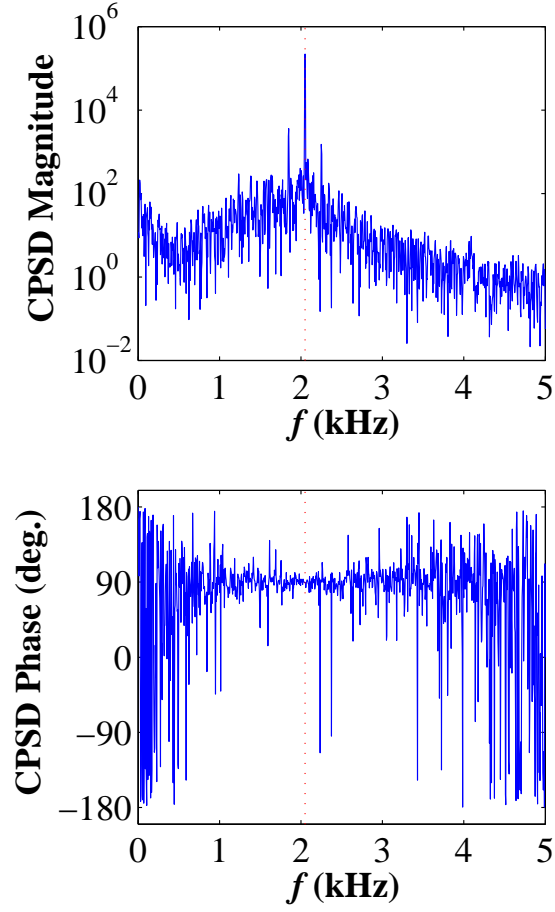


(c)

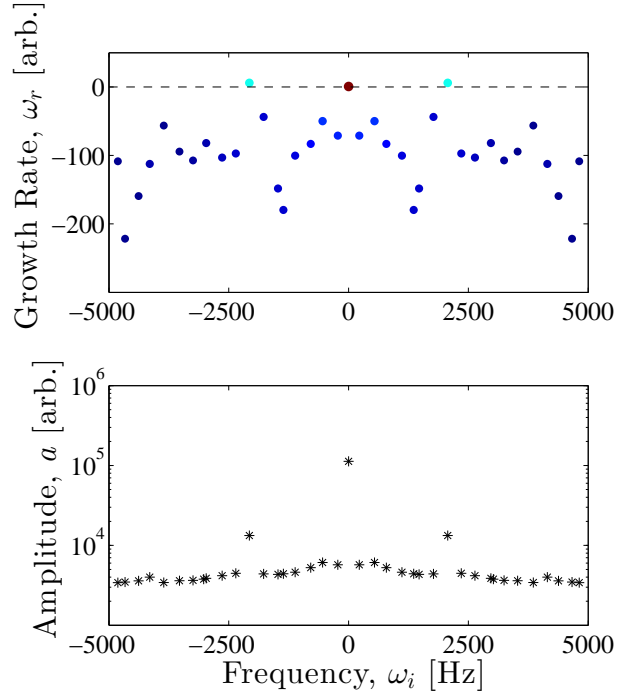
4.23: A snapshot of an acoustically forced LN₂-GHe jet with $J = 2$ and $f_F = 2050$ Hz at a PN is shown in (a), and reconstructed POM images are shown for POD (b) mode-1 and (c) mode-2.



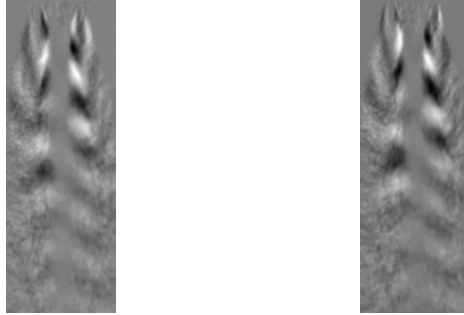
4.24: Power spectral density for mode-1 for an acoustically forced LN₂-GHe jet with $J = 2$ and $f_F = 2050$ Hz at a PN.



4.25: Cross power spectral density magnitude (top) and phase (bottom) for POD mode-1 and mode-2 for an acoustically forced LN_2 -GHe jet with $J = 2$ and $f_F = 2050$ Hz at a PN. The vertical red line located at $f = 2050$ Hz represents the characteristic instability frequency for this condition.



4.26: Top: Real eigenvalues ω_r (growth rate) and imaginary eigenvalues ω_i (frequency) plotted for DMD results computed for an acoustically forced LN₂-GHe jet with $J = 2$ and $f_F = 2050$ Hz at a PN. Each point represents a single mode identified by DMD, and the color and size of each point is scaled with the amplitude of each mode as calculated using eqn. 4.49. Bottom: Mode amplitudes plotted versus ω_i .



4.27: The DMD eigenvectors ϕ_r (left) and ϕ_i (right) for the unstable mode identified by cyan color in Fig. 4.26. $\lambda_i = f_F = 2050$ Hz

CHAPTER 5

Results - Shear-Coaxial Jets

5.1 Qualitative Observations of Liquid Nitrogen-Gaseous Helium Shear-Coaxial Jets

Prior to establishing quantitative conclusions from high-speed imaging results, several key qualitative observations must be mentioned. Figure 5.1 demonstrates many shear-coaxial jet features in a single snapshot, and a reduced field of view is used to increase the clarity of structures near the injector exit. Phenomena previously observed in other research studies appear in this snapshot, and are described below in order to bring to light the possible sources of shear-coaxial jet instability.

At the exit of the injector, a recirculation zone is easily distinguishable. Moving in the radial direction from the center of the jet, one first observes an interface between the liquid nitrogen inner jet and the recirculation zone formed between the inner and outer jets. This feature is labeled as (1) in Fig. 5.1. The width of the recirculation zone is equal to the inner post thickness t at the exit of the injector and converges to zero as the recirculation zone extends downstream. The recirculation zone results from a finite inner post thickness, separating the near-field features of this geometry from that of classical co-flowing streams ($t = 0$) commonly used in linear stability theory [10, 121] and other experimental studies of coaxial jets and shear layers. Note that a different injector geometry or range of flow conditions will result in a recirculation zone shape different from that observed here. Earlier work at AFRL has more thoroughly

explored the influence of t and the behavior of the recirculation zone [23, 81, 104] in nonreactive coaxial jets. As discussed earlier, when a finite value of t is used, the stability computations of Talamelli and Gavarini [108] predict not only that a wake instability can be produced, but also that the wake instability will be absolutely unstable for a small but nonzero wake velocity. Although wake velocity estimations are not included in this study and the results of Talamelli and Gavarini may not be directly applied, the existence of a recirculation zone gives potential for absolute instability.

Farther out in the radial direction, an outer shear layer is identified between the gaseous helium outer jet and the surrounding gaseous nitrogen. Although this interface is less distinguishable in analogous LN₂-GN₂ jet experiments [23, 29], the LN₂-GHe jet shown in Fig. 5.1 reveals significant contrast between the light outer jet and the more dense ambient nitrogen ($\rho_c \approx 7\rho_{oj}$). At this interface, an outer shear layer instability is formed. Since the outer and inner jets are fully turbulent at the exit, this would generally be expected to disrupt the coherence of large-scale structures in the shear layers. Early experimental conclusions by Ko and Kwan [88] found the outer shear layer to take on a different wavelength and instability frequency than those of the inner shear layer, and two different St definitions were used accordingly for the inner and outer shear layers. Far downstream, the shear layers interact and merge, but they behave as isolated shear layers near the exit, as described by the separate St definition of Ko and Kwan. In support of defining a unique scaling law for each shear layer, preliminary POD analysis of LN₂-GHe jets also indicates different instability frequencies exist in each shear layer. This study focuses on the inner shear layer due to its direct relevance to fuel-oxidizer mixing and unsteady heat release, but a low-density outer jet provides the ability to track the outer shear layer with high-speed imaging, which is a valuable feature for future work.

Immediately downstream of the recirculation zone, a dynamic interface forms be-

tween the inner and outer jets. This interface, labeled as (4) in Fig. 5.1, is the most important feature of the jet for this particular set of experiments due to its importance in inner jet atomization and mixing. This region may be called the mixing layer or the inner shear layer, and the latter term is used here for continuity with other works. The extreme contrast between the liquid inner jet with $\rho_{ij} \approx 500 \text{ kg/m}^3$ and the light outer jet with $\rho_{oj} \approx 5 \text{ kg/m}^3$ makes for straightforward image analysis because pixel intensity gradients are most steep at the inner shear layer. Near the end of the recirculation zone, the inner shear layer appears as well-defined interfacial waves. Further downstream, the shear layer thickness increases and these waves develop into vortices. A vortex may form a ligament and break away from the dark core of the inner jet, or remain attached until reaching the end of the dark core ($x = L_b$) where large clumps and ligaments break up in the fully-merged zone. As will be shown by reduced basis methods results, these events occur within a broadband of frequencies accompanied by random noise, but a single characteristic frequency is adopted as the most significant natural instability.

An important observation was also made regarding jet symmetry. When viewing time-averaged images such as that in Fig. 4.20b, asymmetry is seen in the dark core. Upon close inspection of the injector, it was concluded that the observed jet asymmetry results from a lack of concentricity between the inner and outer streams either at the injector exit or in the upstream pathways of the injector. Following a series of efforts to achieve a perfectly symmetric jet, it was concluded that injector hardware adjustments were only sufficient to improve symmetry, but not completely eliminate the problem. Concerning application to LREs, injector asymmetry is considered a challenge, especially for propellant injection systems with dozens of injectors subject to high-volume manufacturing. Manufacturing variability is a likely cause of unpredictable behavior in LREs. Concerning the present research study, small asymmetries may be deemed acceptable if unavoidable and if asymmetric jet structures do not disrupt behaviors relevant to the scientific conclusions of the study. To this end, a verification test was performed to

inspect instability frequencies for the right and left sides of the jet. This study focused specifically on natural instability frequencies determined by POD, and compared f_{nat} for the mixing layer on the left side of the image with f_{nat} for the mixing layer on the right side of the image. For the range of conditions used in this study, the frequency difference was less than 80 Hz and the broadband spectra of each natural mode inhabited approximately the same range of frequencies. (The band of naturally excited frequencies was approximately 200 Hz, and was always found within the range from 720 Hz to 1140 Hz.) It was concluded that differences in spectral behavior are small, and further, these differences are not expected to have a significant effect on the susceptibility of the jet to external acoustic forcing. Future injector configurations should explore improved techniques for maintaining concentric inner and outer injectors without sacrificing the desired injector geometry, but the current injector configuration was accepted for this test campaign.

The natural instabilities of nonreactive shear-coaxial jets discussed above are subject to intense study due to their relevance to coaxial jet flames. As shown in Fig. 5.2, an unforced O₂-H₂ coaxial jet produces pockets of intense heat release rather than an evenly distributed flame. The images shown in Fig. 5.2 represent chemiluminescence of electronically excited OH radicals captured by blocking visible wavelengths using an optical bandpass filter. The bandpass filter was centered near 308 nm, which is the wavelength of peak radiation for OH* chemiluminescence. As discussed in chapter 2, OH* chemiluminescence is a good indication of heat release. Thus, from the sequence of high-speed images in Fig. 5.2, one can conclude that an unforced O₂-H₂ flame produces heat release which is highly dependent on both time and space, and which may experience natural acoustic coupling and/or absolutely unstable shear layer behavior [118] even in the absence of external excitation. Although the qualitative scientific conclusions of this study are limited to nonreactive jets, this sample of high-speed flame images reinforces the need to research naturally occurring instabilities in coaxial jets.

5.2 Comparisons of POD and DMD

Both proper orthogonal decomposition and dynamic mode decomposition are employed to extract organized structure from the visualization data. Although this study applies DMD to coaxial jet images for the first time, both methods have been used for a number of nonreactive and reactive experimental flows where optical techniques are the primary diagnostic tool. The following comparison weighs the advantages and disadvantages of each method such that future application of these methods may be done with specific limitations in mind.

To start the comparison, an argument should be made regarding simplicity. Although the derivations and procedures included in chapter 4 include lengthy details, the resulting code for both POD and DMD can be straightforward. In particular, POD is easier to implement in several ways. When written using singular value decomposition, the mathematical steps of POD are not as complicated as DMD, and creating a POD algorithm simply requires subtracting the time-averaged image from the image set and performing a SVD of the resulting image set. Alternatively, DMD requires separating the image set into \mathbf{A}_1^{N-1} and \mathbf{A}_2^N , performing a SVD of \mathbf{A}_1^{N-1} , calculating the approximate mapping $\tilde{\mathbf{S}}'$, solving the eigenvalue problem of $\tilde{\mathbf{S}}'$, and finally one must use the eigenvalues and eigenvectors to calculate useful frequencies and mode shapes. This lengthy procedure is caused by a more extensive mathematical derivation, and results in DMD codes which are several steps longer than their POD counterpart. In addition, DMD requires more computational time. Using MATLAB, for example, several thousand images can be decomposed with POD in tens of minutes, but with DMD, the same image set will require hours. If instead only a few hundred images are deemed necessary to reconstruct the important modes, then either algorithm can be completed in minutes. But, interpreting the results of each tool brings to light more important differences between POD and DMD.

The most evident difference between POD and DMD is the solution of multi-frequency versus single-frequency results. Proper orthogonal decomposition describes the temporal dynamics of a mode using frequency spectra, whereas DMD represents each mode with a single frequency [152]. Dynamic mode decomposition is more advantageous in this regard. To identify the frequency of a coherent instability, the cross power spectral density from POD obfuscates the mode of interest by including magnitudes for an entire array of frequencies. Figure 5.3 shows the cross power spectral density magnitude and phase for the natural POM pair of an unforced condition at $J = 6$. The vertical red line in Fig. 5.3 is the frequency which best represents the natural mode, because this frequency has the greatest magnitude for a phase near 90° . Thus, this POM pair has a characteristic frequency of 945 Hz and is conjugate according to phase. But, this POM pair exhibits a broadband nature. The spectrum of the natural mode is broadband, and the POM pair also includes the energy of broadband turbulence, or noise, at higher frequencies. Thus, although cross power spectral density calculations were used to determine a single characteristic frequency for the dominant POM pair, each POM encompasses an array of frequencies by definition. Correctly pairing POMs and labeling pairs with a single characteristic frequency is a process which allows for user error in choosing two POMs to make a pair, and again allows for error when determining a single frequency from spectra. Some conditions pose more difficulty than the condition shown in Fig. 5.3. Several cases produced POMs which were particularly challenging to interpret, because a combination of natural and acoustically forced peaks created a spectra of “mixed” modes in a single POM. Dynamic mode decomposition, on the other hand, represents each mode with a single frequency.

As mentioned above, one disadvantage of POD lies in the potential error which results from choosing a pair of conjugate modes to form a single, physical mode. This issue is particularly relevant for unforced conditions or conditions with low levels of forcing, where the natural mode is the most dominant shear layer mode. In such a case,

although the natural mode variance is greater than that of lower ranked modes, the variance contribution is not as large as a forced mode variance contribution from high amplitude acoustic forcing, for example. Figure 5.4 shows a plot of the eigenvalues for the POD modes of an unforced jet; this plot represents the same condition as Fig. 5.3. With the exception of mode-1, there is a gradual decrease in the eigenvalue when viewing the log-log scale in Fig. 5.4. Remember, the eigenvalue of a single mode is proportional to the pixel intensity variance of that mode, as determined by POD ($\Lambda = \sigma^2$). For a very strong natural mode, a mode *pair* would appear with significantly higher eigenvalues which separate the coherent natural mode from other less significant modes. Instead, Fig. 5.4 shows only a single mode with a very large eigenvalue, and this mode merely contains low frequency (<5 Hz), steady-like motion without a conjugate mode pair. Although a coherent natural mode exists, this natural mode did not exhibit particularly strong dominance over other background modes and noise, making it challenging to identify the natural POM pair. One is left to analyze modes two and higher in search of a conjugate mode pair, rather than simply choosing a pair of highly ranked modes which stand out in an eigenvalue plot, such as mode-1 and mode-2 for the acoustically forced case in Fig. 4.22. For the experiments in this study, broadband turbulence contributes a significant amount of energy to the flow field of unforced jets, making the natural mode less distinctive.

In addition to eigenvalue plots, one must also utilize the eigenvector images and the power spectral density for each mode when searching for the conjugate mode pair. As an example, Fig. 5.5 displays the twelve highest ranked eigenvector images for the same unforced condition as Figs. 5.3 and 5.4. The POM ranking is based on eigenvalues, and therefore, is a ranking based on the variance content of each POM as defined using pixel intensity fluctuations from high-speed images sets. Since any mode pair creating a significant pixel intensity variance will be found within the highest ranked modes, Fig. 5.5 will contain the natural mode distributed between two images which have lobe

structures 90° out-of-phase in the direction of convection. The user must find the natural mode pair among these twelve POMs, as opposed to using the twenty highest ranked modes, for example. For the conditions of this study, exploring more than twelve modes was shown to consistently decrease efficiency without altering results. Although mode-1 and mode-2 contain the highest variance contribution, their eigenvector images in Fig. 5.5 do not show flow structures which are 90° out of phase, from simple qualitative inspection. Mode-1 and mode-2 represent two different phenomena. In fact, mode-1 represents low frequency (≈ 5 Hz) jet flapping, rather than a mixing instability. Mode-3 and mode-4, on the other hand, look very similar in lobe structure. Both contain a slightly antisymmetric inner shear layer instability manifested as dark and light lobes and mode-4 appears to be slightly shifted from mode-3. Indeed, these two modes share the same peak frequency, whereupon the pair has 90° phase difference. The PSD and eigenvector images for both mode-3 and mode-4 are shown side by side in Fig. 5.6. Upon reaching this conclusion, modes 5 through 12 need not be inspected for this particular case. Mode-3 and mode-4 represent the natural instability for $J = 6$ at $f_{nat} = 945$ Hz, and although secondary coherent modes may lie in modes 5 through 12, any other modes produce less pixel intensity variance and leave 945 Hz as the most significant natural instability in the jet. Further, a mode with a high pixel intensity variance is presumed to be a mode having a high energy contribution to the flow. A more difficult case requires CPSD inspection of many mode pairs in order to determine the natural instability mode pair. Clearly, this conclusion required thorough inspection and post-processing of the initial POD results.

In comparison, DMD does not require the pairing of modes in post-processing. Rather, the real and imaginary eigenvectors are inherently 90° out of phase, as was shown in Fig. 4.27, for example. As discussed earlier, the dynamic mode decomposition allows eigenvectors and eigenvalues to be negative and complex, whereas proper orthogonal decomposition constrains these matrices to be real and non-negative by en-

forcing orthogonality in \mathbf{V} . In DMD, the eigenvectors stand alone as coherent modes by containing both real and imaginary components within a single dynamic mode Φ which is tied to a single frequency ω . For this reason, many recent demonstrations of DMD [152, 156, 157] support the use of DMD in place of POD because instability information is often not known *a priori*, and one cannot discern the appropriate pairing of conjugate modes. This study supports the same conclusion.

Finally, for the same unforced condition presented in Figs. 5.3 - 5.5, DMD results are shown in Fig. 5.7. The x -axis is the frequency ω_i in Hertz while the y -axis is the growth rate ω_r and the amplitude a for the upper and lower plots, respectively. Each point in Fig. 5.7 represents a single mode which could be visualized by real and imaginary eigenvector images. As stated earlier, since the mean is not subtracted from the image set prior to implementing DMD, then the highest amplitude is a point at $\omega_i = 0$, which represents the mean. A point at $[\omega_i, \omega_r] = [0, 0]$ also represents the mean flow. Otherwise, significant amplitudes are not observed for any other modes. A significant amplitude could be expected at a frequency near f_{nat} , but obvious peaks in amplitude do not exist. Fig. 5.7 should also be compared to Fig. 4.26, where peak amplitudes were observed for an acoustically forced condition. For an unforced condition though, DMD is unable to clearly identify the significant amplitude of a natural mode for the conditions investigated here. If the natural mode consisted of a larger portion of the aggregate flow energy then perhaps a high value of a would be observed near f_{nat} , but such a condition does not exist for the current test matrix. This may be interpreted as an advantage of POD, whereby a mode characterized by a broadband peak from 800 to 1000 Hz is indiscernible in the single frequency dynamics of DMD, but the same natural mode is captured by a POD mode with broadband spectra. Further analysis is recommended prior to concluding that DMD cannot identify coherent structures with broadband frequencies.

In conclusion, the added complexity of DMD offers an algorithm better suited for identifying the dynamic modes in experimental image data. The *individual* modes of POD do not offer dynamic information, but only mode shapes. The eigenvectors of POD only contain a real component. The complex form of the eigenvectors of DMD inherently contains real and imaginary components which describe a single mode with two different points in phase, thus providing dynamic information regarding a single mode. Additionally, this mode is represented by a single frequency, making DMD more useful for experimental studies seeking to compare the amplitudes of different instability frequencies rather than compare the energy of complete frequency spectra, which includes random turbulence and background noise. When input data is in the form of experimental images, background turbulence is expected for high Re coaxial jets of this kind, and will indeed contribute to the result. Further investigation is needed to determine the proper technique for analyzing this flow regime. If the natural mode of interest is broadband, POD may be preferred in order to capture the complete spectra. Detailed refinement of the user inputs may also improve the performance of both DMD and POD. For example, noise filters may be applied as a pre-processing step or an ideal number of images may be shown to optimize identification of real flow dynamics. POD was sufficient for the objectives of this study, but a future implementation of DMD may offer more clarity to the results.

5.3 Susceptibility of Nitrogen-Helium Shear-Coaxial Jets to Acoustic Forcing

Utilizing the proper orthogonal decomposition, nonreactive shear-coaxial jet results are analyzed with respect to three variables at both a pressure antinode (PAN) and a pressure node (PN). These variables are the acoustic forcing amplitude, nondimensional forcing frequency $F = f_F/f_{nat}$, and outer-to-inner jet momentum flux ratio J . Low

and high values of J are used. An effort is made to separately investigate the influence of each of these variables on the susceptibility of jets to external acoustic forcing. Specifically, for a given F and J , how will the jet respond to various amplitudes of acoustic forcing? What is the critical forcing amplitude required for the forced mode to overtake the natural mode and become the most dominant jet instability? If J is altered, will the critical forcing amplitude change? A test matrix which aims to answer these questions requires isolated control of each variable. In order to achieve this, unforced jets were first characterized for a range of flow conditions.

5.3.1 Unforced Shear-Coaxial Jets

To explore the influence of momentum flux ratio on shear-coaxial jet instabilities, the values $J = 2$ and $J = 6$ were chosen to span a range which is applicable to LREs and comparable to J values in analogous $\text{O}_2\text{-H}_2$ combustion experiments. To best isolate the effects of J , the dimensionless forcing frequency F should be held constant while J is varied. For the present experiments with limitations on applied frequencies associated with standing wave conditions, for a given set of acoustic forcing frequencies, the natural jet frequency f_{nat} for $J = 2$ would optimally be equal to that of $J = 6$. This is particularly challenging, because altering J requires a change in the velocities of the inner jet, outer jet, or both. Thus, shear layer instabilities may adopt different natural frequencies as a result of a modified velocity step $U_{oj} - U_{ij}$ and shear layer convective velocity U_c . Since F is dependent on f_{nat} , individually controlling J and F is challenging.

If the jet adopts a single value of St , as in the work of Birbaud *et al.* [107], Ko and Kwan [88], and others [83, 86, 87, 106], then St can be used to predict f_{nat} . When choosing characteristic velocity and length scales to define St , one must be mindful of the source of instability in a way similar to Ko and Kwan [88]. As done in eqns. 1.14 and 1.15, a Strouhal number which scales with an outer shear layer instability could

be defined with $D_h(=D_3 - D_2)$ and U_{oj} , for example. Conversely, a Strouhal number which scales with an inner shear layer instability should use a smaller diameter, such as D_1 , and velocities such as U_{ij} or $(U_{ij} + U_{oj})/2$, which better characterize the inner shear layer region. As shown by works in linear stability theory [10, 121], a change in jet velocities or densities is likely to produce a change in f_{nat} . Thus, to use St as a tool for predicting f_{nat} of the inner shear layer the characteristic definition of St must account for the velocities *and* densities of both the inner and outer jets. Consequently, the shear layer convection velocity of eqn. 1.10 from Dimotakis [89] was chosen as a characteristic velocity for defining St and will be labeled as $U_{c,th}$ hereafter. The formula is included here for convenience.

$$U_{c,th} = \frac{U_{ij}\rho_{ij}^{\frac{1}{2}} + U_{oj}\rho_{oj}^{\frac{1}{2}}}{\rho_{ij}^{\frac{1}{2}} + \rho_{oj}^{\frac{1}{2}}}. \quad (5.1)$$

The dramatically different densities of liquid nitrogen and gaseous helium are included as ρ_{ij} and ρ_{oj} , respectively. By including ρ_{ij} and ρ_{oj} , the shear layer convection velocity better characterizes the present set of experiments. This approach aims to describe the velocity of inner shear layer instabilities represented by vortices which are observed as the most significant structures in the mixing region. For an isodensity shear layer, the convection velocity may be approximated by velocities alone. For example, the mean velocity $U_M = (U_{ij} + U_{oj})/2$ is a more appropriate approximation of U_c in that case, which is found by simply applying eqn. 5.1 for $\rho_{oj} = \rho_{ij}$. Instead, the two-phase flows of interest here ($\rho_{ij} \approx 100\rho_{oj}$) are expected to produce shear layer convection velocities dependent on the density difference as well as the velocity difference. Equation 5.1 is presumed to be an appropriate velocity scale if indeed the natural jet instability frequency matches that of the inner shear layer rather than another source of instability, e.g. the outer shear layer. If the preferred mode of the jet is produced at the outer shear layer or the wake of the recirculation zone, then a different definition of St will be required.

Finally, a definition of St requires a characteristic length scale. Again, to define St for natural jet instability which originates at the inner shear layer, the characteristic length scale is chosen to be approximately equal to the diameter at which the inner and outer jet meet. The exact location at which the outer and inner streams meet is dependent on flow conditions, thus an approximation is required. This characteristic length scale is taken as the average of the inner and outer diameters of the inner injector, D_1 and D_2 , respectively, i.e.

$$D_{eff} = \frac{D_1 + D_2}{2}. \quad (5.2)$$

Traditionally, the most important length scale in shear layer instability is the shear layer thickness at the trailing edge, which is dictated by boundary layer thickness at the injector exit. For the present experimental conditions though, fully developed turbulence creates a boundary layer thickness which is approximately equal to the jet radius, making the diameter an appropriate length scale for this particular St definition. The Strouhal number is then defined as

$$St = \frac{f_{nat} D_{eff}}{U_{c,th}}. \quad (5.3)$$

With the assumption that this experimental configuration manifests a constant, preferred value of St for the unforced jet, this scaling law is used to predict f_{nat} values which will be adopted in experiments at $J = 2$ and $J = 6$. In principle, f_{nat} can be controlled by $U_{c,th}$ as one moves from $J = 2$ to $J = 6$.

The validity of this experimental approach and the assumption of constant Strouhal number is assessed by plots in Figs. 5.8 and 5.9. First, a plot of natural frequency versus $U_{c,th}$ is shown in Fig. 5.8. The values of f_{nat} , as determined by the most dominant POM pair, are shown to increase with $U_{c,th}$ as expected. A series of experiments were conducted for $U_{c,th} \approx 6$ m/s which produced $f_{nat} \approx 1$ kHz, and four additional cases were conducted for $U_{c,th} \approx 12$ m/s which produced a range of f_{nat} from 2 kHz to 3 kHz. More importantly, one must note that half of the points in Fig. 5.8 have a nominal

momentum flux ratio of $J = 2$, while half possess a nominal value of $J = 6$. Specifically, $U_{c,th}$ was held constant at 6 m/s while adjusting both the inner and outer jet velocities to achieve $J = 2$ and $J = 6$. This step was repeated for $U_{c,th} \approx 12$ m/s. Refer to appendix A for a table of results for all cases. Due to the repeatability achieved at 6 m/s, this condition was chosen for all acoustically forced flow conditions presented in the following section, where f_{nat} , and thus F , can be held constant while isolating the effects of J on the susceptibility of jets to acoustic forcing.

For the same data as in Fig. 5.8, a plot of St versus J is shown in Fig. 5.9. Although the collection of points has a calculated mean Strouhal number of 0.30, there is a significant amount of scatter, especially among cases where $U_{c,th} \approx 12$ m/s. Therefore, $St = 0.30$ may be a reasonable constant for the preferred mode, but an improved estimate of a characteristic velocity may reduce scatter in St and increase accuracy when predicting f_{nat} .

To test the validity of eqn. 5.1, shear layer convection velocities were experimentally measured via image analysis. Consider an array of pixels shown by the green curve in Fig. 5.10. The set of pixels along the green curve are chosen to represent the inner shear layer region, where vortices are located on the outer edge of the dark core. For a single pixel lying on the green curve, the pixel intensity will oscillate from low (dark) to high (light) as a pocket of dense fluid leaves the area. The oscillating behavior will continue as vortices pass this point in space over a duration in time. When the entire green curve is considered rather than a single point, then vortices will transcend through the array of pixels, creating areas of dark and light pixels which move in time. Fig. 5.11 demonstrates this concept. On the y -axis the shear layer curve coordinate s is nondimensionalized by D_1 , while the x -axis is time in milliseconds. A diagonal streak illustrates the convection of inner shear layer vortices, or waves, which begin near the injector exit and travel downstream as time advances from one image to the next, and so on. Very close to

the injector, $\frac{s}{D_1} \approx 1$, a dark horizontal bar in Fig. 5.11 results as the signature of the end of the recirculation zone. The convection velocity upstream of this dark horizontal feature is less than the shear layer convection velocity downstream of the recirculation zone, where the much faster outer jet meets the inner jet. The streaks which appear at $\frac{s}{D_1} > 1$ are of interest here. The slope of a single streak, $\Delta s / \Delta t$, is the velocity of the coherent structure represented by the streak. To make an experimental estimate of the shear layer convection velocity $U_{c,meas}$, a collection of eight structures represented by dark diagonal lines in Fig. 5.11 were randomly chosen and their velocities were averaged to find a single estimate of $U_{c,meas}$ for each experimental condition.

Fig. 5.12 shows a plot of the experimental and theoretical convection velocities. For reference, a dashed line is plotted for $U_{c,meas} = U_{c,th}$. For low convection velocities, $U_{c,th}$ is an excellent approximation of the actual velocity. For a limited amount of data acquired for higher convection velocities though, $U_{c,th}$ under-predicts the velocity which is actually observed. This discrepancy may explain the scatter observed in St when defined using $U_{c,th}$. To confirm this, Fig. 5.13 shows a plot of St versus J using only experimentally measured values. The deviation previously caused by low estimates of U_c has been reduced, and the preferred mode of $St = 0.30$ is seen for both $J = 2$ and $J = 6$. Although Crow and Champagne [106] investigated single jets, they also observed a preferred mode of $St = 0.30$. This mode identified by their measurements may be analogous to the natural instability observed in this study, be it with different velocity and length scales used to define St . Further inspection would be required to reach a conclusion in this regard. Regardless, the LN₂-GHe shear-coaxial jet maintains a preferred instability scaling of $St \cong 0.30$ for the range of flow conditions explored in this study, and may be used to predict the most dominant natural jet instability frequency when an accurate inner shear layer convection velocity is used.

5.3.2 Shear-Coaxial Jets Subject to Acoustic Forcing

To explore the influence of acoustic forcing amplitude, nondimensional forcing frequency, and momentum flux ratio, results are organized to portray two important concepts. First, similar to lock-in diagrams created in Getsinger *et al.* [122] and Sreenivasan *et al.* [123], diagrams will be used to show the minimum forcing amplitude required for the natural instability of a given flow condition to be overtaken by external acoustic forcing. Second, the same diagrams will quantify the significance of the forced mode via the forced mode pixel intensity variance contribution Ψ as determined by eqn. 4.25. Two such diagrams will be presented, one with results for jets located at a PN and one for jets located at a PAN.

5.3.2.1 Jets Located at a Pressure Node

The first forcing susceptibility diagram is shown in Fig. 5.14, including 36 points for jets located at a PN. The x -axis is the nondimensional forcing frequency F determined using experimental values of f_F and f_{nat} . Three different values of the forcing frequency, $f_F = [1700, 2050, 2600]$ Hz, and two different values of the natural jet frequency $f_{nat} = [921, 970]$ Hz, are included, creating six different values of F shown in Fig. 5.14. Nondimensional forcing frequencies of 1.85, 2.23, and 2.82 correspond to $J = 2$, where the mean natural frequency is 921 Hz. Nondimensional forcing frequencies of 1.75, 2.11, and 2.68 correspond to $J = 6$, where the mean natural frequency is 970 Hz. Although it is desired to include cases where $F < 1$, F was maintained above unity due to facility constraints. The y -axis is the acoustic forcing amplitude represented by u' rather than the measured p' . This is done to describe amplitude with a variable which is more pertinent to a PN, where pressure amplitudes are approximately zero and the jet is instead perturbed by acoustic velocity fluctuations. The acoustic velocity perturbation is

estimated using

$$u' = \frac{p'_{max}}{\rho_c c}, \quad (5.4)$$

where p' is the average of the maximum pressure perturbation amplitudes at the adjacent PANs located at $y = \lambda/4$ and $y = -\lambda/4$. Equation 5.4 requires that acoustic waves are linear and one-dimensional, which is supported by experimental observation for the amplitudes employed in this study. After assuming that a perfectly sinusoidal wave takes shape in the transverse direction, p' at adjacent PANs were calculated by interpolation using pressure amplitude measurements at a point between a PN and a PAN, e.g. $y = \lambda/8$ and $y = -\lambda/8$. The ambient chamber density ρ_c and speed of sound are determined as functions of the measured chamber pressure and temperature following REFPROP fluid properties. Finally, the forcing susceptibility diagram utilizes different symbol sizes to illustrate the forced mode variance contribution Ψ . For example, a large, black-filled symbol represents a high value of Ψ , common in conditions with high levels of acoustic forcing. Conversely, low forcing amplitudes often result in small values of Ψ . In fact, conditions with low levels of forcing often cause the naturally occurring instability to remain dominant, and this type of result is represented by unfilled symbols and symbols filled with an \times .

First and foremost, Fig. 5.14 shows that an increase in u' increases the likelihood that the forced mode will overtake the natural jet instability as the most dominant mode. This should be expected, and will remain true for all results presented in this study. Next, as u' is increased beyond the point where the forced mode overtakes the natural mode, the variance contribution from the forced mode continues to increase, giving the forced mode greater and greater dominance over the natural behavior of the jet. There are exceptions to this relationship though. For $F = 2.68$ and $J = 6$, increasing the forcing amplitude beyond $u' = 0.3$ m/s did not result in a greater variance contribution from the forced mode.

Secondly, Fig. 5.14 reveals that the susceptibility of the jet to acoustic forcing at a PN is dependent on F . This is readily apparent for $J = 6$. For $J = 6$, the forced mode overtakes the natural mode at $u' \approx 0.1$ m/s for the lowest forcing frequency, but an equivalent amplitude at the highest frequency does not produce a jet response. In fact, the forced mode for the highest frequency was not detected within the twelve highest ranked POMs determined by POD analysis until the forcing amplitude was increased to $u' = 0.17$ m/s. An even greater amplitude was necessary for the forced mode to overtake the natural mode. This result corresponds directly to that of absolute instability lock-in experiments [118, 122, 123], whereby increasing F from unity causes greater resistivity to forcing. While this phenomenon alone does not allow one to conclude that absolute instability exists, it does indicate that naturally occurring instabilities are more difficult to overcome with forcing at higher frequencies, consistent with absolutely unstable behavior [25, 118].

If the natural jet instability is only convectively unstable though, a separate explanation for the results in Fig. 5.14 could possibly exist. Since the work of Buffum and Williams [27], it has been known that transverse acoustic forcing can induce sinusoidal whipping motions in a jet column. An instability of this type is not strictly a shear layer instability, but is instead a bulk column mode resulting from periodic changes in transverse momentum. This behavior is shown in the snapshot sequence in Fig. 5.15 for $J = 2$, and is also supported by the eigenvector images of the forced mode in Fig. 5.16. More recently, Carpentier *et al.* [26] and Baillot *et al.* [16] recognized that side-to-side or sinuous motions observed by Buffum and Williams are highly dependent on frequency, and that a short acoustic period will prevent a jet from gaining significant spanwise momentum prior to a reverse in the transverse acoustic velocity which occurs at a PN. Not only do the qualitative results of this study demonstrate antisymmetric, sinusoidal jet motions, but Fig. 5.14 supports the principle established by Carpentier *et al.*, stating that at a fixed amplitude, increasing f_F will decrease the amplitude of transverse jet

motions. A similar relationship with f_F was also observed in experiments by Graham *et al.* [104] and Rodriguez *et al.* [81], where a higher f_F caused a degraded sensitivity to transverse acoustic forcing. The observation of sinuous or antisymmetric shear-coaxial jet motion in the vicinity of a PN actually shares some similarities with the droplet combustion experiments described in Chapters 2 and 3 of this dissertation. For all fuels explored and for virtually all amplitudes of acoustic excitation, burning droplets situated precisely at a PN during excitation did not have stable, uni-directionally oriented flames. As described in section 3.2.2, the flames under these circumstances switched back and forth in time, and did not stabilize to an orientation to one direction or the other. This asymmetric, sinuous-like distortion of the flame may have similarities to the sinuous motions quantified for shear-coaxial jets situated at a PN.

Lastly, to show the effect of J , Fig. 5.17 shows a plot of Ψ versus u' for $J = 2$ and $J = 6$. For both momentum flux ratios, low values of u' result in negligible variance contribution from the forced mode as determined by the twelve highest ranked POMs. Although it is not clear that J influences the level of forcing necessary to overtake the natural mode, Fig. 5.17 shows that J influences receptivity to acoustic forcing by viewing the magnitudes of Ψ for each case, consistent with absolutely unstable behavior. The forced mode variance contribution values for $J = 6$ reach magnitudes which are generally larger than those for $J = 2$. For $J = 2$, it appears that a form of saturation has occurred when reaching $u' \approx 0.4$ m/s; higher forcing amplitudes do not excite a greater variance contribution from the forced mode. Conversely, $J = 6$ creates more receptive conditions and values of Ψ which are nearly twice as large as their $J = 2$ counterpart.

5.3.2.2 Jets Located at a Pressure Antinode

A second forcing susceptibility diagram is shown in Fig. 5.18, including 41 points for jets located at a PAN. The y -axis is the acoustic forcing amplitude represented by p' as

measured by the dynamic pressure transducer located directly behind the jet as viewed from the camera. This measurement, named $p_{dyn,2}$, is most important when the jet is located at a PAN. At this location, $u' \approx 0$, making p' the primary cause of acoustically induced jet dynamics.

As shown in Fig. 5.18, p' values of approximately 3.5 kPa are required in order to observe the forced mode in the jet dynamics. When viewing the twelve highest ranked POMs, acoustically forced cases with $p' < 3.5$ kPa did not produce any evidence of the forced mode. A further increase in p' produces a POM pair for the forced mode among the highest POMs, but an amplitude of ~ 7 kPa is necessary for the forced mode to overtake the natural mode. This is true for both momentum flux ratios and all nondimensional frequencies shown in Fig. 5.18. For example, results for $J = 6$ and $F = 1.75$ show that a forcing amplitude of $p' = 6.27$ kPa asserts significant forced mode dynamics in the jet, but increasing the amplitude to $p' = 7.58$ kPa caused the forced mode to overtake the natural mode as the most dominant instability.

To best explain the influence of acoustic forcing frequency on jet dynamics, the jet's qualitative behaviors may first reveal the mechanism by which pressure fluctuations induce a forced mode instability. Jets located at a PN exhibit transverse side-to-side motion, while jets located at a PAN were observed to have axisymmetric vortex rings at the inner shear layer. This behavior is shown in the snapshot sequence in Fig. 5.19 for $J = 2$, and is also supported by the eigenvector images of the forced mode in Fig. 5.20. These vortex rings, or “puffs”, are produced at the injector exit and become the most dominant mode for $p' \gtrsim 7$ kPa. Vortex rings have also been observed in previous experiments at AFRL [81, 104, 105]. Baillot *et al.* [16] observed similar axisymmetric instability for shear-coaxial jets at atmospheric pressure, and concluded that vortex rings result from outer jet gas pulsations. A momentary rise in chamber pressure at the beginning of an acoustic pressure cycle was said to impede the flow of the gas annulus,

followed by an increase in jet velocity due to the subsequent decline in pressure in the latter part of the acoustic cycle. Pulsations were not observed for the dense, liquid inner jet [16]. Using the following analytical derivation, the PAN jet pulsation phenomenon is shown to indeed be dependent on jet density as well as acoustic forcing frequency.

Consider Newton's Second Law when applied to the mass of fluid inside an injector. The downstream end of this mass of fluid is subject to a periodic force with an amplitude of F'_{PAN} at the injector exit, due to a pressure fluctuation p' . The mass of the body of fluid is equal to the product of density ρ and volume V , and the body of fluid has a periodic acceleration a which results from a periodic force applied at the exit of the injector. To obtain the streamwise u' resulting at the exit of an injector at a PAN location, Newton's second law is applied to one quarter of an acoustic cycle which yields

$$\begin{aligned}
 F_{PAN} &= ma \\
 \int_0^{\frac{1}{4f_F}} F_{PAN} dt &= \int_0^{\frac{1}{4f_F}} madt \\
 \int_0^{\frac{1}{4f_F}} F'_{PAN} \sin(2\pi f_F t) dt &= \rho V \int_0^{\frac{1}{4f_F}} \frac{du}{dt} dt.
 \end{aligned} \tag{5.5}$$

Carrying out the integration of force and acceleration results in

$$\begin{aligned}
 F'_{PAN} \left[-\frac{1}{2\pi f_F} \cos(2\pi f_F t) \right]_0^{\frac{1}{4f_F}} &= m [u]_0^{\frac{1}{4f_F}} \\
 F'_{PAN} \left[-\frac{1}{2\pi f_F} \left(\cos \frac{\pi}{2} - \cos 0 \right) \right] &= m [0 - (-u')] \\
 \frac{F'_{PAN}}{2\pi f_F} &= mu',
 \end{aligned} \tag{5.6}$$

which can be simplified further by writing F'_{PAN} as the product of the injector exit area A and the pressure amplitude at the jet p' and by writing V as the product of A and the injector length l . These substitutions give a straightforward solution for the injector

fluid velocity fluctuations u' induced by the chamber pressure oscillations p' at a PAN,

$$u' = \frac{p'}{2\pi f_F \rho l} \quad (5.7)$$

This solution may be applied to the inner or outer jet by using ρ_{ij} and l_{ij} or ρ_{oj} and l_{oj} , respectively. If integration is performed over one-half an acoustic cycle rather than one-quarter of an acoustic cycle, then the same solution is reached. Eqn. 5.7 is a relation for injector-acoustic interactions occurring at a PAN, but should be treated as an approximate solution, as it does not account for the geometry of an injector plenum upstream of the constant area section l , nor does it account for potential acoustic resonance in the injector. Eqn. 5.7 also treats the fluid in the injector as a single body with constant mass, neglecting compressibility. Although, the assumptions made to reach this solution limit its applicability, the solution advocates that for a constant p' the pulsation velocity u' is inversely proportional to f_F and ρ .

Therefore, the derivation of the injector pulsation velocity and the results shown in Fig. 5.18 support the conclusions of Baillot *et al.* [16] by asserting an inverse relationship between both f_F and ρ and the amplitude of resulting outer jet pulsations. For the injector of interest here, l_{ij} and l_{oj} are of the same order of magnitude ($l_{ij} = 1.8l_{oj}$), and differences in the pulsation amplitude u' are caused by a difference in ρ_{ij} and ρ_{oj} . Since $\rho_{ij} \approx 100\rho_{oj}$, pulsations in the liquid nitrogen inner jet will be negligible in comparison to those in the gaseous helium outer jet. Therefore, one should expect the forced mode will influence the inner shear layer instability when the outer jet pulsations reach a significant velocity amplitude. Meanwhile, inner jet pulsations can be ignored. The inner jet may be indirectly effected by axisymmetric vortex rings which form at the exit of the outer jet and convect downstream, but will be less effected by chamber pressure fluctuations directly. As a result, the outer jet pulsation phenomenon will control the susceptibility of the jet to acoustic forcing. This concept is reenforced by two conclusions of this study. First, Fig. 5.18 shows that increasing the nondimensional forcing frequency F requires

an increase in p' in order for the forced mode to overtake the natural mode. Second, a critical PAN forcing amplitude will be shown to depend solely on outer jet conditions, because the forced mode is manifested specifically via the outer jet.

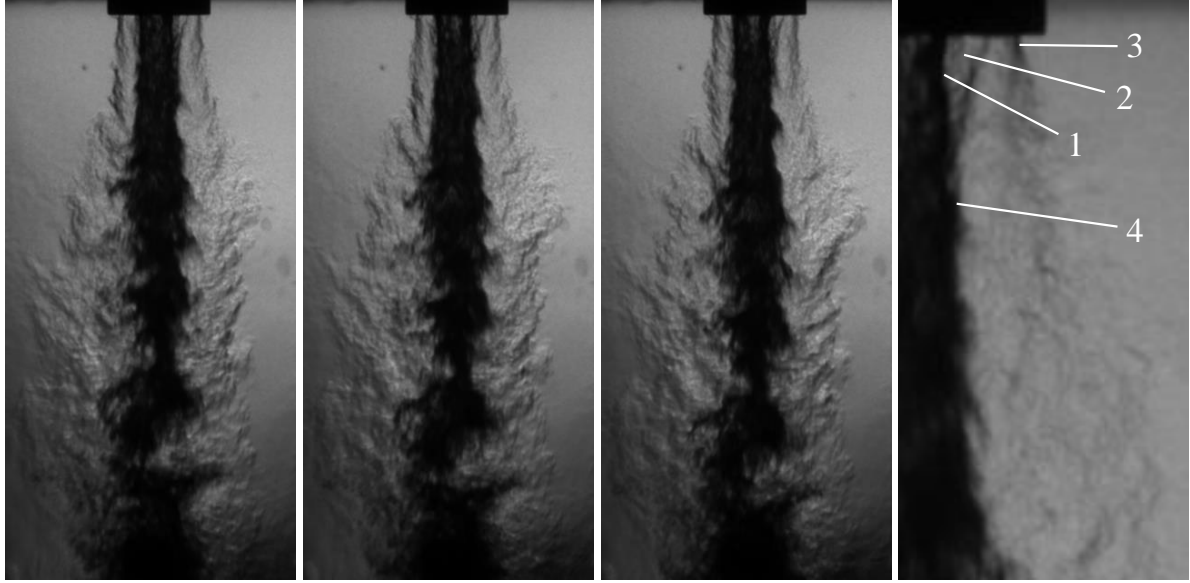
Concerning forcing frequency, comparing the minimum and maximum values of F for both $J = 2$ and $J = 6$ reveals the salient effect of F . Fig. 5.18 shows that for $J = 2$, at $F = 1.85$ a forcing amplitude of $p' = 6.00$ kPa caused the forced mode to overtake the natural mode, but at $F = 2.82$ an increased forcing amplitude of $p' = 7.93$ kPa was insufficient and the natural instability remained most dominant. For $J = 6$, at $F = 1.75$ a forcing amplitude of $p' = 4.55$ kPa and $p' = 6.27$ kPa caused the forced mode to appear within the twelve highest ranked POMs, an indication that the forced mode is nearly as significant as the natural mode in terms of pixel intensity variance. Further increasing the amplitude to $p' = 7.58$ kPa caused the forced mode to overtake the natural mode. Conversely, for $J = 6$ and $F = 2.68$, $p' = 0.95$ did not produce a significant forced mode, as the forced mode POM pair did not appear within the twelve highest ranked POMs.

Note that although the critical amplitude increases with F , one cannot estimate that this relationship holds for $F < 1$ or near $F = 1$. The current test matrix does not include the forcing frequencies necessary to make this conclusion. In a traditional lock-in diagram for absolute instability [122, 123] the minimum amplitude necessary for lock-in forms the well-known “V” shape, and requires an increase in the minimum amplitude as F is decreased below unity. The results in Fig. 5.18 do not precisely assert this type of behavior, but data at lower forcing frequencies are not available to study the phenomenon in detail. Nevertheless, the fact that there are forcing conditions that preclude lock-in does seem to suggest the appearance of absolutely unstable shear layers.

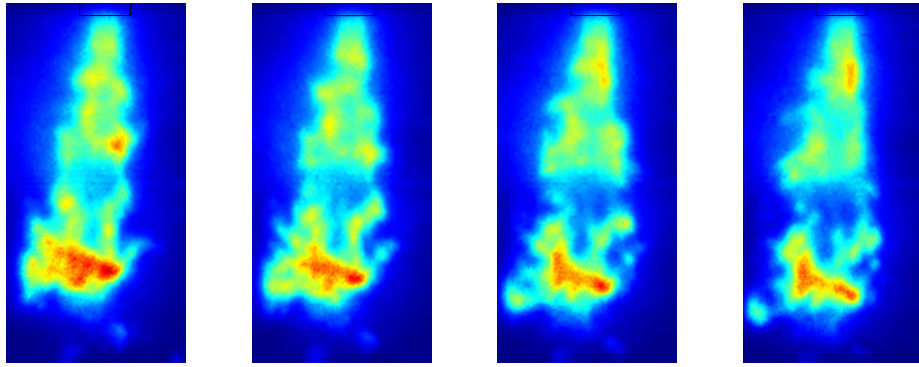
To understand the influence of J , Fig. 5.21 shows a plot of Ψ versus p' for $J = 2$ and $J = 6$ at a PAN. Similar to Fig. 5.17, low values of p' result in approximately zero

variance contribution from the forced mode as determined by the twelve highest ranked POMs. Significant forced mode variance occurs when p' is increased to a value between 3.5 kPa and 7.0 kPa, depending on J and F . Higher amplitudes cause increased values of Ψ , but this relationship is more pronounced for $J = 6$ than $J = 2$. Similar to a PN condition, forced mode variance contributions for $J = 6$ reach values nearly twice as large those for $J = 2$. Thus, holding all other variables approximately constant, $J = 6$ exhibits greater susceptibility to external acoustic forcing than $J = 2$ when the jet is located at a PAN.

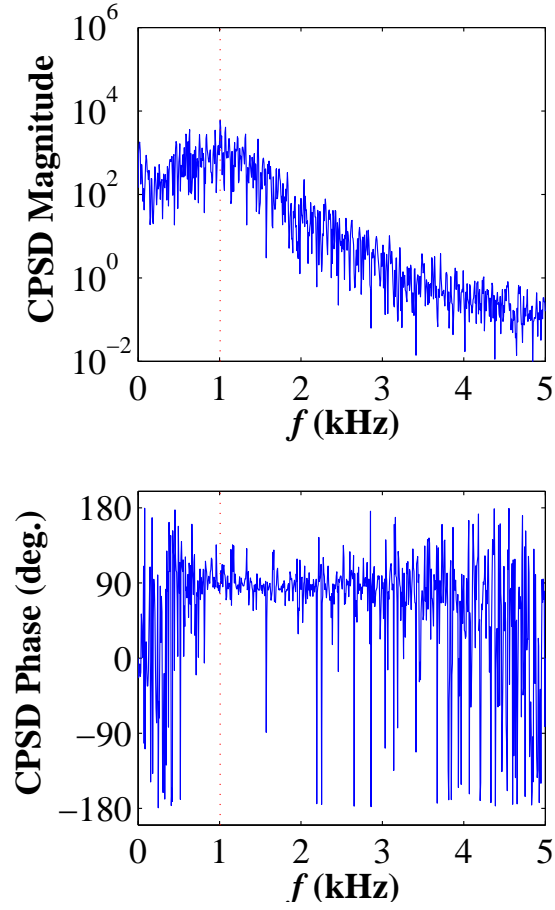
Finally, to emphasize the importance of outer jet pulsations at a PAN, an effort is made to collapse the data in Fig. 5.21 using a nondimensional forcing amplitude on the x -axis rather than the measured quantity p' . If indeed the forced mode infiltrates the inner shear layer by manipulating the outer jet flow, then outer jet pulsations must rival natural turbulence levels which are introduced into the inner shear layer by the outer jet. These natural fluctuations in the outer jet will be proportional to the dynamic pressure of the outer jet $\frac{1}{2}\rho_{oj}u_{oj}^2$, while the forced pulsations at the outer injector exit are shown to be directly proportional to p' in eqn. 5.7. As a result, $p'/\frac{1}{2}\rho_{oj}u_{oj}^2$ was chosen as a nondimensional forcing amplitude and is the new x -axis in Fig. 5.22. When compared with the dimensional plot in Fig. 5.21, Fig. 5.22 shows a more meaningful distribution at $p'/\frac{1}{2}\rho_{oj}u_{oj}^2 = 1$, where both $J = 2$ and $J = 6$ result in positive values of the forced mode variance contribution Ψ . When $p' < \frac{1}{2}\rho_{oj}u_{oj}^2$ the acoustic forcing induces a negligible effect on the jet. In conclusion, when the liquid-gas coaxial jet was acoustically forced at a PAN condition, the forced mode began to influence the inner shear layer instability when the acoustic pressure perturbation p' was nearly equal to or greater than the outer jet dynamic pressure.



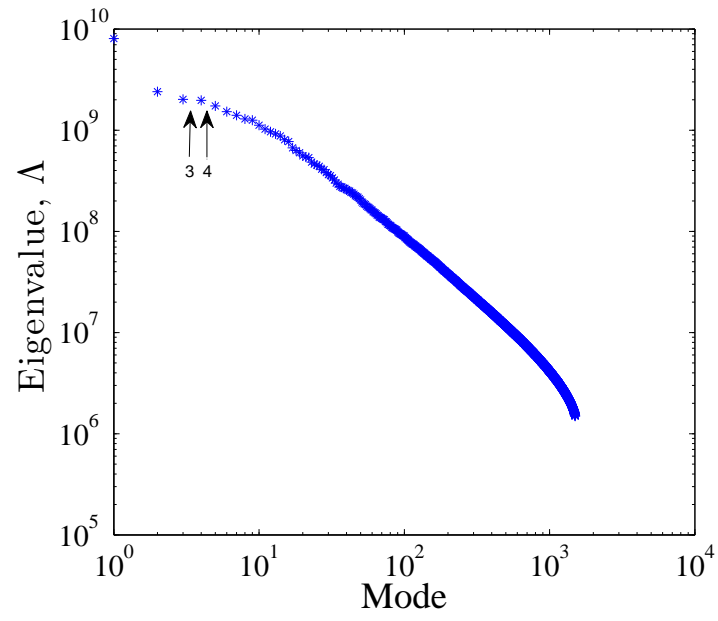
5.1: A sequence of unforced LN₂-GHe jet images acquired at a frame rate of 10 kHz, accompanied by a reduced field of view to show the (1) interface between the liquid nitrogen inner jet and the recirculation zone (2) recirculation zone (3) outer shear layer (4) inner shear layer forming at the downstream end of the recirculation zone.



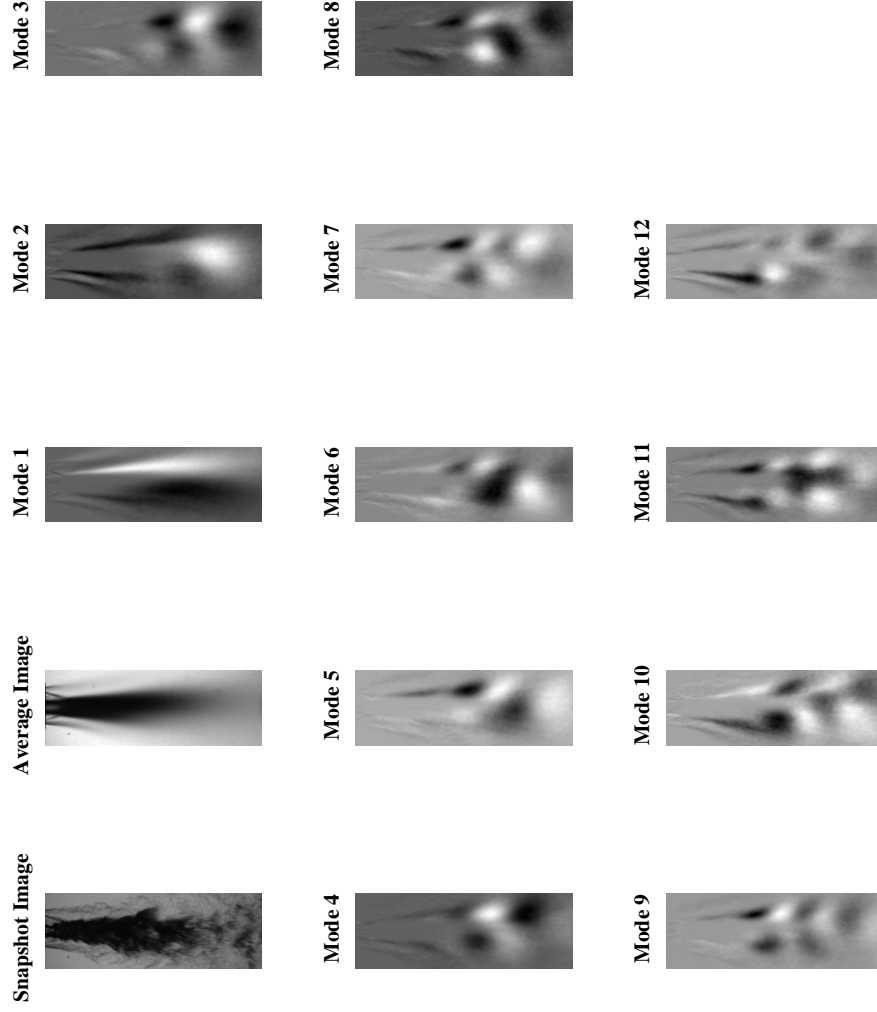
5.2: A consecutive sequence of unforced $\text{O}_2\text{-H}_2$ flame images acquired at a frame rate of 16 kHz. The intensifier gate duration, which is essentially the camera exposure time, is set to 61 ns. Flame structures form near the injector exit and evolve as they travel downstream. $MR = 5.9$ ($\phi_{f/o} = 1.36$), $J = 2$, $p_c \approx 400$ psia = 2.76 MPa.



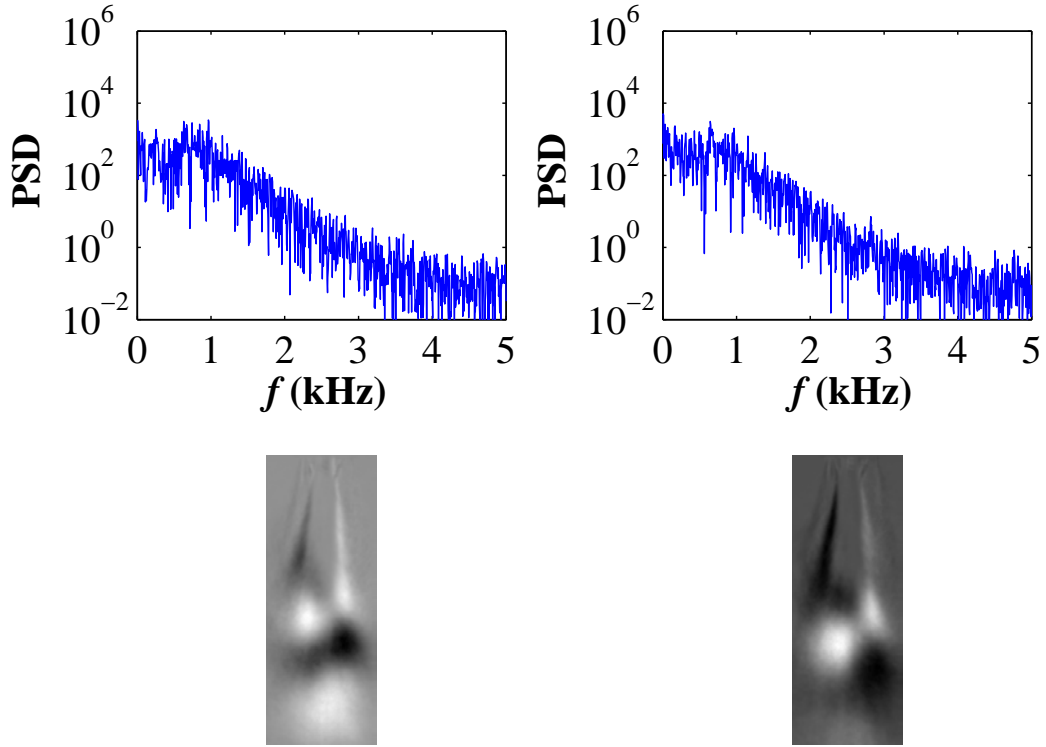
5.3: Cross power spectral density magnitude (top) and phase (bottom) for POD modes 3 and 4 for an unforced LN₂-GHe jet with $J = 6$. A vertical red line is located at $f = 945$ Hz represents the characteristic instability frequency for this particular case.



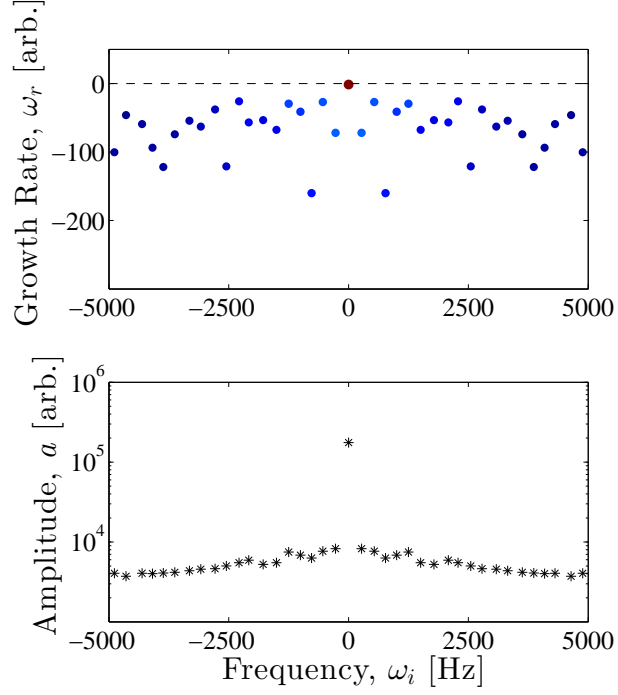
5.4: POD eigenvalues ranked according to magnitude show that although modes 3 and 4 have been chosen to assert the natural instability of the jet, the eigenvalues of modes 5-8 are nearly as high as the eigenvalues of 3 and 4. ($\Lambda = \sigma^2$)



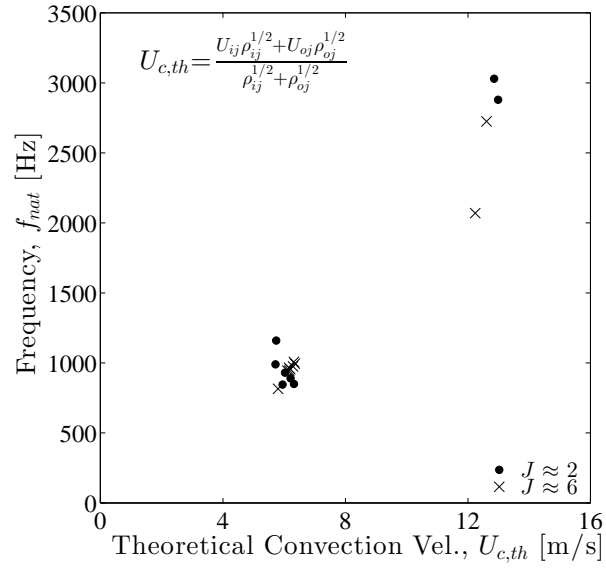
5.5: POM images 1-12 are shown for an unforced LN₂-GHe jet at $J = 6$. Modes 3 and 4 are the highest ranked conjugate mode pair, together demonstrating a natural jet frequency of 945 Hz. The eigenvalues of modes 1 and 2 are greater than 3 and 4, but do not display coherent structures having a 90° phase difference.



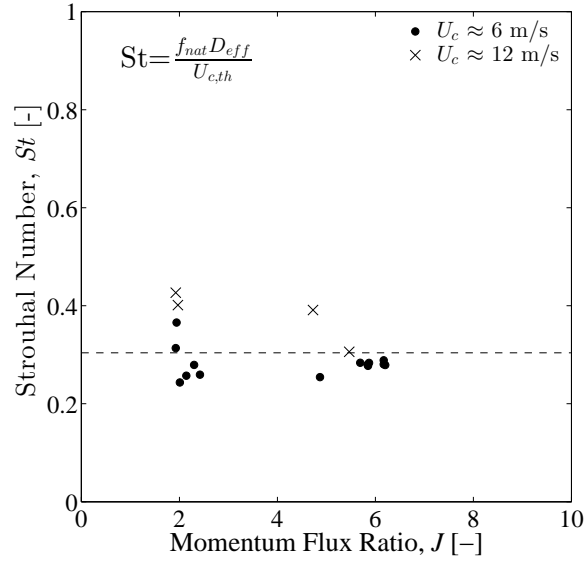
5.6: The naturally occurring mode for $J = 6$ is represented by the POM pair which consists of mode-3 (left) and mode-4 (right). Power spectral density plots are shown (top) with each corresponding eigenvector image (bottom). The natural mode is antisymmetric, and likely a helical instability. The eigenvector images of mode-3 and mode-4 appear to be 90° out-of-phase in the streamwise direction.



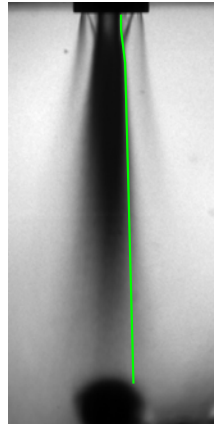
5.7: Top: Real eigenvalues ω_r (growth rate) and imaginary eigenvalues ω_i (frequency) plotted for DMD results computed for an unforced LN₂-GHe jet with $J = 6$. Each point represents a single mode identified by DMD, and the color and size of each point is scaled with the amplitude of each mode as calculated using eqn. 4.49. Bottom: Mode amplitudes plotted versus ω_i . A significant natural mode cannot be identified.



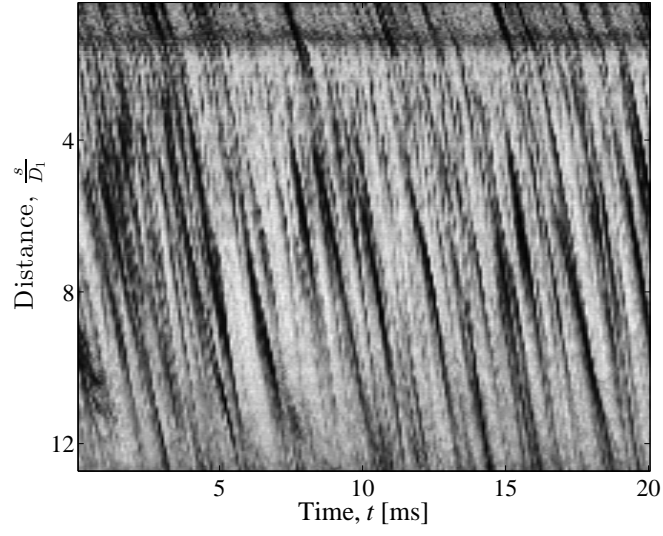
5.8: LN₂-GHe jet instability frequency, as measured by POD, plotted versus shear layer convective velocity. J is nominally maintained between 2 and 6. Each point corresponds to a point in Fig. 5.9 and exact values can be found in appendix A.



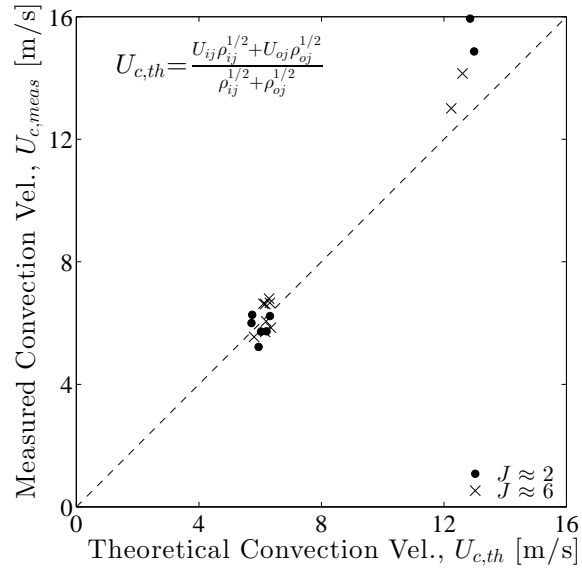
5.9: LN₂-GHe jet Strouhal number plotted versus J based on data in Fig. 5.8, using a theoretical shear layer convection velocity $U_{c,th}$.



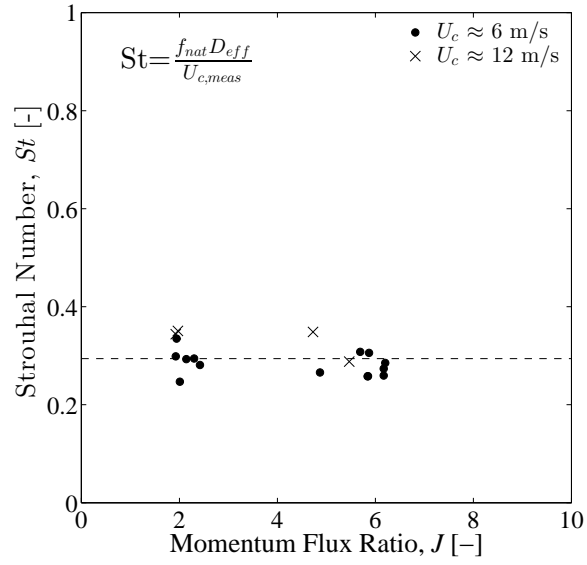
5.10: A time-averaged image of the LN₂-GHe shear-coaxial jet with the location of the inner shear layer curve s in green.



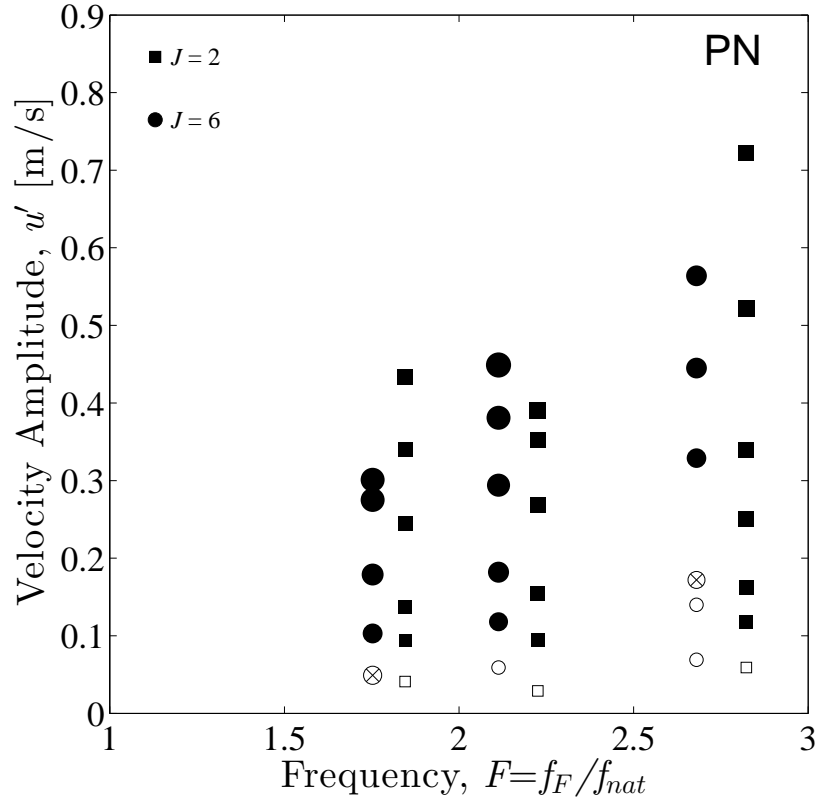
5.11: The pixels located on the shear layer curve s , defined in Fig. 5.10, shown for a period of time spanning 20 ms. Diagonal streaks are the convection of fluid structures of the inner shear layer, and the velocity of each structure is equal to the slope of each respective streak, $\Delta s / \Delta t$.



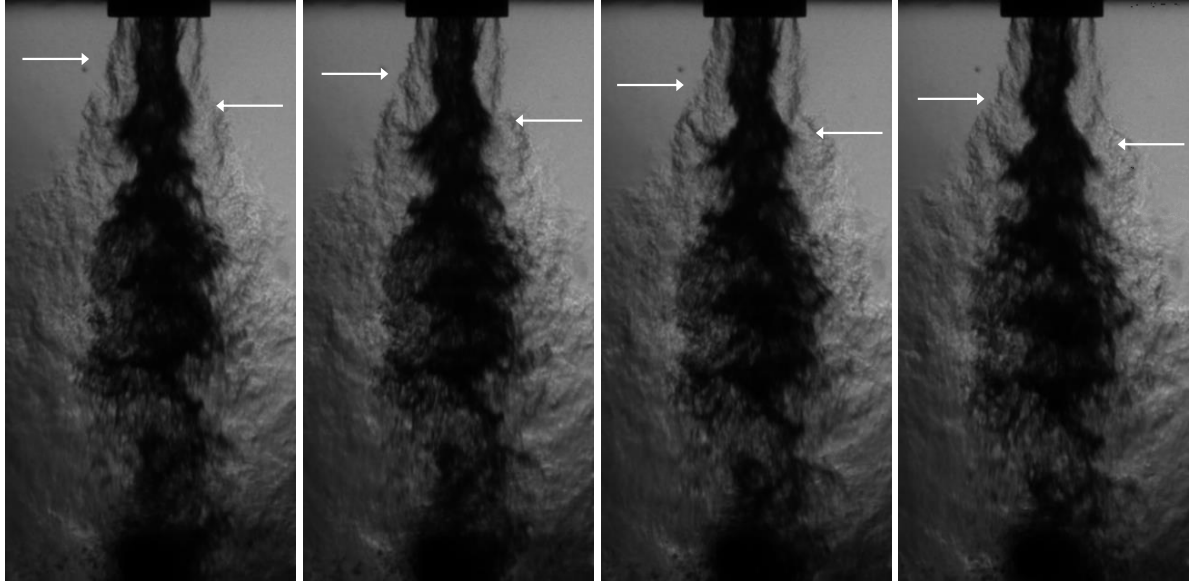
5.12: Measured shear layer convection velocities plotted versus theoretical values.



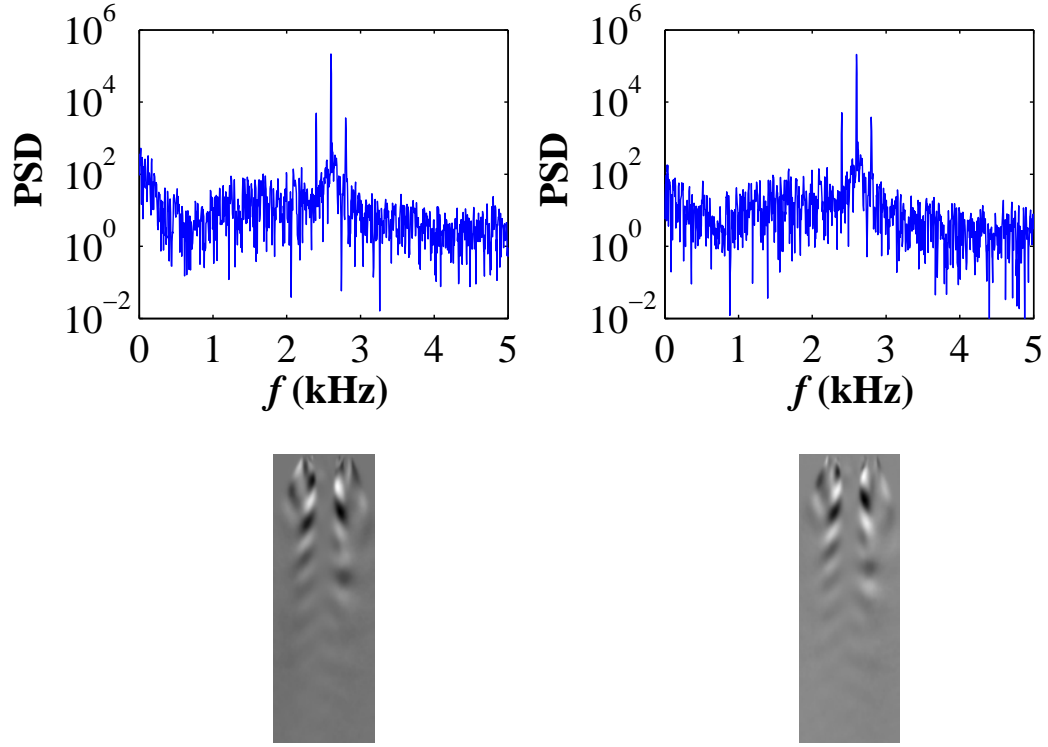
5.13: LN₂-GHe jet Strouhal number plotted versus J , using a measured shear layer convection velocity $U_{c,meas}$.



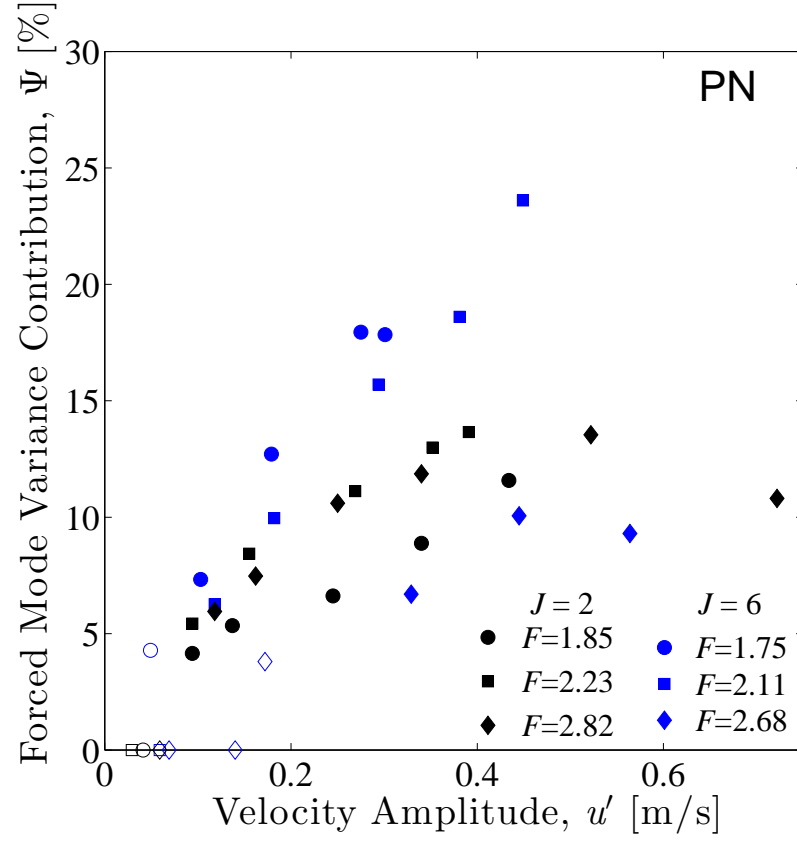
5.14: The acoustic forcing amplitude u' is plotted versus the nondimensional frequency for $J = 2$ and $J = 6$ for a jet located at a PN. Open symbols represent conditions in which the natural mode of the jet was most significant. Closed symbols represent conditions in which the natural mode was overtaken by the forced mode. The size of each symbol is scaled with the forced mode's variance contribution to the flow as determined by POD eigenvalues, e.g. large, filled symbols represent a condition where the forced mode has a large contribution to the total energy of the flow. Very small, open symbols represent a case in which the forced mode did not appear in the POD results. Symbols with an \times represent cases in which the forced mode appeared in the POD results, but did not overtake the natural mode.



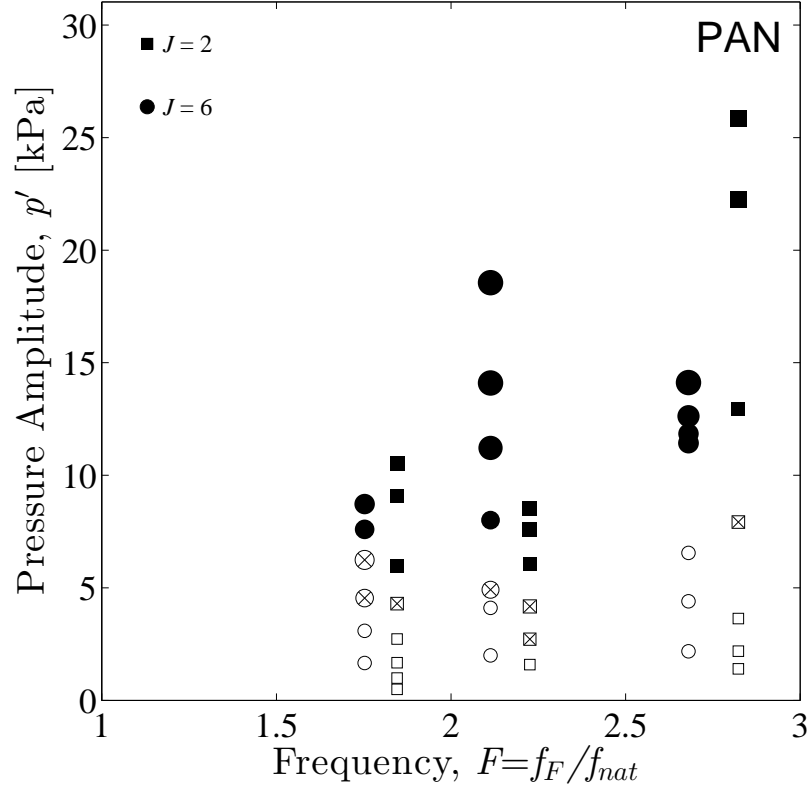
5.15: LN₂-GHe shear-coaxial jets exposed to external, transverse acoustic forcing at a pressure node. Four consecutive images are taken from a set of high-speed images acquired at 10 kHz. An antisymmetric instability forms as periodic spanwise motions caused by the acoustic velocity perturbation u' . $J = 2$, $p_c = 400$ psia = 2.76 MPa, $f_F = 1700$ Hz, $u' = 0.43$ m/s



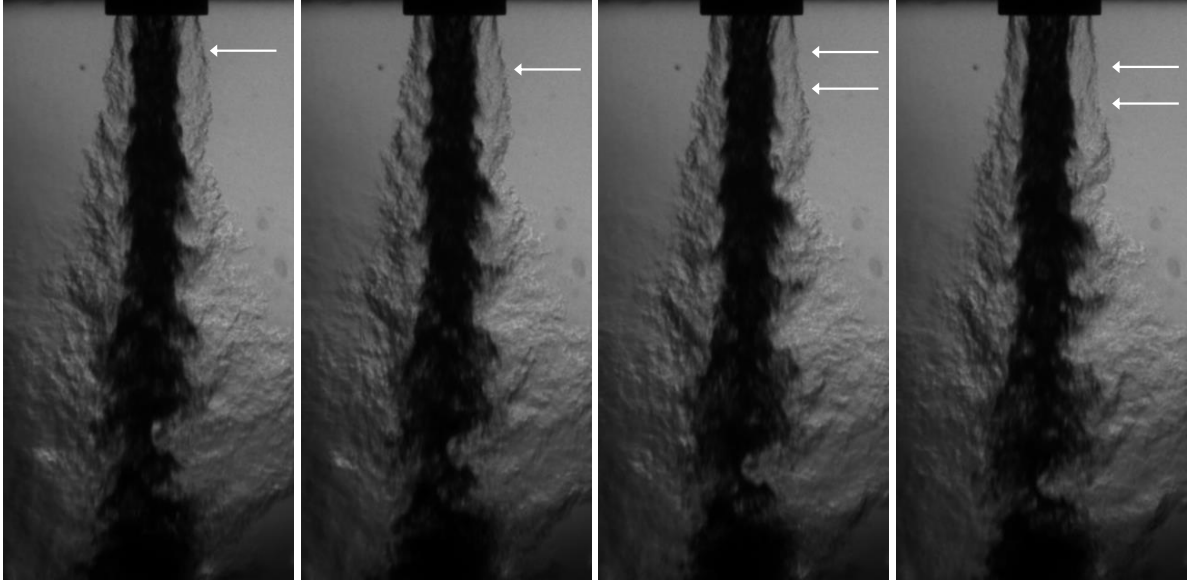
5.16: The forced mode for $J = 2$ at a PN is represented by the POM pair which consists of mode-2 (left) and mode-3 (right). Power spectral density plots are shown (top) with each corresponding eigenvector image (bottom). The forced mode occurring at a PN takes on an antisymmetric appearance. The eigenvector images of mode-2 and mode-3 appear to be 90° out-of-phase in the streamwise direction.



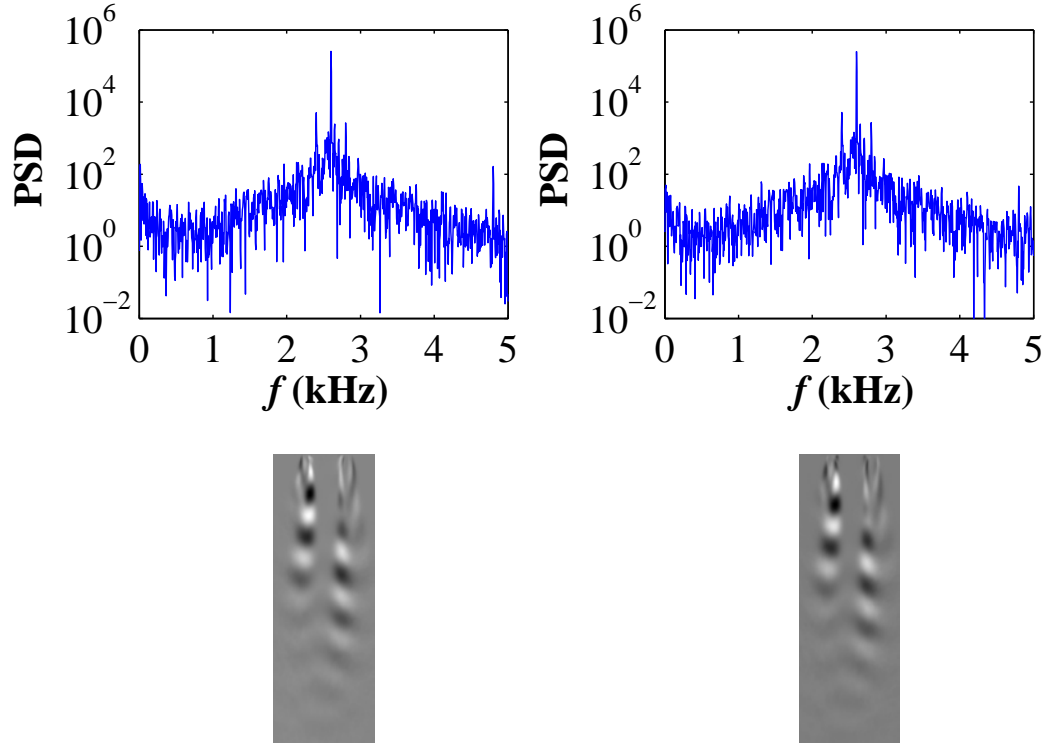
5.17: The forced mode variance contribution is plotted versus the acoustic velocity perturbation amplitude u' for $J = 2$ and $J = 6$ for a jet located at a PN. The nominal natural frequency for $J = 2$ and $J = 6$ is 921 Hz and 970 Hz, respectively. Open symbols represent conditions in which the natural mode of the jet was most significant. Closed symbols represent conditions in which the natural mode was overtaken by the forced mode.



5.18: The acoustic forcing amplitude u' is plotted versus the nondimensional frequency for $J = 2$ and $J = 6$ for a jet located at a PAN. Open symbols represent conditions in which the natural mode of the jet was most significant. Closed symbols represent conditions in which the natural mode was overtaken by the forced mode. The size of each symbol is scaled with the forced mode's variance contribution to the flow as determined by POD eigenvalues, e.g. large, filled symbols represent a condition where the forced mode has a large contribution to the total energy of the flow. Very small, open symbols represent a case in which the forced mode was not exhibited in the POD results. Symbols with an \times represent cases in which the forced mode appeared in the POD results, but did not overtake the natural mode.



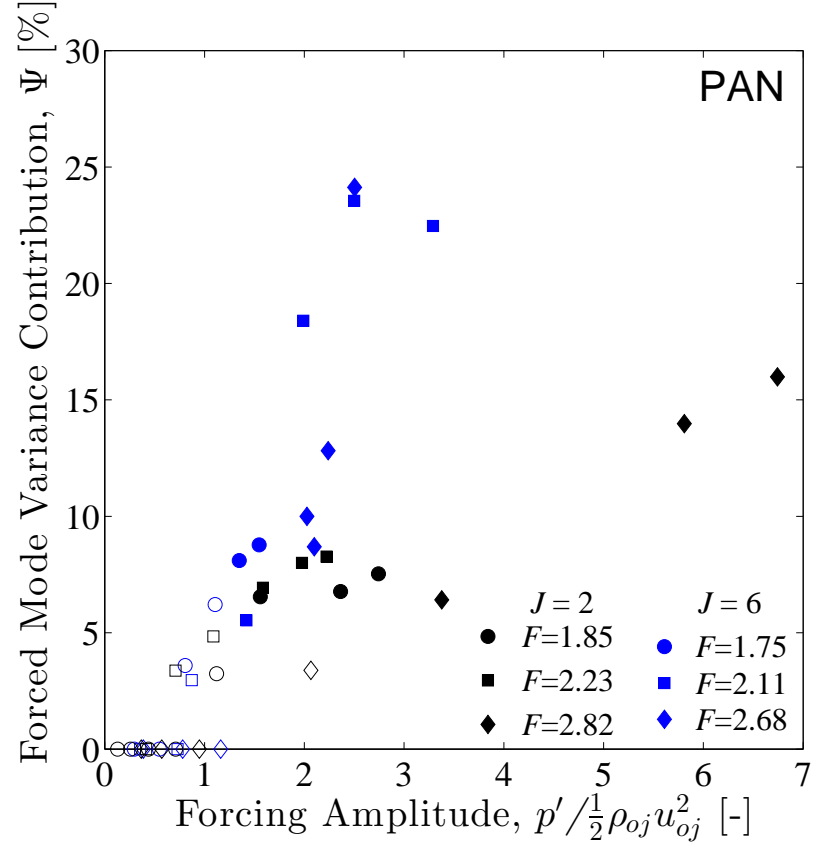
5.19: LN₂-GHe shear-coaxial jets exposed to acoustic forcing at a pressure antinode. Four consecutive images are taken from a set of high-speed images acquired at 10 kHz. An axisymmetric instability forms due to outer jet flow pulsations caused by the acoustic pressure perturbation p' . $J = 2$, $p_c = 400$ psia = 2.76 MPa, $f_F = 1700$ Hz, $p' = 1.53$ psi = 10.55 kPa



5.20: The forced mode for $J = 2$ at a PAN is represented by the POM pair which consists of mode-1 (left) and mode-2 (right). Power spectral density plots are shown (top) with each corresponding eigenvector image (bottom). The forced mode occurring at a PAN takes on an axisymmetric appearance. The eigenvector images of mode-1 and mode-2 appear to be 90° out-of-phase in the streamwise direction.



5.21: The forced mode variance contribution is plotted versus the acoustic pressure perturbation amplitude p' for $J = 2$ and $J = 6$ for a jet located at a PAN. The nominal natural frequency for $J = 2$ and $J = 6$ is 921 Hz and 970 Hz, respectively. Open symbols represent conditions in which the natural mode of the jet was most significant. Closed symbols represent conditions in which the natural mode was overtaken by the forced mode.



5.22: The forced mode variance contribution is plotted versus the acoustic pressure perturbation amplitude p' nondimensionalized by the outer jet dynamic pressure for $J = 2$ and $J = 6$, for a jet located at a PAN. The nominal natural frequency for $J = 2$ and $J = 6$ is 921 Hz and 970 Hz, respectively. Open symbols represent conditions in which the natural mode of the jet was most significant. Closed symbols represent conditions in which the natural mode was overtaken by the forced mode.

CHAPTER 6

Conclusions and Future Work

This dissertation has described extensive experiments relevant to acoustically-coupled combustion and transport processes. While both studies (on acoustically excited droplet combustion at UCLA and acoustically-coupled coaxial jets at AFRL) have helped to answer a number of fundamental scientific questions, there remain a number of issues on which future studies should focus.

6.1 Studies on Acoustically-coupled Droplet Combustion

The results in Chapter 3 on the fuel droplet combustion studies present strong evidence that the acoustic radiation force theory of Tanabe *et al.* [21, 73] does not properly account for the dynamic interactions between condensed phase combustion and acoustic excitation. Quantitatively, the amount of flame deformation and the locations of maximum flame deformation disagree with the prescribed theory. Qualitatively though, the location of flame switch is predicted fairly well, implying that acoustic radiation force theory plays a role in droplet combustion, but perhaps leaves essential combustion phenomena unaccounted for. Thermochemical relationships vital to condensed phase combustion may hold primary influences, rather than secondary influences, on the flame behaviors observed here.

To capture these effects, future work should explore the chemical kinetics frequency response in detail. First, the spatiotemporal relationship between flame standoff dis-

tance and acoustic phase could be enlightening. This relationship was not discussed in detail here, and could reveal a reaction phase delay which is frequency dependent. Any interdependency between chemical kinetics and frequency could contribute to the fact that Tanabe's theory is more accurate for higher frequencies than lower frequencies. Second, the well known Rayleigh criterion may predict different levels of instability for different acoustic flow conditions. The Rayleigh index, a transfer function calculated using the difference in phase between the pressure fluctuation p' and the heat release fluctuation q' , can be found for each flow condition by synchronizing p' measurements with q' measurements, which can be inferred from global or local OH* chemiluminescence intensity. Should these studies provide illuminating results, a revised acoustic radiation force theory could provide a more comprehensive and accurate model of acoustic excitation coupled to condensed phase combustion, giving insight to the field of burning droplets as well as an array of other combustion instability problems.

6.2 Studies on Shear-coaxial Jets

To explore the susceptibility of shear-coaxial jets to external acoustic forcing, this study quantifies the amplitude at which the acoustically forced mode will overcome the naturally occurring mode as the most significant instability in the jet. It is evident that a critical forcing amplitude can indeed be identified, and its value will depend on the nondimensional forcing frequency F and jet flow conditions, such as the momentum flux ratio J . The critical forcing amplitude's dependence on F shares features with V-shaped lock-in diagrams common in absolute instability studies, where values of F which diverge from unity require increasingly large forcing amplitudes in order for the forced mode to overtake the natural mode. Indeed, a potential wake instability may produce absolute instability at the recirculation zone near the injector exit, but further theoretical work is required to determine the likelihood of absolute instability for the range of flow con-

ditions used here. An expanded test matrix to include $F < 1$ is also required to verify a V-shaped curve and confirm this relationship.

Alternatively, the results contain several indications that the natural mode of the jet instability is different from the typical absolutely unstable shear layer. The sinusoidal whipping of jets located at a PN and the streamwise pulsations of jets located at a PAN both are associated with periodic momentum fluctuations, whereby a long acoustic cycle encourages the production of a significant change in fluid momentum. As explained above, this mechanism will prohibit large amplitudes of momentum from being produced if the acoustic cycle is short, and thus an increase in f_F will cause an increase in the critical forcing amplitude for all F . Such a relationship has not been observed in prior studies of absolute instability, although in most studies of lock-in and associated phenomenon, a range of forcing frequencies can be studied without the requirement of creation of a standing wave. Again, an expanded test matrix can verify these relationships. The qualitative behavior of the jet after the acoustically forced mode overtakes the natural mode consistently revealed co-existing modes, whereby the forced mode became most dominant and the natural mode remained a significant mode within the mixing layer. While this is typically observed in absolutely unstable shear layers, there are some differences. The broadband nature of the natural instabilities observed have contrast to that of absolutely unstable flows, which are known to exhibit sharp peaks at a single frequency and higher harmonics. For the range of conditions explored in this study, it is believed that the naturally occurring jet instability is convectively unstable rather than absolutely unstable.

Reduced basis methods were successfully applied using a novel approach which compares the forced mode pixel intensity variance contribution Ψ from one case to another. In this way, quantitative measures of susceptibility to external forcing were obtained. Although qualitative conclusions were a valuable portion of this study, this quantita-

tive method shows great potential for future studies. Dynamic mode decomposition and proper orthogonal decomposition both showed advantages and disadvantages with regard to analyzing experimental images, and future work should continue to utilize and refine these algorithms where harsh environments make it difficult to use intrusive sensors alone. Although proper orthogonal decomposition was used for the majority of post-processing in this study, dynamic mode decomposition is recommended where specific frequencies must be extracted from dynamic flow structures.

The techniques noted above will prove to be powerful when applied to reactive combustion instability experiments, which is a paramount objective of this research campaign. To quantify the susceptibility of oxygen-hydrogen flames to acoustic forcing, reduced based methods will draw spectral information from high-speed images without requiring delicate instrumentation to be placed in a high pressure, high temperature combustion chamber. Ultimately, Strouhal number scaling laws will be refined for reactive conditions and forcing susceptibility diagrams will shine light on the inter-dependencies of the combustion instability feedback loop.

Appendix A

Shear-Coaxial Jet Experimental Methods Details

A.1 Acoustic Forcing System

The acoustic frequency sweeps conducted when characterizing the resonant frequencies of the acoustic system only approximately determined the frequency, amplitude, and phase difference of the sirens necessary to produce transverse standing waves. In order to achieve a more exact PN or PAN condition at the center of the inner chamber, a meticulous set of operations was carried out prior to each acoustically forced flow condition. Each of these operations is manual, and the complete procedure is itemized below.

- *Achieve a steady thermodynamic condition.* Prior to adjusting any acoustic parameters, the chamber speed of sound c must be nominally constant. This is done by setting p_c , \dot{m}_{ij} , \dot{m}_{oj} , T_{ij} , and T_{oj} according to a predetermined test matrix. The correct mean chamber pressure p_c is achieved by setting the chamber pressurization nitrogen flow accordingly. The mass flow rates \dot{m}_{ij} and \dot{m}_{oj} are set by adjusting needle valves in the supply lines, and as expected, T_{ij} and T_{oj} are adjusted separately using each heat exchanger.
- *Set the desired acoustic frequency f_F .* The signal generator, shown by the wiring diagram in Fig. A.3, is used to set f_F on output channels 1 and 2.

- *Set the desired siren phase difference $\Delta\phi$.* The phase difference $\Delta\phi_{SG}$ of signal generator channels 1 and 2 should be set to 0° and 180° to achieve PAN and PN conditions, respectively.
- *Set the pressure perturbation p' to a value approximately equal to the desired level.* The voltage output of signal generator output channels 1 and 2 are set independently.
- *Activate the acoustic sirens.* After activating channels 1 and 2, the sirens will produce an acoustic field which not a standing wave. Inner chamber pressure sensors located on the rear wall provide $p_{dyn,1}$, $p_{dyn,2}$, and $p_{dyn,3}$, which must be actively viewed on the graphical user interface of the data acquisition system. These sensors will reveal an asymmetric condition between the dynamic pressure left of the jet $p_{dyn,1}$ and the dynamic pressure right of the jet $p_{dyn,3}$. This asymmetric condition results from phase delays which are unique to each amplifier and are dependent on both frequency and amplitude.
- *Finalize the siren phase difference $\Delta\phi$.* This step requires the user to view the amplifier output monitor channels. Again, this is performed using the graphical user interface of the data acquisition system. The amplifier output monitor channels will reveal that $\Delta\phi_{AMP} \neq \Delta\phi_{SG}$. Then, $\Delta\phi_{SG}$ must be adjusted until $\Delta\phi_{AMP}$ has reached the desired value according to the data acquisition system. Following this step, the fluctuations observed with $p_{dyn,1}$ and $p_{dyn,3}$ will be nearly equal (symmetric), but output amplitude must often be adjusted to reach true symmetry.
- *Finalize the pressure perturbation p' to obtain symmetry.* Again, due to unequal amplifier frequency responses, equal signal generator output amplitudes may not result in equal amplifier output amplitudes. Thus, the signal generator output

amplitudes must be independently adjusted until the acoustic field of the chamber is symmetric, i.e. $p_{dyn,1} = p_{dyn,3}$. If acoustic drivers do not produce equal amplitudes, then standing waves are theoretically impossible. A successful procedure will result in a maximum p' at $p_{dyn,2}$ for a PAN condition, or will result in $p_{dyn,2} \approx 0$ for a PN condition.

A.2 Positive Semidefinite Proof

Where \mathbf{R} is the covariance matrix of $\tilde{\mathbf{A}}$ and \mathbf{z} is any $m \times 1$ vector,

$$\mathbf{z}^T \mathbf{R} \mathbf{z} = \mathbf{z}^T \tilde{\mathbf{A}}^T \tilde{\mathbf{A}} \mathbf{z} = \left(\tilde{\mathbf{A}} \mathbf{z} \right)^T \left(\tilde{\mathbf{A}} \mathbf{z} \right) \equiv \mathbf{b}^T \mathbf{b} \geq 0. \quad (\text{A.1})$$

Here, $\mathbf{b} \equiv \tilde{\mathbf{A}} \mathbf{z}$, which makes \mathbf{b} an $m \times 1$ vector with a magnitude equal to $\mathbf{b}^T \mathbf{b}$. Thus, $\mathbf{b}^T \mathbf{b}$ is non-negative and

$$\mathbf{z}^T \mathbf{R} \mathbf{z} \geq 0. \quad (\text{A.2})$$

By definition, this makes the covariance matrix \mathbf{R} *positive semidefinite*.

A.1: Data for unforced LN₂-GHe nonreactive experiments. Natural frequencies are determined using proper orthogonal decomposition. St_{th} is calculated using $U_{c,th}$. St_{meas} is calculated using $U_{c,meas}$.

J	R	S	T_c [K]	ρ_c [kg/m ³]	p_c [psia]	T_{oj} [K]	m_{oj} [g/s]	ρ_{oj} [kg/m ³]	U_{oj} [m/s]	Re_{oj} ($\times 10^{-4}$)	T_{ij} [K]	m_{ij} [g/s]	ρ_{ij} [kg/m ³]	U_{ij} [m/s]	Re_{ij} ($\times 10^{-4}$)	f_{nat} [Hz]	$U_{c,th}$ [m/s]	$U_{c,meas}$ [m/s]	St_{th}	St_{meas}
2.42	16.42	0.0090	287.9	32.7	402.7	274.8	0.55	4.8	43.67	0.92	120.0	2.43	534.5	2.66	1.81	890	6.21	5.73	0.259	0.281
2.30	16.18	0.0088	287.8	32.7	402.5	276.7	0.53	4.8	42.39	0.88	119.5	2.42	541.3	2.62	1.76	930	6.03	5.72	0.279	0.294
2.01	14.45	0.0096	287.7	32.7	402.6	274.6	0.52	4.8	41.46	0.87	121.9	2.44	497.8	2.87	2.09	850	6.32	6.23	0.243	0.247
2.14	15.54	0.0089	287.5	32.7	402.5	274.4	0.52	4.8	41.03	0.87	119.6	2.43	540.4	2.64	1.78	845	5.95	5.22	0.257	0.293
1.93	14.48	0.0092	269.7	36.7	421.4	277.0	0.50	5.0	37.98	0.83	119.7	2.42	541.8	2.62	1.76	990	5.72	6.00	0.313	0.299
1.94	14.57	0.0091	269.8	36.8	421.9	277.7	0.50	5.0	38.28	0.83	119.6	2.43	543.5	2.63	1.75	1160	5.74	6.27	0.366	0.335
4.87	23.40	0.0089	287.0	31.9	391.1	281.6	0.55	4.6	46.34	0.91	121.5	1.72	512.7	1.98	1.49	815	5.80	5.55	0.254	0.266
6.17	25.88	0.0092	286.8	32.6	399.3	274.0	0.64	4.8	51.24	1.08	120.8	1.75	518.8	1.98	1.38	975	6.29	6.80	0.281	0.259
5.84	25.11	0.0093	286.7	32.5	398.7	273.0	0.62	4.8	49.22	1.04	120.9	1.73	516.7	1.96	1.37	945	6.11	6.63	0.280	0.258
5.87	25.25	0.0092	286.7	32.5	398.5	275.4	0.62	4.7	49.74	1.03	121.1	1.72	512.5	1.97	1.39	965	6.16	5.71	0.283	0.306
5.85	25.11	0.0093	286.7	32.8	402.0	277.5	0.62	4.7	49.71	1.03	121.2	1.73	512.7	1.98	1.40	945	6.17	6.62	0.277	0.258
6.17	25.50	0.0095	288.6	32.7	402.6	277.3	0.64	4.8	50.75	1.06	121.7	1.70	502.5	1.99	1.44	1007	6.31	6.66	0.289	0.274
5.69	24.33	0.0096	288.4	32.7	403.9	274.0	0.64	4.8	50.11	1.06	121.7	1.76	501.4	2.06	1.48	995	6.35	5.85	0.284	0.308
6.20	25.43	0.0096	288.3	32.7	403.6	272.9	0.63	4.8	49.58	1.06	121.6	1.68	505.4	1.95	1.40	955	6.20	6.06	0.279	0.285
1.97	14.66	0.0092	272.2	34.9	404.3	274.3	1.10	4.8	86.78	1.84	120.5	5.30	525.4	5.92	4.09	2880	12.99	14.87	0.401	0.351
1.93	14.60	0.0090	271.5	35.0	404.2	275.6	1.08	4.8	86.07	1.81	120.2	5.34	531.2	5.90	4.04	3030	12.86	15.94	0.427	0.344
5.47	24.88	0.0088	270.3	35.4	407.3	275.0	1.27	4.8	99.79	2.12	119.0	3.75	548.8	4.01	2.65	2070	12.24	13.01	0.306	0.288
4.73	21.92	0.0098	269.8	37.1	425.8	275.5	1.27	5.1	95.69	2.12	121.5	3.82	513.7	4.37	3.07	2725	12.61	14.15	0.391	0.349

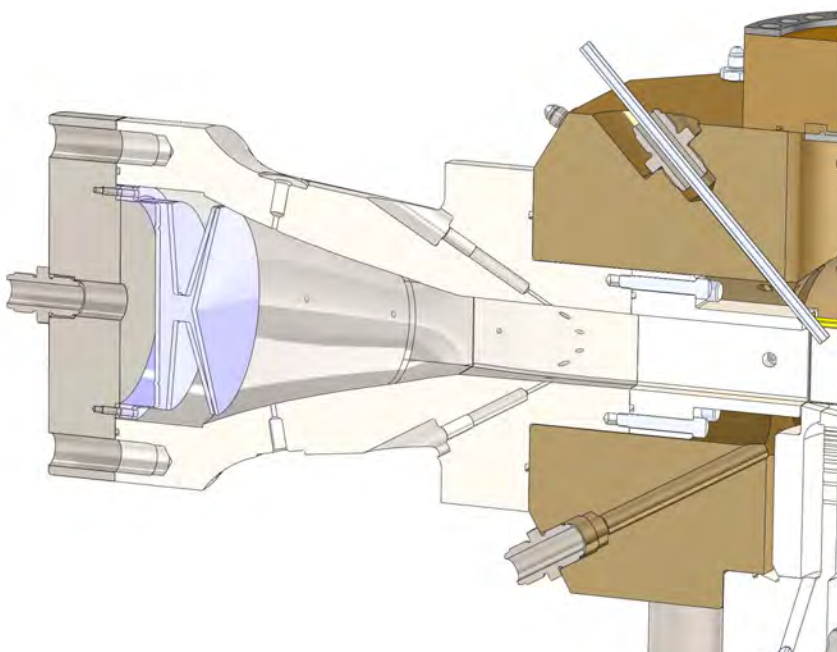
A.2: Data for acoustically forced LN₂-GHe nonreactive experiments. Data is presented for in units of psi (left) and kPa (right). For jets located at a PAN, the p' value is taken as the pressure perturbation at the jet. For jets located at a PN, the p' value is taken as the average of the pressure perturbations occurring at the PANs to the left and right of the jet. The velocity perturbation u' at a PN is calculated using eqn. 5.4, which relies on the p' values of the adjacent PANs.

J	f_F [Hz]	p' [psi]	
		PN	PAN
2	1700	0.05	0.07
		0.12	0.14
		0.17	0.24
		0.30	0.39
		0.42	0.62
		0.53	0.87
		-	1.31
		-	1.53
	2050	0.04	0.23
		0.13	0.39
		0.22	0.61
		0.38	0.88
		0.50	1.10
		0.55	1.24
	2600	0.10	0.20
		0.19	0.32
		0.26	0.53
		0.41	1.15
		0.55	1.88
		0.84	3.23
		1.17	3.75
6	1700	0.06	0.24
		0.12	0.45
		0.20	0.66
		0.31	0.91
		0.34	1.10
		-	1.27
	2050	0.08	0.29
		0.15	0.60
		0.24	0.71
		0.38	1.16
		0.50	1.63
		0.58	2.04
		-	2.69
	2600	0.10	0.32
		0.21	0.64
		0.26	0.95
		0.49	1.66
		0.67	1.72
		0.84	1.83
		-	2.05

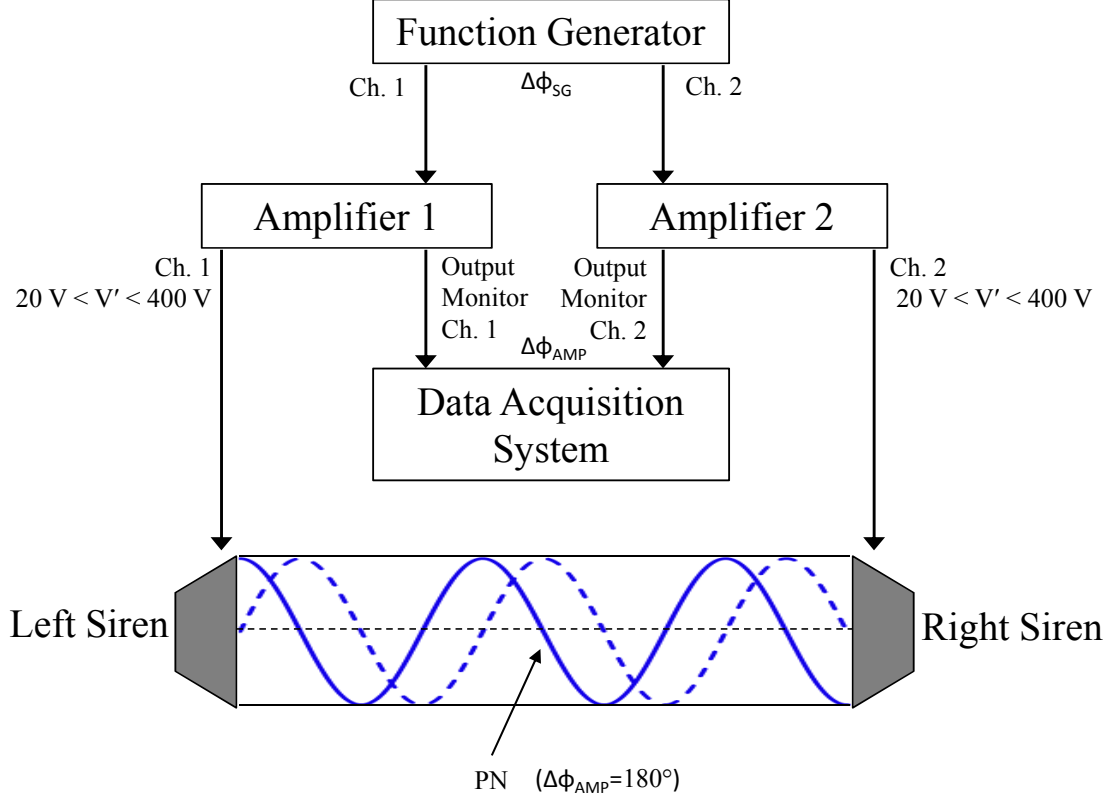
J	f_F [Hz]	p' [kPa]	
		PN	PAN
2	1700	0.35	0.49
		0.80	0.99
		1.17	1.67
		2.08	2.72
		2.89	4.29
		3.69	5.98
		-	9.06
		-	10.52
	2050	0.28	1.59
		0.92	2.72
		1.51	4.17
		2.62	6.08
		3.43	7.58
		3.81	8.52
	2600	0.66	1.40
		1.31	2.18
		1.80	3.64
		2.79	7.92
		3.79	12.95
		5.82	22.27
		8.05	25.85
6	1700	0.38	1.66
		0.81	3.09
		1.40	4.55
		2.14	6.24
		2.34	7.60
		-	8.72
	2050	0.53	2.00
		1.05	4.11
		1.63	4.91
		2.64	8.00
		3.42	11.22
		4.03	14.10
		-	18.56
	2600	0.71	2.18
		1.45	4.40
		1.78	6.55
		3.40	11.43
		4.59	11.85
		5.82	12.62
		-	14.12



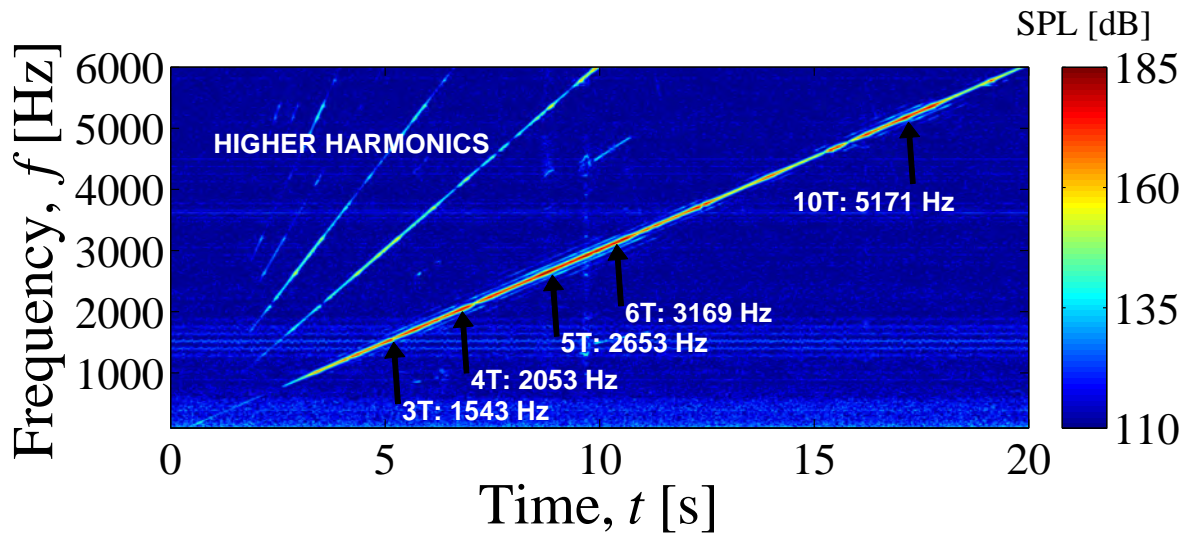
A.1: Piezoelectric acoustic siren, of aluminum construction.



A.2: Cross sectional CAD rendering of the left waveguide.



A.3: Acoustic wiring flow chart. The acoustic piezoelectric sirens are controlled using a dual-channel signal generator. Each of the two channels are controlled to have equal frequency, but unequal phase ϕ . Separate amplifiers produce high voltage signals for each siren, and the amplifiers also send an equivalent low voltage signal to the data acquisition system. The siren phase difference, then, is equal to $\Delta\phi_{AMP}$, which must be 0° to create a PAN at the center of the chamber and 180° to create a PN at the center. As a result of unique phase delays applied by each amplifier, the signal generator phase difference $\Delta\phi_{SG}$ must be dynamically adjusted for each acoustic condition in order to achieve a standing wave, i.e. for $\Delta\phi_{AMP} = 0^\circ \rightarrow \Delta\phi_{SG} \neq 0^\circ$, and for $\Delta\phi_{AMP} = 180^\circ \rightarrow \Delta\phi_{SG} \neq 180^\circ$



A.4: Acoustic pressure spectra results for a PAN condition measured using a pressure transducer in the center of the chamber. Magnitude is scaled with a sound pressure level (SPL) colormap, and key regions of transverse resonance are annotated. $p_c=400$ psia

BIBLIOGRAPHY

- [1] T. C. Lieuwen and V. Yang. *Progress in Astronautics and Aeronautics: Combustion Instabilities in Gas Turbine Engines: Operational Experience, Fundamental Mechanisms, and Modeling*. AIAA, 2006.
- [2] K. R. McManus, T. Poinsot, and S. M. Candel. A review of active control of combustion instabilities. *Progress in Energy and Combustion Science*, 19:1–29, 1993.
- [3] F.E.C. Culick and V. Yang. Overview of combustion instabilities in liquid rocket engines. In V. Yang and W.E. Anderson, editors, *Progress in Astronautics and Aeronautics: Liquid Rocket Engine Combustion Instability*, pages 3–38. AIAA, 1995.
- [4] A. M. Annaswamy and A. F. Ghoniem. Active control of combustion instability: Theory and practice. *Control Systems*, 22(6):37–54, 2002.
- [5] Q. Diao. *Propellant injection strategy for suppressing acoustic combustion instability*. PhD thesis, University of Maryland, College Park, Mechanical and Engineering Department, June 2010.
- [6] S. Candel. Combustion dynamics and control: progress and challenges. Number 29 in Proceedings of the Combustion Institute, pages 1–28, 2002.
- [7] T. Lieuwen, H. Torres, C. Johnson, and B.T. Zinn. A mechanism for combustion instability in lean premixed gas turbine combustors. *J. of Engineering for Gas Turbines and Power*, 123:182–189, 2001.
- [8] F. Richecoeur. *Experiments and numerical simulations of interactions between*

transverse acoustic modes and cryogenic flames. PhD thesis, Ecole Centrale Paris, November 2006.

- [9] Y.C. Yu, S.M. Koeglmeier, J.C. Sisco, and W.E. Anderson. Combustion instability of gaseous fuels in a continuously variable resonance chamber (cvrc). 44th Joint Propulsion Conference and Exhibit, 2008. AIAA 2008-4657.
- [10] P. Yecko, S. Zaleski, and J.-M. Fullana. Viscous modes in two-phase mixing layers. *Physics of Fluids*, 14(12):4115–4122, 2002.
- [11] K.C. Kim and R.J. Adrian. Very large-scale motion in the outer layer. *Physics of Fluids*, 11(2):417–422, 1999.
- [12] P. Givi, W.-H. Jou, and R.W. Metcalfe. Flame extinction in a temporally developing mixing layer. *Twenty-First Symposium (International) on Combustion*, pages 1251–1261, 1986.
- [13] H.K. Chelliah, C.K. Law, T. Ueda, M.D. Smooke, and F.A. Williams. An experimental and theoretical investigation of the dilution, pressure and flow-field effects on the extinction condition of methane-air-nitrogen diffusion flames. *Twenty-Third Symposium (International) on Combustion*, pages 503–511, 1990.
- [14] W.O.H. Mayer and J.J. Smith. Fundamentals of supercritical mixing and combustion of cryogenic propellants. In et al. Yang, V., editor, *Progress in Astronautics and Aeronautics: Liquid Rocket Engine Thrust Chambers*, page 339367. AIAA, 2004.
- [15] Q. Diao, A. Ghosh, and K. H. Yu. Suppression of GO₂/GH₂ combustion instability using CH₄ addition. Number AIAA-2008-1000 in 46th AIAA Aerospace Sciences Meeting, Reno, NV, January 2008.

- [16] F. Baillot, J.-B. Blaisot, G. Boisdron, and C. Dumouchel. Behaviour of an air-assisted jet submitted to a transverse high-frequency acoustic field. *J. of Fluid Mechanics*, 640:305–342, 2009.
- [17] J.C. Sisco, Y.C. Yu, V. Sankaran, and W.E. Anderson. Examination of mode shapes in an instable model combustor. *Journal of Sound and Vibration*, 330:61–74, 2011.
- [18] J.S. Hardi, M. Oswald, and B. Dally. Acoustic characterisation of a rectangular rocket combustor with liquid oxygen and hydrogen propellants. *Proceedings of the Institution of Mechanical Engineers, Part G: Journal of Aerospace Engineering*, 227(3):436–446, 2013.
- [19] Y. Mery, L. Hakim, P. Scoufflaire, L. Vingart, S. Ducruix, and S. Candel. Experimental investigation of cryogenic flame dynamics under transverse acoustic modulations. *Comptes Rendus Mecanique*, 341:100–109, 2013.
- [20] M. Tanabe, T. Morita, K. Aoki, K. Satoh, T. Fujimori, and J. Sato. Influence of standing sound waves on droplet combustion. *Proc. Comb. Inst.*, 28:1007–1013, 2000.
- [21] M. Tanabe, T. Kuwahara, S. Kimiyoshi, T. Fujimori, J. Sato, and M. Kono. Droplet combustion in standing sound waves. *Proc. Comb. Inst.*, 30:1957–1964, 2005.
- [22] S. Dattarajan, A. Lutomirski, R. Lobbia, O.I. Smith, and A.R. Karagozian. Acoustic excitation of droplet combustion in microgravity and normal gravity. *J. Combustion and Flame*, 144:299–317, 2006.
- [23] S. Teshome. *Droplet Combustion and Non-Reactive Shear-Coaxial Jets with Trans-*

- verse Acoustic Excitation*. PhD thesis, University of California, Los Angeles, Department of Mechanical and Aerospace Engineering, March 2012.
- [24] J. Hardi. *Experimental Investigation of High Frequency Combustion Instability in Cryogenic Oxygen-Hydrogen Rocket Engines*. PhD thesis, The University of Adelaide, School of Mechanical Engineering, June 2012.
 - [25] P. Huerre and P. A. Monkewitz. Local and global instabilities in spatially developing flows. *Annual Review of Fluid Mechanics*, 22:473–537, 1990.
 - [26] J.-B. Carpentier, F. Baillot, J.-B. Blaisot, and C. Dumouchel. Behavior of cylindrical liquid jets evolving in a transverse acoustic field. *Physics of Fluids*, 21(2): 1–15, 2009.
 - [27] F.G. Buffum and F.A. Williams. The response of a turbulent jet to transverse acoustic fields. Proceedings of the 1967 Heat Transfer and Fluid Mechanics Institute, pages 247–276, 1967.
 - [28] B. W. Davis and B. Chehroudi. The effects of pressure and acoustic field on a cryogenic coaxial jet. *42nd AIAA Aerospace Sciences Meeting & Exhibit*, 2004. Washington, D.C.
 - [29] I. A. Leyva, J. I. Rodriguez, B. W. Davis, and B. Chehroudi. Preliminary results on coaxial jet spread angles and the effects of variable phase transverse acoustic fields. *46nd AIAA Aerospace Sciences Meeting & Exhibit*, 2008. Reno, NV.
 - [30] S. Teshome, I.A. Leyva, and D.G. Talley. Proper orthogonal decomposition analysis of shear-coaxial injector flows with and without transverse acoustic forcing. *JANNAF Joint Subcommittee Meeting*, 2011. Huntsville, AL.
 - [31] J.W.S. Rayleigh. *The Theory of Sound*. vol. 2, New York: Dover, 1945.

- [32] D.A. Smith and E.E. Zukoski. Combustion instability sustained by unsteady vortex combustion. *Twenty-first Joint Propulsion Conference*, AIAA-85-1248, 1985.
- [33] K.H. Yu, A. Trouve, and J.W. Daily. Low-frequency pressure oscillations in a model ramjet combustor. *J. Fluid Mechanics*, 232:47–72, 1991.
- [34] K.C. Schadow and E. Gutmark. Combustion stability related to vortex shedding in dump combustors and their passive control. *Progress in Energy and Combust. Sci.*, 18:117–132, 1992.
- [35] H.C. Mongia, T.J. Held, G.C. Hsiao, and R.P. Pandalai. Incorporation of combustion instability issues into design process: General electric aeroderivative and aero engines experience. In *Progress in Astronautics and Aeronautics: Combustion Instabilities in Gas Turbine Engines: Operational Experience, Fundamental Mechanisms, and Modeling*, pages 89–107. AIAA, 2006.
- [36] Standards of Performance for Stationary Gas Turbines Environmental Protection Agency, Standards of Performance for New Stationary Sources. Title 40. 2011. Sections 60.330-60.335, <http://www.epa.gov/region7/air/nsps/nspsstandardcontacts.htm>.
- [37] C.T. Bowman. Control of combustion-generated nitrogen oxide emissions: Technology driven by regulation. volume 24 of *Twenty-Fourth Symposium on Combustion*, pages 859–878, 1992.
- [38] K. O. Smith and J. Blust. Combustion instabilities in industrial gas turbines: Solar turbines’ experience. In *Progress in Astronautics and Aeronautics: Combustion Instabilities in Gas Turbine Engines: Operational Experience, Fundamental Mechanisms, and Modeling*, pages 29–41. AIAA, 2006.

- [39] T. Scarinci. Combustion instability and its passive control: Rolls-royce aeroderivative engine experience. In *Progress in Astronautics and Aeronautics: Combustion Instabilities in Gas Turbine Engines: Operational Experience, Fundamental Mechanisms, and Modeling*, pages 65–88. AIAA, 2006.
- [40] B. Wassener. Airlines weigh the advantages of using more biofuel. 2011. The International Herald Tribune, October 10.
- [41] G.P. Sutton and O. Biblarz. *Rocket propulsion elements*. John Wiley and Sons, 2001.
- [42] NASA. J-2 engine fact sheet. *Saturn V News Reference*, December, 1968. retrieved by NASA 22 February 2012.
- [43] D. Haeseler. Peenemuende roots and lessons. In *Liquid Propulsion History I: LOX/HC Propulsion I: Goddard - Peenemuende - Sputnik (8K71PS/8A91 R-7), Vanguard, Juno 1 to Titan, Atlas, Falcon and Beyond*. AIAA Joint Propulsion Conference Presentation Series, July 16, 2013.
- [44] S. Bouley and B. Anderson. Rs-27, md-1, ma-5a-7, lr-89-105, h-1, f-1, s-3d, rs-84 (atlas, delta, thor, saturn 1b and v, jupiter. In *Liquid Propulsion History I: LOX/HC Propulsion I: Goddard - Peenemuende - Sputnik (8K71PS/8A91 R-7), Vanguard, Juno 1 to Titan, Atlas, Falcon and Beyond*. AIAA Joint Propulsion Conference Presentation Series, July 16, 2013.
- [45] J. Hulka and J.J. Hutt. Instability phenomena in liquid oxygen/hydrogen propellant rocket engines. In V. Yang and W.E. Anderson, editors, *Progress in Astronautics and Aeronautics: Liquid Rocket Engine Combustion Instability*, pages 39–72. AIAA, 1995.

- [46] F. E. C. Culick. Unsteady motions in combustion chambers for propulsion systems. 2006. AGARDograph, NATO/RDO-AG-AVT-039.
- [47] J. C. Oefelein and V. Yang. Comprehensive review of liquid propellant combustion instabilities in F-1 engines. *Propulsion and Power*, 9(5):657–677, 1993.
- [48] G. A. Dressler and J. M. Bauer. Trw pintle engine heritage and performance characteristics. Number AIAA-2000-3871 in 36th AIAA/ASME/SAE/ASEE Joint Propulsion Conference and Exhibit, July 2000.
- [49] M. Habiballah, D. Lourme, and F. Pit. Numerical model for combustion stability studies applied to the ariane viking engine. *Propulsion and Power*, 7(3):322–329, 1991.
- [50] H.E. Scott, H.E. Bloomer, and A.H. Mansour. M-1 engine subscale injector tests. *NASA Lewis Research Center*, TN D-4053, 1967.
- [51] S.C. Fisher, F.E. Dodd, and R.J. Jensen. Scaling techniques for liquid rocket combustion stability testing. In V. Yang and W.E. Anderson, editors, *Progress in Astronautics and Aeronautics: Liquid Rocket Engine Combustion Instability*, pages 545–564. AIAA, 1995.
- [52] A. R. Karagozian, W. J. A. Dahm, E. Glasgow, R. Howe, I. Kroo, R. Murray, and H. Shyu. Technology options for improved air vehicle fuel efficiency. 2006. Air Force Scientific Advisory Board Report, Technical Report SAB-TR-06-04.
- [53] SrA Jason Hernandez. SECAF certifies synthetic fuel blends for B-52H. *Edwards Air Force Base, CA*, 2007. Edwards Air Force Base, CA. <http://www.safie.hq.af.mil/news/story.asp?id=123064095>.
- [54] A. D. Sagar and S. Kartha. Bioenergy and sustainable development. *Annual Rev. of Environmental Resources*, 32:131–167, 2007.

- [55] G. A. Mills and E. E. Ecklund. Alcohols as components of transportation fuels. *Annual Review of Energy*, 12(1):47–80, 1987.
- [56] P. M. Morse, R. H. Boden, and H. Schecter. Acoustic vibrations and internal combustion engine performance, i. standing waves in the intake pipe system. *Applied Physics*, 9:16–23, 1938.
- [57] D. E. Winterbone and R. J. Pearson. *Theory of Engine Manifold Design: Wave Action Methods for IC Engines*. Professional Engineering Publishing, London, 2000.
- [58] F. Fischer. *The Conversion of Coal*. Ernst Benn, Ltd., 1925.
- [59] 1st Lt Amanda Ferrell. Air force energy initiatives focus on fuel, beyond. *Edwards Air Force Base, CA*, 2007. <http://www.af.mil/news/story.asp?id=123069617>.
- [60] G.A.E. Godsave. Burning of fuel droplets. *Combustion and Flame*, pages 818–830, 1953. Baltimore, MD. Williams and Wilkins.
- [61] A. Williams. Combustion of droplets of liquid fuels - a review. *Combustion and Flame*, 21, 1973.
- [62] C. K. Law and G. M. Faeth. Opportunities and challenges of combustion in microgravity. *Progress in Energy and Combustion Science*, 20, 1994.
- [63] C. K. Law. Recent advances in droplet vaporization and combustion. *Progress in Energy and Combustion Science*, 8(3):171–201, 1982.
- [64] S. R. Turns. *An Introduction to Combustion*. McGraw Hill, 2000.
- [65] P. M. Struk, M. Ackerman, V. Nayagam, and D. L. Dietrich. On calculating burning rates during fibre supported droplet combustion. *Microgravity Science and Technology*, 11, 1998.

- [66] A.J. Marchese, F.L. Dryer, V. Nayagam, and R.O. Colantino. Hydroxyl radical chemiluminescence imaging and the structure of microgravity droplet flames. Twenty-sixth Symposium (International) on Combustion, pages 1219–1226, 1996.
- [67] A.J. Marchese, R.O. Colantino, F.L. Dryer, and V. Nayagam. Microgravity combustion of methanol and methanol/water droplets: Drop tower experiments and model predictions. Twenty-sixth Symposium (International) on Combustion, pages 1209–1217, 1996.
- [68] S. Kumagai and H. Isoda. Combustion of fuel droplets in a vibrating air field. Fifth Symposium (International) on Combustion, 1955.
- [69] J. Blaszczyk. Acoustically disturbed fuel droplet combustion. *Fuel*, 70(3):1023–1025, 1973.
- [70] M. Saito, M. Sato, and I. Suzuki. Evaporation and combustion of a single fuel droplet in acoustic fields. *Fuel*, 73, 1994.
- [71] M. Saito, M. Hoshikawa, and M. Sato. Enhancement of evaporation/combustion coefficient of a single fuel droplet by acoustic oscillation. *Fuel*, 75, 1996.
- [72] K. Okai, O. Moriue, M. Araki, M. Tsue, M. Kono, J. Sato, and D. L. Dietrich. Combustion of single droplet and droplet pairs in a vibrating field under microgravity. *Proc. Comb. Inst.*, 28, 2000.
- [73] M. Tanabe. Drop tower experiments and numerical modeling on the combustion-induced secondary flow in standing acoustic fields. *J. Microgravity Sci. Technol.*, 22:507–515, 2010.
- [74] D.J. McKinney and D. Dunn-Rankin. Acoustically driven extinction in a droplet stream flame. *Combust. Sci. and Tech.*, 161:27–48, 2000.

- [75] J.I. Rodriguez. *Acoustic Excitation of Liquid Fuel Droplets and Coaxial Jets*. PhD thesis, University of California, Los Angeles, Department of Mechanical and Aerospace Engineering, June 2009.
- [76] M. Faraday. On a peculiar class of acoustical figures; and on certain forms assumed by groups of particles upon vibrating elastic surfaces. *Phil. Trans. R. Soc. Lond.*, 121:229, 1831.
- [77] J.W.S. Rayleigh. On the pressure of vibrations. *Philos. Mag.*, 10:364–374, 1902.
- [78] L.P. Gor’kov. On the forces acting on a small particle in an acoustical field in an ideal fluid. *Soviet Phys.-Doklady*, 6(9):773–775, 1962.
- [79] W.L. Nyborg. Radiation pressure on a small rigid sphere. *J. Acoust. Soc. Am.*, 16(1):947–952, 1967.
- [80] C.P. Lee and T.G. Wang. Acoustic radiation pressure. *J. Acoust. Soc. Am.*, 94(2):1099–1109, 1993.
- [81] J.I. Rodriguez, S. Teshome, H.-S. Mao, A. Pezeshkian, O.I. Smith, and A.R. Karagozian. Acoustically driven droplet combustion with alternative liquid fuels. *46th AIAA Aerospace Sciences Meeting and Exhibit*, 2008.
- [82] S. Teshome, A. Pezeshkian, O.I. Smith, and A.R. Karagozian. Influence of standing acoustic waves on combustion of alternative fuels. *Proc. Am. Phys. Soc.*, 2008.
- [83] A.S.H. Kwan and N.W.M. Ko. Coherent structures in subsonic coaxial jets. *Journal of Sound and Vibration*, 48:203–219, 1976.
- [84] W. Forstall and A.H. Shapiro. Momentum and mass transfer in coaxial gas jets. Massachusetts Institute of Technology, Guided Missiles Program, 1949.

- [85] N.A. Chigier and J.M. Beer. The flow region near the nozzle in double concentric jets. *Journal of Basic Engineering*, 86:797–804, 1964.
- [86] F.H. Champagne and I.J. Wygnanski. An experimental investigation of coaxial turbulent jets. *International Journal of Heat and Mass Transfer*, 14:1445–1464, 1971.
- [87] N.W.M. Ko and A.S.H. Kwan. Experimental investigation of sub sonic coaxial jets. *Proceedings of the 5th Australian Conference on Hydraulics and Fluid Mechanics, University of Canterbury, New Zealand*, 1974.
- [88] N.W.M. Ko and A.S.H. Kwan. The initial region of subsonic coaxial jets. *Journal of Fluid Mechanics*, 73:305–332, 1976.
- [89] P.E. Dimotakis. Two-dimensional shear-layer entrainment. *AIAA Journal*, 24: 1791–1796, 1986.
- [90] W.J.A. Dahm and P.E. Dimotakis. Mixing at large schmidt number in the self-similar far field of turbulent jets. *Journal of Fluid Mechanics*, 217:299–330, 1990.
- [91] P.E. Dimotakis. *Turbulent free shear layer mixing and combustion*. AIAA, 1991.
- [92] W.J.A. Dahm, C.E. Frieler, and G. Tryggvason. Vortex structure and dynamics in the near field of a coaxial jet. *Journal of Fluid Mechanics*, 241:371–402, 1992.
- [93] J.-P. Matas, S. Marty, and A. Cartellier. Experimental and analytical study of the shear instability of a gas-liquid mixing layer. *Physics of Fluids*, 23:094112, 2011.
- [94] N. Chigier and Z. Farago. Morphological classification of disintegration of round liquid jets in a coaxial air stream. *Atomization and Sprays*, 2:2, 1992.
- [95] J.C. Lasheras and E.J. Hopfinger. Liquid jet instability and atomization in a coaxial gas stream. *Annual Review of Fluid Mechanics*, 32:275–308, 2000.

- [96] J.A. Newman and T.A. Brzustowski. Behavior of a liquid jet near the thermodynamic critical region. *AIAA Journal*, 9:1595–1602, 1971.
- [97] M. Oswald, J. J. Smith, R. Branam, J. Hussong, A. Schik, B. Chehroudi, and D. Talley. Injection of fluids into supercritical environments. *Combustion Science and Technology*, 178, 2006.
- [98] B. Chehroudi, D. Talley, and E. Coy. Visual characteristics and initial growth rates of round cryogenic jets at supercritical and supercritical pressures. *Physics of Fluids*, 14:850861, 2002.
- [99] B. Chehroudi and D. Talley. Fractal geometry of a cryogenic nitrogen round jet injected into sub- and super-critical conditions. *Atomization and Sprays*, 14:81–91, 2004.
- [100] J. Telaar, G. Schneider, and W. Mayer. Experimental investigation of breakup of turbulent liquid jets. *ILASS-Europe Conference*, 2000. Darmstadt, Germany.
- [101] M. Oswald, A. Schik, M. Klar, and W. Mayer. Investigation of coaxial ln_2gh_2 -injection at supercritical pressure by spontaneous raman scattering. *AIAA 99-2887, 35th Joint Propulsion Conference*, 1999. Los Angeles, CA.
- [102] B. W. Davis and B. Chehroudi. Shear-coaxial jets from a rocket-like injector in a transverse acoustic field at high pressures. *44th AIAA Aerospace Sciences Meeting & Exhibit*, 2006. Reno, NV.
- [103] DW Davis. *On the Behavior of a Shear-Coaxial Jet Spanning Sub-to Supercritical Pressures With and Without an Externally Imposed Acoustic Field*. PhD thesis, PhD Thesis, Dept. of Mech. and Nuc. Eng., the Pennsylvania State University, 2006.

- [104] J.J. Graham, I.A. Leyva, J.I. Rodriguez, and D. Talley. On the effect of a transverse acoustic field on a shear coaxial injector. *45th AIAA/ASME/SAE/ASEE Joint Propulsion Conference and Exhibit*, 2009-5142.
- [105] I.A. Leyva, B. Chehroudi, and D. Talley. Dark core analysis of coaxial injectors at sub-, near-, and supercritical pressures in a transverse acoustic field. *43rd AIAA/ASME/SAE/ASEE Joint Propulsion Conference and Exhibit*, 5:275–282, 2007-5456.
- [106] S.C. Crow and F.H. Champagne. Orderly structure in jet turbulence. *Journal of Fluid Mechanics*, 48:547–591, 1971.
- [107] Anne-Laure Birbaud, Daniel Durox, Sébastien Ducruix, and S Candel. Dynamics of free jets submitted to upstream acoustic modulations. *Physics of Fluids*, 19: 013602, 2007.
- [108] A. Talamelli and I. Gavarini. Linear instability characteristics of incompressible coaxial jets. *Flow Turbulence Combust*, 76:221–240, 2006.
- [109] A. Segalini and A. Talamelli. Experimental analysis of dominant instabilities in coaxial jets. *Physics of Fluids*, 23:024103, 2011.
- [110] J.-M. Chomaz. Global instabilities in spatially developing flows: Non-normality and nonlinearity. *Annual Review of Fluid Mechanics*, 37:357–392, 2005.
- [111] P. A. Monkewitz, D. W. Bechert, B. Barsikow, and B. Lehmann. Self-excited oscillations and mixing in a heated round jet. *Journal of Fluid Mechanics*, 213: 611–639, 1990.
- [112] D. M. Kyle and K. R. Sreenivasan. The instability and breakdown of a round variable-density jet. *Journal of Fluid Mechanics*, 249:619–664, 1993.

- [113] P.J. Strykowski and D.L. Niccum. The stability of countercurrent mixing layers in circular jets. *Journal of Fluid Mechanics*, 227:309, 1991.
- [114] P.J. Strykowski and D.L. Niccum. The influence of velocity and density ratio on the dynamics of spatially developing mixing layers. *Physics of Fluids*, 4:770, 1992.
- [115] M. Provansal, C. Mathis, and L. Boyer. Benard-von karman instability: transient and forced regimes. *Journal of Fluid Mechanics*, 182:1–22, 1987.
- [116] D. Hammond and L. Redekopp. Global dynamics of symmetric and asymmetric wakes. *Journal of Fluid Mechanics*, 331:231–260, 1997.
- [117] S. Megerian, J. Davitian, L. S. de B. Alves, and A. R. Karagozian. Transverse jet shear-layer instabilities. part 1. experimental studies. *Journal of Fluid Mechanics*, 593:93–129, 2007.
- [118] M.P. Juniper, L.K.B. Li, and J.W. Nichols. Forcing of self-excited round jet diffusion flames. *Proceedings of the Combustion Institute*, 32:1191–1198, 2009.
- [119] M. P. Hallberg and P. J. Strykowski. Open-Loop Control of Fully Nonlinear Self-Excited Oscillations. *Physics of Fluids*, 20:041703, 2008.
- [120] B. Pier. Open-Loop Control of Absolutely Unstable Domains. *Royal Society of London Proceedings Series A*, 459(2033):1105–1115, 2003.
- [121] S. Jendoubi and P.J. Strykowski. Absolute and convective instability of axisymmetric jets with external flow. *Physics of Fluids*, 6:3000–3009, 1994.
- [122] D.R. Getsinger, C. Hendrickson, and A.R. Karagozian. Shear layer instabilities in low-density transverse jets. *Exp Fluids*, 53:783–801, 2012.
- [123] K.R. Sreenivasan, S. Raghu, and D. Kyle. Absolute instability in variable density round jets. *Exp Fluids*, 7:309–317, 1989.

- [124] C.C. Miesse. The effect of ambient pressure oscillations on the disintegration and dispersion of a liquid jet. *Jet Propulsion*, 25:525–530, 1955.
- [125] Ray Snyder, Gerald Herding, JUAN CARLOS ROLON, and Sébastien Candel. Analysis of flame patterns in cryogenic propellant combustion. *Combustion science and technology*, 124(1-6):331–370, 1997.
- [126] S. Candel, G. Herding, R. Snyder, P. Scoufflaire, C. Rolon, D. Stepowski, A. Cessou, and P. Colin. Experimental investigation of shear coaxial cryogenic jet flames. *J. of Propulsion and Power*, 14(5):826–834, 1998.
- [127] Louis Baker and Fred W Steffen. *Screaming Tendency of the Gaseous-hydrogen-Liquid-oxygen Propellant Combination*. National Advisory Committee for Aeronautics, 1958.
- [128] Marcus F Heidmann. *Oscillatory combustion of a liquid-oxygen jet with gaseous hydrogen*. National Aeronautics and Space Administration, 1965.
- [129] G. Singla, P. Scoufflaire, C. Rolon, and S. Candel. Planar laser-induced fluorescence of oh in high-pressure cryogenic LOx/GH2 jet flames. *Combustion and Flame*, 144: 151–169, 2006.
- [130] G. Singla, P. Scoufflaire, C. Rolon, S. Candel, and L. Vingert. Oh planar laser-induced fluorescence and emission imaging in high-pressure LOx/Methane flames. *J. of Propulsion and Power*, 23(3):593–602, 2007.
- [131] F. Richecoeur, S. Ducruix, P. Scoufflaire, and S. Candel. Effect of temperature fluctuations on high frequency acoustic coupling. *Proc. of the Combustion Institute*, 32:1663–1670, 2009.
- [132] Cédric Rey, Sébastien Ducruix, Franck Richecoeur, Philippe Scoufflaire, Lucien

- Vingert, and Sébastien Candel. High frequency combustion instabilities associated with collective interactions in liquid propulsion. *AIAA Paper*, 3518:11–14, 2004.
- [133] S. Pavithran and L.G. Redekopp. The absolute-convective transition in subsonic mixing layers. *Physics of Fluids*, 1:1736, 1989.
- [134] P.A. Monkewitz, D.W. Bechert, B. Barsikow, and B. Lehmann. Self-excited oscillations and mixing in a heated round jet. *Journal of Fluid Mechanics*, 213:611, 1990.
- [135] J. Eldredge. Private communications. *UCLA*, 2009.
- [136] K.T. Walsh, M.B. Long, M.A. Tanoff, and M.D. Smooke. Experimental and computational study of CH, CH*, and OH* in an axisymmetric laminar diffusion flame. Twenty-sixth Symposium (International) on Combustion, pages 615–623, 1998.
- [137] H.N. Najm, P.H. Paul, C.J. Mueller, and P.S. Wyckoff. On the adequacy of certain experimental observables as measurements of flame burning rate. *Combustion and Flame*, 113:312–332, 1998.
- [138] J. Kojima, Y. Ikeda, and T. Nakajima. Spatially resolved measurement of OH*, CH*, and C*₂ chemiluminescence in the reaction zone of laminar methane/air premixed flames. *Proc. Comb. Inst.*, 28:1757–1764, 2000.
- [139] A. F. Mills and B. H. Chang. Error analysis of experiments. *UCLA, Los Angeles, CA*, 2004.
- [140] C. J. Dasch. One-dimensional tomography: a comparison of abel, onion-peeling, and filtered backprojection methods. *J. Applied Optics*, 31(8):1146–1152, 1992.
- [141] L. Hoogterp-Decker and P. Schihl. The use of synthetic jp-8 fuels in military engines. 2009. RDECOM-TARDEC, Warren, MI.

- [142] S. Teshome, O.I. Smith, and A.R. Karagozian. Droplet combustion in the presence of altered acceleration fields via acoustic excitation. *Western States Sections of the Combustion Institute*, 2009.
- [143] W.L. Nyborg. Acoustic streaming due to attenuated plane waves. *J. Acoust. Soc. Am.*, 25(1):68–75, 1953.
- [144] W.L. Nyborg. Acoustic streaming near a boundary. *J. Acoust. Soc. Am.*, 30(4): 329–339, 1958.
- [145] A. L. Smith and C. C. Graves. Drop burning rates of hydrocarbon and nonhydrocarbon fuels. In *NACA RME 57*. F11, 1957.
- [146] B. Vielle, C. Chauveau, X. Chesneau, A. Odeide, and I. Gokalp. High pressure droplet burning experiments in microgravity. *Proc. Combustion Inst.*, 26, 1996.
- [147] B.R. Munson, A.P. Rothmayer, T.H. Okiishi, and W.W. Huebsch. *Fundamental Fluid Mechanics*. Wiley, 5th edition, 2005.
- [148] Frank M White. *Viscous Fluid Flow 3e*. Tata McGraw-Hill Education, 1974.
- [149] O.J. Haidn. Advanced rocket engines. In *Advances on Propulsion Technology for High-Speed Aircraft, Educational Notes RTO-EN-AVT-150*, pages 6–1 6–40. Neuilly-sur-Seine, France: RTO, 2008.
- [150] A.G. Webster. Acoustical impedance, and the theory of horns and of the phonograph. *Proceedings of the National Academy of Sciences*, 5:275–282, 1919.
- [151] A. D. Pierce. *Acoustics: An Introduction to Its Physical Principles and Applications*. Acoustical Society of America, 1991.
- [152] P.J. Schmid. Dynamic mode decomposition of numerical and experimental data. *Journal of Fluid Mechanics*, 656:5–28, 2010.

- [153] M. Arienti, M. Corn, G.S. Hagen, R.K. Madabhushi, and M.C. Soteriou. Proper orthogonal decomposition applied to liquid jet dynamics. *21st Annual ILASS-Americas Conference*, 2008. Orlando, FL.
- [154] M. Arienti and M.C. Soteriou. Dynamics of free jets submitted to upstream acoustic modulations. *Physics of Fluids*, 21:112104, 2009.
- [155] MR Jovanovic, PJ Schmid, and JW Nichols. Low-rank and sparse dynamic mode decomposition. pages 139–152, 2012.
- [156] P.J. Schmid. Application of the dynamic mode decomposition to experimental data. *Experiments in Fluids*, 50:1123–1130, 2011.
- [157] P.J. Schmid, L. Li, M.P. Juniper, and O. Pust. Applications of the dynamic mode decomposition. *Theor. Comput. Fluid Dyn.*, 25:249–259, 2011.
- [158] National Institute of Standards and Technology. Thermophysical properties of fluid systems, 2011.
- [159] R.D. Woodward, S. Pal, S. Farhangi, G.E. Jensen, and R.J. Santoro. LOx/GH2 shear coaxial injector atomization studies: effect of recess and non-concentricity. *45th AIAA Aerospace Sciences Meeting and Exhibit*, pages 1–22, 2007-571.